EXPLORING PARTICLE FLOW IN A HYDROCYCLONE CLASSIFIER THROUGH POSITRON EMISSION PARTICLE TRACKING (PEPT)

Joshua Mitchell Sovechles

Department of Mining and Materials Engineering

McGill University

Montreal, Canada

November 2017

A THESIS SUBMITTED TO MCGILL UNIVERSITY
IN PARTIAL FULFILMENT OF THE REQUIREMENTS OF THE DEGREE OF
DOCTOR OF PHILOSOPHY

Abstract

The hydrocyclone is a continuously operating classifying device that utilises differences in drag and inertial forces to separate particles based on size, shape and density. Hydrocyclones are used extensively in the mineral processing industry, with their primary use being in closed circuit grinding. The importance of their performance on the efficiencies of both the grinding circuit and downstream processes has led to their characterisation *via* empirical models. However, empirical models are limited to the range of process conditions used in their creation, and often require additional testing to calibrate the results to specific applications. Computational Fluid Dynamics (CFD) provides a more fundamental approach to the modelling and prediction of the flow of water and particles within the hydrocyclone. A thorough literature review determined that while computationally expensive, CFD is able to accurately predict fluid flow and particle classification at low solid concentrations (< 10 % by volume). The modelling of high solid concentration slurries, which are more consistent with industrial conditions, is currently the focus of many researchers. The validation of such models also provides a significant challenge. Due to the opacity of slurries, visual or laser diffraction techniques are only able to measure particle velocities in flows with low solid concentrations (< 1 % by weight). Positron Emission Particle Tracking (PEPT) is a technique that allows for a radioactive particle to be tracked through the triangulation of the emitted gamma rays, therefore no optical observation is required. The high particle velocities, coupled with the tight curvature, within the hydrocyclone fall outside of the typical dynamic range studied by PEPT, which has limited previous PEPT experimentation. The implementation of a new modular positron camera design allowed for the creation of a highly sensitive field of view, necessary for the tracking of high speed, low activity tracers. The tracking performance of this cross-pattern assembly was first analysed to determine the 3D location error and location frequency as a function of tracer activity and speed. Using this information, trajectories for particle sizes down to the 106-212 µm size range were determined, a large improvement when compared with previous studies. Results showed that repeatable velocity fields can be produced, which is the first time a velocity profile has been reported for the hydrocyclone using the PEPT technique. A CFD simulation of the trajectory of a 1 mm quartz sphere was conducted to compare to the results of PEPT. While the trajectory was found to closely match that measured by PEPT, the velocity magnitude, and therefore residence time, of the particle was found to vary greatly from the measured value. This indicated that more work is required to model particle flow behaviour.

Résumé

L'hydrocyclone est un dispositif de classification à fonctionnement continu qui utilise les différences de forces de traînée et d'inertie pour séparer les particules en fonction de la taille, de la forme et de la densité. Les hydrocyclones sont largement utilisés dans l'industrie du traitement des minéraux, leur principale utilisation étant le broyage en circuit fermé. L'importance de leurs performances sur les efficacités du circuit de broyage et des processus en aval a conduit à leur caractérisation par des modèles empiriques. Cependant, les modèles empiriques sont limités à la gamme des conditions des processus utilisés dans leur création, et nécessitent souvent des tests supplémentaires afin de calibrer les résultats à des applications spécifiques. La dynamique des fluides computationnelle (DFC) fournit une approche plus fondamentale de la modélisation et de la prédiction du flux d'eau et de particules dans l'hydrocyclone. Un examen approfondi de la littérature a permis de déterminer que, bien que coûteux en termes de calcul, le DFC est capable de prédire avec précision le débit et la classification des particules à de faibles concentrations de solides (<10% en volume). La modélisation des suspensions à haute concentration de solides, qui sont plus compatibles avec les conditions industrielles, est actuellement l'enjeu de nombreux chercheurs. La validation de ces modèles constitue également un défi important. En raison de l'opacité des suspensions, les techniques de diffraction visuelle ou par laser ne permettent de mesurer les vitesses des particules que dans des écoulements à faible concentration de solides (<1% en poids). Le suivi des particules à émission de positrons (PEPT) est une technique qui permet de suivre une particule radioactive à travers la triangulation des rayons gamma émis, et donc, aucune observation optique n'est requise. Les vitesses de particules élevées, couplées à la courbure serrée, à l'intérieur de l'hydrocyclone tombent en dehors de la plage dynamique typique étudiée par le PEPT, ce qui a limité les expérimentations PEPT faites par le passé. La mise en œuvre d'une nouvelle conception de caméra à positron modulaire a permis la création d'un champ de vision très sensible, nécessaire au suivi des traceurs à haute vitesse et à faible activité. La performance de poursuite de cet ensemble de motifs croisés a d'abord été analysée afin de déterminer l'erreur de localisation 3D et la fréquence de localisation en fonction de l'activité et de la vitesse du traceur. En utilisant cette information, des trajectoires pour des tailles de particules allant jusqu'à 106-212 μm ont été déterminées, une amélioration importante par rapport aux études précédentes. Les résultats ont démontré que des champs de vitesse reproductibles peuvent être produits, ce qui est la première fois qu'un profil de vitesse a été rapporté pour l'hydrocyclone en

utilisant la technique PEPT. Une simulation CFD de la trajectoire d'une sphère de quartz de 1 mm a été réalisée afin de la comparer aux résultats du PEPT. Bien que la trajectoire ait été trouvée proche de celle mesurée par PEPT, l'amplitude de la vitesse, et par conséquent le temps de résidence, de la particule s'est révélée être très différente de la valeur mesurée. Cela indique que davantage de travail est requis sur le comportement de l'écoulement des particules.

Acknowledgements

I wish to express my deepest appreciation to all those that have contributed towards the completion of my PhD and to those who have indirectly helped me throughout. However, one person, in particular, was with me throughout the entirety of the project and always supported me. So, thank you for everything Camille, this could not have been done without you.

To my main supervisor Professor Kristian E. Waters, thank you for taking me as your student and for always making yourself available for discussion. Your relaxed demeanour and approachable nature meant I was never too stressed. Our many business meetings at the Old Dublin and games of soccer or hockey will be remembered fondly.

To my co-supervisor Professor Agus P. Sasmito, thank you for your help with the very challenging subject of computational modelling. Considering I knew nothing about CFD at the beginning of the project, your patience and time was always appreciated.

To the McGill mineral processing group, there are many highly skilled individuals, both past and present, who have in some way furthered my understanding of mineral processing. While there are too many names to mention, Dr Darryel Boucher needs a special mention for the countless hours spent discussing our projects and mineral processing in general and for introducing me to the wonders of the Côte-Nord. For the other members, memories such as the ski trips, hockey games, plant work, BBQs or conferences, will always be remembered.

To the collaborators outside of the McGill research group, Dr Randolph Pax (RAP Innovation & Development Pty Ltd) and Dr Thomas Leadbeater (University of Cape Town), your help with the PEPT electronics and signal processing was invaluable to this project and was greatly appreciated.

To my Australian family and friends, although you still do not fully understand what I do, I thank you for your endless support and love. To my brothers and sister thanks for giving me a happy reason to take the 16,000 km flight home to Newcastle, and to my parents Mitchell and Mandy for always being there to pick me up. Going home was like a refuge from the constant challenge of my PhD.

To my Montreal family and friends, and those I convinced to come visit, although you also do not fully understand what I do, thanks for making me fall even more in love with Montreal and making it feel like a second home.

Contribution of Authors

I, Joshua Sovechles (the PhD candidate), performed all PEPT experimentation; wrote all the Matlab Code and completed all the data analysis; and wrote and completed final revisions of all the manuscripts. However, this thesis was made possible due to the help of my co-authors. Darryel Boucher (PhD graduate, McGill University) was a constant source of help and was present for all PEPT experimentation and provided a great deal of insight for the processing of PEPT data. Luis Vinnett (PhD candidate, McGill University) helped with the trajectory fitting process and provided an excellent source for discussion. Dr Randolph Pax (RAP Innovation & Development Pty Ltd) assisted with the creation of the Matlab code for the results shown in Chapter 4 and again was a constant source for discussion. Dr Thomas Leadbeater (University of Cape Town) carried out all the electrical set-up for the modular camera assembly and data acquisition system. He also provided the track code for the analysis of the particle locations. Ray Langlois (Technician, McGill University) handled all the logistical problems associated with the PEPT test work that was completed at the University of Birmingham. This involved handling the shipping of the equipment, ordering supplies for the camera support structure and being present during the PEPT experimentation. Finally, my supervisor Professor Kristian Waters and my co-supervisor Doctor Agus Sasmito supported me throughout the entirety of the project.

Table of Contents

List of Figures

List of Tables

Nomenclature

C_D	Drag Coefficient
C_s	Smagorinsky Lilly constant
d_p	Particle diameter
d_{25}	Diameter at which 25 % of feed particles report to underflow
d_{50}	Diameter at which 50 % of feed particles report to underflow
d_{75}	Diameter at which 75 % of feed particles report to underflow
D_w	Distance to the closest wall
E	Average Distance Between LoRs
f	Fraction of LoRs kept
F_B	Buoyancy Force
F_D	Drag Force
g	Gravity
I	Imperfection Parameter
L_S	Length scale of the SGS stresses
N	Number of LoRs
p	Smoothing Parameter
Re_p	Relative Reynolds Number
S	Number of Times a LoR is reused
S_{ij}	Mean strain rate
t	Time
u_i	i component of velocity
V_g	Volume of finite grid cell
w_i	Weighting function
x_i	i coordinate

Greek Symbols

α_k	Volume fraction of phase k
δ_{ij}	Kronecker delta
κ	von Kármán constant
$\mu_{t,s}$	SGS eddy viscosity
ρ	Density
$\tau_{ij}{}^{sgs}$	Turbulent or SGS stress tensor
τ_{kk}	Isotropic part of the SGS stresses

Chapter 1:   Introduction

1.1   Background

1.1.1   Minerals, Rocks and Ores

The formations in which metals are found in the Earth's crust are determined by their reactivity with their environment, in particular with oxygen, sulphur, and carbon dioxide. Non-reactive metals such as gold and platinum are predominantly found in their native or metallic form. Reactive metals, on the other hand, are always found in compound form, such as oxides, silicates or sulphides. These naturally occurring chemical compounds are known as minerals. Minerals by definition are natural, inorganic substances possessing a defined chemical composition and atomic structure. The term mineral processing, however, is often used in a much broader context. It includes the processing of any material with economic value that is extracted from the earth, including coal, chalk, specific clays, and granite. Such materials are, in fact, rocks, which are not homogeneous in chemical or physical composition, but generally consist of a variety of minerals. Coal is the exception to this rule as it does not technically meet the criteria of being a rock or mineral, as it is made up of organic material. However, for all intents and purposes coal is considered an organic sedimentary rock.

The crustal abundance of metals is relatively low, with copper, the most important non-ferrous metal, only accounting for 0.0055 % of the earth's crust. It is therefore apparent that if the minerals containing important metals were uniformly distributed throughout the earth, they would be so thinly dispersed that their economic extraction would be impossible. However, due to the action of geological events, minerals have concentrated in certain areas and therefore are at a suitable level to be profitably extracted, thus becoming an ore deposit. Most ores are mixtures of economically extractable minerals and extraneous non-valuable material described as gangue. Mineral processing involves the liberation (*via* size reduction) and separation of the valuable material from the gangue. This concentration, often conducted in close proximity to the mine's location, allows for previously uneconomical ore deposits to be upgraded to level deemed useful to society (Wills and Finch, 2016).

1.1.2   The Basics of Mineral Processing

The operations of mineral processing can be broken down into three broad categories: comminution, separation and product handling (Figure 1.1a). Comminution involves a series of size reduction steps, undertaken by multiple crushing and grinding units (Figure 1.1b), to liberate the valuable materials from the waste rock (gangue). Liberation, shown in Figure 1.2, is achieved when the grinding product is a mixture of relatively pure mineral and gangue particles.

(a)   (b)
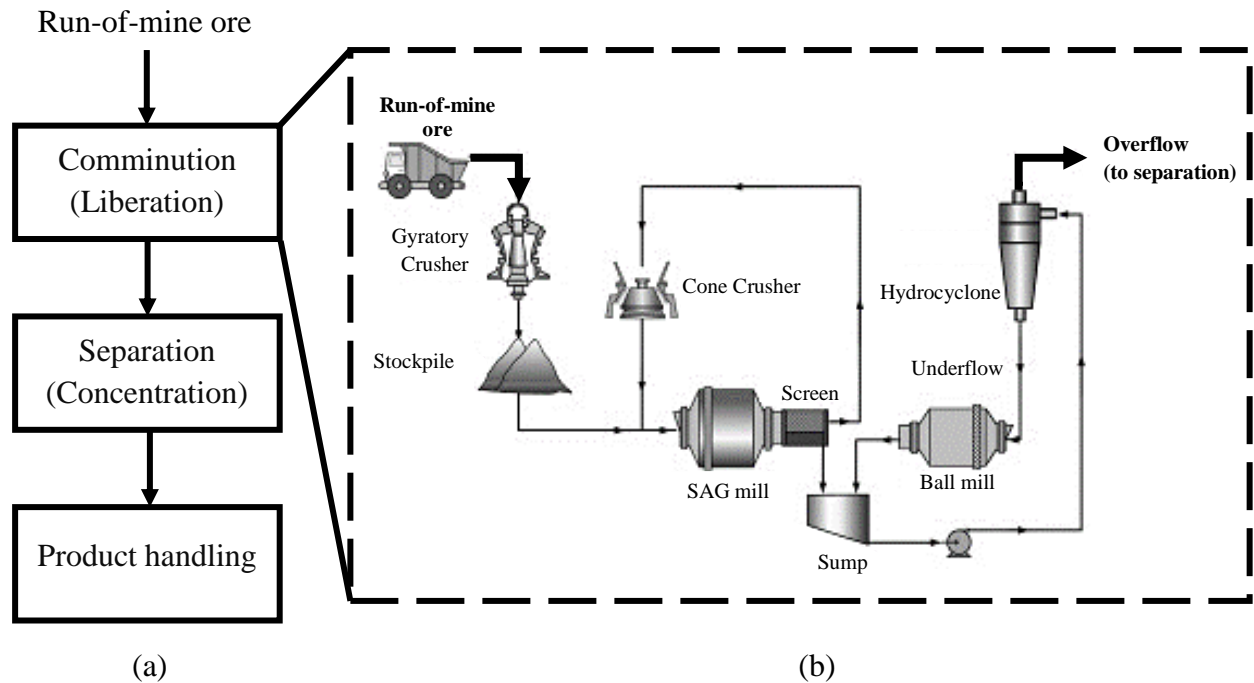
Figure 1.1: (a) Simplified block flowsheet of mineral processing, with (b) a more detailed flowsheet of a typical comminution circuit. Adapted from Wills and Finch (2016).

Ore, taken directly from the mining process and termed run-of-mine (ROM), is crushed from sizes of 1.5 m down to approximately 1-2 cm. Grinding follows crushing, further reducing the size to 25-300 µm depending on the grain sizes of the valuable material. Grinding is known to be extremely energy intensive, consuming up to 50 % of a concentrator's energy consumption (Radziszewski, 2013). Therefore, the objective of comminution is to liberate the valuable mineral(s) at the coarsest possible particle size. Once the particles reach the correct size, determined by their degree of liberation, they are forwarded to a separation stage. This is achieved *via* classification, using units such as the hydrocyclone. Proper classification will reduce energy consumption and improve downstream separation processes (discussed further in Section 2.3).
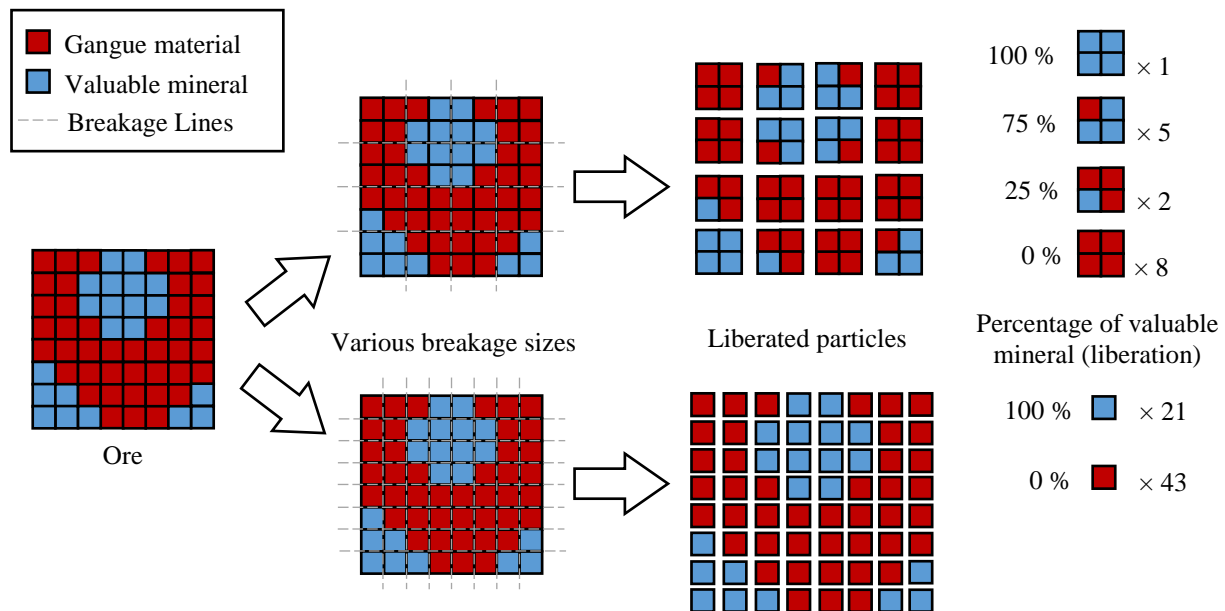
Figure 1.2: Liberation of the components of a binary ore. The diagram shows the relationship between size reduction and liberation, where the decreased particle size led to greater liberation of the valuable mineral.

The separation process allows for the valuable material to be removed from the gangue by exploiting differences in physical or chemical properties. Froth flotation is the most versatile method of mineral concentration. It involves the attachment of mineral particles to air bubbles within an agitated pulp, with the valuable material collected in the froth phase. Other common physical properties used to concentrate ores include: density (*via* gravity concentration); magnetic susceptibility (*via* high or low intensity magnetic separators); and electrical conductivity (*via* electrostatic separation). Regardless of the chosen separation process, two outputs will be produced: a concentrate stream (with a high concentration of the valuable material) and a tailings stream (consisting primarily of waste material). Product handling includes all the additional processes needed in the production of a saleable product and for waste removal. This includes dewatering and filtering, tailings disposal (back filling), and shipment of concentrates (Wills and Finch, 2016).

1.1.3 Mineral Demand, Depletion and Need for Development

The practice of mineral processing, in its crudest form, is as old as human civilisation itself. From the flint and obsidian blades of the Stone Age, to the uranium ores of Atomic Age, the use of

minerals or rocks has had a key role in the development of society as we know it today. Mineral production is driven by the continued consumption of said resources in middle to high income countries, and by the unprecedented levels required by the rapid development of low income countries (Prior *et al.*, 2012). While mineral stocks are unquestionably finite, improved technology and rising resource prices have allowed mining companies to produce minerals and metals at greater rates than at any other time in history (Mudd, 2010). This current oversupply of raw materials, however, masks a persistent underlying global challenge: namely, how to supply raw materials to an expanding global population that is expected to reach 8.5 billion by 2030 (Ali *et al.*, 2017). This puts increased focus on our future ability to access mineral resources and the economic, social and environmental costs of doing so. As high grade, quality deposits continue to reach extinction, newly operational deposits are continuing to decline in both grade and quality (Figure 1.3). This increases the environmental and processing challenges that comes from issues such as ore depth and location, fineness of grain, mineralogy complexity or impurities such as arsenic or mercury. This is represented in part by the increase in both processed ore and mined waste material (Figure 1.4)
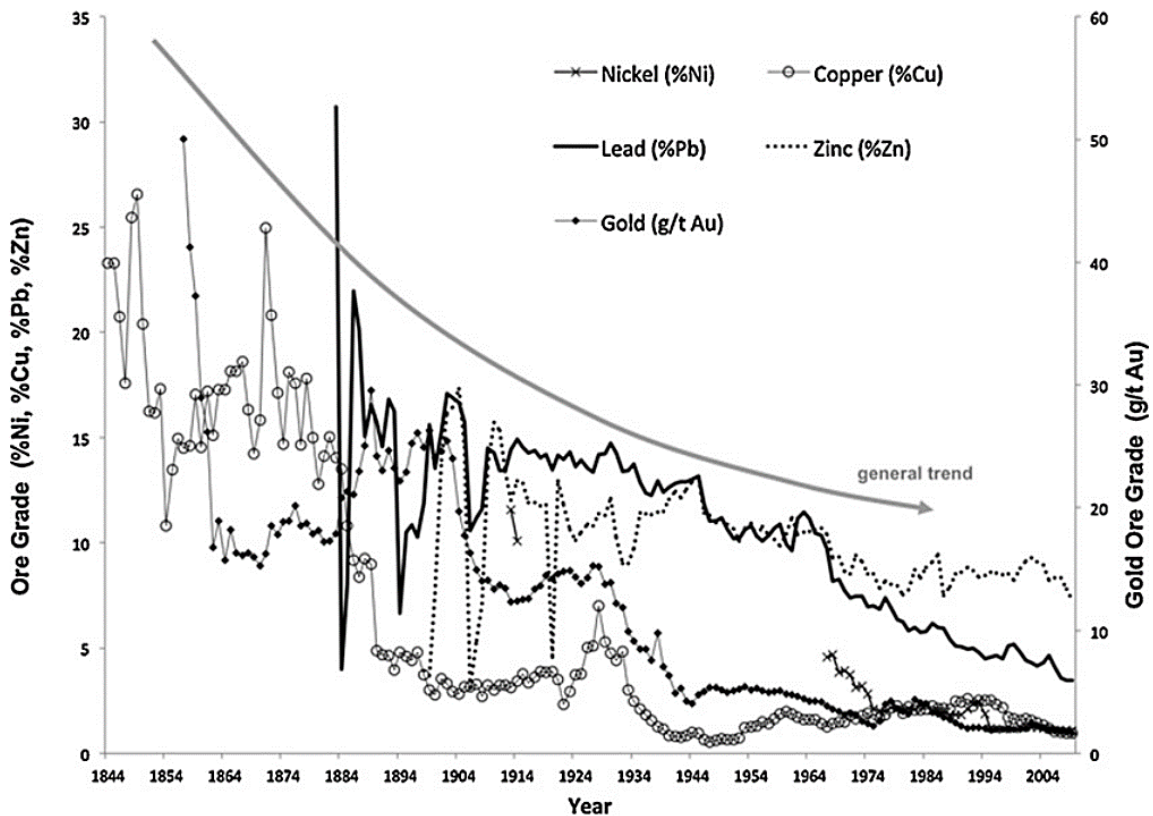
Figure 1.3: The steadily declining trend for ore grades, based upon data from a variety of base and precious metal operations in Australia. Reproduced with permission from Prior *et al.* (2012).

4
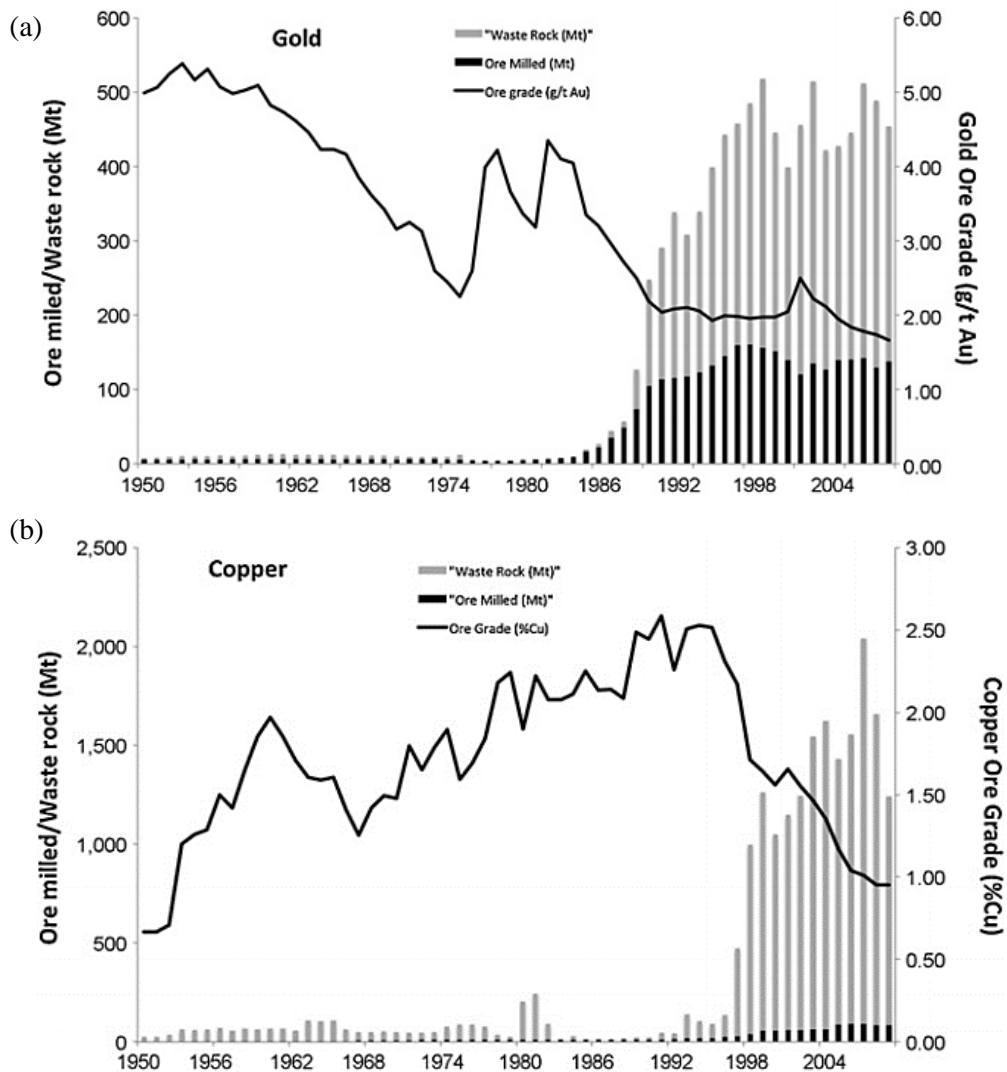
Figure 1.4: The relative quantity of waste rock compared to ore milled for (a) gold and (b) copper, which has increased dramatically in the last 20 years. Reproduced with permission from Prior *et al.* (2012).

1.1.4 Designing the Future – The Need for Computers

The minerals industry must continue to demand a high level of productivity and efficiency in the processing of raw materials. In this mindset, to produce products at the lowest possible environmental and economic cost, it is essential that mineral processing and metal production companies optimise, as far as possible, every element of their processing plant. The increased scale of modern mining sites means that incremental improvement represents a large economic benefit. Modern Computational Fluid Dynamics (CFD) is a powerful tool which can be utilised to significantly enhance the understanding of various unit operations. The continued advancements

5

in computational hardware and software, coupled with the increased experience of practitioners and expanded literature database, have led to the successful implementation of CFD models in many industrial design applications. The ability to accurately model a unit system, such as the dense multiphase flow in a hydrocyclone, allows for the assessment of multiple geometrical designs and various flow behaviour, without the requirement of expensive material or manufacturing costs (Mittoni and Schwarz, 1998). Proper modelling, however, must always be used in conjunction with experimentally determined results. It is therefore important to develop a range of measurement techniques to study particle and fluid flows to build such databases (Grace and Taghipour, 2004).

1.2 Thesis Objectives

The primary goal of this research project was to further the accuracy and applications of hydrocyclone models. Empirical models have gained widespread use due to their simplicity and lack of a better alternative. However, their limited versatility and requirements for additional experimental testing means these models can never provide true prediction or optimisation. After a comprehensive review of the literature on computational models of hydrocyclones (presented in Chapter 3), it was evident that experimental data for particle velocities in high solid content flows (< 10 % by weight) was a major area of study missing in the field.

Positron Emission Particle Tracking (PEPT) was selected as an area of interest, as it allows for the tracking of particles in opaque dense flows, not possible *via* optical techniques. Previous work conducted by Radman *et al.* (2014) demonstrated that the conventional positron camera used for PEPT, the ADAC Forte (Parker *et al.*, 2002), was not sensitive enough to capture the high speed, curved flow in the hydrocyclone. Therefore, the tracking of particles using a new camera design was required. This was accomplished by completing the following sub-objectives:

1. Design a modular positron camera with a field of view suited to the geometry of the hydrocyclone.
2. Study the location accuracy (three-dimension location error) of the new modular camera assembly, for a range of different tracer activities and speeds, by comparing calculated trajectories to a known path.

3. Determine the optimum processing parameters (for the *track* code) for a range of different tracer activities and speeds, using the location error as a metric.

4. Produce three-dimensional trajectories and velocity profiles of mineral particles in the hydrocyclone.

The final objective was to create a preliminary CFD model of the hydrocyclone, based upon the theory presented in Chapter 3. This entails the two-phase (air-water) modelling of the flow in the hydrocyclone, with the addition of a single particle. The experimental results obtained from the PEPT experimentation was used to validate the model's results.

1.3   Thesis Structure

The following thesis is structured as a manuscript based thesis. A manuscript thesis is presented as a collection of papers written by the candidate, which are either published or to be published. As with a traditional thesis an introduction, literature review and conclusions are all still necessary. The current chapter contains a brief introduction to mineral processing and outlines the project goals and thesis structure. Chapter 2 presents a literature review of classification, with particular focus on the hydrocyclone. Chapters 3 to 6 contain the four manuscripts, which in order are:

Chapter 3:   A review of the computational modelling of hydrocyclones – a need for understanding and prediction. (To be submitted as: Sovechles, J.M., Sasmito, A.P., Waters, K.E., 2017. A review of the computational modelling of hydrocyclones – a need for understanding and prediction.)

Chapter 4:   Performance analysis of a new positron camera geometry for high speed, fine particle tracking. (Published as: Sovechles, J.M., Boucher, D., Pax, R., Leadbeater, T., Sasmito, A.P., Waters, K.E., 2017. Performance analysis of a new positron camera geometry for high speed, fine particle tracking. Measurement Science and Technology 28, 095402.)

Chapter 5:   Improvements in positron emission particle tracking within a hydrocyclone. (Submitted to Chemical Engineering Science in September 2017: Sovechles, J.M., Boucher, D., Vinnett, L., Pax, R., Leadbeater, T., Langlois, R., Sasmito, A.P., Waters, K.E.,

2017. Improvements in positron emission particle tracking within a hydrocyclone. Current Status – Under review)

Chapter 6:   A CFD simulation of a single particle's flow inside a hydrocyclone with validation through PEPT (To be submitted as: Sovechles, J.M., Sasmito, A.P., Waters, K.E., 2017. A CFD simulation of a single particle's flow inside a hydrocyclone with validation through PEPT.)

As the four manuscripts are presented as published, the reader should note that some aspects of the literature reviews may be repetitious. In between Chapters 3 to 6, linking text is provided to help give the reader context for the progression from one chapter to the next. To finish Chapter 7 provides the conclusions, contributions to knowledge, and suggestions for future work.

1.4   References

Ali, S.H., Giurco, D., Arndt, N., Nickless, E., Brown, G., Demetriades, A., Durrheim, R., Enriquez, M.A., Kinnaird, J., Littleboy, A., Meinert, L.D., Oberhänsli, R., Salem, J., Schodde, R., Schneider, G., Vidal, O., Yakovleva, N., 2017. Mineral supply for sustainable development requires resource governance. Nature 543, 367-372.

Grace, J.R., Taghipour, F., 2004. Verification and validation of CFD models and dynamic similarity for fluidized beds. Powder Technology 139, 99-110.

Mittoni, L.J., Schwarz, M.P., 1998. Computational fluid dynamics as a tool in the minerals processing and metal production industries 13th Australiasian Fluid Mechanics Conference, Melbourne, Australia, pp. 671-674.

Mudd, G.M., 2010. The environmental sustainability of mining in Australia: key mega-trends and looming constraints. Resources Policy 35, 98-115.

Parker, D.J., Forster, R.N., Fowles, P., Takhar, P.S., 2002. Positron emission particle tracking using the new Birmingham positron camera. Nuclear Instruments and Methods in Physics Research Section A: Accelerators, Spectrometers, Detectors and Associated Equipment 477, 540-545.

Prior, T., Giurco, D., Mudd, G., Mason, L., Behrisch, J., 2012. Resource depletion, peak minerals and the implications for sustainable resource management. Global Environmental Change 22, 577-587.

Radman, J.R., Langlois, R., Leadbeater, T., Finch, J., Rowson, N., Waters, K., 2014. Particle flow visualization in quartz slurry inside a hydrocyclone using the positron emission particle tracking technique. Minerals Engineering 62, 142-145.

Radziszewski, P., 2013. Energy recovery potential in comminution processes. Minerals Engineering 46, 83-88.

Wills, B.A., Finch, J.A., 2016. Chapter 1 - Introduction, Wills' Mineral Processing Technology (Eighth Edition). Butterworth-Heinemann, Boston, pp. 1-27.

Chapter 2: Literature Review - Classification

2.1 Chapter Overview

This chapter explores the importance and role of classification in mineral processing, with particular interest placed on the hydrocyclone. The performance, characterisation and deficiencies of hydrocyclones are also examined. The principles and design of the hydrocyclone was first patented in the late nineteenth century, however it was not until the 1950s that it gained widespread use as a particle classifier. Prior to this era, gravitational classifiers, such as the rake and spiral classifier monopolised particle separation in mineral processing. However, as the demand for high-capacity and fine grind sizes increased, the application of hydrocyclones in closed grinding circuits increased dramatically. This increased use spurred investigations into the separation mechanisms that govern hydrocyclones in order to construct predictive models. Flow behaviour such as by-pass, the fish-hook effect, and short-circuiting were found to cause misclassification of fine or coarse particles. This ultimately leads to decreased efficiency in both the size reduction and separation stages of mineral processing. The complexity of the turbulent, three-phase system within the hydrocyclone has limited performance prediction to empirical models, based on large databases of experimental data. The large number of geometrical and operational variables, however, means that the empirical models lack true predictive power and often require additional testing before being applied. To combat this, theoretically based computational models have recently been a focus of study and will discussed further in Chapter 3.

2.2 Introduction

Classification refers to sizing operations that exploit the differences in settling velocities exhibited by particles of different sizes or phases of different densities. This can include phase separation (gas-solid, liquid-solid), density separation (liquid-liquid) or size separation (solid-solid). Classification is one of the most important industrial unit processes (Schubert, 2010), with applications in the oil, food, paper, and drilling industries. In the case of mineral processing, classifiers are primarily used as particle classifiers in closed-circuit grinding, but have found use in desliming, degritting, and thickening (dewatering) (Wills and Finch, 2016).

Heiskanen (1993) defines particle classification as a method of separating particle mixtures into two or more products based upon the resulting forces acting on the fine and coarse fractions. The

forces acting on a particle can be divided into accelerating forces, such as gravitational or inertial forces, and opposing forces, such as drag. Other forces can include buoyancy, particle-particle interaction and turbulent forces. The movement of the carrying fluid is often used to obtain a large enough difference in the resulting velocities to enable the products to be efficiently separated. This carrying fluid can be a liquid or a gas. In mineral processing, this fluid is usually water, and wet classification is generally applied to mineral particles that are considered too fine (< 200 µm) to be sorted efficiently by screening. Dry classification has some disadvantages such has dust control and can only be used when dry grinding takes place (Lynch and Rowland, 2005). Dry grinding is still relatively rare in mineral processing, as such this chapter will only discuss wet classification.

2.3   Importance of Classification in Mineral Processing

As mentioned previously, mineral processing can be broken down into three principle stages: size reduction (liberation), separation and product handling. The last stage of size reduction, grinding, was first operated in open circuit (no recirculation) (Lynch and Rowland, 2005). This meant that products contained a large fraction of very fine particles, if all the particles larger than the required top size were to be eliminated, or too many coarse particles if overgrinding was to be avoided. This was a major problem as most downstream separation processes, such as flotation or gravity separation, require a specific and narrow particle size range to optimise performance. Figure 2.1 shows the drop in flotation recovery if particle sizes are two small (< 10 µm) or too large (> 100 µm).
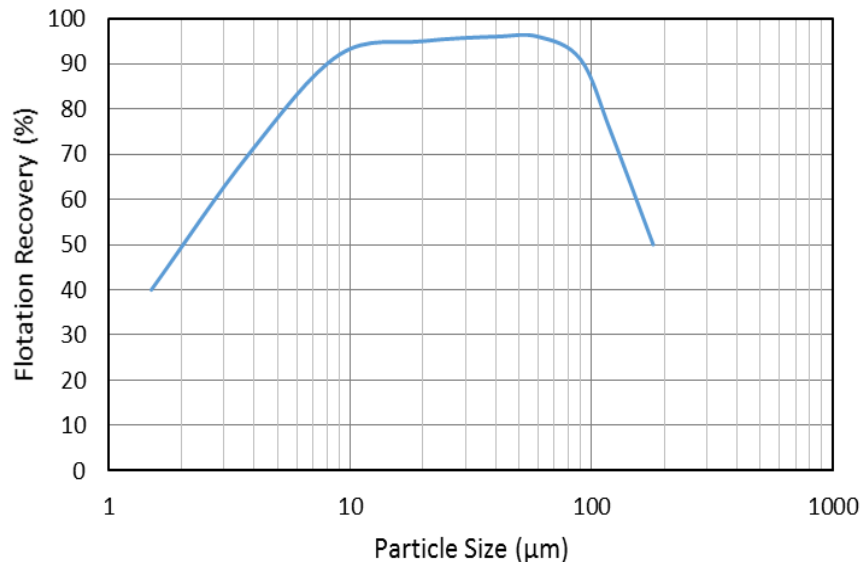
Figure 2.1: A typical flotation recovery curve showing the effect of particle size on recovery. Adapted from data presented by Gaudin *et al.* (1931) and Trahar (1981).

Closed circuit grinding eliminated this problem by discharging particles from the grinding mill before overgrinding occurs, classifying it, and sending the coarse particles back for further grinding. An example of the now standard SABC (Semi Autogenous, Ball mill, Crusher) circuit is shown in Figure 1.1. The benefits of proper classification can include: improved comminution efficiency; improved product (classifier overflow) quality; and greater control of the circulating load to avoid overloading the circuit. The improvement in efficiency of the grinding circuit is seen as either a reduction in energy consumption or an increase in throughput (capacity). The main increase in efficiency is due to the reduction of overgrinding. By removing the finished product-size particles from the circuit, they are not subject to further unnecessary grinding (overgrinding), which would be a waste of comminution energy. This, combined with the recycling of unfinished (oversize) particles, results in the circuit product (classifier overflow) having a narrower size distribution than is the case for open circuit grinding. This narrow size distribution and restricted amount of excessively fine material benefits downstream mineral separation processes. Other benefits from proper classification come from reduced particle-particle contact cushioning from fines in the grinding mill and less misplaced coarse material in the overflow, which would reduce downstream efficiencies. Therefore, classifier performance is critical to the optimal running of a mineral processing plant. A simplified summary of this process is presented in Figure 2.2.
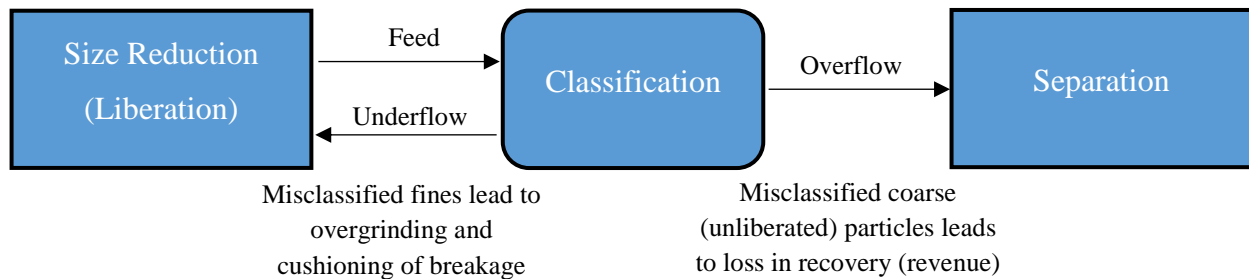
Figure 2.2: Simplified flow diagram of a typical mineral processing plant, showing the importance of proper classification.

2.4　Types of classifiers

Wet classifiers can be categorised by many features. The most typical aspect of classifier characterisation is the applied force field to the unit: either gravitational or centrifugal. Gravitational classifiers can be further separated into two categories, depending on the movement of the carrier fluid and the particle settling direction. The first is sedimentation classification, where the fluid movement is perpendicular to gravity and thus forms an angular particle trajectory. Alternatively, if the fluid movement and particle settling direction are opposite, the unit is defined as a hydraulic or counter flow classifier. Both of these concepts are displayed graphically in Figure 2.3.
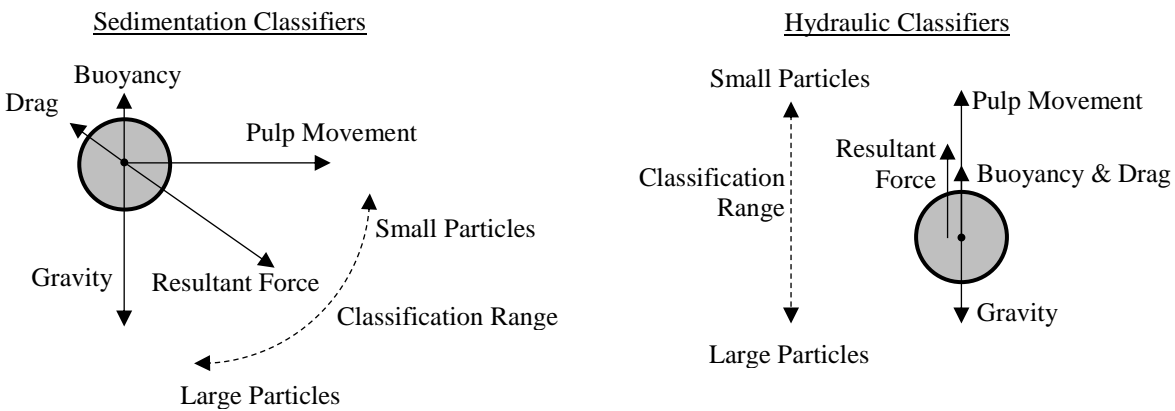
Figure 2.3: Forces affecting settling particle in different types of gravitational classifiers. Adapted from Heiskanen (1993).

The simplest form of sedimentation classifier is the settling cone (shown in Figure 2.4a). Feed is distributed into the top of the tank, with the spigot discharge valve, S, initially closed. Large particles accumulate in the cone, forming a dense bed, while the fine particles overflow with the majority of water. Once the bed is formed, the spigot valve is opened, and sand is discharged at a rate equal to that of the input. Classification occurs radially across zone D from the feed pipe to the overflow lip. As it relies solely on the force of gravity for separation (non-mechanical), it is not suitable for the classification of fine particles. Two other forms of sedimentation classifiers are the rake and spiral classifier (Figure 2.4b and Figure 2.4c respectively). The settled particles are conveyed up an inclined trough by a mechanical rake or helical screw. These conveying mechanisms also act as agitation to help keep the fine particles in suspension.

A major disadvantage of mechanical sedimentation classifiers is their inability to produce overflows at fine particle sizes and reasonable pulp densities. To produce fine particle separations, the pulp is diluted to such an extent that the overflow becomes too dilute for subsequent operations and therefore requires thickening. This is disadvantageous as, apart from the increase capital cost and space requirements, surface reactions (such as the oxidation of sulphide particles or the addition of flocculants) may occur in the thickener, which may affect subsequent processes, especially froth flotation.
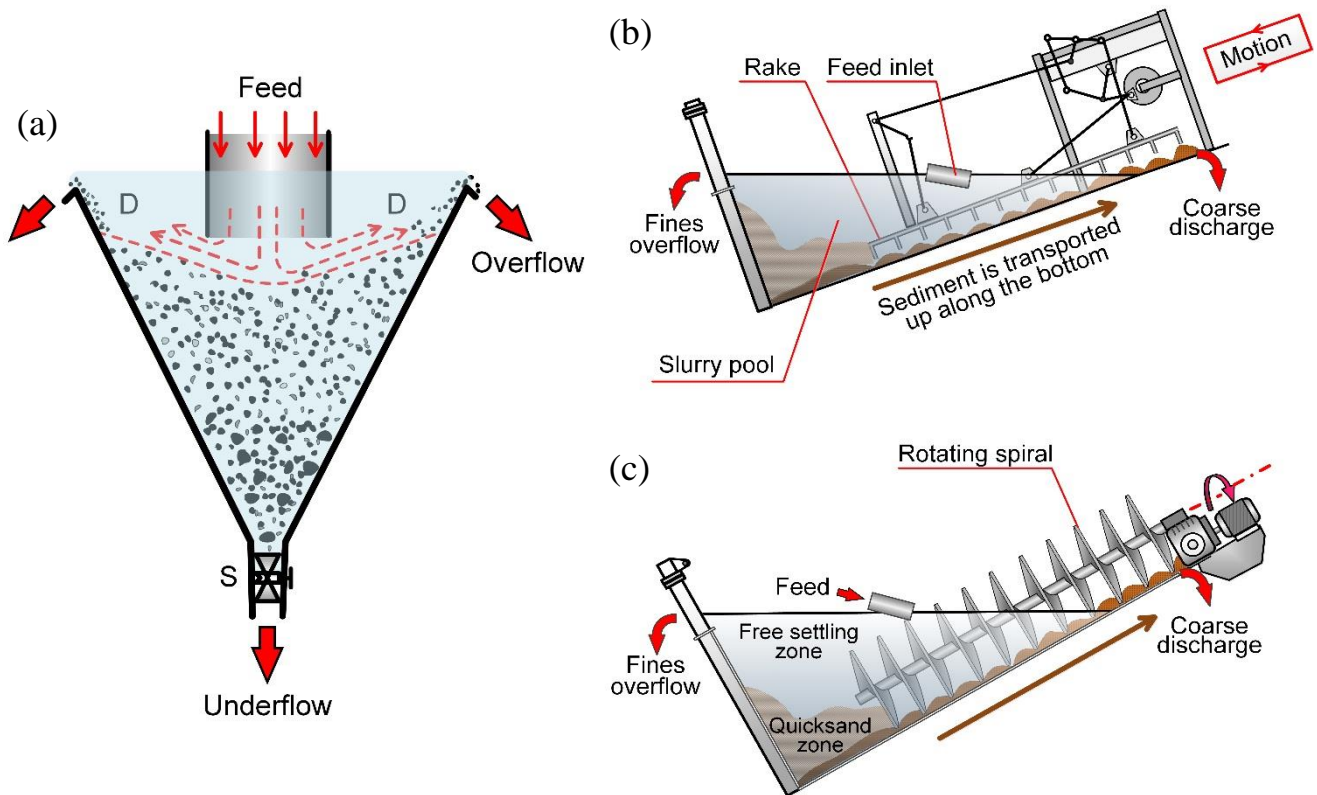
Figure 2.4: Principles of operation for: (a) the settling cone (non-mechanical sedimentation classifier); (b) rake classifier and (c) spiral classifier (mechanical sedimentation classifiers). Reproduced with permission from Wills and Finch (2016).

Hydraulic classifiers, which typically consist of a series of sorting columns, are characterised by the use of water, additional to the feed pulp, introduced in a direction counter to that of the settling particles. The continuous increase in size of each sorting column creates a varied rising current, ranging from a relatively high velocity in the first sorting column, to a relatively low velocity in the last. This produces a series of underflow products, with coarser, denser particles in the first underflow and progressively finer products in the subsequent underflows. These features are illustrated in Figure 2.5.
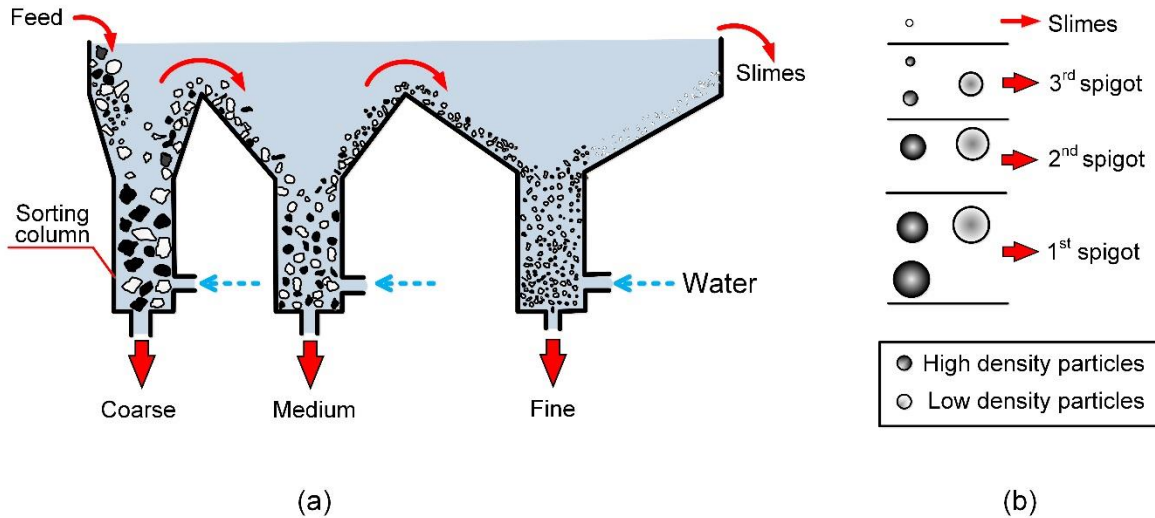
Figure 2.5: (a) Principles of operation for a hydraulic classifier with (b) representation of spigot products. Reproduced with permission from Wills and Finch (2016).

Gravitational classifiers are best suited for coarser classification, where the influence of gravity is more pronounced. Their main benefits include: low energy usage; their ability to give very high solids content in the sand fraction; and the independence of cut-size and capacity. This makes them useful for dewatering applications. Centrifugal classifiers, on the other hand, have smaller footprints and high efficiencies at small particle sizes ($< 70\,\mu$m). The main centrifugal classifier is the hydrocyclone. Hydrocyclones have many advantages over gravitational classifiers, including high specific capacity, low investment cost, and simple operation. This has led to their universal application in closed circuit grinding, as well as uses in dewatering and desliming. A summary of the key features of both gravitational and centrifugal classifiers is shown in Table 2.1. Hydrocyclones will be discussed further in Section 2.6.

Table 2.1: Comparison of key parameters for centrifugal and gravitational classifiers. Adapted from Wills and Finch (2016).

Item	Centrifugal Classifiers (Hydrocyclones)	Gravitational Classifiers (Spiral, Cone, Rake, *etc.*)
Footprint (m^2)	Small	Large
Specific Capacity (t·m^{-2})	High	Low
Particle Cut-size range (µm)	Fine to coarse (1 - 300)	Coarse (> 70)
Capacity/Cut-size Dependency	Yes	No
Energy Consumption	High (Feed pressure)	Low
Initial Investment ($)	Low	High

15

2.5   Classification Vs. Screening

Classification in a fluid medium is not only dependent on the particle size, but specific density and shape. Screens, on the other hand, make two-dimensional (width and thickness, but not length) size separations according to the size of the openings in the screens' surface. This means they are not directly influenced by the density spread in the feed minerals, giving them a much higher separation efficiency when compared to classifiers. With the invention of modern high-frequency, vibratory screens, industrial screening has been extensively used for size separations from 300 mm down to 250 µm. This eliminated any use for gravitational classifiers for coarse size particle separation. For the fine particle range, the selection between screening and classification is typically influenced by the large areas of screening surface needed for fine separation, which substantially increases the capital cost for high throughput operations. Although there are screen types that are capable of efficient size separations down to 40 µm, efficiency in terms of specific capacity decreases rapidly with fineness. Therefore, sizing below 250 µm is more commonly undertaken by classification, in particular: hydrocyclones.

Figure 2.6 shows a comparison of the performance curve (performance, or partition, curves are discussed in detail in Section 2.6.2) for a screen and hydrocyclone in the grinding circuit of the El Brocal concentrator in Peru. The data was gathered at different times to allow for both units to operate as the final classification stage (this is the same as the hydrocyclone shown in Figure 1.1). As expected, the screens were able to produce a much steeper slope, meaning a higher particle separation efficiency. It must be noted, however, that it was at a substantial higher cut-size (~500 µm) when compared to the hydrocyclone operation (~50 µm). If the cut-size of a screen operation is lowered, the particle separation efficiency decreases, illustrated by Figure 2.7. Hydrocyclones are therefore still the optimal choice for fine particle sizing in closed grinding circuits.
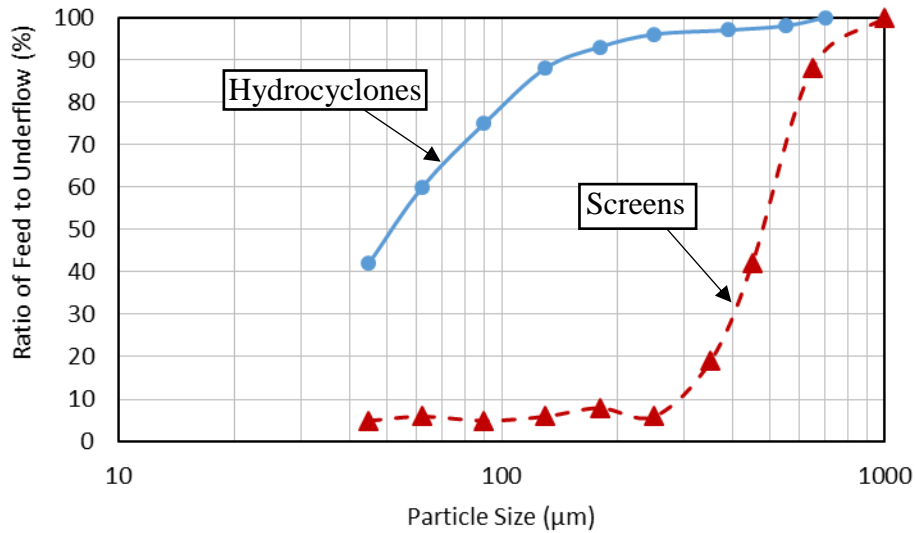
Figure 2.6: Performance curves for hydrocyclones and screens in the grinding circuit at El Brocal concentrator, Peru. Adapted from data published by Dündar *et al.* (2014).
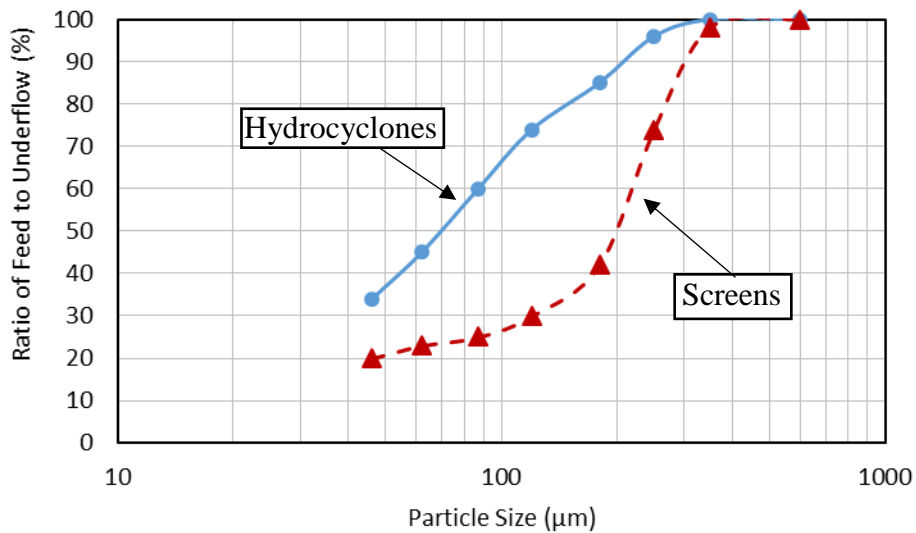
Figure 2.7: Performance curves for hydrocyclones and screens in the grinding circuit at Cerro Lindo concentrator, Peru. Adapted from data published by Dündar *et al.* (2014).

2.6   The Hydrocyclone

2.6.1   *Basic design, operation and sizing*

The hydrocyclone is a continuously operating classifying device that utilises differences in drag and inertial forces in high speed flows to accelerate the settling rate of particles or liquids. Hydrocyclones, often shortened to cyclone, have gained widespread use in number of industries since their inception in the 1940's (Aldrich, 2015), despite the first patent being obtained in 1891

(Bretney, 1891). A modern hydrocyclone, shown in Figure 2.8a, consists of two main sections: a conically shaped vessel, open at its apex (also referred to as spigot or underflow); attached to a cylindrical chamber, which contains a tangential or involute feed inlet. An overflow pipe, namely the vortex finder, passes through the roof of the cylindrical section, with the remaining area sealed. The feed enters under pressure to the stationary cyclone body, creating a swirling, vortex flow pattern, which due to the intrusion of the vortex finder is forced downwards. This minimises the short-circuiting of feed directly to the overflow. Once the flow leaves the feed zone, also referred to as the cylindrical section, and travels downwards, the increasing constriction in the adjoining conical section forces some of the flow to reverse its direction. This forms a secondary upwards-travelling inner vortex. This flow pattern is aided by the formation of an air core in the low-pressure zone along the vertical axis of the cyclone. The air core is created largely from the atmosphere through the apex opening, but in part by dissolved air in the feed. The upward rotating flow continues to the vortex finder, which both shields the inner vortex from the high inlet velocity and stabilises its swirling motion. This double vortex flow pattern is illustrated in Figure 2.8b.
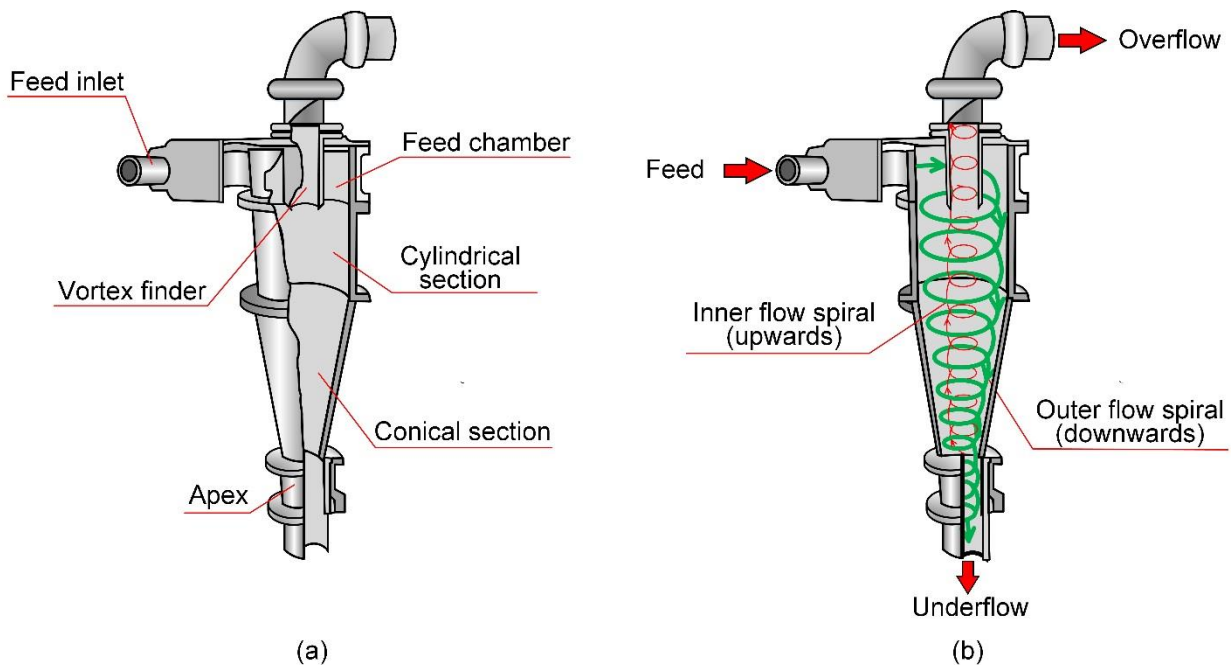
Figure 2.8: A hydrocyclone showing (a) main components, and (b) principle flows. Reproduced with permission from Wills and Finch (2016).

Particles within the hydrocyclone's flow pattern are subjected to two opposing forces: an 'outward' acting inertial force, and an opposing inwardly acting drag force provided by the carrying fluid. The inertial force, sometimes misinterpreted as a 'centrifugal force', develops as a particle wishes to continue its motion, which at any moment is tangential to the circular path. This force balance, shown in Figure 2.9a, is dependent upon mass and surface area, thereby separating particles according to their size, specific gravity and shape. Particles with a larger mass, therefore having a greater momentum than drag, move to the wall of the cyclone, and migrate down to the apex opening. Particles whose inertia is lower in magnitude than the force required to overcome the drag of the carrier fluid, migrate toward the zone of low pressure along the hydrocyclone's vertical axis and are carried upwards through the vortex finder to the overflow. There will, naturally, be a particle size at which the orbiting radius will coincide with the contour of zero vertical velocity. Theoretically this contour is formed at a location between the opposite moving vortices, illustrated in Figure 2.9b. This particle size therefore has an equal chance of reporting to either the overflow or underflow, and is referred to as the 'cut-size'. The cut size and the behaviour of particles near this size determine the selection and performance of the hydrocyclone and is typically represented by a partition curve.
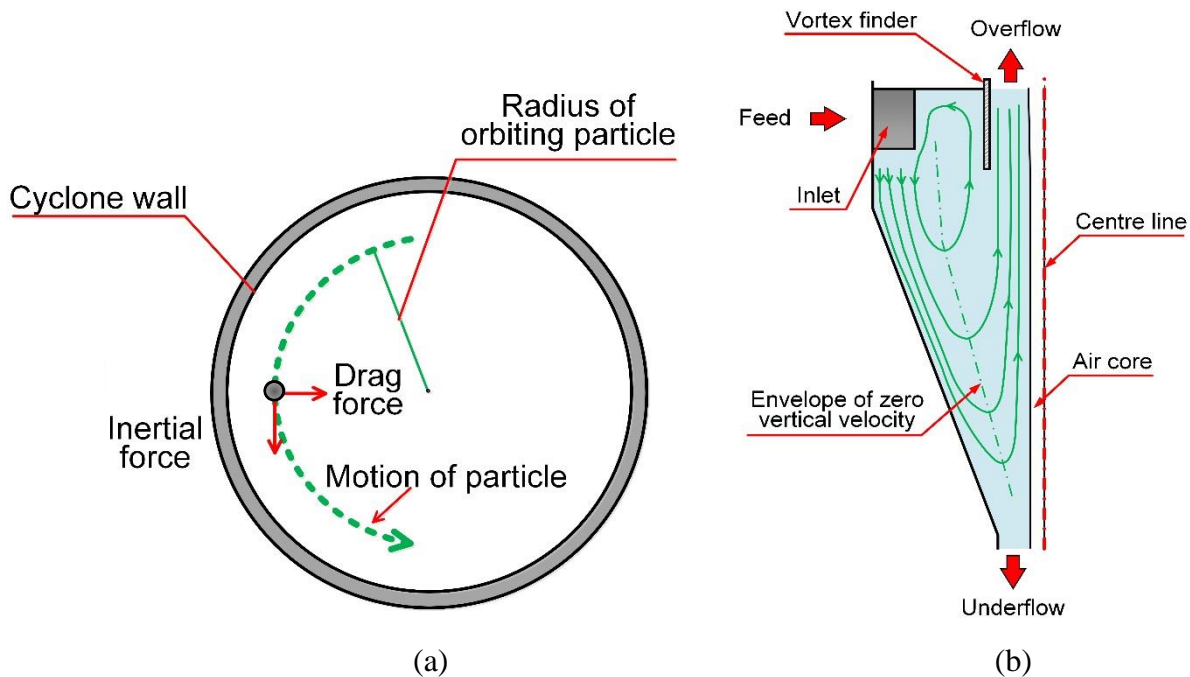
Figure 2.9: Principles of hydrocyclone separation: (a) forces acting on an orbiting particle in the hydrocyclone and (b) distribution of the vertical components of velocity in a hydrocyclone. Reproduced with permission from Wills and Finch (2016).

Theoretically, the cut-size should be determined to a large extent by the diameter of the hydrocyclone. Larger hydrocyclones will have their envelope of zero velocity at a greater radius than that of a smaller hydrocyclone, and will therefore recover only the heaviest of particles. This has also been shown to be true in practice, with hydrocyclones manufactured in a range of sizes. The size required for a particular application can be estimated from empirical models, such as that proposed by Arterburn (1982). However it is more common to rely on the suppliers' experience and to select the required model by referring to manufacturers' charts (Arterburn, 1982), which show capacity and separation size ranges in terms of cyclone size. A typical performance chart is shown in Figure 2.10 (where the *D* designation refers to cyclone diameter in inches). Alternatively, Table 2.2 details a different range of hydrocyclone designs with their associated diameters, capacities, pressure drops and cut-sizes shown (Bradley, 1965).
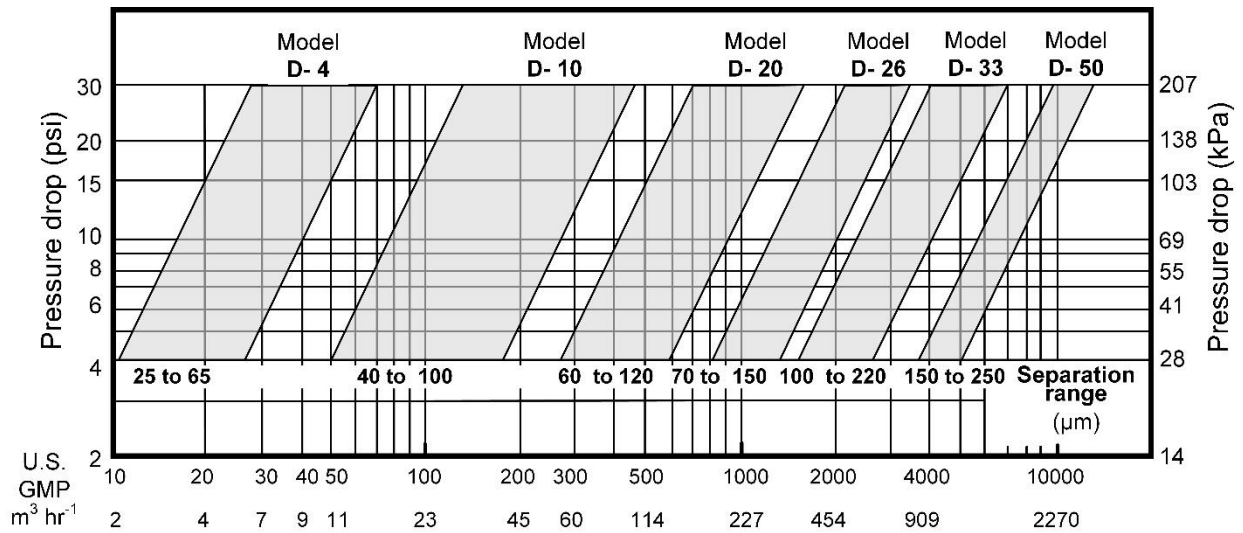
Figure 2.10: Hydrocyclone performance chart for a Krebs hydrocyclone, where *D* represents the hydrocyclone diameter in inches. Reproduced with permission from Wills and Finch (2016).

Table 2.2: Hydrocyclone performance data for a Heyl and Patterson hydrocyclone. Adapted from Bradley (1965).

Diameter (mm)	Capacity ($m^3 \cdot s^{-1}$)	Pressure Drop (kPa)	Cut-size (µm)
28	0.2-0.4	276-414	2-10
76	1-3	138-276	5-20
203	11-45	138-207	20-80
356	34-159	103-172	80-300
610	159-454	69-138	150-500
914	454-908	28-83	200-600

Hydrocyclone manufacturers only produce a limited range of cyclone diameters. Therefore, in order to cover a wide range of cut sizes and flow rates, each cyclone of a given size can be operated with different aperture sizes (inlet, overflow and underflow) through the use of interchangeable parts. This approach requires an accurate knowledge of how geometric variables affect the equipment performance (Castilho and Medronho, 2000).

2.6.2   *Characterisation of hydrocyclone performance*

The analysis of the fluid and particle flow inside a hydrocyclone is undoubtedly a complex problem. Hydrocyclone performance is typically characterised by the holistic performance of the unit. This includes the ratio of two outlet streams (flow split), the particle size distribution in these streams and the pressure drop within the cyclone. While this information does not provide detailed explanations of the impact of various geometrical and operational parameters, it does allow for the discovery of various phenomena that negatively impact hydrocyclone performance.

2.6.2.1   Flow Split

The simplest and most obvious way to measure classification efficiency is to relate the mass flow rate of the coarse (underflow) and fine (overflow) fractions. This is defined as the mass flow split, and is calculated by dividing the mass flow rate of either outlet streams, depending on the quantity

of interest, by the feed. While simple to calculate with experimental data, the actual flow split in hydrocyclones is difficult to predict and has been referred to as one of the least understood aspects of hydrocyclone operation (Romero *et al.*, 2004).

2.6.2.2 The Partition Curve

A much more detailed and precise method of measuring and comparing classifier performance is by considering each particle size class separately. The fractional recoveries (probabilities) to the underflow of each particle size class is calculated and plotted against particle size, creating a '*partitioned*' mass split. The partition curve (also referred to as the performance curve, efficiency curve, selectivity curve, or Tromp curve) is the most common method of representing hydrocyclone efficiency. A key parameter determined by the partition curve is the cut-size, or separation size, which is defined as the size at which 50 % of the particles in the feed report to the underflow. This point is referred to as the d_{50} size, and is the particle size that has an equal chance of going to either the overflow or underflow. Figure 2.11 displays the key features of a standard partition curve for a hydrocyclone.
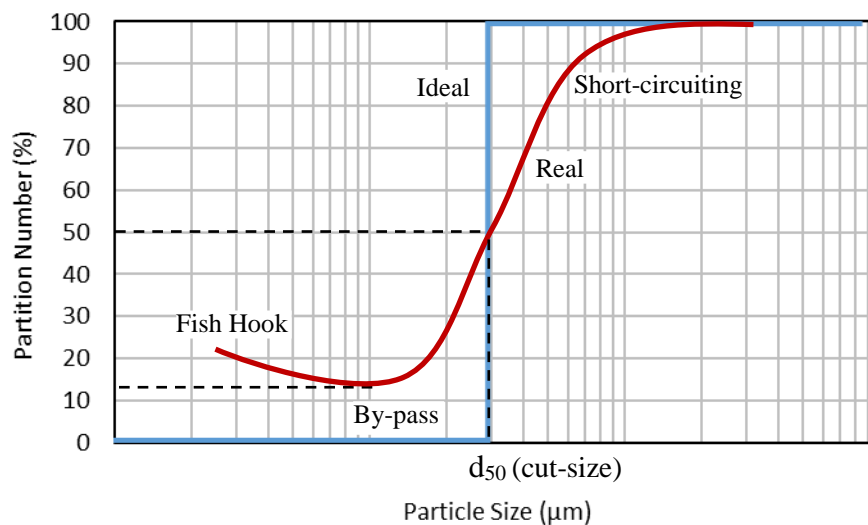
Figure 2.11: Partition curve showing the difference between ideal and real classification, the cut-size, and the features responsible for the misclassification of particles.

2.6.2.3 Sharpness of Cut

Distribution efficiency curves are not easily comparable. Therefore, a sharpness, or imperfection, parameter, *I*, was developed for easier comparison between different partition curves. The value is determined by the slope of the central section of the partition curve; by taking the points at which

75 % and 25 % of the feed particles report to the underflow. These are the d_{75} and d_{25} sizes, respectively.

$$I = \frac{d_{75} - d_{25}}{2d_{50}}$$

Equation 2.1

The closer the slope is to vertical, the lower the value of I, and the greater the classification efficiency. Perfect classification would give $I = 0$; but in reality values range between 0.2 and 0.8 (Heiskanen, 1993).

2.6.2.4   By-pass Fraction in Underflow

When constructing the partition curve for a hydrocyclone, it is observed that as particle size reduces the partition value does not appear to approach zero, but instead approaches some constant value. This is illustrated in Figure 2.11. To explain, Kelsall (1953) suggested that solids of all sizes are entrained in the coarse product liquid, by-passing classification in direct proportion to the fraction of feed water reporting to the underflow. The logic for this was that particles with sizes analogous to water molecules (approaching zero) would show no tendency to classify (*i.e.*, have a zero settling velocity) in the hydrocyclone, and would thus split with the water (Kelly, 1991). This analysis was validated by the fact that water injection at the underflow discharge markedly reduces the by-pass (Kelsall and Holmes, 1960).

To correct for this occurrence, the measured partition curve is adjusted based on the fraction of the total water which is discharged through the underflow, $R_{w/u}$. The corrected curve is calculated by Equation 2.2 (Kelsall, 1953; Wills and Finch, 2016):

$$C_{m_i} = \frac{m_i - R_{w/u}}{1 - R_{w/u}}$$

Equation 2.2

where C_{m_i} is the corrected mass fraction of a particular particle size reporting to underflow, and m_i is the measured mass fraction of a particular size reporting to the underflow. The corrected curve describes particle recovery to the underflow by true classification and introduces a corrected cut-size term, $d50_c$. Both the actual partition curve and the corrected curve are important as they show both the efficiency of the classification action within the hydrocyclone, without the bias of the underflow water, and the magnitude of the by-pass, which is to be minimised.

2.6.2.5   Fish-hook effect

In some situations, the by-pass fraction is not consistent, causing an increase in partition number as the particle size approaches zero. This is described as "fish-hooking". While not always present it has occurred sufficiently often to invite examination (Finch, 1983; Kelly, 1991). There have been many theories put forth about the origin of the fish hook effect. Luckie and Austin (1975) attributed the fish hook to the internal recycling of fines, therefore increasing the probability of reporting to the coarse fraction. Finch (1983) stated that while modelling the device as two cyclones in series did simulate the fish-hook, internal recycle seems an unlikely explanation. Finch (1983) and others (Del Villar and Finch, 1992; Kelly, 1991) argued against the common assumption that bypass is a constant for all particle classes, suggesting that particle entrainment in the water recovered to the underflow is size dependent. This means that smaller particles have a higher chance of being entrained in the liquid, leading to the hook at fine particle sizes. Despite continued literature (Lv *et al.*, 2015; Vakamalla *et al.*, 2014) describing the occurrence of the fish-hook, others question its significance or even existence. Nageswararao and Karri (2016) stated that the fish-hook effect is a consequence of erroneous particle size analyses, and that its practical significance is zero.

2.6.2.6   Short-Circuiting of Feed to Overflow

Short-circuiting refers to the flow of particles or water directly from the feed inlet to the overflow outlet due to the recirculating eddy flows in the feed region, as shown in Figure 2.12. The insertion of the vortex finder attempts to avoid the entrainment of feed particles into the overflow stream. Kelly (1991) stated that if the vortex finder is operating correctly there will be no short-circuiting. However, there is still no standard length for the vortex finder (ranging from 0.33 - 0.67 D_C) as it depends on geometry, feed particle size and feed concentration; and therefore needs to be determined *via* experimentation (Martínez *et al.*, 2008; Silva *et al.*, 2015). The short-circuiting flow is a source of inefficiency since it carries particles directly from the inlet to the overflow stream without subjecting the particles to the classifying action of the swirling flow within the hydrocyclone. Experimental work by Kelsall (1953) showed that the tested hydrocyclone had 15 % of the feed water short-circuit directly from the inlet to the vortex finder, and that 15% of the feed particles short-circuited, independent of their size. Other authors have also noted its presence (Bradley and Pulling, 1959; Martínez *et al.*, 2008; Milin *et al.*, 1992; Silva *et al.*, 2015).
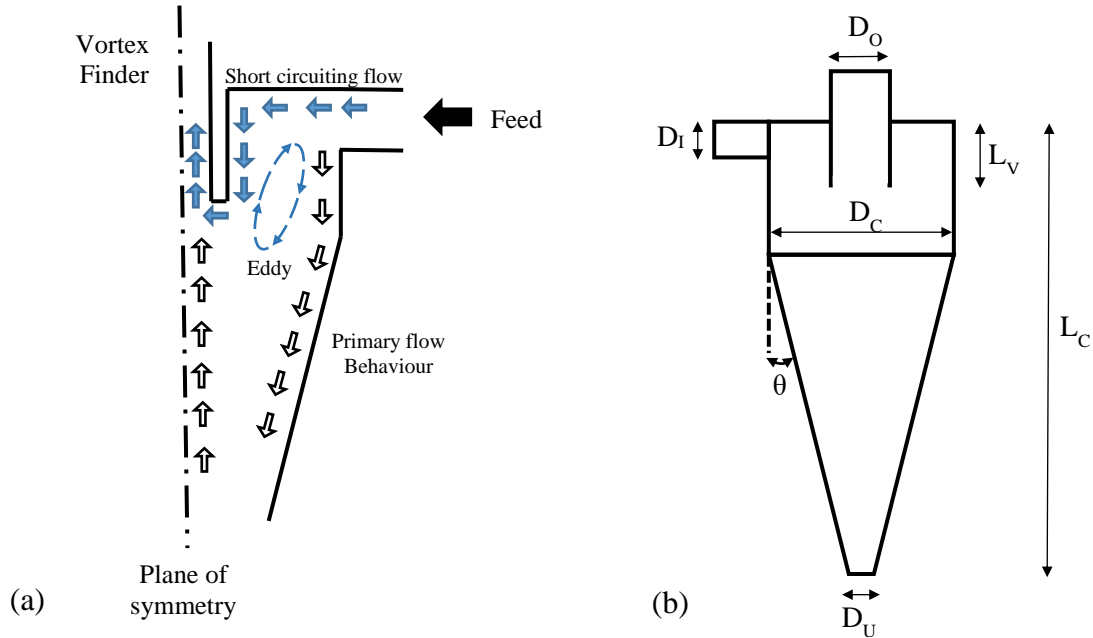
Figure 2.12: (a) Flow pattern of eddy flows and short-circuiting. Adapted from Milin *et al.* (1992) and Bradley and Pulling (1959). (b) A diagram of the hydrocyclone showing design features.

2.6.3   Factors affecting hydrocyclone performance

The hydrocyclone geometry consists of many parameters that may be used to alter performance, including the hydrocyclone (D_C), inlet (D_I), overflow (D_O), and underflow (D_U) diameters; the length of the cyclone (L_C) and vortex finder (L_V); and the cone angle (θ) (as seen in Figure 2.12b). When coupled with the numerous operating variables, such as feed pressure, particle size distribution and pulp density, the number of experiments needed for proper optimisation becomes a significant challenge. It is therefore common to simplify the geometry by using ratios of the different geometrical properties in relation to the diameter of the hydrocyclone. Most hydrocyclones operating in industry are a result of these suggested ratios. Outlined below is the general behaviour of some of these factors.

2.6.3.1   Cyclone Diameter

The diameter of the hydrocyclone is taken as the diameter of the cylindrical section. Theoretically, the hydrocyclone diameter, along with the feed pressure and flow rate, controls the radius of orbit and thus the inertial forces acting the particles. In general, the smaller the diameter of the hydrocyclone the smaller the cut-size. This is paid for by an increased energy requirement (pressure) at the same flow rate, or a smaller flow rate per hydrocyclone at the same pressure 0requirement. Some investigators have concluded that the inlet and outlet diameters (feed, apex

and vortex finder) are the critical design variables, and that the cyclone diameter has no effect on the cut-point. The authors argue that the cyclone diameter is merely the size required to accommodate the correct size apertures, and that for geometrically similar cyclones the partition curve and cut-size is only a function of the feed material characteristics (Lynch *et al.*, 1974; Lynch *et al.*, 1975; Rao *et al.*, 1976). The phrase 'geometrically similar hydrocyclones' refers to the necessity to observe geometrical similarity between the different design parameters in order to maintain performance. This means smaller diameter hydrocyclones will also have comparatively smaller aperture diameters and therefore it is difficult to determine the true effect of cyclone diameter (Bradley, 1965; Wills and Finch, 2016).

The range of hydrocyclone diameters used in industry has an upper limit, because with increasing particle sizes the need for the increased inertial forces (energy input) diminishes (when compared to gravity). The difficulties of handling large particles in suspension, and the severe abrasion, would also contribute to this upper limit (which is approximately 2.3 m) (Gupta and Yan, 2006). At the other end of the spectrum, difficulties in the construction and manifolding together of many very small diameter cyclones (needed to give capacities of practical interest) restricts sizes below 10 mm. There is also evidence for which tests with a 4 mm diameter unit gave inferior classification ability relative to the 10 mm size (Bradley, 1965). The relationship between hydrocyclone diameter and cut-size (for geometrically similar hydrocyclones) has been estimated by many authors (Bradley, 1965; Flintoff *et al.*, 1987; Heiskanen, 1993). The relationship is given as $d_{50} \propto D_c{}^x$, where x varies from 1.18-1.875.

2.6.3.2 Feed Inlet Diameter and Type

The area of the inlet determines the entrance velocity, therefore controlling the pressure drop, separation size and capacity. It is quite evident that a lower inlet velocity decreases the inertial forces and this gives a coarser cut size, smaller pressure drop and decreased capacity. Kelsall (1953) measured the feed flow rates for a range of inlet diameters at various pressure drops (Figure 2.13). He showed that the injection of momentum (calculated as total flow rate multiplied by inlet velocity) increased to a maximum as feed diameter increased but then decreased with further increases in diameter, suggesting that the feed aperture should be chosen based on this maximum. It was theorised that this optimum feed diameter resulted in an average inlet velocity approximately the same as the tangential velocity at the same radius. This would reduce 'wasted'

energy as excessive turbulent mixing would decrease, and particle separation would be more efficient. This symmetry was found to occur at an inlet diameter of $D_c/3.7$ by Bradley (1965), but was argued to be too close to the maximum allowable diameter to avoid direct impingement of the feed stream on to the outside wall of the vortex finder. The full range of inlet diameters measured from industrially operating hydrocyclones extended from $D_c/3$ down to $D_c/15$, however values ranging from $D_c/6$ and $D_c/7$ are more common (Bradley, 1965). Inlet diameters for four well-known families of hydrocyclones are shown in Table 2.3.
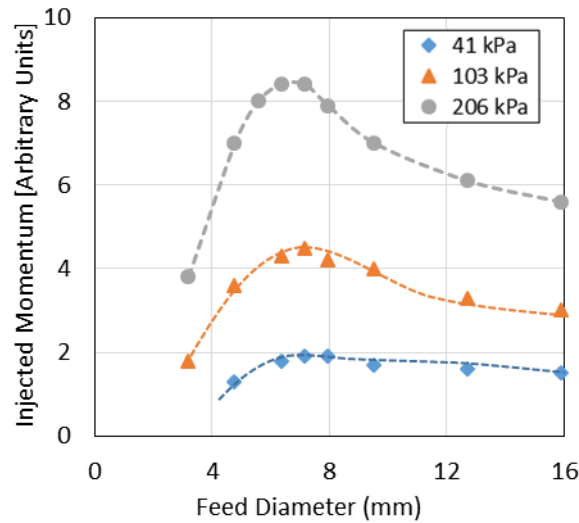
Figure 2.13: Injected momentum (calculated as inlet velocity multiplied by total throughput) as a function of feed diameter for various pressure drops. Adapted from data publish by Kelsall (1953).

Table 2.3: Inlet diameter **proportions of well-known families of hydrocyclones. Adapted from data published by Bradley (1965), Castilho and Medronho (2000), Plitt (1976) and Silva *et al.* (2012).**

Hydrocyclone Type	Bradley	Plitt	Krebs	Rietema
Vortex Finder Diameter	$D_c/7$	$D_c/7$	$D_c/3.7$	$D_c/3.6$

The geometry of the feed inlet is also important, as it helps determine the turbulence in the feed zone. The inlet typically develops from a circular to rectangular cross section at the entrance to the cylindrical section of the cyclone. This helps to spread the flow along the wall of the chamber, reducing turbulent eddies as the feed mixes with the developed flow and has been shown to improve separation efficiency (Kelsall, 1953). Feed entries are available in four main four forms: outer wall tangential; centre line tangential; involute; and top entry (Figure 2.14). This list ranges from least to most expensive to manufacture but also lowest to highest performance ability. Top

feed and involute entries minimise turbulence and reduce wear by slowly conforming the feed conditions to that of the hydrocyclone body, and so can be seen in designs such as Weir's CAVEX[©] and Krebs' gMAX[©] units (Wills and Finch, 2016).

Outer wall tangential

Involute

Centre line tangential

Top entry
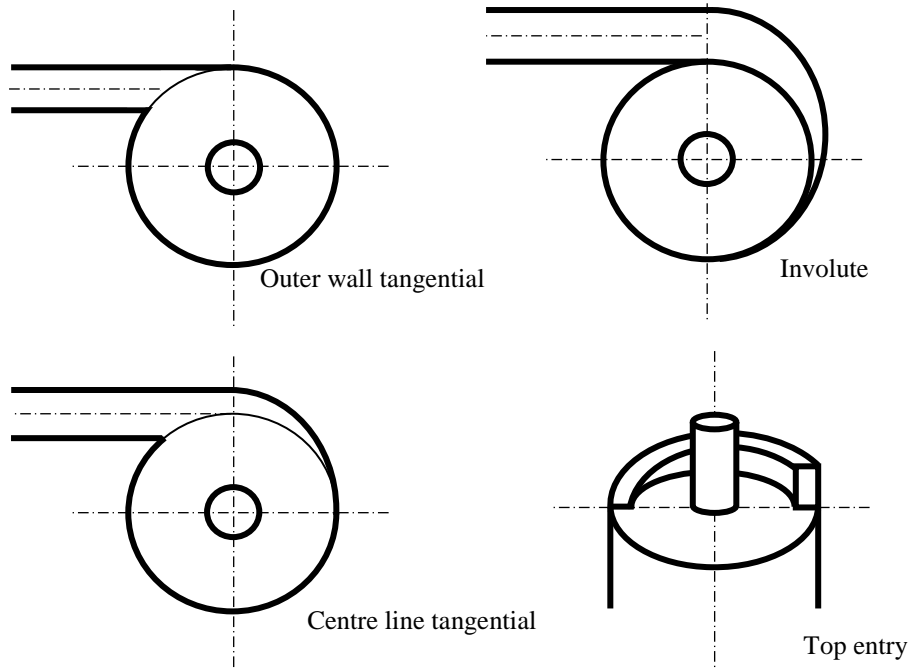
Figure 2.14: Feed entry designs for hydrocyclones.

2.6.3.3   Vortex Finder Diameter and Length

There are two important factors in deciding the optimal diameter of the vortex finder: the short-circuiting flow (Figure 2.12); and the locus of zero vertical velocity (Figure 2.9). Firstly, the vortex finder must not be larger than the diameter of the locus of zero vertical velocity. This causes a collapse of the normal patterns of inward radial flow (Bradley and Pulling, 1959). At the other extreme, it appears to be undesirable to have the overflow diameter smaller than the position of the maximum tangential velocity. In doing so, it allows for the short-circuiting particles to have an increased resistance (by the increasingly large tangential velocities) and therefore greater chance of being re-entrained into the main flow pattern (Bradley, 1965; Kelsall, 1953). This sets a maximum and minimum limit of $D_c/2.3$ and $D_c/8$ respectively, however many designs tend to favour the smaller end of the range with a view to minimising the loss of coarse particles to overflow (Bradley, 1965). The effect of overflow diameter on pressure drop and water split to the underflow is not typical taken into account when selecting the optimum diameter (Bradley, 1965). It is known that both water split to underflow and pressure drop decrease (this is equivalent to an

increase in capacity for a given pressure drop) with increasing overflow diameter, which are both favourable outcomes (Wang and Yu, 2008). These considerations were taken into account in the case of Rietema (1961) and Plitt (1976), hence why their optimum diameter is markedly different from the others.

For the vortex finder length, the effects on both coarse and fine particle classes must be considered. The main purpose of the intruding vortex finder is to allow an opportunity for the re-entrainment of the particles in the short circuit flow. As most coarse particles discharged in the overflow stream are due to short-circuiting, increasing the length of the vortex finder allows more time for the re-entrainment of the coarse particles and increases their separation efficiency. Alternatively, finer particles which are discharged through the overflow have passed down the cyclone, outside the locus of zero vertical velocity. In the lower regions of the cyclone, they are then carried inwards by the water radial velocity components and join the high velocity upward flow near the central air column. For shorter vortex finders, particles have an extended time to be pushed outside of this upward vertical flow and re-circulate with the feed, causing only the finest particles to be collected (increasing the separation efficiency) (Kelsall, 1953). An optimum length therefore exists, dependent upon the desired cut-size and partition curve. A range of typical values for both vortex finder length and diameter, of well-known families of hydrocyclones, can be found in Table 2.4.

Table 2.4: Vortex finder diameter **proportions of well-known families of hydrocyclones. Adapted from data published by Bradley (1965), Castilho and Medronho (2000), Plitt (1976) and Silva *et al.* (2012).**

Hydrocyclone Type	Bradley	Plitt	Krebs	Rietema
Vortex Finder Diameter	$D_c/5$	$D_c/2.5$	$D_c/6.3$	$D_c/2.9$
Vortex Finder Length	$D_c/3$	$D_c/3$	-	$D_c/2.5$

2.6.3.4   Apex or Spigot Diameter

In general, a decrease in the underflow diameter will increase the cut-size. This restriction increases both the particle density and the radial velocity around the apex region, which in turn increases the amount of material recirculating upwards towards the vortex finder. As there is a greater amount of particles and water exiting out of the vortex finder, only the very coarse particles

exit *via* the underflow, increasing the cut-size. Limiting the fraction of water in the underflow also increases the separation efficiency, as explained in Section 2.6.2.4. Therefore, it is suggested that cyclones should be operated at the highest possible underflow density, or the smallest possible apex diameter.

An important consideration for determining the smallest possible apex diameter is the behaviour of the underflow discharge or spray. Hydrocyclone performance is very sensitive to the shape of the underflow spray; thus the shape has long been suggested as a performance monitoring tool (Dubey *et al.*, 2016; Neesse *et al.*, 2004). The discharge can be categorised into three main shapes: roping, spraying and an intermediate zone considered to be correct operation (Figure 2.15). Roping is initiated by excessive particle crowding in the conical part of the hydrocyclone, which occurs when the apex diameter is too small. This causes a high solids content stream of pulp to exit the underflow. As air is no longer able to enter the apex, the air core disappears, oversized material exits *via* the overflow and separation efficiency decreases. On the other hand, if the apex diameter is too large the underflow will be excessively dilute resulting in a wide angled spray pattern. The additional water will increase the by-pass fraction, carrying unclassified fine solids that would otherwise report to the overflow. The best separation efficiency is therefore obtained by ensuring the underflow spray is as close to the roping discharge regime as possible, while still maintaining an air core (Neesse *et al.*, 2004). While the underflow diameter is important, operating hydrocyclones will typically have interchangeable apex pieces that are changed to meet the desired performance. Therefore, their diameter is not considered in the design process (Bradley, 1965).
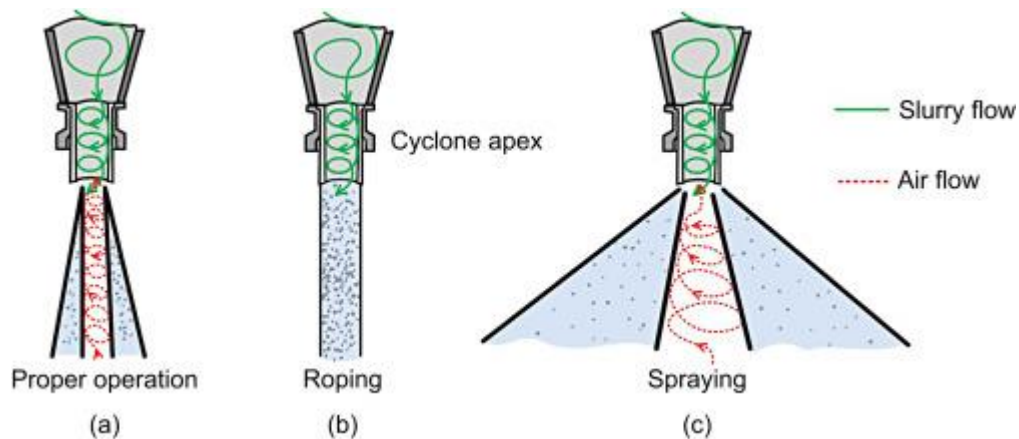
Figure 2.15: Nature of underflow discharge: (a) correct apex size - proper operation, (b) apex too small - "roping" leading to loss of air core, and (c) apex too large - "spraying" which leads to lower sharpness of separation. Reproduced with permission from Wills and Finch (2016).

30

2.6.3.5   Cone Angle, Hydrocyclone Length

In general, an increase in the length of the hydrocyclone decreases the cut size. The cone angle and length of the cyclone are explicitly linked, with an increase in cone angle decreasing the length of the cyclone. The length of the cylindrical section can also increase overall length, without changes to the angle of the conical section. It has also been shown that an increase in the overall length of a hydrocyclone gives an increase in both capacity (by reducing the pressure drop) and efficiency (Ghodrat *et al.*, 2014a). The increased separation efficiency stems from the increased particle residence time, allowing more time for a particle to separate into the correct zone for classification. The optimal cone angle and cylindrical section length is one of the least well defined aspects of hydrocyclone design (Bradley, 1965). Table 2.5 presents a list of suggested values for hydrocyclone length and cone angle.

Table 2.5: Overall length and cone angle proportions of well-known families of hydrocyclones. Adapted from data published by Bradley (1965), Castilho and Medronho (2000), Plitt (1976) and Silva *et al.* (2012).

Hydrocyclone Type	Bradley	Plitt	Krebs	Rietema
Length	$6.85*D_c$	$3*D_c$	$5.874*D_c$	$5*D_c$
Angle	9°	12° for $D_c < 250$ mm 20° for $D_c > 250$ mm	12.7°	20°

2.6.3.6   Inclination of Hydrocyclone

In general, an increase in inclination increases the separation efficiency. For small hydrocyclones, the large inertial forces exhibited on the particles means the direction of gravity has little effect on the overall force balance. Therefore, inclination has little effect on separation efficiency in these cyclones. Large cyclones, however, have been shown to be affected by the degree of inclination: especially when treating minerals with a high density difference. Authors (Hochscheid, 1987; Verde *et al.*, 1991) have shown a significant reduction of misclassified fines (-74 µm) to the underflow, when 500 mm cyclones were inclined to almost horizontal. This is due to the decreased water split to the underflow, and the decreased downward force on the fine particles (Heiskanen, 1993).

2.6.3.7   Feed Rate (Capacity) and Pressure Drop

The pressure drop (or loss) across the hydrocyclone determines the cut-size and capacity for a given hydrocyclone geometry. The pressure drop is a key requirement for the design of the pumping system for a given capacity or to determine the capacity for a given installation, and so is often estimated empirically. In practice, the pressure drop is determined from a pressure gauge located immediately before the feed entry. However, the pressure drop is equivalent to feed pressure only under free discharge conditions, and so in some cases outlet pressures (typically overflow) are also needed (Bradley, 1965). The relationship between pressure drop, capacity and cut-size is shown in Figure 2.16. The practical limits for pressure drop ranges from around 35 kPa (below this, the instability of the air core begins to effect performance) to 350 kPa (where wear from friction and pumping costs start to impede the economics of performance).
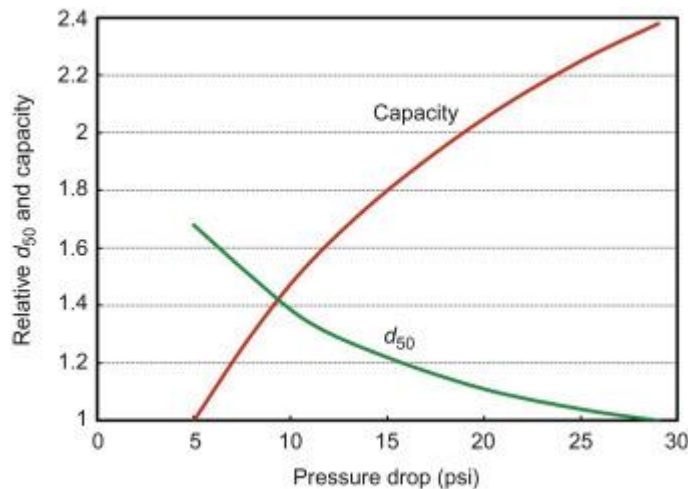
Figure 2.16: Effect of pressure on capacity and cut-point of hydrocyclone. Reproduced with permission from Wills and Finch (2016).

2.6.3.8   Pulp Density (Viscosity)

Slurry rheology is a very important variable in any particle classifier. For hydrocyclones an increase in the feed pulp density (viscosity) increases the cut-size, as shown in Figure 2.17. The high solids concentrations in the rotating mass of fluid reduces the rotational movement, and therefore the inertial forces acting on the particles, causing an increase in cut-size (Bradley, 1965; Wills and Finch, 2016). The decrease in friction also causes a reduction in pressure drop (for constant feed rate); or an increase in feed rate (for constant pressure drop). Another effect of the increased feed pulp density is a reduction in the sharpness of the separation. This due to the increase in hindered settling, which reduces a particles ability to move into the correct classification zone (Heiskanen, 1993).

32
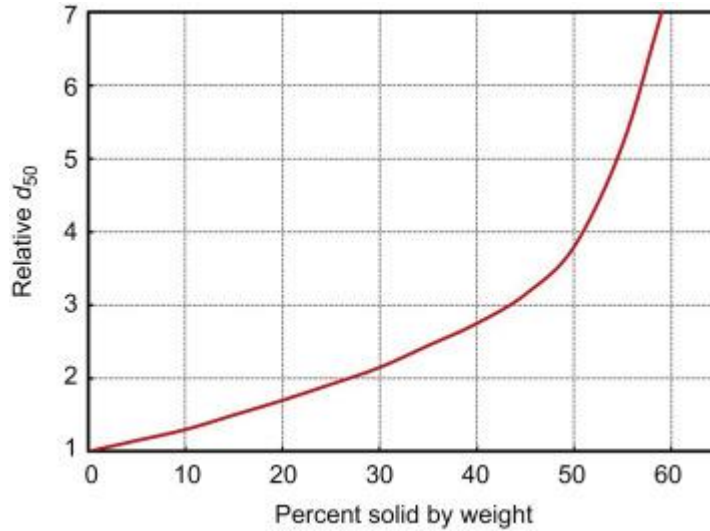
Figure 2.17: Effect of feed solids concentration on cut-point of hydrocyclone. Reproduced with permission from Wills and Finch (2016).

2.6.4 Mathematical Models of hydrocyclones

The qualitative description of swirling turbulent flows is a naturally complex problem. When the continuous phase is loaded with a dispersed phase the complexity of the problem is increased further, as the interactions between the two phases need to be adequately modelled. Numerous models have been proposed to estimate the relationships between the key input variables (operating and geometric variables) and the measured outputs (namely cut size, pressure drop, flow split ratio). These include purely empirical models, calibrated against large databases of experimental data, as well as semi-empirical models based on theoretical assumptions. These relationships have been shown to be useful for the design and selection of hydrocyclones, however they are inherently limited in scope. An undesired consequence is that any extrapolation of results to a different geometry or operating condition must be made with extreme caution. There is still no widely accepted model to allow for proper optimisation of hydrocyclones, with many applications still relying on performances of other installations to guide selection. Below is a summary of underlying principles in the most common hydrocyclone models.

2.6.4.1 Equilibrium Orbit theory

One of the longest standing theoretical models was the equilibrium orbit theory put forth by Bradley (1958, 1965). It is based on the assumption that there is a location in the hydrocyclone, for each particle, where the outward acting inertial forces and the inward acting drag forces are in equilibrium. Those particles orbiting at the radial distance that coincidences with the locus of zero

vertical velocity will have equal probability of reporting to both products, and therefore represent the cut-size. The existence of the locus of zero velocity, the basis of the model, has been shown to exist (Marins *et al.*, 2010). However, several key assumptions made about the flow within the hydrocyclone, including laminar flow, free settling conditions and Stokesian particle slip velocity have all been criticised. While this model does describe some of the process trends well, it cannot be used directly in design or operational situations. Mueller and Bohnet (1998) extended this model to incorporate a large number of additional parameters, for implementation in hydrocyclone design. However, this model includes a number of empirical friction factors, for the cyclone inlet, cyclone top, conical section and walls, which are difficult to predict without experimental data.

2.6.4.2   Residence Time Theory

Another theoretical approach, which was first proposed by Rietema (1961), is the Residence Time Theory. This model is not concerned with particular flow phenomena within the hydrocyclone, instead, it proposes that the cut size is equal to the size of particle which can just traverse the distance to the cyclone wall region within the residence time (if injected at the centre point of the feed inlet). While this approach is not common, Dwari *et al.* (2004) did propose an updated version of the model. The authors found the predicted cut-size varied by up to 40 % from the measured values. This error could be attributed to the questionable assumptions that the turbulent eddy diffusion has a negligible effect on the separation and the particles' Reynolds number are so low that Stokes aw for the free flow velocity applies (Dwari *et al.*, 2004).

2.6.4.3   Crowding Theory

Crowding Theory (Bloor *et al.*, 1980; Fahlstrom, 1963; White, 1991) is based on the observation that for a cyclone operating at high feed concentrations (above 20 % by volume), the cut size is primarily determined by the discharge capacity of the spigot; and the feed size distribution. The theory states that when the underflow area becomes too crowded with particles the discharge capacity has been reached, forcing additional particles to exit *via* the overflow. This controls the cut-size. The spigot discharge capacity, however, is effected by feed rate (pressure drop) and the outlet and inlet dimensions of the hydrocyclone (Slechta and Firth, 1984). These complex relationships between the geometrical properties of the hydrocyclone and the spigot discharge capacity must first be established, before cut-size can be considered. Therefore, there are still no simple correlations for cut-size based upon this theory, limiting its practicality (Svarovsky, 1990).

2.6.4.4   Turbulent Diffusion Theory

The Turbulent Diffusion Theory (also referred to as the Turbulent Two-Phase Flow Theory) attributes separation to the turbulent cross flow moving in perpendicular direction to the force field. The model based on this theory, put forth by the Forschunginstitut Aufbereitung research group and most recently described by Schubert (2010), predicts the cut-size for cyclone operations in both dilute and dense particle concentrations. This theory, however, assumes a homogenous turbulence field which is not representative of the real conditions in a hydrocyclone (Chen *et al.*, 2000).

2.6.4.5   Empirical Models

Unlike the above semi-empirical models, empirical models are not based on any specific theory of hydrocyclone operation and are derived by fitting models to experimental data. This involves the development of a set of regression equations for the chosen performance characteristics (both operational and geometrical). The Plitt and the Nageswararao models, are the two most widely used hydrocyclone models (Nageswararao *et al.*, 2004; Narasimha *et al.*, 2010; Wills and Finch, 2016), most likely due to the ease in which these models can be incorporated into spreadsheets. This means they are particularly useful for industrial scale simulation studies of comminution and classification circuits using dedicated computer simulators such as JKSimMet (Nageswararao *et al.*, 2004) and MODSIM (King, 2012; Nageswararao *et al.*, 2004), or the flowsheet simulator Limn (Hand and Wiseman, 2010).

In 1962, a small group at the University of Queensland initiated research on the control, modelling and optimisation of mineral processing plants; with the modelling of industrial cyclone classifiers being an integral part of the project (Nageswararao *et al.*, 2004). The first ever comprehensive model for the description of the performance of industrial hydrocyclones and its application at Mount Isa Mines were significant outcomes (Lynch and Rao, 1968). Further research (Lynch *et al.*, 1975; Marlow, 1973; Nageswararao, 1978) resulted in the formulation of the Nageswararao model, published in its most recent form by Nageswararao *et al.* (2004). This model consists of four basic equations: flow rate (given feed pressure); water recovery to the underflow; volumetric recovery of feed slurry to the underflow, and corrected cut point. The model is known to under-predict water recovery values in the low water recovery region and under-predicts the cut size in the fine particle size region. This is a particular problem at low feed concentrations, and arises

partly because this region is outside the range of the data set originally used to fit the model (Narasimha *et al.*, 2010).

Combining the first industrial database for hydrocyclones generated by Rao (1966), with his own laboratory data, Plitt (1976) developed an alternative general purpose cyclone model, revised by Flintoff *et al.* (1987). The model, based on the results of 297 experiments, provided an empirical equation for direct calculations of corrected cut size, sharpness of separation, flow split and throughput. The large, and varied, data set for which Plitt based his studies on, meant the equations were capable of covering a large range of operating variables. However, Plitt maintained the assumption that his model could predict cyclone performance independent of feed material characteristics (Nageswararao *et al.*, 2004). This was later revised by the inclusion of a feed calibration factor, which needs to be determined based upon experimental data as without this there is a large associated error, with the accrued errors being as great as ± 50 % (Kelly and Spottiswood, 1982).

A comprehensive review of both models was presented by Nageswararao *et al.* (2004). The authors found that both models were still heavily reliant on material constants, obtained *via* experimentation. Figure 2.18 also shows the large variability in the predicted flow split and water recovery when compared to the data these equations were based upon, further illustrating the error associated with these models.
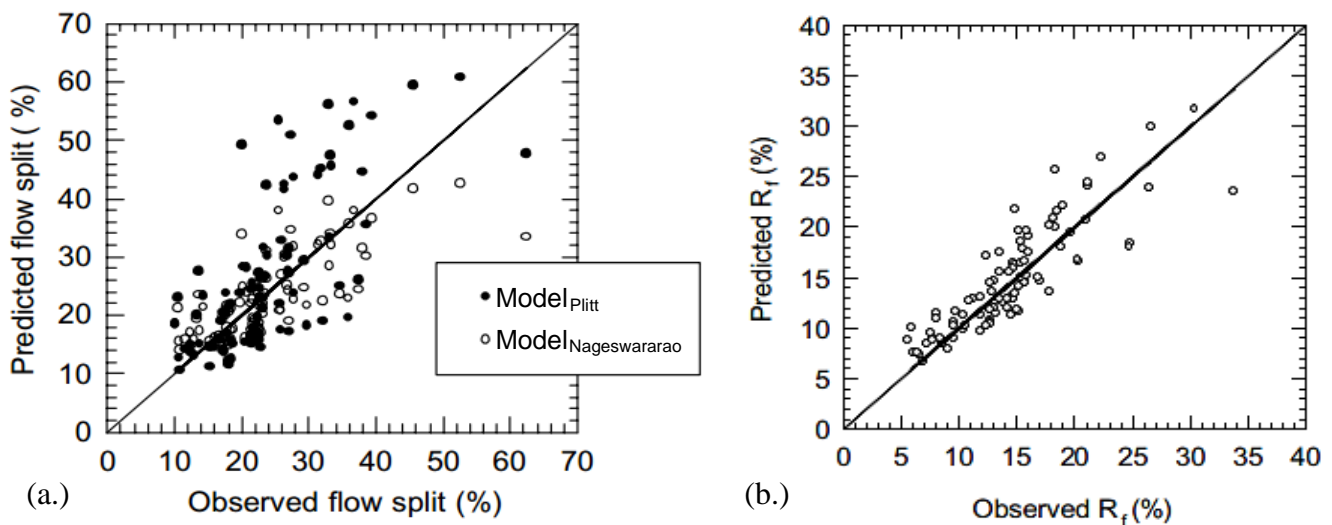
Figure 2.18: (a) Prediction of the flow split using the Plitt and Nageswararao models compared to the data of Plitt (1976) and (b) prediction of the water recovery to the underflow using the Nageswararao model and data of Rao (1966). Reproduced with permission from Nageswararao *et al.* (2004).

2.6.4.6   Model Summary

All models are subject to the limitation that they are merely approximations of the physical reality, based on simplifying assumptions or hypotheses and (usually) process measurements. Errors in any measured data used for evaluating model parameters will also be carried forward into the model, and hence into the simulation results. As a consequence, the model predictions from any model will never be perfect (Nageswararao *et al.*, 2004). Chen *et al.* (2000) undertook a comprehensive study comparing seven of the main empirical and semi-empirical hydrocyclone models used to size and select hydrocyclones in industrial applications. These models included semi-empirical models based upon the equilibrium orbit theory, turbulent diffusion theory, and residence time theory; as well as the empirical model of Plitt. The authors concluded that these models often have limitations due to the specific system the model development was based on. (Nageswararao *et al.*, 2004) states that their model was based upon data collected from a hydrocyclone operating as a classifier in a closed grinding circuit, and so therefore when the cyclone is used as a thickener, washer, or if the feed solids concentration is low (20 % by weight) the reliability of predictions is doubtful.

Due to the complexity of hydrocyclone operations, most of the existing models are a combination of 'sub models', each describing a certain property in a cyclone operation. With these different considerations, assumptions and adjustable parameters, it is possible to select a combination of parameters to fit any particular set of hydrocyclone data very well, within ± 5 % (Chen *et al.*, 2000). However, this method may not necessarily be suitable for another system; or even the same system operated under different conditions. As yet, there is no one model that can reliably simulate the majority of current hydrocyclone operations. This has led to the use of Computational Fluid Dynamics (CFD) in an attempt to create a more fundamental model of the hydrocyclone. This will be the focus of the following chapter.

2.7   References

Aldrich, C., 2015. Chapter One - Hydrocyclones, Progress in Filtration and Separation. Academic Press, Oxford, pp. 1-24.

Arterburn, R.A., 1982. The sizing and selection of hydroyclones, in: Mular, A.L., Jergensen, G.V. (Eds.), Design and Installation of Comminution Circuits. AIME, New York, USA, pp. 597-607.

Bloor, M.I.G., Ingham, D.B., Laverack, S.D., 1980. An analysis of boundary layer effects in a hydrocyclone, Proceedings of the International Conference on Hydrocyclones. BHRA, Cambridge, England, pp. 49–62.

Bradley, D., 1958. A theoretical study of the hydraulic cyclone. The Industrial Chemist 34, 473-480.

Bradley, D., 1965. The Hydrocyclone, 4th ed. Pergamon Press, London.

Bradley, D., Pulling, D.J., 1959. Flow patterns in the hydraulic cyclone and their interpretation in terms of performance. Transactions Institution of Chemical Engineers 37, 34-45.

Bretney, E., 1891. US Patent No. 453, 105.

Castilho, L.R., Medronho, R.A., 2000. A simple procedure for design and performance prediction of Bradley and Rietema hydrocyclones. Minerals Engineering 13, 183-191.

Chen, W., Zydek, N., Parma, F., 2000. Evaluation of hydrocyclone models for practical applications. Chemical Engineering Journal 80, 295-303.

Del Villar, R., Finch, J.A., 1992. Modelling the cyclone performance with a size dependent entertainment factor. Minerals Engineering 5, 661-669.

Dubey, R.K., Climent, E., Banerjee, C., Majumder, A.K., 2016. Performance monitoring of a hydrocyclone based on underflow discharge angle. International Journal of Mineral Processing 154, 41-52.

Dündar, H., Kalugin, A., Delgado, M., Palomino, A., Türkistanli, A., Aquino, B., Lynch, A.J., 2014. Screens and cyclones in closed grinding circuits, Proceedings of the 27th International Mineral Processing Congress (IMPC), Santiago, Chile, pp. 1–11.

Dwari, R.K., Biswas, M.N., Meikap, B.C., 2004. Performance characteristics for particles of sand FCC and fly ash in a novel hydrocyclone. Chemical Engineering Science 59, 671-684.

Fahlstrom, P.H., 1963. Studies of the Hydrocyclone as a Classifier, in: Roberts, A. (Ed.), Proceedings of the Sixth International Mineral Processing Congress, Cannes, pp. 87-113.

Finch, J.A., 1983. Modelling a fish-hook in hydrocyclone selectivity curves. Powder Technology 36, 127-129.

Flintoff, B.C., Plitt, L.R., Turak, A.A., 1987. Cyclone modelling: a review of present Technology. CIM Bulletin 80, 39-50.

Gaudin, A.M., Groh, J.A., Henderson, H.B., 1931. Effects of particle size on flotation. American Institute of Mining and Metallurgy 414, 3-23.

Ghodrat, M., Kuang, S.B., Yu, A.B., Vince, A., Barnett, G.D., Barnett, P.J., 2014. Numerical analysis of hydrocyclones with different conical section designs. Minerals Engineering 62, 74-84.

Gupta, A., Yan, D.S., 2006. Chapter 12 - Classification, Mineral Processing Design and Operation. Elsevier Science, Amsterdam, pp. 354-400.

Hand, P., Wiseman, D., 2010. Addressing the envelope. Journal of the Southern African Institute of Mining and Metallurgy 110, 365-370.

Heiskanen, K., 1993. Particle Classification. Chapman & Hall, London.

Hochscheid, R.E., 1987. Horizontal cyclone in closed-circuit grinding. Mining Engineering 39, 262-266.

Kelly, E.G., 1991. The significance of by-pass in mineral separators. Minerals Engineering 4, 1-7.

Kelly, E.G., Spottiswood, D.J., 1982. Introduction to mineral processing. John Wiley & Sons, New York.

Kelsall, D.F., 1953. A further study of the hydraulic cyclone. Chemical Engineering Science 2, 254-272.

Kelsall, D.F., Holmes, J.A., 1960. Improvement of Classification Efficiency in Hydraulic Cyclones by Water Injection, 5th International Mineral Processing Congress. IMM, London, England, pp. 159-170.

King, R.P., 2012. Modeling and Simulation of Mineral Processing Systems, 2nd ed. SME, Colorado, USA.

Luckie, P.T., Austin, L.G., 1975. Mathematical analysis of mechanical air separator selectivity curves. Transactions of the Institute of Mining and Metallurgy 84.

Lv, W.-j., Huang, C., Chen, J.-q., Liu, H.-l., Wang, H.-l., 2015. An experimental study of flow distribution and separation performance in a UU-type mini-hydrocyclone group. Separation and Purification Technology 150, 37-43.

Lynch, A.J., Rao, T.C., 1968. Studies on the operating characteristics of hydrocyclone classifiers. Indian Journal of Technology 6, 106–114.

Lynch, A.J., Rao, T.C., Bailey, C.W., 1975. The influence of design and operating variables on the capacities of hydrocyclone classifiers. International Journal of Mineral Processing 2, 29-37.

Lynch, A.J., Rao, T.C., Prisbrey, K.A., 1974. The influence of hydrocyclone diameter on reduced-efficiency curves. International Journal of Mineral Processing 1, 173-181.

Lynch, A.J., Rowland, C.A., 2005. The History of Grinding. Society for Mining, Metallurgy, and Exploration, Colorado, USA.

Marins, L.P.M., Duarte, D.G., Loureiro, J.B.R., Moraes, C.A.C., Freire, A.P.S., 2010. LDA and PIV characterization of the flow in a hydrocyclone without an air-core. Journal of Petroleum Science and Engineering 70, 168-176.

Marlow, D., 1973. A mathematical analysis of hydrocyclone data, JKMRC. University of Queensland, Brisbane, Australia.

Martínez, L.F., Lavín, A.G., Mahamud, M.M., Bueno, J.L., 2008. Vortex finder optimum length in hydrocyclone separation. Chemical Engineering and Processing: Process Intensification 47, 192-199.

Milin, L., Hsieh, K.T., Rajamani, R.K., 1992. The leakage mechanisms in the hydrocyclone. Minerals Engineering 5, 779-794.

Mueller, M., Bohnet, M., 1998. Pressure Drop and Grade Efficiency of a Newly Developed Hydrocyclone for the Separation of Two Different Solids from a Liquid Flow, Third International Conference on Multiphase Flow, Lyon, France.

Nageswararao, K., 1978. Further developments in the modelling and scale-up of industrial hydrocyclones, JKMRC. University of Queensland, Brisbane, Australia.

Nageswararao, K., Karri, B., 2016. Fish hook in classifier efficiency curves: An update. Separation and Purification Technology 158, 31-38.

Nageswararao, K., Wiseman, D.M., Napier-Munn, T.J., 2004. Two empirical hydrocyclone models revisited. Minerals Engineering 17, 671-687.

Narasimha, M., Brennan, M.S., Mainza, A.N., Holtham, P.N., Powell, M.S., 2010. Towards the improved hydrocyclone models; Contributions from CFD, XXV International Mineral Processing Congress IMPC 2010, Brisbane, Australia, pp. 3299-3312.

Neesse, T., Schneider, M., Dueck, J., Golyk, V., Buntenbach, S., Tiefel, H., 2004. Hydrocyclone operation at the transition point rope/spray discharge. Minerals Engineering 17, 733-737.

Plitt, L.R., 1976. A mathematical model of the hydrocyclone classifier. CIM Bulletin 69, 114–123.

Rao, T.C., 1966. The characteristics of hydrocyclones and their application as control units in comminution circuits, JKMRC. University of Queensland, Brisbane, Australia.

Rao, T.C., Nageswararao, K., Lynch, A.J., 1976. Influence of feed inlet diameter on the hydrocyclone behaviour. International Journal of Mineral Processing 3, 357-363.

Rietema, K., 1961. Performance and design of hydrocyclones - Parts I-IV. Chemical Engineering Science 15, 298-325.

Romero, J., Sampaio, R., Gama, R.S.d., 2004. Numerical simulation of flow in a hydrocyclone. Latin American Applied Research 34, 1-9.

Schubert, H., 2010. Which demands should and can meet a separation model for hydrocyclone classification? International Journal of Mineral Processing 96, 14-26.

Silva, A.C., Silva, E.M.S., Matos, J.D.V., 2012. A modification in Plitt's for hydrocyclones simulation. International Journal of Recent Research and Applied Studies 13, 753-758.

Silva, N.K.G., Silva, D.O., Vieira, L.G.M., Barrozo, M.A.S., 2015. Effects of underflow diameter and vortex finder length on the performance of a newly designed filtering hydrocyclone. Powder Technology 286, 305-310.

Slechta, J., Firth, B.A., 1984. Classification of fine coal with a hydrocyclone. International Journal of Mineral Processing 12, 213-237.

Svarovsky, L., 1990. Chapter 6 - Hydrocyclones, Solid-Liquid Separation. Butterworth-Heinemann, London.

Trahar, W.J., 1981. A rational interpretation of the role of particle size in flotation. International Journal of Mineral Processing 8, 289-327.

Vakamalla, T.R., Kumbhar, K.S., Gujjula, R., Narasimha, M., 2014. Computational and experimental study of the effect of inclination on hydrocyclone performance. Separation and Purification Technology 138, 104-117.

Verde, F.S., Manto, A.T., Cortes, R.N., 1991. Horizontal hydrocyclone at ACMDC's Biga concentrator, 4th Asian Symposium on Mineral Processing, Manilla, The Philippines.

Wang, B., Yu, A.B., 2008. Numerical study of the gas–liquid–solid flow in hydrocyclones with different configuration of vortex finder. Chemical Engineering Journal 135, 33-42.

White, D.A., 1991. Efficiency curve model for hydrocyclones based on crowding theory. Transactions Section C: Mineral Processing and Extractive Metallurgy 100, 135-138.

Wills, B.A., Finch, J.A., 2016. Chapter 9 - Classification, Wills' Mineral Processing Technology (Eighth Edition). Butterworth-Heinemann, Boston, pp. 199-221.

Chapter 3: A review of the computational modelling of hydrocyclones – a need for understanding and prediction

3.1 Abstract

The application of computational fluid dynamics (CFD) to model the flow within a hydrocyclone is continuing to grow in popularity. This chapter presents an amalgamation of previous literature on CFD modelling of hydrocyclones, to act as a guideline for future studies. Areas of focus include: turbulence and multiphase modelling in the hydrocyclone; boundary conditions; mesh development; numerical discretisation schemes and convergence criteria; initialisation procedures; and model validation. It is well understood that the modelling of the turbulence within the hydrocyclone is significant, with numerous studies comparing the performance of the k-ε models, the Reynolds Stress Model (RSM) and the Large Eddy Simulation (LES) model. The LES model has unanimously been shown to be the most accurate turbulence model, in particular when predicting the tangential velocity components. However, due to the large computational expense of the LES model the RSM is often used, as it still provides reasonable predictions at a lower computational cost. The air core, a feature of the hydrocyclone which has a large impact on its performance, has been shown to be modelled well with both the Volume Of Fluid (VOF) model and Mixture model. The simulation techniques for two-phase (water-air) flows appear to be well understood as numerous publications have shown CFD to accurately predict the water split, pressure drop, air core diameter and velocity components when compared to experimental measurements. Current research is focused on the modelling of high solid concentration flow, which are more in line with industrial conditions, and this type of simulation has not yet been validated to the same degree as the two-phase simulations. This is primarily due to the lack of experimental data of particle flow in high solids concentration, an area of study which should be focused on in the future.

3.2 Introduction

The hydrocyclone is a continuously operating classifying device that utilises differences in drag and inertial forces in high speed flows to accelerate the settling rate of particles or liquids. Hydrocyclones, often shortened to cyclone, have gained widespread use in a number of industries since their inception in the 1940's (Aldrich, 2015). This is primarily due to their low capital and

operational cost, simple design, large throughput relative to size, and low maintenance (Wills and Finch, 2016). Industrial applications include the removal of sand, staples or other contaminants in paper mills; particle classification in closed grinding circuits in mineral processing plants; and the separation of oil and water in the oil industry.

In a hydrocyclone, a conically shaped vessel that is open at its apex (also referred to as spigot or underflow), sits below a cylindrical section, which contains a tangential or involute feed inlet. The feed enters under pressure to the stationary body, creating a swirling, vortex flow pattern, which is forced downwards due to the intrusion of the vortex finder. This minimises the short-circuiting of feed directly to the overflow. Once the flow leaves the feed zone, also referred to as the cylindrical section, the constriction in the adjoining conical section forces some of the flow to reverse its direction. This forms a secondary upwards-travelling inner vortex. Along the vertical axis exists a low-pressure zone, created by the vortexing feed. As the apex is open to the atmosphere an air core develops along this central axis. Air entrained in the feed is also said to contribute to this phenomena (Wills and Finch, 2016).

Particles within the hydrocyclone's flow pattern are subjected to two opposing forces: an *'outward'* acting inertial force, and an opposing inwardly acting drag force provided by the carrying fluid. The inertial force, sometimes misinterpreted as a *'centrifugal force'*, develops as a particle wishes to continue its motion, which at any moment is tangential to the circular path. This force balance is dependent upon mass and surface area, thereby separating particles according to their size, specific gravity and shape. Particles with a larger mass, and therefore having a greater momentum than drag, move to the wall of the cyclone, and migrate down to the apex opening. Particles whose inertia is lower in magnitude than the force required to overcome the drag of the carrier fluid, move towards the zone of low pressure along the hydrocyclones vertical axis and are carried upward through the vortex finder to the overflow. There will naturally be a particle size at which these forces are approximately equal. This is referred to as the 'cut-size' and represents the particle size which has a 50 % chance of reporting to either the overflow or underflow. The cut size and the behaviour of particles near this size determine the selection and performance of the hydrocyclone and is typically represented by a partition curve.

The qualitative description of this swirling turbulent flow is a complex problem. When the continuous phase is further loaded with dispersed phases, the complexity increases further as the

interrelations between the two phases need to be adequately modelled. This has meant that performance prediction and selection of hydrocyclones for industrial applications is typically based upon empirical models (Marins *et al.*, 2010). These models are based on a phenomenological description of the process, including effects from operating conditions and geometric parameters, with the numerical constants determined from a large database of experimental results. While these models have gained widespread use in industry, their application in situations where the process conditions are outside of the initial database of experiments can lead to loses in performance. Examples of this include the Nageswararao model (Nageswararao *et al.*, 2004), which under predicts the water recovery at low water recovery rates and the cut size in small hydrocyclones (Narasimha *et al.*, 2010).

Alternatively, more fundamental models, based upon Computational Fluid Dynamics (CFD), can be used to predict hydrocyclone performance. Modelling is not without its difficulties, however, as the dominance of turbulent length scales on particle classification; and the multiphase interactions between particles, carrier fluid, cyclone walls and the air core all need to be suitably modelled. In recent years, with the advancement of computational hardware, and the associated improvement in software capabilities, the interest in computational models of hydrocyclones has increase significantly. Figure 3.1 shows a clear upward trend in the number of journal publications related to hydrocyclone or cyclone modelling (which includes gas cyclones or dense medium cyclones) since 1995. With previous review papers Nowakowski *et al.* (2004) and Narasimha *et al.* (2007) published more than ten years ago, this growth has made it important to collate and analyse the vast amount of published information and results to ensure that hydrocyclone models continue to progress.
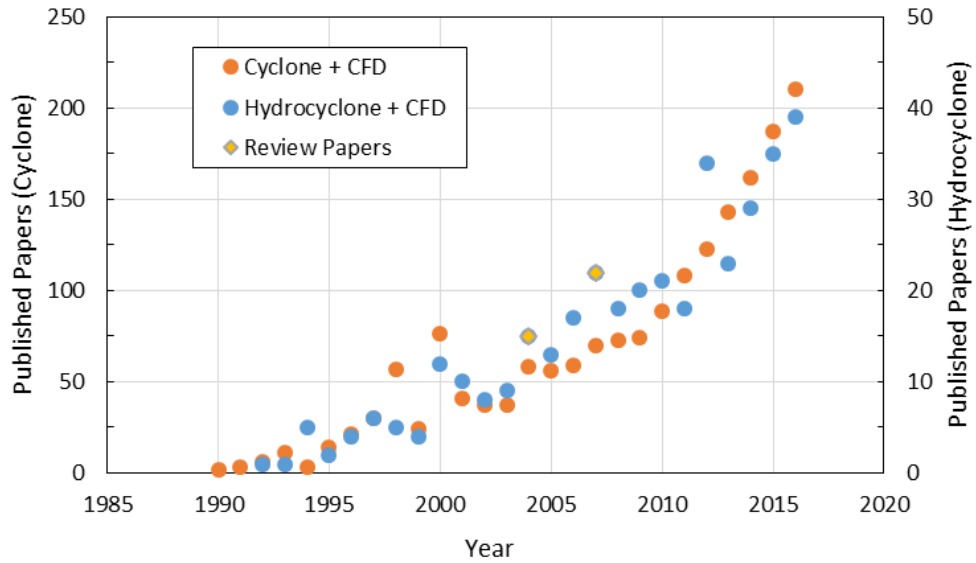
Figure 3.1: Number of journal papers publish since 1995 that contain the key words hydrocyclone and CFD or cyclone and CFD based off a science direct search.

The modelling of hydrocyclones is computationally expensive, and so has limited the optimisation of different factors or choices inside the model. To help alleviate this issue, this chapter aims to collect and assess all the published information on hydrocyclone modelling. This will clarify areas which need further study, reduce superfluous repetition of known correlations, and to obtain consistency in fields where the optimal parameters are known. Areas of focus include:

- Turbulence and multiphase modelling in the hydrocyclone
- Boundary conditions
- Mesh development
- Numerical discretisation schemes and convergence criteria
- Initialisation procedures
- Model validation

3.3   Turbulence Modelling in the Hydrocyclone

All flows encountered in engineering practice can be divided into three flow regimes: laminar, turbulent, or a transitional phase between the two. Laminar flows are characterised by smoothly varying velocity fields in both time and space, in which individual layers (or 'laminae') of fluid slide past one another without generating cross currents (Versteeg and Malalasekera, 2007). Industrial hydrocyclones, however, typically operate at velocities where the flow is turbulent (Narasimha *et al.*, 2006a). Turbulence is observed in fluids at moderate to high Reynolds numbers (> 4000), and describes a three-dimensional, unsteady, random state of motion. The flow reversal and separation near the underflow; the strong swirling motion; and the free surface of the air core all introduce anisotropy and strain into the turbulence. This makes the modelling of turbulence particularly difficult.

Turbulence is, in principle, described by the Navier-Stokes equations, however in most cases the computational requirements to resolve the wide range of scales in both time and space by Direct Numerical Simulation (DNS) far exceeds the current level of computing power. Therefore estimates, or averages, must be applied to the Navier-Stokes equations to filter out all (Reynolds Averaged Navier-Stokes (RANS) equations), or at least parts (Scale-Resolving Simulation (SRS) models), of the turbulent spectrum. These averaging processes introduce additional unknown terms into the transport equations (Reynolds Stresses and Fluxes) that need to be provided by suitable turbulence models (turbulence closures).

No single turbulence model is universally accepted as being superior for all classes of problems. The choice of turbulence model for a particular application will be guided by the established practice in the field but is dependent upon factors such as the physics of the flow; the required level of accuracy; the available computational resources; and the time available for the simulation. The choice of turbulence model is therefore a trade-off between simulation time/power and accuracy. Below outlines some of the most popular choices of turbulence models for hydrocyclones, followed by a review of the comparative turbulent model studies found in literature. The detailed mathematics and principles of the turbulence models are described in detail elsewhere (Versteeg and Malalasekera, 2007).

3.3.1   The k-ε Turbulence Models

The most widely used turbulence models in industrial CFD applications are the two-equation models (Versteeg and Malalasekera, 2007). They solve two additional transport equations and model the Reynolds Stresses using the Eddy Viscosity approach. The standard k-ε model (Launder and Spalding, 1974) falls into this category, solving partial differential equations (PDEs) for the turbulent kinetic energy, k, and its dissipation rate, ε. Due to its economic use of computational power and reasonable accuracy in a wide range of applications, this turbulence closure was favoured in early hydrocyclone models (Dai *et al.*, 1999); simulations with limited resources (Gao *et al.*, 2011; Sripriya *et al.*, 2007); or complex multiphase models (Narasimha *et al.*, 2005; Swain and Mohanty, 2013). However, one of the underlying assumptions of the k-ε model is that the turbulent viscosity is isotropic, meaning the ratio between the Reynolds stress and the mean rate of deformation (strain) is the same for all directions (based on the Boussinesq approximation). The turbulence also is assumed to be isotropic as only one scalar velocity fluctuation is modelled. These assumptions are known to be unrealistic for swirling turbulent flows (Narasimha *et al.*, 2006a; Versteeg and Malalasekera, 2007). Several authors have since shown that the k-ε model is not suitable for modelling turbulence in hydrocyclones (Bhaskar *et al.*, 2007a; Fraser *et al.*, 1997; He *et al.*, 1999; Ma *et al.*, 2000; Mousavian *et al.*, 2009; Petty and Parks, 2001; Suasnabar, 2000). To overcome these inefficiencies, several modifications to the standard k-ε model have been proposed. An example of this is the curvature correction factor, which has been implemented (Fraser *et al.*, 1997; He *et al.*, 1999) to help model the curved flow in a hydrocyclone.

A more sophisticated approach is the RNG k-ε model, which gets its name from the statistical technique from which it is based, namely the renormalisation group theory. Similar in form to the standard k-ε model, it includes several refinements that make it more suitable for modelling the turbulence in the hydrocyclone. This includes an additional term in the dissipation rate ε equation, which significantly improves the accuracy in rapidly strained flows. The effect of swirl on turbulence is also included, *via* a swirl factor, enhancing accuracy for swirling flows (Gupta *et al.*, 2008). This has been shown to provide an increased accuracy over the standard k-ε model (Gupta *et al.*, 2008; Safa and Soltani Goharrizi, 2014). Many others, however, have shown that it is still unable to fully describe the turbulent flow within the hydrocyclone, with some authors noting the models' inability to form an air core in conditions where more sophisticated turbulences models do (Bhaskar *et al.*, 2007a; Delgadillo and Rajamani, 2005; Narasimha *et al.*, 2006a; Suasnabar,

2000; Vakamalla and Narasimha, 2017). It should be noted that while it is possible to use the curvature correction for the RNG k-ε model, it is not recommended, as it already contains terms to include rotational or swirl effects.

3.3.1.1   Model Constants

A summary of the model constants reported in literature for the k-ε and RNG k-ε models is shown in Gupta *et al.* (2008) and Narasimha *et al.* (2005) both outlined the use of the default model constants when utilising the k-ε model. Suasnabar (2000), however, studied the effect of the different model constants and concluded that $C_{2\varepsilon}$ has a significant effect on the predicted axial and tangential velocities. The optimum value was determined to be 1.36. Modifications to the values for the C_μ and Prandtl Number ε parameters were also shown to improve results, although to a much lesser extent. Suasnabar (2000) noted that while these adjustments improved predictive accuracy, their true predictive power is limited, as they were chosen empirically to fit only one particular data set. This statement is supported by the work of Dai *et al.* (1999), who concluded that values of $C_\mu = 0.085$, $C_{1\varepsilon} = 1.62$ and $C_{2\varepsilon} = 1.79$ were best suited for their experimental data. Suasnabar (2000) also found that to improve predictions the swirl constant in the RNG k-ε model needed to be increased from the default value (0.07), which is defined for weakly to moderately swirling flows. However, beyond a certain point (0.10), further increases caused numerical instability.

Table 3.1. Gupta *et al.* (2008) and Narasimha *et al.* (2005) both outlined the use of the default model constants when utilising the k-ε model. Suasnabar (2000), however, studied the effect of the different model constants and concluded that $C_{2\varepsilon}$ has a significant effect on the predicted axial and tangential velocities. The optimum value was determined to be 1.36. Modifications to the values for the C_μ and Prandtl Number ε parameters were also shown to improve results, although to a much lesser extent. Suasnabar (2000) noted that while these adjustments improved predictive accuracy, their true predictive power is limited, as they were chosen empirically to fit only one particular data set. This statement is supported by the work of Dai *et al.* (1999), who concluded that values of $C_\mu = 0.085$, $C_{1\varepsilon} = 1.62$ and $C_{2\varepsilon} = 1.79$ were best suited for their experimental data. Suasnabar (2000) also found that to improve predictions the swirl constant in the RNG k-ε model needed to be increased from the default value (0.07), which is defined for weakly to moderately

swirling flows. However, beyond a certain point (0.10), further increases caused numerical instability.

Table 3.1: Model Constants for the *k-ε* and RNG *k-ε* models (grey cells represent default values).

Turbulence Model	Reported Constants						References
	C_μ	$C_{1\varepsilon}$	$C_{2\varepsilon}$	Prandtl Number k	Prandtl Number ε	Swirl Factor	
k-ε	0.09	1.44	1.92	1	1.3	-	(Gupta *et al.*, 2008; Mousavian *et al.*, 2009; Narasimha *et al.*, 2005; Swain and Mohanty, 2013)
	0.105		1.36		1.7	-	(Suasnabar, 2000)
	0.085	1.62	1.79			-	(Dai *et al.*, 1999)
RNG *k-ε*	0.0845	1.42	1.68	-	-		(Delgadillo and Rajamani, 2005)
				-	-	0.10	(Suasnabar, 2000)

3.3.2 *Reynolds stress model (RSM)*

The Reynolds stress model (RSM) is one of the most complex RANS turbulence models. Also referred to as the second-order or second-momentum closure model, the RSM solves transport equations for each of the six independent Reynolds stresses (Elsayed and Lacor, 2010). This enables the model to account for complex interactions in turbulent flow fields, such as the directional effects of the Reynolds stresses. Effects of streamline curvature, swirl, rotation, and rapid changes in strain rate are modelled in a more rigorous manner than the *k-ε* models, making the RSM a more suitable turbulence model for the hydrocyclone. The added calculations do come at a significantly higher computing cost.

The RSM is generally accepted as the simplest model that can predict the anisotropic turbulence behaviour seen in the hydrocyclone (Versteeg and Malalasekera, 2007). Even though it has been shown to be not as accurate as the LES model (discussed below) it represents a good compromise between computational accuracy and expense. This has led to widespread application of the RSM for modelling turbulence in the hydrocyclone (Bhaskar *et al.*, 2007b; Cui *et al.*, 2014; Cullivan *et al.*, 2003; Cullivan *et al.*, 2004; Davailles *et al.*, 2012a; Davailles *et al.*, 2012b; Dlamini *et al.*, 2005; Ghodrat *et al.*, 2014a; Ghodrat *et al.*, 2014b; Ghodrat *et al.*, 2016; Hwang *et al.*, 2013;

Hwang and Chou, 2017; Kuang *et al.*, 2012; Leeuwner and Eksteen, 2008; Olson and Van Ommen, 2004; Schuetz *et al.*, 2004; Slack *et al.*, 2004; Suresh *et al.*, 2010; Vakamalla *et al.*, 2014; Vakamalla *et al.*, 2017; Wang and Yu, 2006; Wang *et al.*, 2007; Wang and Yu, 2008; Xu *et al.*, 2012; Xu *et al.*, 2013; Yang *et al.*, 2010).

A downside to the RSM is that it can suffer from convergence problems due to the numerical issues associated with the coupling of the mean velocity and turbulent stress fields through source terms. Multiple authors have noted a reduced rate of convergence when using the RSM model. Bhaskar *et al.* (2007b) and Slack *et al.* (2004) required a large number of iterations (6000-8000), beyond normal convergence criteria, for the solution to stabilise. While Schuetz *et al.* (2004) required an initialisation of a laminar flow field, before implementing the RSM, to ensure convergence.

3.3.2.1   Modelling the Pressure-Strain Term

The pressure-strain interactions constitute one of the most important elements in the RSM, however remain the most difficult to predict (Versteeg and Malalasekera, 2007). Cullivan *et al.* (2003) stated that the pressure-strain term is expected to be significant for high swirl flow, which features significant anisotropy, and therefore careful consideration should be given to its modelling. The authors compared the predictions of the linear (LPS) and quadratic pressure-strain (QPS) model and concluded that the quadratic pressure-strain correlation of Speziale *et al.* (1991) was a minimum order of accuracy for the RSM. Alternatively, Brennan (2006) stated that the simpler LPS correlation, with the wall reflection effects included, predicted similar velocity values to the QPS once the air core had been established. Narasimha *et al.* (2006a) agreed with this finding, showing that the LPS and QPS models predicted similar velocity profiles and air core structures, which were both found to be less accurate than the large eddy simulation model (discussed in Section 3.3.3). Dlamini *et al.* (2005) also commented on the importance of the pressure-strain term, but found the QPS to induce solution instability, therefore requiring the use LPS. This uncertainty has meant that both the LPS (Chu *et al.*, 2012; Kuang *et al.*, 2012; Mousavian *et al.*, 2009) and QPS (Cullivan *et al.*, 2004; Vakamalla *et al.*, 2017; Vakamalla and Narasimha, 2017) have been used in hydrocyclone modelling.

3.3.2.2   Model Options and Constants

Brennan (2006) , Dlamini *et al.* (2005), and Kuang *et al.* (2012) all reported the use of the RSM (LPS) with the standard wall functions for the near-wall treatment and the wall reflection effects

option. Suasnabar (2000), however, found that the inclusion of the wall reflection term in the RSM had a negative impact on the predicted velocity components. While this was the only work to directly compare results from both methods, the model was very simplified (with an assumed solid air core), as such additional study is recommended. Brennan (2006) also studied the effect of the two adjustable pressure-strain constants ($C1_{PS}$ and $C2_{PS}$) in the LPS model, in an attempt to increase the accuracy of the RSM model. It was found that changing $C2_{PS}$ from the default value of 0.6 to 0.9 improved both the axial and tangential velocity predictions. Further increases damped the Reynolds stress components in the axial direction, impacting negatively on predictions. $C1_{PS}$ was decreased down to 1.0 from 1.8 (default) but was found to have little effect on the predict velocities. For the QPS model, both Cullivan *et al.* (2003) and Vakamalla *et al.* (2017) achieved reasonable results with the use of the default values for all constants.

3.3.3 The Large Eddy Simulation (LES) Model

It is understood that the behaviour of large and small scale turbulent eddies is markedly different. Smaller eddies are nearly isotropic and have a universal behaviour for turbulent flows at sufficiently high Reynolds numbers. Alternatively, larger scale eddies are more anisotropic as their behaviour is dictated by their interaction with the mean flow; the geometry of the problem domain; the boundary conditions; and body forces (Versteeg and Malalasekera, 2007). In many flows these larger turbulent scales carry out most of the turbulent mixing of momentum and mass. Following this logic, the LES model (which falls within the SRS category) resolves the difficult to predict large turbulent eddies, while modelling the behaviour of the small-scale eddies. This limits LES to transient simulations and is recommended for 3D grids (Narasimha *et al.*, 2007).

This more fundamental approach should in principle give more accurate mean flow predictions than the RANS models. The LES model has been shown to accurately predict the velocity components in the hydrocyclone, particularly the peak tangential velocity, when compared to other turbulent models (Banerjee *et al.*, 2016; Brennan, 2006; Brennan *et al.*, 2007; de Souza *et al.*, 2012; Delgadillo and Rajamani, 2005; Karimi *et al.*, 2012; Lim *et al.*, 2010; Narasimha *et al.*, 2006a; Narasimha *et al.*, 2012a; Vakamalla and Narasimha, 2017). Many authors have recommended that LES is the most appropriate turbulence model to capture all the unsteady aspects of hydrocyclone flow structure because the simulation technique preserves the unsteady nature of the 3D large-scale structures of the flow (Banerjee *et al.*, 2016). Predicted values for water split (Brennan *et al.*, 2007; Narasimha *et al.*, 2006a), air core size (Delgadillo and Rajamani, 2005; Narasimha *et al.*, 2006a; Vakamalla *et al.*, 2014), pressure drop (Marthinussen *et al.*, 2014), and particle separation efficiencies (Brennan *et al.*, 2007; de Souza *et al.*, 2012; Delgadillo and Rajamani, 2005; Marthinussen *et al.*, 2014; Narasimha *et al.*, 2012a; Vakamalla *et al.*, 2014; Vakamalla and Narasimha, 2017) have all been shown to be in close agreement with experimental data. The is attributed to the influence of the time dependent large scale turbulent oscillations that impact the formation of the air core as well as the mixing and re-entrainment of particles, which is not considered when modelling the mean flow (Brennan *et al.*, 2007; Slack *et al.*, 2000).

This added accuracy does come at a significant computational cost (Slack *et al.*, 2000) (discussed more in Section 3.5.1). Along with the additional calculation requirements, the application of LES to any flow requires particular care regarding mesh quality and refinement, the order of numerical

schemes and the time step size (de Souza *et al.*, 2012). Smaller eddies are separated *via* spatial filtering, which typically removes all eddies finer than the associated grid size (as any finer detail would be lost anyway). This requires LES models to have substantially smaller grid sizes than other turbulence models, to enable to capture of the relevant turbulent scales. Smaller time steps are also required to ensure turbulence scales are fully developed and not damped out (Narasimha *et al.*, 2006a).

3.3.3.1   Subgrid-Scale Models

The modelling of the small scale turbulent eddies is achieved through subgrid scale models. Karimi *et al.* (2012) compared three different subgrid methods: the Smagorinsky-Lilly model, the WALE model and the dynamic kinetic energy model. Results from all three subgrid models were shown to match closely with the experimental data, suggesting that uncertainties owing to the subgrid model used are small and can be ignored. However, the Smagorinsky-Lilly model was shown to slightly outperform the other two models, with an average difference from the tangential velocity of 6.4%, 10.9% and 10.1% for the Smagorinsky, WALE and kinetic energy models, respectively. The Smagorinsky-Lilly model is simple in structure, and so adding to its accuracy, has become the most prevalent choice of subgrid model (Banerjee *et al.*, 2016; Brennan, 2006; Brennan *et al.*, 2007; de Souza *et al.*, 2012; Delgadillo and Rajamani, 2005, 2007; Marthinussen *et al.*, 2014; Narasimha *et al.*, 2006a; Narasimha *et al.*, 2010; Narasimha *et al.*, 2012a; Vakamalla and Narasimha, 2017). The constant for the Smagorinsky-Lilly model, C_s, has been reported to perform well at its default value of 0.1 (Brennan *et al.*, 2007; Narasimha *et al.*, 2006a), however, a parametric analysis has not been conducted, likely due to the computational expense of the LES model.

3.3.4   Comparative studies of turbulence models

The selection of the turbulence model for hydrocyclone modelling is undoubtedly an important decision. Table 3.2 summarises some of the published comparative studies on turbulence models. It is clear that as models incorporate more fundamental approaches, which comes at significant computational expense, predictions are improved. This is most apparent with the peak tangential velocity component and the air core diameter. The hydrocyclone's complex flow pattern requires the explicit resolving of the turbulent eddies, which the LES model provides. However, the approximations of the RSM have been shown to provide a computationally cheap way of providing

relatively accurate predictions for engineering applications. This should be considered to be the minimum order of accuracy for modelling hydrocyclone flow turbulence, as simpler models provide erroneous results.

The Detached Eddy Simulation (DES) turbulence model, which was not discussed earlier, is a combination of a RANS turbulence model and LES. The RANS model is applied in regions where the turbulent length scale is less than maximum grid dimension (such as near the wall region) and the LES model is applied in the regions where the turbulence length scales are greater than grid dimension. As this model is a hybrid, the computation time and grid levels are expected to be lower than a purely LES turbulence model. The accuracy of the DES turbulence has been shown to be lower than that of the RSM (Vakamalla and Narasimha, 2017; Xu *et al.*, 2009), and therefore it has not gained widespread use in hydrocyclone modelling.

Table 3.2: Summary of literature on the comparison of turbulence models in hydrocyclones, with models ranked based upon their predictive performance.

Authors	Turbulence Model Ranking					Major Conclusions
	k-ε	k-ε RNG	RSM	DES	LES	
Vakamalla and Narasimha (2017)	5	4	2	3	1	• Compared air core diameters, velocity components, and water split values • No air core formation with the k-ε models • DES performed poorly • LES was much better at predicting peak tangential velocities. For all other things RSM and LES were close. • Larger cyclones could use RSM
Bhaskar *et al.* (2007a)	3	2	1			• Compared water throughput and split values for different apex diameters
Narasimha *et al.* (2006a)		3	2		1	• No air core formation with the k-ε models • LES predicted air core diameter more accurately than RSM • LES peak tangential velocity much better than RSM • Axial very similar for LES and RSM
Delgadillo and Rajamani (2005)		3	2		1	• No air core formation with the k-ε models • LES predicted the axial and tangential velocity components, air core diameter, pressure drop, and flow split much more accurately than RSM and k-ε
Mousavian *et al.* (2009)	2		1			• Compared axial and tangential velocity components, RSM was much better
Brennan (2006)			2		1	• Compared axial and tangential velocity components • LES was better at predicting the peak tangential velocities, but other results were fairly similar • Adjustment of parameters in RSM model was able to increase accuracy of peak tangential velocity predictions
Xu *et al.* (2009)		4	2	3	1	• Compared air core diameters, velocity components, pressure drop, and water split values • No air core formation with the k-ε model • LES, DES & RSM were close for all tested components
Slack *et al.* (2000)			2		1	• Compared axial and tangential velocity components • RSM is suitable for inexpensive estimations but LES is best.
Suasnabar (2000)	3	2	1			• Compared axial and tangential velocity components • Adjusted constants for k-ε models and still could not simulate RSM behaviour, the peak tangential velocity being the main difference

3.4 Multiphase Modelling of the Hydrocyclone and its Interphase Transfer

3.4.1 Introduction to Multiphase Modelling

Multiphase modelling refers to the prediction of flows in which there are two or more phases. While the physical phases of matter are defined as gas, liquid, and solid, the concept of phase in multiphase modelling has a much broader meaning. In this case, a phase is defined as an identifiable class of material that has a particular inertial response to, and interaction with, the flow. For example, particles that are made up of the same material but have different sizes can be treated as different phases because each size range of particles will have a particular response to the flow field. For modelling the hydrocyclone, phases include the water carrier fluid, the dynamic air core, and the solid particle phase (which can be made subdivided further into multiple different phases depending on the composition, size and density range tested). The complexity in hydrocyclone modelling is in part due to these complex multiphase interactions.

There are currently two main approaches for the numerical calculation of multiphase flows: the Lagrangian or Eulerian approach. Put simply, the Lagrangian method follows a quantity of interest (for instance a particle) as it moves throughout, and interacts with, the whole domain. The Eulerian method, however, focuses on a single area of a domain (a cell) as flow moves in and out of it. The water and air phases are only solved using the Eulerian approach, *via* either the Mixture, Volume Of Fluid (VOF), or Eulerian models. Particles can be modelled *via* the Eulerian approach, using either the Mixture or Eulerian models, or the Lagrangian technique, using the Discrete Phase Model (DPM). A brief description of these models is provided below.

3.4.1.1 The Volume Of Fluid (VOF) Model

The VOF model is designed for the modelling of two or more immiscible fluids, where the position of the interface between the fluids is of interest (such as the air core in a hydrocyclone). It therefore cannot, on its own, be used to determine particle flows. A single set of momentum equations is shared by all the fluids, making it very computationally efficient, and the volume fraction of each of the fluids in each computational cell is tracked throughout the domain. The volume fraction is then used to determine the air-water interface. One issue with the VOF can be the numerical diffusion of the air-water interface, however, this can be managed using the appropriate discretisation schemes (discussed further in Section 3.6.2.2). More details about the VOF model can be found elsewhere (Hirt and Nichols, 1981).

3.4.1.2   The Mixture Model

In the Mixture model, unlike the VOF model, phases are treated as interpenetrating continua. This means the model can be used to model two or more phases (either fluid or particle). Like the VOF model the governing equations of mass and momentum conservation are solved only for the mixture of liquid, air and solids. Phase segregation is accounted for by including a drift velocity component, meaning phases can move at different velocities. The mixture model assumes that the primary phase is the continuous fluid phase and the volume fraction of each phase present in the mixture is given according to the continuity equation, considering the relative drift velocity among phases (Brennan *et al.*, 2007). The Mixture model is also sometimes referred to as the simplified Two Fluid Model (TFM) or the Algebraic Slip Model (ASM). More information on the mixture can be found elsewhere (Manninen *et al.*, 1996).

3.4.1.3   The Eulerian Model

The Eulerian model is the most fundamentally correct but computationally expensive multiphase model. Momentum and continuity equations are solved for each phase and, like the Mixture model, the phases can be liquid, gas or solid.

3.4.1.4   The Discrete Particle Model (DPM)

The Discrete Phase Model (DPM) allows for the modelling of a discrete particle phase in a Lagrangian frame of reference. Individual particle trajectories are calculated by integrating the force balance on particles. Forces can include the discrete phase inertia, hydrodynamic drag, buoyancy and gravity. The DPM can be used to predict the effects of turbulence on the dispersion of particles due to turbulent eddies present in the continuous phase for both steady and unsteady flows, with the interaction of the particles on the continuous phase able to be included or excluded. As particle-particle interaction is not included in the DPM, only dilute flows should be modelled using this technique. Computational requirements also scale with the number of modelled particles and with the large number of particles in high solids concentration flows ($\sim 10^9$ for a single process unit) this type of modelling is currently impractical (Kuang *et al.*, 2012).

3.4.2   Air-core Modelling

Most hydrocyclones operate with a central air core. The swirling flow within the hydrocyclone creates a low-pressure zone along the vertical axis. This draws air from the underflow opening, which is open to atmosphere. Several authors have noted its impact on the efficient operation of

the hydrocyclone (Davailles *et al.*, 2012a; Delgadillo and Rajamani, 2009; Dlamini *et al.*, 2005; Doby *et al.*, 2008; Gupta *et al.*, 2008; Sripriya *et al.*, 2007). The presence of the air core reduces the effective area available for the fluid to exit through the underflow, which effects both the pressure drop and water flow split. A more in depth explanation of the air core can be found elsewhere (Doby *et al.*, 2008; Neesse and Dueck, 2007).

3.4.2.1   Simplifications of the Air-core

The modelling of an additional phase in an already complex flow has proven to be a computationally expense task (Davailles *et al.*, 2012a; Karimi *et al.*, 2012). There is also some doubt to the validity in the coupling between turbulent and multiphase models, due to the lack of validation on benchmark two-phase flows (Banerjee *et al.*, 2016; Davailles *et al.*, 2012a). This has meant that multiple studies have been reported on hydrocyclone flow without simulating the air core features (Banerjee *et al.*, 2016; Bhaskar *et al.*, 2007a; 2007b; Dlamini *et al.*, 2005; Hwang *et al.*, 2013; Murthy and Bhaskar, 2012; Swain and Mohanty, 2013) or by considering the air core as a hollow or metal tube with a set diameter (Davailles *et al.*, 2012a; Evans *et al.*, 2008; Sripriya *et al.*, 2007). When conducting single phase simulations the air core is often assumed to be represented by the low pressure core at the centre of the hydrocyclone (Banerjee *et al.*, 2016; Bhaskar *et al.*, 2007b).

Davailles *et al.* (2012a) evaluated the differences in simulated results between a 'real' air core modelled using the multiphase model VOF and a 'fake' cylindrical air core of an assumed diameter. The cylinder, set at a fixed location centred around the vertical axis, had a shear free boundary condition applied to the interface between the modelled domain and the hollow tube (meaning there is no resistance between the fluid phase and the cylinder's boundary). This approach aimed to reduce the computational expense associated with the additional phase (reducing simulation time by almost half). Results showed that the simulations with the hollow tube did not perform as well as the modelled air core, however, the results were still in reasonable agreement with the experimental data. Another conclusion made by the work was the importance of correctly matching the diameter of the hollow tube to that of the actual air core. This was done by testing multiple diameters and comparing the water split values to experimental values to determine the correct diameter. This added workload somewhat defeats the sole purpose of this method, which was to reduce computational expense. Other authors (Evans *et al.*, 2008; Sripriya

et al., 2007) have conducted simulations in which the air core was replaced by a steel rod insert (meaning a non-slip boundary was imposed). This was not focused on reducing computational time but instead increasing the performance of the hydrocyclone by reducing the amount of turbulence caused by the fluctuating air core. It was determined that the metal insert did help improve the performance of the hydrocyclone, however; Evans *et al.* (2008) also mentioned that this improvement was dependent on correctly sizing the metal rod.

Karimi *et al.* (2012) compared the difference in the predicted tangential and axial velocities from single phase (water) simulations (using the LES turbulence model and assuming no air core formation), and two-phase simulations (using LES-VOF). The authors found a clear improvement in the quantitative agreement between the numerical predictions and experimental measurements for both velocity components. It was noted, however, that the increase in accuracy (43.4% error down to 26.3% at Plane 60 and from 49.1% to 42.5% at Plane 120) came at a significant computational cost, suggesting that single phase tests provide computationally inexpensive and reasonably accurate predictions of the flow patterns in a hydrocyclone. Mousavian *et al.* (2009) also noted an increase in accuracy with the modelling of the air core. Results for particle separation efficiencies and tangential and axial velocity components were both shown to improve with the addition of the air core (using RSM-VOF).

3.4.2.2   Applications of the VOF Model

The application of VOF model in hydrocyclone simulations typically falls into three main categories. The first is its use in two phase flows (air-water), where it has been shown to accurately predict the air core diameter with both the LES and RSM turbulence models (Cui *et al.*, 2014; Leeuwner and Eksteen, 2008; Narasimha *et al.*, 2006a; Xu *et al.*, 2013). Results from Delgadillo and Rajamani (2009), using the LES model, showed that the VOF model was able to accurately predict the air core diameter (and therefore the water split) for a range of different hydrocyclone geometries and fluid viscosities. The second application is when modelling particle flow *via* the Lagrangian Discrete Phase Model (DPM). The DPM can be coupled with the VOF model, and has been used to predict particle trajectories in hydrocyclones by incorporating drag, gravity, buoyancy (pressure gradient) and 'centrifugal' forces (Delgadillo and Rajamani, 2005, 2007; Wang and Yu, 2006; Wang *et al.*, 2007; Wang and Yu, 2008; Xu *et al.*, 2012). Its last common application is when it is used as a precursor to the mixture model in complex three phase flows (Chu *et al.*, 2012;

Ghodrat *et al.*, 2016; Ji *et al.*, 2017; Vakamalla *et al.*, 2014; Vakamalla and Narasimha, 2017; Vakamalla *et al.*, 2017). In simulations with high solids content the particle must be modelled *via* the Eulerian approach. This is not possible using the VOF model, therefore it is used as a computationally cheap and accurate way to initialise the air-water system before particles are added to the simulation. It should also be noted that the surface tension between air and water needs to be applied when using the VOF model, with a value of 0.078 N·m^{-1} being standard (Narasimha *et al.*, 2006a; Vakamalla and Narasimha, 2017).

3.4.2.3   Applications of the Mixture Model

As previously mentioned, the primary use of the mixture model for air core development is when modelling particulate flows above 10 % solids by weight. It has been successfully used to model the air core in slurries with particle concentrations ranging from 10 to 30 % by weight (Brennan, 2003; Brennan *et al.*, 2007; Ghodrat *et al.*, 2013; Ghodrat *et al.*, 2014b; Ghodrat *et al.*, 2014a; Ghodrat *et al.*, 2016; Ji *et al.*, 2017; Kuang *et al.*, 2012; Narasimha *et al.*, 2012a; Olson and Van Ommen, 2004; Slack *et al.*, 2004; Vakamalla *et al.*, 2014; Vakamalla and Narasimha, 2017; Vakamalla *et al.*, 2017). There are two approaches used to model the air core when using the Mixture model. The first is to disable the slip velocity calculations, meaning the slip velocity is always zero for the air phase. This in effect means the air phase is being solved *via* the VOF model (Brennan *et al.*, 2007; Narasimha *et al.*, 2012a; Vakamalla and Narasimha, 2017; Vakamalla *et al.*, 2017). The second is to assign an air bubble diameter (assuming the bubbles to be rigid spheres). The appropriate bubble diameter has been reported to be 1×10^{-5} m (Ghodrat *et al.*, 2014b; Ghodrat *et al.*, 2016; Kuang *et al.*, 2012) or 1×10^{-4} m (Brennan, 2006), which was determined by comparing the air core diameters to that of the VOF model. The drag law used for the bubbles was the Schiller and Naumann drag law (Ghodrat *et al.*, 2014b; Ghodrat *et al.*, 2016; Kuang *et al.*, 2012).

3.4.2.4   Comparison between Mixture and VOF Models

Brennan (2006) compared the performance of both the Mixture and VOF models with the RSM and LES turbulence models. The authors found that the predicted tangential and axial velocity components were virtually identical. A similar conclusion was also made by Kuang *et al.* (2012) and Ghodrat *et al.* (2016), who also found both models to predict similar pressure drops and water split ratios. As both of these models have been able to accurately predict the air core formation

there has been no requirement to use the more sophisticated and computationally expensive Eulerian model to simulate the air core.

3.4.3   *Particle Modelling*

3.4.3.1   Low vs High solid concentration flows

Particle modelling can be divided into two main areas: low solids concentration modelling and high solids concentration modelling. For low particle concentration flows the DPM (also referred to as the Lagrangian Particle Tracking (LPT) method); a TFM (either the Eulerian or Mixture Model); or the Discrete Element Method (DEM) can be used to model particle flow. Both the TFM and DEM are explained in detail by Zhou *et al.* (2010). The DPM is suited to systems where the dispersed phases are dilute and particles interact mostly with the fluid without significantly changing the fluid transport properties, as particle-particle interactions and the effects of the particle volume fraction on the liquid phase are neglected (Narasimha *et al.*, 2007). It has been shown to accurately predicted particle flow in systems with solid concentrations under 5 % by volume (Delgadillo and Rajamani, 2005, 2007; Hwang *et al.*, 2013; Wang and Yu, 2006; Wang *et al.*, 2007; Wang and Yu, 2008; Xu *et al.*, 2012) and due to its low computational demand has meant it is the default choice when modelling low solids concentration flows. As mentioned earlier the force balances can include the discrete phase inertia, hydrodynamic drag, buoyancy and gravity. In all referenced cases, the pressure gradient force (buoyancy) and gravity were applied, the turbulent dispersion was set to the discrete random walk model, and the drag was calculated using Equation 3.1. In Equation 3.1, μ represents the fluid viscosity (for low solids density mixtures this is assumed to be equal to water), and d_p, Re_p, and ρ_p represent the particle's diameter, Reynolds number and density respectively. In the referenced papers, no information was given for the calculation of the drag coefficient (C_D). This is a significant omission and should not be continued in future publications.

$$F_D = \frac{18\mu}{d_p{}^2 \rho_p} C_D \frac{Re_p}{24} \qquad\qquad \text{Equation 3.1}$$

For high particle concentration flows, the Mixture model has been shown to be an adequate selection (Brennan, 2003; Brennan *et al.*, 2007; Ghodrat *et al.*, 2013; Ghodrat *et al.*, 2014b; Ghodrat *et al.*, 2014a; Ghodrat *et al.*, 2016; Ji *et al.*, 2017; Kuang *et al.*, 2012; Narasimha *et al.*,

2012a; Olson and Van Ommen, 2004; Slack *et al.*, 2004; Vakamalla *et al.*, 2014; Vakamalla and Narasimha, 2017; Vakamalla *et al.*, 2017). Narasimha *et al.* (2012a) noted that the key to modelling classification in a cyclone is to calculate the drift velocity of the dispersed phase relative to the mixture. The authors made two modifications to the default slip velocity calculation: a shear dependent lift force based on the work of Saffman (1965) and a gradient of granular pressure (as calculated by the granular options) to model the Bagnold (1954) dispersive forces. This was first undertaken by Narasimha *et al.* (2006b) when modelling a dense medium cyclone, noting that the lift force coefficient needed to be increased substantially over the value used by Saffman to achieve accurate results. The lift force has also been implemented by other authors (Vakamalla and Narasimha, 2017; Vakamalla *et al.*, 2017).

There are multiple drag laws that have been applied for the modelling of particles with the mixture model, including the Schiller Naumann drag law with an additional correction for hindered settling based on the Richardson and Zaki (1954) drag coefficient (Narasimha *et al.*, 2012a; Vakamalla *et al.*, 2014; Vakamalla and Narasimha, 2017; Vakamalla *et al.*, 2017); the Gidaspow *et al.* (1992) drag law (Brennan *et al.*, 2007); and the Ergun and Wen–Yu correlation (Ghodrat *et al.*, 2014b; Ghodrat *et al.*, 2016; Kuang *et al.*, 2012). There does not appear to be any consensus as to which drag law is most suited to modelling the particle motion in a hydrocyclone, and to the authors' knowledge no study on various drag laws has been completed in hydrocyclone flow.

The implementation of viscosity effects also becomes important as particle loading increases. It is well understood that the particles will impact the apparent viscosity of the fluid. Several authors (Brennan *et al.*, 2007; Ghodrat *et al.*, 2014b; Kuang *et al.*, 2012) have applied a solid viscosity term consisting of a collisional viscosity (arising from particle momentum exchange due to transition and collision) and a kinetic viscosity. This solid viscosity was then added to the fluid viscosity to create a mixture viscosity. For particle collisions, a restitution coefficient of 0.9 (which is the default value in Fluent) has been used (Ghodrat *et al.*, 2014b; Kuang *et al.*, 2012; Vakamalla and Narasimha, 2017); whereas for collisions with the walls of the hydrocyclone, a value of 0.3 has been reported (Hwang and Chou, 2017). Narasimha *et al.* (2012a) used a modified viscosity model which contained a correction factor for the influence of fine particles (below 53 µm) which was calibrated based upon experimental data. Comparing with experimental data showed that the

fines correction factor improved simulation accuracy. This technique has since been used elsewhere (Vakamalla *et al.*, 2014; Vakamalla *et al.*, 2017; Vakamalla and Narasimha, 2017).

3.4.3.2   Comparison of the LPT and Mixture models

Kuang *et al.* (2012) compared the particle recovery to the underflow predicted from the LPT method (*via* the DPM) and the Mixture model. Results showed that both methods could accurately predict the particle separation behaviour, when compared to experimental results, at a particle concentration of 4.11 % by volume. However, when modelling the separation behaviour with a feed solids concentration of 7.04 % by volume, the results predicted by the LPT model deviated significantly from the experimental results. Alternatively, the Mixture model was able to accurately predict the separation behaviour at the higher solids concentration. This confirms the suitability of the Mixture model over the DPM for high solids flows. It should be noted that due to the different materials of the tests (limestone – 2700 kg·m^{-3} vs coal – 1400 kg·m^{-3}) the weight fraction of the lower volume fraction test was higher than that of the high-volume fraction test, approximately 10.7 % compared to 9.6 %. This confirms that it is the volume density of the particles which defines the particle-particle interaction threshold. Many authors quote weight fractions when simulating particle flows in the hydrocyclone, which may be misleading. Vakamalla and Narasimha (2017) also compared the performance of the DPM and Mixture model for a hydrocyclone with a feed solids concentration of 27.2 % by weight. The standard mixture model predicted particle separation values closer to that of the DPM, however, a modified Mixture model (accounting for the increased slurry viscosity and hindered settling rates that occur in high solid content flows) was able to match the experimental data much more closely than both the DPM and standard Mixture model. This demonstrates the importance of viscosity and settling rates when modelling high solids content flows.

3.4.3.3   Particle sphericity

Typically, for simplicity, particles are modelled as perfect inert spheres (Chu *et al.*, 2012; Vakamalla and Narasimha, 2017). While this may not match reality, there have only been limited studies to validate the use of any other value. Olson and Van Ommen (2004) compared a shape factor of 1 (perfect sphere) and 0.8 to experimental data and found that the lower shape factor produced results closer to those of the measured data. Vakamalla *et al.* (2017) also used a particle

sphericity of 0.8 to account for the effect of particle shape on the drag force and to simulate realistic behaviour of particles, however, this approach was not validated.

3.4.3.4 Phase Coupling and Interactions

When modelling a discrete phase, such as particles in the hydrocyclone, the degree of interaction between the phases can be divided into three categories. The first is to predict the discrete phase patterns based on a fixed continuous phase flow field, meaning the particle's effect on the fluid is ignored. This uncoupled approach, referred to as one-way coupling, is not suited to flows where the particle loading is significant enough to impact the carrying fluids flow pattern. It is therefore limited to use in dilute particle streams (< 5 % by volume) (Delgadillo and Rajamani, 2005).

Alternatively, a coupled approach can be used where the effect of the discrete phase on the continuum is included, termed two-way coupling. In this coupled approach, the continuous phase flow pattern is impacted by the discrete phase and *vice versa*. Calculations alternate between the continuous phase and discrete phase equations until a converged coupled solution is achieved. This is inherently more accurate but computationally expensive. Mousavian *et al.* (2009) investigated the effects of both one-way and two-way coupling on the simulation accuracy of a hydrocyclone modelled with a feed inlet volume fraction of 10 %. The goal was to determine, at this particle concentration, if the discrete phase had a measurable effect on the continuous phase. A comparison of the particle classification curves for the two coupling techniques, to the experimental results presented by Bhaskar *et al.* (2007b), showed that the two-way coupling technique provided better results than the one-way coupling. It was concluded that the increased concentration of particles in the apex region led to improper definition of the flow pattern in this area for the uncoupled case, which clearly affects the underflow flow rate and particle classification.

For high particle concentration flows, particle-particle interactions become significant and should also be included. This type of modelling is referred to as four-way coupling. This type of modelling is computationally very expensive, which has limited its application in hydrocyclone modelling (Swain and Mohanty, 2013). Chu *et al.* (2009) applied four-way coupling in the modelling of a dense medium cyclone using DEM. However, as this method, like any Lagrangian technique, requires the modelling of potentially billions of individual particles, a simplified parcel–particle technique was applied.

3.5 Boundary Conditions and Computational Requirements

3.5.1 Computational Time and Memory

The computational expense to conduct simulations on the multiphase, highly turbulent flow pattern within the hydrocyclone is extremely large. Simulation times from one week up to two months have been reported (Brennan *et al.*, 2007; Delgadillo and Rajamani, 2005), even when conducting runs on computer clusters such as the National Computational Infrastructure in Australia (Ghodrat *et al.*, 2014b; Ghodrat *et al.*, 2016; Ji *et al.*, 2017) or the University of Queensland Silicon Graphics Origin 3000 (Brennan, 2003). The largest influences on solution time are turbulence model choice; the addition of a secondary or tertiary phase; and the mesh size. Narasimha *et al.* (2006a) noticed a considerable increase in processing time of 50 % when comparing RSM and LES models, with Brennan (2006) also noticing a similar trend. Karimi *et al.* (2012) reported an increase from 34 h to 136 h when moving from a single-phase water simulation, to the addition of air as a secondary phase. With respect to mesh, Ghodrat *et al.* (2014b) stated that an increase in mesh size from 100,000 to 195,268 increased simulation time from 1 week to three weeks respectively.

3.5.2 Two-Dimensional Vs Three-Dimensional Analysis

It is well understood that the complex nature of the flow and the asymmetric feed inlet means that the modelling of hydrocyclones in three dimensions is required (Cullivan *et al.*, 2004; Mousavian *et al.*, 2009). The large computational time needed for three-dimensional models, however, ensures that their application to industrial processes is far from occurring. Nageswararao *et al.* (2004) estimated that computational models of hydrocyclones were not going to be practically useful until 2029. Schuetz *et al.* (2004) concluded that future work should entail the use of the older style two-dimensional simulations as this dramatically reduces the calculation time. Pressure drop and velocity profiles were obtained and shown to be in close agreement to the experimental results, providing evidence that crude two-dimensional models could be used in industrial applications in the near future.

3.5.3 Boundary Conditions

When solving the Navier-Stokes and continuity equations, appropriate initial conditions and boundary conditions need to be applied in order to form a well-posed mathematical model of the hydrocyclone (Versteeg and Malalasekera, 2007). Boundary conditions specify the flow variables at the boundaries of the physical model and, for the hydrocyclone, consist of the feed inlet; the

overflow and underflow outlets; and the wall of the hydrocyclone. The following sections outline the application of different boundary conditions for the hydrocyclone.

3.5.3.1   Feed inlet

The reported inlet boundary conditions for the feed have included velocity inlet, mass flow rate and pressure inlet conditions. Uniform velocity and mass flow inlets are by far the most common inlet conditions, with authors using measured flow rates as a metric for input values (typically converting mass flow rates to velocities *via* the surface area of the feed inlet). Pressure inlet boundary conditions for the feed are far less common, with only a few published cases (Banerjee *et al.*, 2016; Bhaskar *et al.*, 2007a). This is a more fundamental technique as industrial hydrocyclones are controlled *via* feed pressure, meaning predictions can be directly correlated to industrial processes.

For the k-ε and RSM turbulence models additional turbulence conditions are required for the boundary conditions For the feed inlet, turbulence intensity values of 5 % (Elsayed and Lacor, 2010; Karimi *et al.*, 2012) and 10 % (Cullivan *et al.*, 2003; Vakamalla and Narasimha, 2017) have been reported. As for the length scale, Cullivan *et al.* (2003) used a value of 0.01 m (with a 24.5 mm diameter feed inlet), while Suasnabar (2000) and Elsayed and Lacor (2010) stated that a length scale 0.07 times the inlet width should be used (Elsayed and Lacor (2010) used a 40 mm wide by 100 mm rectangular feed inlet). The volume fraction of air in the feed is set to 0 (Brennan *et al.*, 2007; Cui *et al.*, 2014; Mousavian *et al.*, 2009).

3.5.3.2   Pressure outlets

The selection of the overflow and underflow outlet boundary conditions is a straight-forward choice. All referenced hydrocyclone models utilise the pressure outlet condition, with the gauge pressure set to 0 (atmospheric pressure). Multiple authors have noted that a radial pressure gradient is established at the two outlets, due to the swirl generated in the hydrocyclone flow field (Bhaskar *et al.*, 2007a; Cullivan *et al.*, 2004; Dlamini *et al.*, 2005; Murthy and Bhaskar, 2012; Slack *et al.*, 2004; Swain and Mohanty, 2013). Dlamini *et al.* (2005) also noted that if a constant pressure is specified at the discharge orifices, the swirl is artificially suppressed and the internal hydrocyclone flow structure adversely influenced. This is accounted for by allowing for radial pressure distribution across the hydrocyclone discharge orifices (zero at centre, radially increasing to reflect local swirl prediction) (Cullivan *et al.*, 2004).

The air back flow volume fraction is typically set to 1.0 (equivalent to setting water to 0) (Brennan *et al.*, 2007; Leeuwner and Eksteen, 2008; Mousavian *et al.*, 2009; Narasimha *et al.*, 2010; Narasimha *et al.*, 2012a; Vakamalla *et al.*, 2014; Vakamalla and Narasimha, 2017; Vakamalla *et al.*, 2017). This enables the simulation to generate an air core by drawing air in through the overflow and underflow outlets when the swirl generates a region of negative pressure along the vertical axis. This can either be done for initialisation, or after the water phase has had time to equilibrate. Backflow direction is commonly specified as normal to the boundary zones (Bhaskar *et al.*, 2007a; Murthy and Bhaskar, 2012) and backflow turbulence intensity has been assigned a value of 5 % (Karimi *et al.*, 2012) and 10% (Bhaskar *et al.*, 2007a; Murthy and Bhaskar, 2012; Vakamalla and Narasimha, 2017) for the overflow, and 10 % for the underflow (Bhaskar *et al.*, 2007a; Karimi *et al.*, 2012; Murthy and Bhaskar, 2012; Vakamalla and Narasimha, 2017).

Some authors specified a flow split for the overflow and underflow boundaries, based upon measured data (Hwang *et al.*, 2013; Hwang and Chou, 2017; Marthinussen *et al.*, 2014). Cullivan *et al.* (2003) criticised this practice, stating that by defining the flow split the system becomes over constrained. The authors went on to state that while the pressure outlet boundary conditions for the underflow and overflow are not ideal, they represent a best estimate at the present time. Their main concerns included the rapid expansion of the flow exiting through the underflow, which indicates that a significant pressure drop may occur in this vicinity; and that the outlet conditions are the reflective type rather than the transmissive type. It was suggested that mesh refinement adjacent to the outlets should be conducted, to reduce the size of the numerical boundary layer.

3.5.3.3   Wall functions

The walls of the hydrocyclone are uniformly designated as the stationary wall boundary condition, with a no slip shear condition (Banerjee *et al.*, 2016; Cui *et al.*, 2014; Cullivan *et al.*, 2004; Dlamini *et al.*, 2005; Evans *et al.*, 2008; Gao *et al.*, 2011; Hwang *et al.*, 2013; Hwang and Chou, 2017; Karimi *et al.*, 2012; Kępa, 2013; Leeuwner and Eksteen, 2008; Lim *et al.*, 2010; Marthinussen *et al.*, 2014; Mokni *et al.*, 2015; Narasimha *et al.*, 2012a; Swain and Mohanty, 2013; Zhang *et al.*, 2017). For the k-ε and RSM turbulence models the wall roughness height and roughness constant are required. No mention of these terms in any of the referenced material suggests that these values remain at the default values. Standard wall functions are also used to approximate flow variables

in the near-wall region when using the *k-ε* and RSM models (Dlamini *et al.*, 2005; Ji *et al.*, 2017; Murthy and Bhaskar, 2012; Swain and Mohanty, 2013)

3.6 Numerical Method and Simulation Conditions

The accuracy of any simulation depends on the mesh quality, refinement and independence; the order of the numerical discretisation schemes; the chosen convergence criteria, and time step independence (de Souza *et al.*, 2012; Zhu *et al.*, 2012). This section will discuss the application of these parameters with regards to hydrocyclone modelling. Unless stated otherwise, all comments will be made based on a 3D simulation using the double precision, pressure-based solver.

3.6.1 Mesh Development and Independence studies

The partial differential equations that govern fluid flow are not usually amenable to analytical solutions, except for very simple cases. Therefore, in order to analyse fluid flows, flow domains are split into smaller subdomains or cells. The governing equations are then discretised and solved inside each of these grids (typically *via* the finite volume method). The accuracy of a CFD solution is governed by the number, type and arrangement of cells in the overall domain or grid (Ghodrat *et al.*, 2016). In general, both the accuracy of a solution and its cost in terms of computer hardware and convergence time are dependent upon the fineness of the grid. Optimal meshes are often non-uniform: finer in areas where large variations occur from point to point and coarser in regions with relatively little change. As there are no automated mesh production procedures, over 50% of the time spent in industry on a CFD project is devoted to the definition of the domain geometry and grid generation, further highlighting its importance (Versteeg and Malalasekera, 2007).

3.6.1.1 Types of Meshing

Meshes can be classified based upon the type of elements present or the connectivity of the mesh, being structured or unstructured. While structured meshes reduce computational memory, as they can be stored as arrays, they sometimes produce skewed or elongated cells. Therefore, unstructured meshes are the predominant choice for cyclone modelling. As for the various types of elements they include tetrahedrons, hexahedrons, pyramids or triangular prisms (wedges). Tetrahedral meshes, due to the nature of their shape, cannot be aligned with the direction of flow. This can lead to false diffusion in strongly convective flows, such as in a hydrocyclone (Patankar, 1980). Tetrahedral meshes have therefore been deemed unsuitable in the discretisation of the

hydrocyclone geometry (Bhaskar *et al.*, 2007b; Mousavian *et al.*, 2009; Murthy and Bhaskar, 2012; Slack *et al.*, 2004) and so have had limited use (Bhaskar *et al.*, 2007a; Noroozi and Hashemabadi, 2011; Swain and Mohanty, 2013). For some complex or acute inlet geometries (in particular the point where the inlet joins the cylindrical cyclone), however, tetrahedral meshes are sometimes necessary to improve the quality of the mesh in these regions (Gupta *et al.*, 2008; Leeuwner and Eksteen, 2008). In general the most common type of mesh for the hydrocyclone geometry is the unstructured hexahedral mesh (Delgadillo and Rajamani, 2005; Ghodrat *et al.*, 2013; Leeuwner and Eksteen, 2008; Slack *et al.*, 2004; Wang and Yu, 2006, 2008; Xu *et al.*, 2013; Zhang *et al.*, 2017) as this element type allows for the alignment of the cell with the primary flow direction. This typically entails the combination of structured hexahedral grid in the outer region of the cyclone, and a unstructured hexahedral grid for the inner air-core region (removing the occurrence of skewed or elongated cells at the centre) (Schuetz *et al.*, 2004).

3.6.1.2   Mesh Refinement

In order to achieve enhanced capture of the flow features inside a hydrocyclone and reduce numerical error, mesh refinement is necessary in certain critical regions (Murthy and Bhaskar, 2012). These areas include: near the cyclone walls; around the air-core; within and near the vortex finder; the feed inlet and surrounding area; and the apex region.

Boundary layer mesh has been implemented by numerous authors (Bhaskar *et al.*, 2007b; Cullivan *et al.*, 2003; Ghodrat *et al.*, 2013; Ghodrat *et al.*, 2014b; Ghodrat *et al.*, 2016; Ji *et al.*, 2017; Kuang *et al.*, 2012; Safa and Soltani Goharrizi, 2014; Schütz *et al.*, 2009; Wang and Yu, 2006; Wang *et al.*, 2007; Wang and Yu, 2008; Xu *et al.*, 2012; Zhang *et al.*, 2017) in an attempt to get a better definition of the velocity near the cyclone walls as the flow usually varies more significantly there (Ghodrat *et al.*, 2014b; Ghodrat *et al.*, 2016). Contrary to this, Slack *et al.* (2004) states that boundary layer resolution is not critical when modelling cyclones as the turbulence is generated in the main flow. However, they then go on to state that the boundary layer mesh helps resolve the velocity profile in the narrow annular gap that may form at the underflow due to the development of the air core. Accurate modelling of the underflow region is critical as it controls the air core formation, water flow split and particle classification. Multiple authors have implemented mesh refinement in this region, with Mousavian *et al.* (2009) and Bhaskar *et al.* (2007b) further limiting the aspect ratio to under 10. This aspect was also highlighted by Brennan (2006) who graded the

grid radially near the underflow so that a fairly coarse grid existed in the region expected to be occupied by the air-core but the grid was fine around the wall region. Other authors have stated that their grids were refined where there was high pressure, phase or velocity gradients. This refers to the region around the central air core (Hwang *et al.*, 2008; Hwang *et al.*, 2013; Mousavian *et al.*, 2009; Noroozi and Hashemabadi, 2011) or around the vortex finder (Bhaskar *et al.*, 2007b; Cullivan *et al.*, 2003; Ghodrat *et al.*, 2013; Ghodrat *et al.*, 2014b; Ghodrat *et al.*, 2016; Ji *et al.*, 2017; Kuang *et al.*, 2012; Safa and Soltani Goharrizi, 2014; Wang and Yu, 2006; Wang *et al.*, 2007; Wang and Yu, 2008; Xu *et al.*, 2012; Zhang *et al.*, 2017).

In some cases, the geometry of the cyclone is changed to simplify the simulation or increase numerical stability. An example of this is the feed inlet which is sometimes simplified to a rectangular shape of the same surface area, even if in reality it is a circular shape or has a constriction that narrows from a circular to rectangular shape (Kuang *et al.*, 2012; Vakamalla and Narasimha, 2017).

It is also known that with LES an overall finer mesh size is needed. Grid resolution must be high enough to compute the scales up to the inertial range of the energy spectrum (de Souza *et al.*, 2012). Brennan (2006) reported that for a hydrocyclone simulation using the LES turbulence model a mesh size an order of magnitude larger than the equivalent RSM turbulence model simulation was needed. This is seen as a significant draw back to the LES model.

3.6.1.3   Mesh Independence and Quality Analysis

The number of discrete elements used to approximate the continuous solution will affect the accuracy of the model. As the mesh size decreases, the numerical error decreases and the results will approach that of the analytical solution. However, this increased accuracy is paid for in computational expense. It is therefore necessary to optimise the grid size to obtain a solution that minimises computational power while producing a solution within an acceptable level of tolerance. This is done through a mesh independence study, where a particular quantity of the model's solution is compared at a range of mesh sizes. An example of this is shown in Figure 3.2, where the tangential velocity of water as a function radial position in the hydrocyclone was compared. It was determined that mesh sizes above 550 000 cells gave similar results and no appreciable increase in accuracy was achieved (Banerjee *et al.*, 2016). Other authors have conducted similar studies with comparisons of axial and tangential velocities being the most prevalent (Bhaskar *et*

al., 2007b; Brennan, 2006; Cui *et al.*, 2014; Vakamalla *et al.*, 2014). As for accepted levels of change between grid sizes, Evans *et al.* (2008) reported a maximum difference of 4.8 % between the selectivity curves determined by consecutive grids as the criteria for mesh convergence. Alternatively, Zhu *et al.* (2012) required a threshold of 0.5 % between grids for the time-averaged overflow mass flow rate.
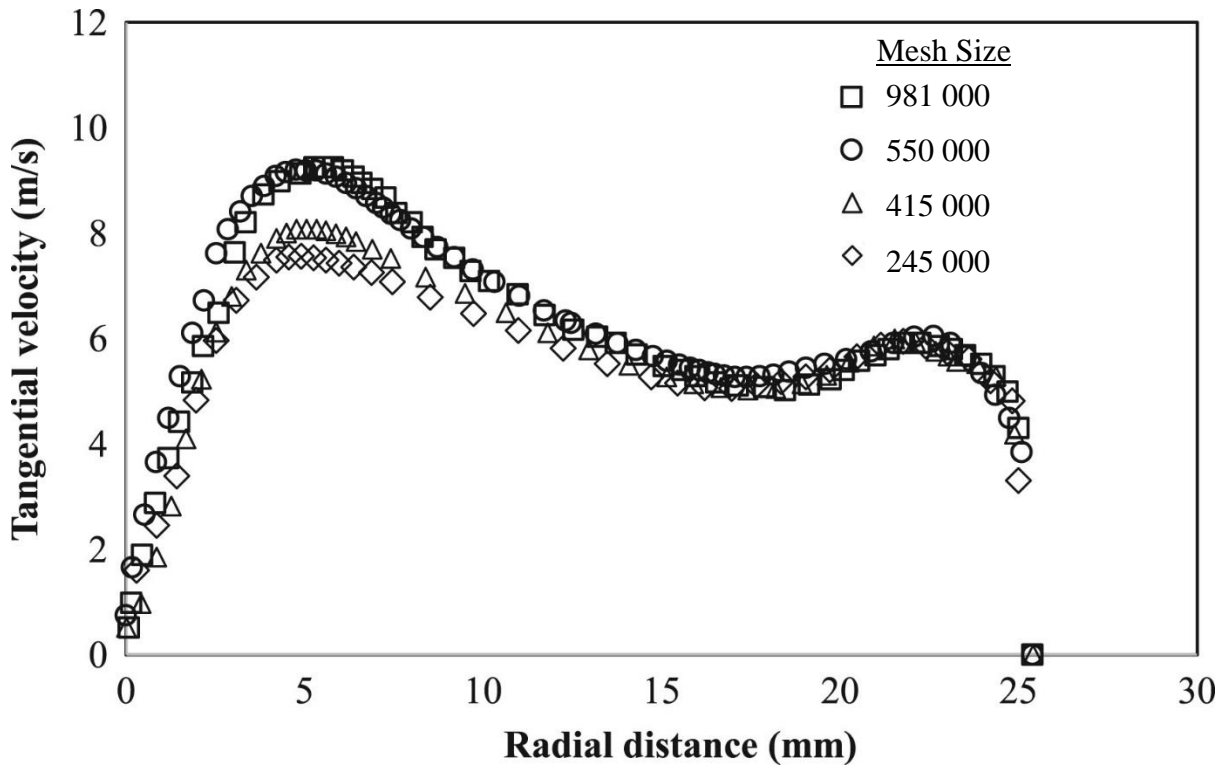
Figure 3.2: Effect of mesh resolution on the tangential velocity in a hydrocyclone at different radii. Reproduced with permission from Banerjee *et al.* (2016).

The inherent inaccuracies in CFD modelling, caused by the discretisation of a continuous domain, are not often quantified due to the absence of an accepted metric and the additional computational resources required. (Karimi *et al.*, 2012) studied these inaccuracies and concluded that the Grid Convergence Index (GCI) was a practical method to estimate the numerical uncertainty of a certain mesh size. The GCI compares the discrete solutions of at least three different mesh sizes and determines the influence of the grid on the final solution. An example of this is shown in Figure 3.3, where the greyed region represents how far the numerical solution is from the asymptotic value and indicates how much the solution would change with further grid refinement. Results for tangential velocities were able to show that for the central air core and wall regions the differences

between the simulated and experimentally measured data was not due to the mesh characteristics. This meant effects from other sources, such as the chosen multiphase model or wall boundary conditions, were a determining factor. Results for axial velocities, however, showed that in their case grid refinement around the walls and at the outer boundary of the air core region did improve results. This aligns with the information detailed in Section 3.6.1.2, which outlines the importance of mesh refinement near the wall and air core region. While this approach is an ideal way to study the effects of mesh size, it is very computationally expensive and so is rarely done.
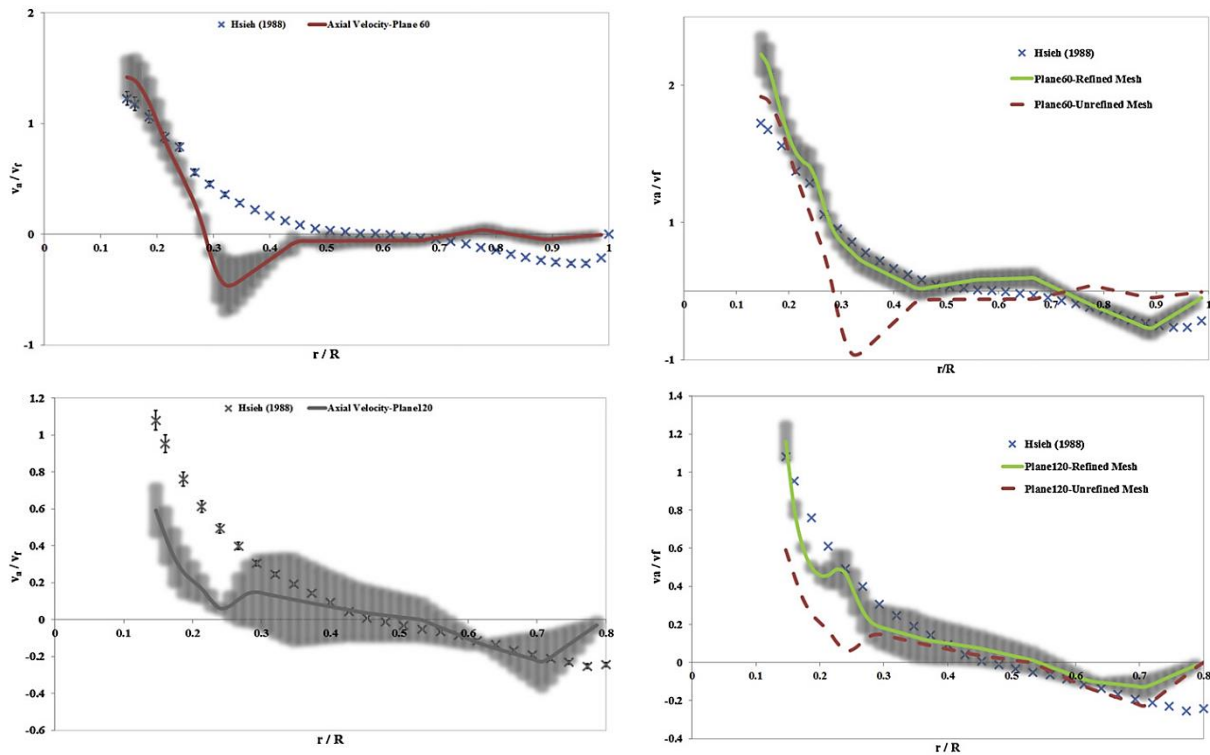
Figure 3.3: Comparison of the predicted axial velocity to experimental data. Greyed region represents the GCI error bars, which represent the amount of variance caused by the mesh density. Reproduced with permission from (Karimi *et al.*, 2012).

The quality of the mesh is not only dictated by its size, as the smoothness, aspect ratio, and skewness will also have an effect and should be monitored (Hwang *et al.*, 2013). Smoothness is determined by the ratio of size between adjacent cells, with values close to unity being ideal. The aspect ratio is defined as the ratio of the longest to shortest side in a cell, and, to ensure best results, should be close to 1. For hydrocyclone modelling, Leeuwner and Eksteen (2008) stated that an unstructured hexahedral mesh is more tolerant of high aspect ratios. However, this only applies if

the flow is aligned in the direction of the stretching, and there is no strong flow variation. Several authors have expressed that the maximum aspect ratio in the spigot region should be restricted to under 10 (Bhaskar *et al.*, 2007b; Mousavian *et al.*, 2009; Murthy and Bhaskar, 2012).

Mesh skewness has a significant impact upon numerical stability and accuracy (Cullivan *et al.*, 2003). It determines how close to ideal (*i.e.* equilateral or equiangular) a face or cell is. Typically, skewness is presented as a distribution of values, calculated from each cell, ranging from 0 to 1, with values closer to 0 being preferred. Karimi *et al.* (2012) presented values of mesh skewness (shown in Table 3.3) by determining the percentage of cells with a skewness less than 0.2. This is the only reported data of skewness in hydrocyclone meshes. Future reports should include the number of cells with a skewness above 0.85, as it is the highly skewed cells that cause numerical inaccuracies.

While the importance of the chosen mesh on the CFD solution is well understood, in hydrocyclone modelling very few authors detail mesh quality characteristics or independence studies. Some authors have even explicitly stated the lack of a mesh independence study, due to the lack of computational resources (Cullivan *et al.*, 2003; Cullivan *et al.*, 2004; Swain and Mohanty, 2013).

Table 3.3: Mesh properties reported by Karimi *et al.* (2012), with accompanying computational expense for an Intel Corei7 CPU 1.6 GHz workstation using ANSYS FLUENT 12.1 (note computational time was for single phase water tests, multiphase (air-water) simulations increased computational time by a factor of 4).

Mesh Type	Size Interval (mm)	Number of Cells	Cells with skewness under 0.2 (%)	Computational Time (hours)
Hexagonal	6.0	3460	74.65	1.48
Hexagonal	3.0	13,578	89.19	2.67
Hexagonal	1.5	983,642	94.32	157.23

3.6.2 Solution Methods

3.6.2.1 Pressure-Velocity Coupling

Velocity fields are calculated through the simultaneous solving of the momentum and continuity equations. For incompressible flows, the coupling or linking between pressure and velocity introduces a constraint in the solution of this flow field. This can be done in one of two ways. The

first, is the predictor-corrector (or guess-check-improve guess) approach, which means that once the correct pressure field (calculated iteratively in a sequential manner) is applied in the momentum equations, the resulting velocity field should satisfy continuity. The most popular choice of algorithm for pressure-velocity coupling in hydrocyclone modelling, SIMPLE (Semi-Implicit Pressure Linked Equations), is an example of this iterative method. The SIMPLE algorithm is relatively straightforward and has been successfully implemented in numerous CFD procedures, hence its popularity. In some cases, extensions of the SIMPLE algorithm such as SIMPLEC (SIMPLE-Consistent) (Cullivan *et al.*, 2004; Dlamini *et al.*, 2005; Evans *et al.*, 2008) or PISO (Pressure-Implicit with Splitting of Operators) (Zhu *et al.*, 2012) have also been used in cyclone modelling. These extensions offer increased convergence rates for relatively uncomplicated problems (laminar flows with no additional models enabled) in which convergence is limited by the pressure-velocity coupling (SIMPLEC) or for transient flow calculations, especially when one wants to use a large time step (PISO). For problems that require small time steps, such as when using the LES turbulence model, using PISO may result in an increased computational expense and therefore should not be used. This could explain the limited use of these extensions in hydrocyclone modelling. While the above segregated or decoupled methods can be used for VOF and mixture multiphase models if the Eulerian multiphase model is chosen, a coupled scheme must be used. The Phase Coupled SIMPLE algorithm is the standard choice and has been applied to hydrocyclone modelling (Swain and Mohanty, 2013). The coupled algorithm solves the momentum and pressure-based continuity equations together, which provides a robust and more accurate result when compared to the segregated algorithms but is therefore more computationally expensive with slower convergence rates.

3.6.2.2   Spatial Discretisation

Firstly, gradient selection is required as they help calculate values of the scalar at the cell faces from the stored values at the cell centres. The selection of gradients for hydrocyclone modelling to this author's knowledge has not been mentioned in any of the referenced material. Based on theory, however, the recommended method is the Least Squares Cell-Based gradient evaluation as it combines both increased accuracy over the Green-Gauss Cell-Based gradient evaluation and decreased computational expense when compared to the Green-Gauss Node-Based method. Future papers could include this detail to confirm its application for hydrocyclone modelling. As for the choice of the pressure interpolation scheme, it is relatively straight forward. The PRESTO

(PREssure STaggering Option) scheme is recommended for high swirl numbers, high-Rayleigh-number natural convection, high-speed rotating flows, and flows in strongly curved domains. This has led to its unanimous use in hydrocyclone modelling (Mousavian *et al.*, 2009; Murthy and Bhaskar, 2012; Zhu *et al.*, 2012).

The selection of a discretisation scheme for the convection terms of each governing equation is also required. This can include terms such as volume fraction, momentum or turbulent kinetic energy. The accuracy of various schemes can be thought of in terms of Taylor series truncation errors (TSTE): first order schemes are very stable and obey the transportiveness requirement but have lower accuracy which makes them prone to numerical diffusion errors. Higher-order schemes involve more neighbour points and reduce the discretisation errors by bringing in a wider influence. For simulating complex rotating or swirling flows, such as those found in hydrocyclones, higher order discretisation schemes are recommended in order to reduce the effects of false or numerical diffusion. (Bhaskar *et al.*, 2007a; Mousavian *et al.*, 2009; Murthy and Bhaskar, 2012; Noroozi and Hashemabadi, 2011; Slack *et al.*, 2004) This includes discretisation schemes such as QUICK (quadratic upstream interpolation for convective kinetics) or the third-order MUSCL scheme (Monotonic Upstream-centred Scheme for Conservation Laws). The QUICK scheme is typically more accurate on structured meshes aligned with the flow direction but is only applicable to quadrilateral or hexahedral meshes, defaulting to second-order upwind discretisation scheme in other cells. The MUSCL scheme does not have this limitation. While these higher order discretisation schemes are widely used (QUICK being the most prevalent), some authors have published models using lower discretisation models such as the second order upwind scheme (Brennan, 2003; Karimi *et al.*, 2012; Schuetz *et al.*, 2004; Wang *et al.*, 2007; Xu *et al.*, 2012), the power law scheme (Gupta *et al.*, 2008) or the first order upwind scheme (Swain and Mohanty, 2013). Lower order schemes help reduce computational time by increasing the convergence rate, which is sometimes necessary in complex simulations, while for large mesh sizes or steady state solvers lower order discretisation schemes are sometimes necessary to obtain a converged solution. The results obtained using the first order upwind or power law scheme, however, where not validated experimentally and so this practice is questionable. Lim *et al.* (2010) stated that the application of the second-order upwind scheme produced numerical results that were in poor agreement with their experimental measurements. This led to the use of the higher order QUICK scheme which then led to more accurate results.

In some specific cases the aforementioned schemes are unavailable for selection or are not the optimal choices. When using the VOF multiphase model, the selection of the discretisation schemes available for volume fraction depend on the type of interface modelling. For hydrocyclones, the modified HRIC (High Resolution Interface Capturing) and QUICK schemes have been shown to predict essentially the same water velocities, but the HRIC option allows for a sharper resolution of the air/water free surface and so should be selected (Brennan, 2006). Another case is when choosing the discretisation scheme for momentum when using the LES turbulence model. The bounded central differencing scheme is the default and has been used by numerous authors (Brennan *et al.*, 2007; Narasimha *et al.*, 2012a; Vakamalla *et al.*, 2014; Vakamalla and Narasimha, 2017). Brennan *et al.* (2007) found that at coarser grid sizes the third-order MUSCL scheme gave better predictions of the velocities than the bounded central differencing scheme on a coarse grid, but on a finer grid (recommend for LES simulations) both discretisation schemes gave similar velocity predictions

3.6.2.3   Temporal Discretisation

For transient simulations, the governing equations must be discretised in both space and time. Slack *et al.* (2000) used a second-order implicit transient formulation. This scheme uses information from the two adjacent time steps to calculate the time derivative. A first order implicit formulation has also been reported to be used (Swain and Mohanty, 2013); however this practice is questionable.

3.6.3   Steady State vs Transient Solutions (Time Steps)

Hydrocyclones have been shown, both experimentally and by CFD analysis to have a number of unstable flow features particularly in the low-pressure central core (Slack *et al.*, 2004). In steady state simulations a transient pattern will occur in the velocity and pressure fields that can be detected by a cycling in the residuals (Dlamini *et al.*, 2005; Schuetz *et al.*, 2004; Slack *et al.*, 2004). This means that while a steady state solution can be used to initialise a system (discussed further in Section 3.6.5), a transient solution is required for improved definition of the air core as well as the velocity and pressure fields (Dlamini *et al.*, 2005; Slack *et al.*, 2004). For transient solutions, relevant time steps must be chosen so that the simulation accuracy and computational expense are at an acceptable level. A general rule for CFD modelling is to ensure that the time step of the simulation is defined such that Courant number (C) is less than 1 according to Courant–Friedrichs–

Lewy (CFL) stability condition (Anderson, 1995). Higher numbers signify that the flow speed is too fast to be calculated at that time step size or at that grid size This method has only been reported to be used by Vakamalla *et al.* (2014) who varied time steps between 1.0×10^{-5} and 5.0×10^{-5} s to ensure this condition was met. Alternatively, time step dependence studies can be completed which determine how results change with various time steps (Kuang *et al.*, 2012; Wang and Yu, 2006; Wang *et al.*, 2007; Xu *et al.*, 2012; Xu *et al.*, 2013; Zhu *et al.*, 2012). This is by far the most reliable technique but can be time consuming. Typical values for the time step range from 5.0×10^{-4} down to 1.0×10^{-5} s, with lower values typically reported when using the LES turbulence model.

3.6.4   Judging Convergence – Residuals and Quantity Balancing

The residual is one of the most fundamental measures of an iterative solution's convergence as it directly quantifies the error in the solution of the system of equations. The residual measures the local imbalance of a conserved variable in each control volume. Therefore, every cell in the model will have its own residual value for each of the equations being solved. While there are no universal metrics for judging convergence, for hydrocyclone models, RMS residual levels of 10^{-3} appear to be considered to be the minimum level of acceptable convergence (Dlamini *et al.*, 2005; Gupta *et al.*, 2008; Noroozi and Hashemabadi, 2011). While this is considered sufficient, residual levels of 10^{-5} and 10^{-6} are considered to be more tightly converged and so are much more common (Bhaskar *et al.*, 2007a; Evans *et al.*, 2008; Hwang *et al.*, 2013; Hwang and Chou, 2017; Karimi *et al.*, 2012; Leeuwner and Eksteen, 2008; Lim *et al.*, 2010; Mousavian *et al.*, 2009; Sripriya *et al.*, 2007; Vakamalla and Narasimha, 2017; Xu *et al.*, 2016; Zhu *et al.*, 2012).

While the monitoring of residuals allows for a transient solution to progress from one time step to the next, it is still necessary to determine when a final steady state solution has been achieved. This type of steady state convergence is determined by monitoring relevant integrated quantities such as: pressure drop; net mass flow rate between feed, overflow and underflow; or tangential and axial velocities (Brennan *et al.*, 2007; Ghodrat *et al.*, 2014a; Vakamalla and Narasimha, 2017; Zhu *et al.*, 2012). Figure 3.4, reproduced from Vakamalla and Narasimha (2017), is an example of this type of monitoring and shows that even though oscillations do occur the solution has reached a steady value. Ensuring that these values have reached a steady solution means that results are based upon a single repeatable value. Resultant values should then be averaged over a set number of

iterations after convergence is reached. This is suggested to be 1000 iterations (Delgadillo and Rajamani, 2007) or two seconds of simulated time (Vakamalla and Narasimha, 2017).
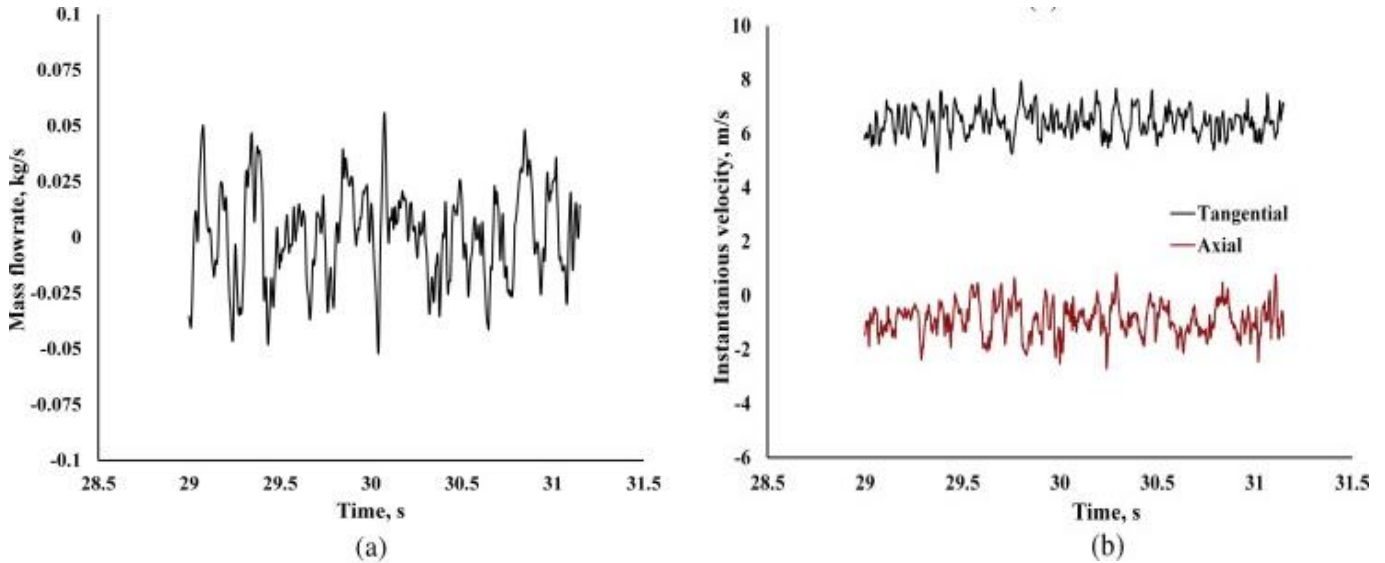
Figure 3.4: Variation of (a) net mass flow rate and (b) mean tangential and axial velocities with simulation time in the 75 mm hydrocyclone. Reproduced with permission from Vakamalla and Narasimha (2017).

3.6.5   Solution Initialisation and Controls

Before starting any CFD simulation an initial estimate for the solution flow field is needed. The uniqueness of a result depends on the choice of boundary conditions, physical data and numerical settings. Therefore, initialisation should not affect the final results, meaning that regardless of how the case is initialised, the same results should be obtained once steady state convergence has been reached. Initialisation will, however, affect the time taken to reach convergence. There have been a wide range of initialisation techniques used for hydrocyclones. If studying the steady state operation of the cyclone (pressure drop, classification behaviour, velocity profiles), initialisation of the computational domain has been conducted using a hydrocyclone full of water at rest and atmospheric pressure (Cullivan *et al.*, 2003; Davailles *et al.*, 2012a; Mousavian *et al.*, 2009; Murthy and Bhaskar, 2012; Swain and Mohanty, 2013); or with the properties of the feed inlet (Karimi *et al.*, 2012; Vakamalla and Narasimha, 2017). To complement the no-flow initial condition the turbulence kinetic energy and dissipation rate are recommended to initialized, when applicable, as 0.001 $m^2 \cdot s^{-2}$ and 0.1 $m^2 \cdot s^{-3}$ respectively (Cullivan et al., 2003). Cullivan *et al.* (2003), after using high speed video, also came to the conclusion that the initial water-filled condition was appropriate for the numerical prediction of air-core inception and development, since the air was

79

first flushed from the hydrocyclone before air-core development occurs. Alternatively, Cui *et al.* (2014) stated that the domain must be initially filled with air to simulate the start-up conditions of an actual operation, if studying the formation of the air core.

As discussed previously, hydrocyclone modelling is severely limited by the computational expense of the simulations. Brennan (2006) detailed a simulation strategy to help reduce the time needed for a simulation to reach completion. It began by first simulating a water only case, with the backflow air volume fraction set to zero for the overflow and underflow boundary conditions, using a steady solver and the standard k-ε turbulence model. These simplifications, ran for approximately 200 iterations, allowed for a better initial approximation of the pressure and velocity flow fields within the hydrocyclone without the increased computational expense of added phases or complex turbulence models. The turbulence model was changed to a more accurate but computationally expensive model, such as the LES or RSM model, and continued using the steady solver for a further 25 iterations. This solution can be used for the initialisation of simulations with various model parameters. The simulation was then changed to the unsteady solver and continued until a central axial core of negative pressure was formed. The back-flow air volume fraction on both the overflow and underflow boundary conditions was then set to 1 and the simulation was run using the unsteady solver until convergence. While this methodology does not represent the real transient conditions in a hydrocyclone, as the back-flow air volume fraction is 1 from start-up, the final converged solution was shown to be independent of this initialisation procedure. This method has been employed by other authors (Dlamini *et al.*, 2005; Leeuwner and Eksteen, 2008; Mousavian *et al.*, 2009) and extended further by Brennan *et al.* (2007). They used a coarse grid (56,000 cells) for the initialisation procedure and a finer grid (450,000 cells) to obtain a more accurate final solution. Other simplifications include incrementally increasing the hydrocyclone inlet speed up to the required speed, or assuming a laminar flow to determine an initial guess of the pressure and velocity fields (Schuetz *et al.*, 2004).

Under-relaxation factors help stabilise numerical simulations by limiting the change in the solution per iteration. This dampening, however, can give false confidence when observing residuals, further highlighting the need for the monitoring of key parameters. Ideally, under-relaxation factors should not be lowered from the default values provided by the software package (such as ANSYS), however if a simulation is diverging, variations in the under-

relaxation values may be necessary. Swain and Mohanty (2013) relied on varying the under-relaxation values for the velocity and the volume fraction between 0.05 and 0.2 and for pressure between 0.05 and 0.6, to get a converged solution. This was most likely necessary as they used first-order discretisation with a tetrahedral mesh which would lead to numerical diffusion. Dlamini *et al.* (2005) also required the use of relaxation factors as they relied on the steady state solver to initialise their flow field, following the procedure of Brennan (2006). It was concluded that under-relaxation factors of 0.35 and 0.5 for the momentum and turbulent viscosity equations respectively was required to stop divergence. Dlamini *et al.* (2005) and Cullivan *et al.* (2003) also concluded that for improved stability when initialising simulations using the RSM turbulence model, the linear pressure-strain (LSP) model should be used for the first few iterations. If possible, the quadratic pressure-strain (QSP) can then be used once a crude flow structure is established for which the turbulence and pressure and velocity fields are more in balance.

3.7   Validation of Hydrocyclone Models

The validation of computational models is crucial to the confidence and wide spread acceptance of their predictions. Validation can be divided into two main disciplines: local (microscopic) or global (macroscopic) behaviour. Global validation describes comparing behaviour of the entire flow domain, whereas local validation involves the comparison of characteristics at individual locations. Global validation parameters for the hydrocyclone include measurements such as flow split to the underflow, pressure drop, or particle separation efficiencies. This type of experimental data is typically simple to obtain and allows for the validation at a range of process conditions. However, global data cannot fully explain the intricate flow interactions with different geometrical features, which effect flow phenomena such as short circuiting, the by-pass or supposed fish-hook effect. It is clear that the fundamental behaviour, such as water and particle velocity fields, air core diameter, or solids concentration fields, are needed to ensure that the model is correctly capturing the behaviour inside the hydrocyclone. This type of validation requires point by point comparison. This data is much more difficult and time consuming to obtain, particularly particle flow in dense medium flows, and requires specialised equipment. The most common data set used by all modellers is that obtained by Hsieh (1988), in a 75 mm hydrocyclone, with numerous authors citing this work to avoid the complex measurements required for local validation (Brennan, 2006;

Brennan *et al.*, 2007; Davailles *et al.*, 2012a; Delgadillo and Rajamani, 2005; Ghodrat *et al.*, 2016; Ji *et al.*, 2017; Karimi *et al.*, 2012; Kuang *et al.*, 2012; Narasimha *et al.*, 2006a; Vakamalla and Narasimha, 2017; Wang and Yu, 2006; Wang *et al.*, 2007). Below outlines some of the most common validation techniques for the hydrocyclone, broken up into validation of the three phases: water, air and particles.

3.7.1 Water flow validation

3.7.1.1   Global Validation

The flow rate of water through the hydrocyclone (when velocity or pressure inlet boundary conditions are applied), the pressure drop and the volume split ratio (when not already specified) can be used to validate water flow. The water volume split ratio is typically defined as the percentage of feed water that exits *via* the underflow. Prediction of the water split *via* CFD is often reported to be very close to the measured values (within 10 %) (Banerjee *et al.*, 2016; Bhaskar *et al.*, 2007b; Davailles *et al.*, 2012a; Ghodrat *et al.*, 2016; Kuang *et al.*, 2012; Narasimha *et al.*, 2006a; Olson and Van Ommen, 2004; Vakamalla and Narasimha, 2017; Wang *et al.*, 2007). Wang and Yu (2006) compared water flow splits for different cyclone diameters, cylindrical lengths and conical lengths to the empirical models of Plitt (Flintoff *et al.*, 1987; Plitt, 1976). This was then extended to hydrocyclones with different vortex finder diameters and lengths (Wang and Yu, 2006). The CFD predictions correlated well with the results from the Plitt model; however, when compared to the experimental data of Hsieh (1988) the CFD predictions were marginally closer. This suggests that CFD is a good tool for predicting water splits in hydrocyclones. Murthy and Bhaskar (2012) and Bhaskar *et al.* (2007a) noted, however, that for water splits above 50 % (meaning more water to the underflow), predictions are not as accurate as those below 50 %.

Murthy and Bhaskar (2012) also compared experimentally measured water throughput rates to the predicted values for a range of feed velocities. As the feed inlet velocities were set from the experimental data it was a very close match, as expected. Alternatively, Bhaskar *et al.* (2007a), who used a pressure inlet boundary condition, found that the water throughput was sensitive to the chosen turbulence model, with error values of around 20 % for the $k–\varepsilon$ model, 15 % for the RNG $k–\varepsilon$ model and 8% for the RSM. This suggest that while setting the inlet pressure is a more desirable approach, it does produce another level of complexity.

Pressure drop represents the difference in pressure between the feed and outlet streams. For a hydrocyclone with its apex open to atmosphere, this is equivalent to the feed pressure. Again pressure drop has been reported to be closely predicted by CFD models (to within 10 %) (Ghodrat *et al.*, 2016; Kuang *et al.*, 2012; Olson and Van Ommen, 2004; Wang *et al.*, 2007). As with flow split Wang and Yu (2006, 2008) compared pressure drop to the Plitt model, and found that the predictions are quantitatively comparable.

3.7.1.2   Local Validation

There are three velocity components within the hydrocyclone: the tangential, radial and axial velocities. Velocity measurement techniques such as Laser Doppler Velocimetry (LDV) and Particle Image Velocimetry (PIV) provide useful tools for the measurement of water flow in hydrocyclones. Wang *et al.* (2016) summarised the application of LDV and PIV in hydrocyclones. The authors stated that due to the difficulty in measuring the radial components of the flow, it is often omitted. Hsieh (1988) cited fluctuations of the air-core as the primary reason for the inability to measure the radial velocity. Therefore the comparison of just the measured tangential and axial velocities to those predicted *via* computational models is common (Brennan, 2006; Cui *et al.*, 2014; Davailles *et al.*, 2012a; Delgadillo and Rajamani, 2005; Delgadillo *et al.*, 2013; Ghadirian *et al.*, 2013; Ghodrat *et al.*, 2016; Karimi *et al.*, 2012; Kuang *et al.*, 2012; Lim *et al.*, 2010; Mousavian *et al.*, 2009; Narasimha *et al.*, 2006a; Slack *et al.*, 2004; Vakamalla and Narasimha, 2017; Wang and Yu, 2006; Wang *et al.*, 2007; Xu *et al.*, 2012; Zhang *et al.*, 2017). The data of Hsieh (1988), obtained *via* LDV, is by far the most frequent data set used by modellers for validation. Ghodrat *et al.* (2016) compared their modelling results, as well as water velocity predictions from multiple other authors, to the work of Hsieh (1988). It was evident that the axial velocities, over the whole radius of the hydrocyclone, can be accurately predicted using either the RSM or LES turbulence model. However, for the tangential velocities, the models varied in accuracy. Around the interface between the liquid and air core, the peak tangential velocities are often underestimated, with LES models showing the highest accuracy. Near the wall region the velocities also exhibited some inaccuracies, under predicting the velocities, when compared to the measured results. Over a majority of the hydrocyclone radius, however, the tangential velocities are well predicted.

While authors typically just compare velocities over a single one dimensional line (at a given height and plane), some compare velocity vector fields over an entire two dimensional plane. Cui *et al.* (2014) and Lim *et al.* (2010) compared simulated velocity vector fields to PIV measurements and showed that the flow direction of the captured vortexes are very similar. Non-ideal short circuiting flow near the inlet; large vortices at the interface between the cylindrical and conical sections; and highly asymmetric flow patterns in the bottom of the cyclone were all present in both the simulated and measured flow fields (Lim *et al.*, 2010). It is clearly evident that the fundamental flow behaviour of water, while complex, can be modelled accurately through the use of sophisticated techniques such as the LES or RSM turbulence models.

3.7.2   Air-Core Validation

The validation of the air core diameter is crucial to determine the overall flow structure generated inside the hydrocyclone (Mousavian *et al.*, 2009). The air-core is an important process parameter used to assess the stability of cyclone performance and is sensitive to almost all operating conditions and design parameters (Vakamalla *et al.*, 2014). The proper resolution of the air core has been shown to help produce more accurate velocity profiles (Karimi *et al.*, 2012; Mousavian *et al.*, 2009), and water flow splits (Vakamalla and Narasimha, 2017). Vakamalla *et al.* (2014) obtained experimental data of the air-core diameter at different hydrocyclone inclinations using Electrical Resistance Tomography (ERT) and High-Speed Video (HSV) for the purpose of CFD validation. Using an average air core diameter, the authors found that the CFD results closely matched those from the HSV for all tested inclinations. The ERT measurements were shown to over-estimate the air core size, which was attributed to its numerical diffusivity and limitation of inherent reconstruction algorithms. Lim *et al.* (2010) used images obtained from PIV experiments to compare the air core at various heights. It was found that despite the highly unsteady and fluctuating structure of the air core, which is well recognised to be difficult to model, there was a close quantitative agreement (average error of 7.7 %). Other authors have also used air core diameters as a metric to assess the performance of turbulence models (Delgadillo and Rajamani, 2005; Narasimha *et al.*, 2006a; Vakamalla and Narasimha, 2017), or empirically based prediction models (Narasimha *et al.*, 2012b).

A few authors have modelled the flow domain of the hydrocyclone transiently, to investigate the dynamics of the hydrocyclone start-up and the mechanisms of air-core inception and development.

Cui *et al.* (2014) compared the results from high speed video and a transient simulation of the air core formation. Qualitative results showed that their CFD simulation was able to mimic the formation of the air core from an air filled hydrocyclone to fully developed air core (after 1.7 s of real time flow). Wang *et al.* (2007) noticed a similar behaviour, with the hydrocyclone filling from the underflow upward. The simulations showed that eventually all air is expelled through the overflow and, after approximately 2 s, the air core becomes relatively stable. Other authors have also been successful in the simulation of air core formation (Leeuwner and Eksteen, 2008; Lim *et al.*, 2010; Xu *et al.*, 2012; Xu *et al.*, 2013).

3.7.3   Particle flow validation

Nowakowski *et al.* (2004) summarised particle validation techniques for hydrocyclones, stating that for meaningful validation, the measurements of both detailed internal flow fields (for confidence in the fundamental prediction) and overall separation efficiencies are needed. Davailles *et al.* (2012b) also expressed the need for both levels of validation, as processes at both the macroscopic and microscopic scales have some influence on the hydrocyclone's behaviour.

3.7.3.1   Global Validation

The ultimate goal of any hydrocyclone model is it correctly predict the separation efficiency for a given set of conditions. This is typically represented by a partition curve which displays the fraction of feed particles, of a particular size, reporting to the underflow. Partition, or separation efficiency, curves are extensively used for the validation of particle flow. Hwang *et al.* (2013) compared separation efficiencies for different inlet velocities, and while the predicted efficiencies for particle sizes close to the cut size were accurate, other values were predicted poorly. Similar behaviour was also seen by Vakamalla *et al.* (2014) and Bhaskar *et al.* (2007b). Others have shown simulated results to closely match the measured values over the whole range of the partition curve (Bhaskar *et al.*, 2007a; Brennan *et al.*, 2007; Delgadillo and Rajamani, 2005; Hwang and Chou, 2017; Narasimha *et al.*, 2005; Olson and Van Ommen, 2004; Wang *et al.*, 2007; Xu *et al.*, 2012). Partition curves have been used as a validation tool over a wide range of solids concentrations, ranging from low (~ 1 % by weight); medium (~ 10 %) (Bhaskar *et al.*, 2007a; Brennan, 2003; Davailles *et al.*, 2012a; Kuang *et al.*, 2012; Slack *et al.*, 2004; Vakamalla *et al.*, 2014; Zhang *et al.*, 2017); and high (up to 50 %) concentrations (Davailles *et al.*, 2012b; Ghodrat *et al.*, 2016;

Narasimha *et al.*, 2012a; Vakamalla and Narasimha, 2017). For high solids concentrations, the partition curve represents a simple, and sometimes only, form of experimental validation.

While the behaviour over the whole tested size range is of importance, the partition curve is sometimes simplified to the presentation of just the cut size. Wang and Yu (2006, 2008) compared the cut sizes calculated from CFD models for hydrocyclones with different vortex finder diameters and lengths; cyclone diameters; and cylindrical and conical lengths, to those predicted by the Plitt model. While the results showed that CFD could closely mimic the various trends seen in the results from the empirical model, the overall magnitudes were vastly different (errors of around 50 %). As both results were not compared to actually measured data, it is difficult to truly understand the extent of the errors. Murthy and Bhaskar (2012) compared the predicted cut size *via* CFD to actual measured results for a range of different design and operating parameters and found that the greatest error was approximately 20 % (representing a difference of only 3.5 µm). Similar accuracy was also noted by Bhaskar *et al.* (2007a).

3.7.3.2   Local Validation

Several authors have expressed the need for local validation of particle flow through the direct comparison with measured velocity or concentration fields (Cullivan *et al.*, 2004; Davailles *et al.*, 2012b; Nowakowski *et al.*, 2004; Vakamalla and Narasimha, 2017). However, this type of comparison is rare as the measurement of slurry velocity profiles or solids spatial distribution anywhere inside the hydrocyclone is an experimentally challenging task (Davailles *et al.*, 2012b) and can be expensive (Vakamalla and Narasimha, 2017).

The LDV and PIV techniques, as for fluid flow, can be used to determine the flow of particles inside the hydrocyclone. However these techniques have been shown to only be effective in flows with less than 1 % solids by weight (Chu *et al.*, 2002; Fisher and Flack, 2002; Zhang *et al.*, 2011), which is not consistent with industrial conditions. The measurement of velocity profiles in high solid concentration flows prohibits the application of laser or visual tracking methods due to light extinction. Therefore the development of tomographic techniques such as nuclear magnetic resonance, ultrasound, Electrical Impendence Tomography (EIT), or Positron Emission Particle tracking (PEPT) is required to ensure predictions of the complex high solids flow are properly validated. Nowakowski *et al.* (2004) described the principle behind EIT, suggesting that the technique provides potential for the measurements of particle concentration fields. A drawback to

this technique, however, is the requirement of the detailed knowledge of the inter-relation between particle concentration fields and size distributions to the bulk conductivity.

In one of the few applications of local validation, Vakamalla and Narasimha (2017) compared CFD results for mean density contours to experimental results obtained *via* Gamma Ray Tomography (GRT). The results showed very similar behaviour for the 40 % (by weight) slurry. This was, however, for a 350 mm dense medium cyclone. While this provides some added insight to the inner flow behaviour of the modelled cyclone, it still does not allow for the validation of the particle velocities, which are integral to classification behaviour. Positron Emission Particle Tracking (PEPT), described in detail by Parker *et al.* (1993) and more recently by Leadbeater *et al.* (2012), is a technique that can provide three dimensional trajectories of particles in high solid concentration, opaque flows. While early studies were limited in nature (Chang *et al.*, 2011; Radman *et al.*, 2014), Chapters 4 and 5 will show that detailed trajectories and representative velocity profiles can be obtained for real mineral particles down to approximately 100 µm in diameter. While the current database is very limited, this technique provides researchers a valuable tool for obtaining particle velocities and residence times in high solid concentration flows. This information is easily obtainable from CFD models, with multiple authors having already presented particle trajectories (Evans *et al.*, 2008; Hwang *et al.*, 2013; Hwang and Chou, 2017; Slack *et al.*, 2004; Vakamalla *et al.*, 2017) or velocity field plots (Ji *et al.*, 2017).

3.8 Conclusions and Future Direction

It is clear that in many cases the most appropriate model for simulating the flow within the hydrocyclone is known. However, these are often complex formulations and the associated large computational expense requires the implementation of simplifications to allow the simulation to be undertaken in a reasonable time frame. In some cases, these simplifications are sufficient, such as the Mixture and VOF models (compared to the Eulerian model) for simulating the air core. Removing the air core, while not as accurate, can also be used to provide engineering estimations with less computational expense. In comparison, the turbulence within the hydrocyclone has been conclusively shown to require the added accuracy that comes with the RSM and LES models and should not be modelled with the simpler k-ε turbulence models. While the RSM is not as accurate as the LES model, it is much less computational expensive and so is often used in complex multiphase simulations. With the development and growing accessibility of high power computing

clusters these limitations will continue to diminish, and simulations will be allowed to use more fundamental principles.

High order discretisation schemes and hexahedral meshes are required to reduce the numerical diffusion. Mesh quality is also critical for the proper resolution of the flow domain, with suggested areas of refinement including the apex and vortex finder regions, and around the air core. The presentation of more detailed mesh statistics including aspect ratio and skewness distributions will help determine appropriate minimum requirements for mesh quality.

CFD has been conclusively shown to be an accurate method for the simulation of two phase air-water flows, as both the water and air flow within the hydrocyclone have been well validated with both global and local comparison to experimental data. Future study will focus on the addition of particle flow, with the flow of particles in high concentration slurries representing the most significant challenge. Corrections for slurry viscosity, hindered settling and lift forces have all been used to help model the complex particle interactions. To date particle modelling in the hydrocyclone has only been validated through separation efficiency data (global). This is in part due to the difficulty in the measurement of particle velocities in high solid concentration flows. In the review by Nowakowski *et al.* (2004), the authors stated that the development of experimental techniques to provide solids concentration profiles or velocity fields, while a significant challenge, should be an area of focus. This statement is still valid. Recent studies have shown the applicability of tomography techniques, such as PEPT, as a useful tool for the acquisition of particle velocity data. This will allow for more rigorous validation of particle flows in hydrocyclones.

3.9 Acknowledgments

3.10   References

Aldrich, C., 2015. Chapter One - Hydrocyclones, Progress in Filtration and Separation. Academic Press, Oxford, pp. 1-24.

Anderson, J.D., 1995. Computational Fluid Dynamics. McGraw Hill.

Bagnold, R.A., 1954. Experiments on Gravity-Free Dispersion of Large Solid Spheres in a Newtonian Fluid Under Shear.

Banerjee, C., Climent, E., Majumder, A.K., 2016. Mechanistic modelling of water partitioning behaviour in hydrocyclone. Chemical Engineering Science 152, 724-735.

Bhaskar, K.U., Murthy, Y.R., Raju, M.R., Tiwari, S., Srivastava, J.K., Ramakrishnan, N., 2007a. CFD simulation and experimental validation studies on hydrocyclone. Minerals Engineering 20, 60-71.

Bhaskar, K.U., Murthy, Y.R., Ramakrishnan, N., Srivastava, J.K., Sarkar, S., Kumar, V., 2007b. CFD validation for flyash particle classification in hydrocyclones. Minerals Engineering 20, 290-302.

Brennan, M.S., 2003. Multiphase CFD simulations of dense medium and classifying hydrocyclones, CFD in Minerals and Process Industries. CSIRO, Melbourne, VIC, pp. 59-63.

Brennan, M.S., 2006. CFD Simulations of Hydrocyclones with an Air Core: Comparison Between Large Eddy Simulations and a Second Moment Closure. Chemical Engineering Research and Design 84, 495-505.

Brennan, M.S., Narasimha, M., Holtham, P.N., 2007. Multiphase modelling of hydrocyclones – prediction of cut-size. Minerals Engineering 20, 395-406.

Chang, Y.F., Ilea, C.G., Aasen, Ø.L., Hoffmann, A.C., 2011. Particle flow in a hydrocyclone investigated by positron emission particle tracking. Chemical Engineering Science 66, 4203-4211.

Chu, K.W., Wang, B., Yu, A.B., Vince, A., 2012. Computational study of the multiphase flow in a dense medium cyclone: Effect of particle density. Chemical Engineering Science 73, 123-139.

Chu, K.W., Wang, B., Yu, A.B., Vince, A., Barnett, G.D., Barnett, P.J., 2009. CFD–DEM study of the effect of particle density distribution on the multiphase flow and performance of dense medium cyclone. Minerals Engineering 22, 893-909.

Chu, L.-Y., Chen, W.-M., Lee, X.-Z., 2002. Effects of geometric and operating parameters and feed characters on the motion of solid particles in hydrocyclones. Separation and Purification Technology 26, 237-246.

Cui, B.-y., Wei, D.-z., Gao, S.-l., Liu, W.-g., Feng, Y.-q., 2014. Numerical and experimental studies of flow field in hydrocyclone with air core. Transactions of Nonferrous Metals Society of China 24, 2642-2649.

Cullivan, J.C., Williams, R.A., Cross, R., 2003. Understanding the Hydrocyclone Separator Through Computational Fluid Dynamics. Chemical Engineering Research and Design 81, 455-466.

Cullivan, J.C., Williams, R.A., Dyakowski, T., Cross, C.R., 2004. New understanding of a hydrocyclone flow field and separation mechanism from computational fluid dynamics. Minerals Engineering 17, 651-660.

Dai, G.Q., Li, J.M., Chen, W.M., 1999. Numerical prediction of the liquid flow within a hydrocyclone. Chemical Engineering Journal 74, 217-223.

Davailles, A., Climent, E., Bourgeois, F., 2012a. Fundamental understanding of swirling flow pattern in hydrocyclones. Separation and Purification Technology 92, 152-160.

Davailles, A., Climent, E., Bourgeois, F., Majumder, A.K., 2012b. Analysis of swirling flow in hydrocyclones operating under dense regime. Minerals Engineering 31, 32-41.

de Souza, F.J., de Vasconcelos Salvo, R., de Moro Martins, D.A., 2012. Large Eddy Simulation of the gas–particle flow in cyclone separators. Separation and Purification Technology 94, 61-70.

Delgadillo, J.A., Rajamani, R.K., 2005. A comparative study of three turbulence-closure models for the hydrocyclone problem. International Journal of Mineral Processing 77, 217-230.

Delgadillo, J.A., Rajamani, R.K., 2007. Exploration of hydrocyclone designs using computational fluid dynamics. International Journal of Mineral Processing 84, 252-261.

Delgadillo, J.A., Rajamani, R.K., 2009. Computational fluid dynamics prediction of the air-core in hydrocyclones. International Journal of Computational Fluid Dynamics 23, 189-197.

Delgadillo, J.A., Rosales-Marin, G., Perez-Alonso, C., Ojeda, C., 2013. CFD analysis to study the effect of design variables on the particle cut size in hydrocyclones. Asia-Pacific Journal of Chemical Engineering 8, 627-635.

Dlamini, M.F., Powell, M.S., Meyer, C.J., 2005. A CFD simulation of a single phase hydrocyclone flow field. The Journal of The South African Institute of Mining and Metallurgy 105, 711-718.

Doby, M.J., Nowakowski, A.F., Yiu, I., Dyakowski, T., 2008. Understanding air core formation in hydrocyclones by studying pressure distribution as a function of viscosity. International Journal of Mineral Processing 86, 18-25.

Elsayed, K., Lacor, C., 2010. Optimization of the cyclone separator geometry for minimum pressure drop using mathematical models and CFD simulations. Chemical Engineering Science 65, 6048-6058.

Evans, W.K., Suksangpanomrung, A., Nowakowski, A.F., 2008. The simulation of the flow within a hydrocyclone operating with an air core and with an inserted metal rod. Chemical Engineering Journal 143, 51-61.

Fisher, M.J., Flack, R.D., 2002. Velocity distributions in a hydrocyclone separator. Experiments in Fluids 32, 302-312.

Flintoff, B.C., Plitt, L.R., Turak, A.A., 1987. Cyclone modelling: a review of present Technology. CIM Bulletin 80, 39-50.

Fraser, S.M., Abdel-Razek, A.M., Abdullah, M.Z., 1997. Computational and experimental investigations in a cyclone dust separator. Proceedings of the Institution of Mechanical Engineers, Part E: Journal of Process Mechanical Engineering 211, 247-257.

Gao, S., Wei, D., Liu, W., Ma, L., Lu, T., Zhang, R., 2011. CFD numerical simulation of flow velocity characteristics of hydrocyclone. Transactions of Nonferrous Metals Society of China 21, 2783-2789.

Ghadirian, M., Hayes, R.E., Mmbaga, J., Afacan, A., Xu, Z., 2013. On the simulation of hydrocyclones using CFD. The Canadian Journal of Chemical Engineering 91, 950-958.

Ghodrat, M., Kuang, S.B., Yu, A.B., Vince, A., Barnett, G.D., Barnett, P.J., 2013. Computational Study of the Multiphase Flow and Performance of Hydrocyclones: Effects of Cyclone Size and Spigot Diameter. Industrial & Engineering Chemistry Research 52, 16019-16031.

Ghodrat, M., Kuang, S.B., Yu, A.B., Vince, A., Barnett, G.D., Barnett, P.J., 2014a. Numerical analysis of hydrocyclones with different conical section designs. Minerals Engineering 62, 74-84.

Ghodrat, M., Kuang, S.B., Yu, A.B., Vince, A., Barnett, G.D., Barnett, P.J., 2014b. Numerical analysis of hydrocyclones with different vortex finder configurations. Minerals Engineering 63, 125-138.

Ghodrat, M., Qi, Z., Kuang, S.B., Ji, L., Yu, A.B., 2016. Computational investigation of the effect of particle density on the multiphase flows and performance of hydrocyclone. Minerals Engineering 90, 55-69.

Gidaspow, D., Bezburuah, R., Ding, J., 1992. Hydrodynamics of circulating fluidized beds, kinetic theory approach, Proceedings of the 7th Engineering Foundation Conference on Fluidization, Gold Coast, Australia, pp. 75–82.

Gupta, R., Kaulaskar, M.D., Kumar, V., Sripriya, R., Meikap, B.C., Chakraborty, S., 2008. Studies on the understanding mechanism of air core and vortex formation in a hydrocyclone. Chemical Engineering Journal 144, 153-166.

He, P., Salcudean, M., Gartshore, I.S., 1999. A Numerical Simulation of Hydrocyclones. Chemical Engineering Research and Design 77, 429-441.

Hirt, C.W., Nichols, B.D., 1981. Volume of fluid (VOF) method for the dynamics of free boundaries. Journal of Computational Physics 39, 201-225.

Hsieh, K.T., 1988. Phenomenological model of the hydrocyclone, PhD thesis. The University of Utah, Salt Lake City, USA.

Hwang, K.-J., Chou, S.-P., 2017. Designing vortex finder structure for improving the particle separation efficiency of a hydrocyclone. Separation and Purification Technology 172, 76-84.

Hwang, K.-J., Hwang, Y.-W., Yoshida, H., 2013. Design of novel hydrocyclone for improving fine particle separation using computational fluid dynamics. Chemical Engineering Science 85, 62-68.

Hwang, K.-J., Wu, W.-H., Qian∗, S., Nagase†, Y., 2008. CFD Study on the Effect of Hydrocyclone Structure on the Separation Efficiency of Fine Particles. Separation Science and Technology 43, 3777-3797.

Ji, L., Kuang, S., Qi, Z., Wang, Y., Chen, J., Yu, A., 2017. Computational analysis and optimization of hydrocyclone size to mitigate adverse effect of particle density. Separation and Purification Technology 174, 251-263.

Karimi, M., Akdogan, G., Dellimore, K.H., Bradshaw, S.M., 2012. Quantification of numerical uncertainty in computational fluid dynamics modelling of hydrocyclones. Computers & Chemical Engineering 43, 45-54.

Kępa, A., 2013. The efficiency improvement of a large-diameter cyclone – The CFD calculations. Separation and Purification Technology 118, 105-111.

Kuang, S.B., Chu, K.W., Yu, A.B., Vince, A., 2012. Numerical study of liquid–gas–solid flow in classifying hydrocyclones: Effect of feed solids concentration. Minerals Engineering 31, 17-31.

Launder, B.E., Spalding, D.B., 1974. The numerical computation of turbulent flows. Computer Methods in Applied Mechanics and Engineering 3, 269-289.

Leadbeater, T.W., Parker, D.J., Gargiuli, J., 2012. Positron imaging systems for studying particulate, granular and multiphase flows. Particuology 10, 146-153.

Leeuwner, M.J., Eksteen, J.J., 2008. Computational fluid dynamic modelling of two phase flow in a hydrocyclone. The Journal of The Southern African Institute of Mining and Metallurgy 108, 231-236.

Lim, E.W.C., Chen, Y.-R., Wang, C.-H., Wu, R.-M., 2010. Experimental and computational studies of multiphase hydrodynamics in a hydrocyclone separator system. Chemical Engineering Science 65, 6415-6424.

Ma, L., Ingham, D.B., Wen, X., 2000. Numerical modelling of the fluid and particle penetration through small sampling cyclones. Journal of Aerosol Science 31, 1097-1119.

Manninen, M., Taivassalo, V., Kallio, S., 1996. On the Mixture Model for Multiphase Flow. Valtion Teknillinen Tutkimuskeskus, Espoo, Finland.

Marins, L.P.M., Duarte, D.G., Loureiro, J.B.R., Moraes, C.A.C., Freire, A.P.S., 2010. LDA and PIV characterization of the flow in a hydrocyclone without an air-core. Journal of Petroleum Science and Engineering 70, 168-176.

Marthinussen, S.-A., Chang, Y.-F., Balakin, B., Hoffmann, A.C., 2014. Removal of particles from highly viscous liquids with hydrocyclones. Chemical Engineering Science 108, 169-175.

Mokni, I., Dhaouadi, H., Bournot, P., Mhiri, H., 2015. Numerical investigation of the effect of the cylindrical height on separation performances of uniflow hydrocyclone. Chemical Engineering Science 122, 500-513.

Mousavian, S.M., Ahmadvand, M., Najafi, A.F., 2009. One-Way and Two-Way Coupling Analyses on Three Phase Flows in Hydrocyclone Separator. Journal of Applied Mechanics 76, 061005-061005-061010.

Murthy, Y.R., Bhaskar, K.U., 2012. Parametric CFD studies on hydrocyclone. Powder Technology 230, 36-47.

Nageswararao, K., Wiseman, D.M., Napier-Munn, T.J., 2004. Two empirical hydrocyclone models revisited. Minerals Engineering 17, 671-687.

Narasimha, M., Brennan, M., Holtham, P.N., 2006a. Large eddy simulation of hydrocyclone— prediction of air-core diameter and shape. International Journal of Mineral Processing 80, 1-14.

Narasimha, M., Brennan, M., Holtham, P.N., 2007. A Review of CFD Modelling for Performance Predictions of Hydrocyclone. Engineering Applications of Computational Fluid Mechanics 1, 109- 125.

Narasimha, M., Brennan, M.S., Holtham, P.N., 2006b. Numerical simulation of magnetite segregation in a dense medium cyclone. Minerals Engineering 19, 1034-1047.

Narasimha, M., Brennan, M.S., Holtham, P.N., 2012a. CFD modeling of hydrocyclones: Prediction of particle size segregation. Minerals Engineering 39, 173-183.

Narasimha, M., Brennan, M.S., Mainza, A.N., Holtham, P.N., Powell, M.S., 2010. Towards the improved hydrocyclone models; Contributions from CFD, XXV International Mineral Processing Congress IMPC 2010, Brisbane, Australia, pp. 3299-3312.

Narasimha, M., Mainza, A.N., Holtham, P.N., Brennan, M.S., 2012b. Air-core modelling for hydrocyclones operating with solids. International Journal of Mineral Processing 102, 19-24.

Narasimha, M., Sripriya, R., Banerjee, P.K., 2005. CFD modelling of hydrocyclone—prediction of cut size. International Journal of Mineral Processing 75, 53-68.

Neesse, T., Dueck, J., 2007. Air core formation in the hydrocyclone. Minerals Engineering 20, 349-354.

Noroozi, S., Hashemabadi, S.H., 2011. CFD analysis of inlet chamber body profile effects on de-oiling hydrocyclone efficiency. Chemical Engineering Research and Design 89, 968-977.

Nowakowski, A.F., Cullivan, J.C., Williams, R.A., Dyakowski, T., 2004. Application of CFD to modelling of the flow in hydrocyclones. Is this a realizable option or still a research challenge? Minerals Engineering 17, 661-669.

Olson, T.J., Van Ommen, R., 2004. Optimizing hydrocyclone design using advanced CFD model. Minerals Engineering 17, 713-720.

Parker, D.J., Broadbent, C.J., Fowles, P., Hawkesworth, M.R., McNeil, P., 1993. Positron emission particle tracking - a technique for studying flow within engineering equipment. Nuclear Instruments and Methods in Physics Research Section A: Accelerators, Spectrometers, Detectors and Associated Equipment 326, 592-607.

Patankar, S.V., 1980. Numerical heat transfer and fluid flow. Hemisphere Publishing, Washington.

Petty, C.A., Parks, S.M., 2001. Flow predictions within hydrocyclones. Filtration & Separation 38, 28-34.

Plitt, L.R., 1976. A mathematical model of the hydrocyclone classifier. CIM Bulletin 69, 114–123.

Radman, J.R., Langlois, R., Leadbeater, T., Finch, J., Rowson, N., Waters, K., 2014. Particle flow visualization in quartz slurry inside a hydrocyclone using the positron emission particle tracking technique. Minerals Engineering 62, 142-145.

Richardson, J.F., Zaki, W.N., 1954. Sedimentation and Fluidization: Part I.

Safa, R., Soltani Goharrizi, A., 2014. CFD simulation of an industrial hydrocyclone with Eulerian–Eulerian approach: A case study. International Journal of Mining Science and Technology 24, 643-648.

Saffman, P.G., 1965. The Lift on a Small Sphere in a Slow Shear.

Schuetz, S., Mayer, G., Bierdel, M., Piesche, M., 2004. Investigations on the flow and separation behaviour of hydrocyclones using computational fluid dynamics. International Journal of Mineral Processing 73, 229-237.

Schütz, S., Gorbach, G., Piesche, M., 2009. Modeling fluid behavior and droplet interactions during liquid–liquid separation in hydrocyclones. Chemical Engineering Science 64, 3935-3952.

Slack, M.D., Del Porte, S., Engelman, M.S., 2004. Designing automated computational fluid dynamics modelling tools for hydrocyclone design. Minerals Engineering 17, 705-711.

Slack, M.D., Prasad, R.O., Bakker, A., Boysan, F., 2000. Advances in Cyclone Modelling Using Unstructured Grids. Chemical Engineering Research and Design 78, 1098-1104.

Speziale, C.G., Sarkar, S., Gatski, T.B., 1991. Modelling the pressure–strain correlation of turbulence: an invariant dynamical systems approach. Journal of Fluid Mechanics 227, 245-272.

Sripriya, R., Kaulaskar, M.D., Chakraborty, S., Meikap, B.C., 2007. Studies on the performance of a hydrocyclone and modeling for flow characterization in presence and absence of air core. Chemical Engineering Science 62, 6391-6402.

Suasnabar, D.J., 2000. Dense medium cyclone performance enhancement via computational modelling of the physical processes, Mining Engineering, Faculty of Engineering. University of New South Wales.

Suresh, P.D., Kumar, V., Sripriya, R., Chakraborty, S., Meikap, B.C., 2010. Performance characteristics of pilot plant dense media hydrocyclone for beneficiation of coal and 3-D CFD simulation. Chemical Engineering Science 65, 4661-4671.

Swain, S., Mohanty, S., 2013. A 3-dimensional Eulerian–Eulerian CFD simulation of a hydrocyclone. Applied Mathematical Modelling 37, 2921-2932.

Vakamalla, T.R., Koruprolu, V.B.R., Arugonda, R., Mangadoddy, N., 2017. Development of novel hydrocyclone designs for improved fines classification using multiphase CFD model. Separation and Purification Technology 175, 481-497.

Vakamalla, T.R., Kumbhar, K.S., Gujjula, R., Mangadoddy, N., 2014. Computational and experimental study of the effect of inclination on hydrocyclone performance. Separation and Purification Technology 138, 104-117.

Vakamalla, T.R., Mangadoddy, N., 2017. Numerical simulation of industrial hydrocyclones performance: Role of turbulence modelling. Separation and Purification Technology 176, 23-39.

Versteeg, H., Malalasekera, W., 2007. An Introduction to Computational Fluid Dynamics: The Finite Volume Method, 2nd ed. Pearson, London.

Wang, B., Chu, K.W., Yu, A.B., 2007. Numerical Study of Particle−Fluid Flow in a Hydrocyclone. Industrial & Engineering Chemistry Research 46, 4695-4705.

Wang, B., Yu, A.B., 2006. Numerical study of particle–fluid flow in hydrocyclones with different body dimensions. Minerals Engineering 19, 1022-1033.

Wang, B., Yu, A.B., 2008. Numerical study of the gas–liquid–solid flow in hydrocyclones with different configuration of vortex finder. Chemical Engineering Journal 135, 33-42.

Wang, J., Bai, Z., Yang, Q., Fan, Y., Wang, H., 2016. Investigation of the simultaneous volumetric 3-component flow field inside a hydrocyclone. Separation and Purification Technology 163, 120-127.

Wills, B.A., Finch, J.A., 2016. Chapter 9 - Classification, Wills' Mineral Processing Technology (Eighth Edition). Butterworth-Heinemann, Boston, pp. 199-221.

Xu, P., Wu, Z., Mujumdar, A.S., Yu, B., 2009. Innovative Hydrocyclone Inlet Designs to Reduce Erosion-Induced Wear in Mineral Dewatering Processes. Drying Technology 27, 201-211.

Xu, W., Li, Q., Wang, J., Jin, Y., 2016. Performance evaluation of a new cyclone separator – Part II simulation results. Separation and Purification Technology 160, 112-116.

Xu, Y., Song, X., Sun, Z., Lu, G., Li, P., Yu, J., 2012. Simulation Analysis of Multiphase Flow and Performance of Hydrocyclones at Different Atmospheric Pressures. Industrial & Engineering Chemistry Research 51, 443-453.

Xu, Y., Song, X., Sun, Z., Tang, B., Li, P., Yu, J., 2013. Numerical Investigation of the Effect of the Ratio of the Vortex-Finder Diameter to the Spigot Diameter on the Steady State of the Air Core in a Hydrocyclone. Industrial & Engineering Chemistry Research 52, 5470-5478.

Yang, Q., Wang, H.-l., Liu, Y., Li, Z.-m., 2010. Solid/liquid separation performance of hydrocyclones with different cone combinations. Separation and Purification Technology 74, 271-279.

Zhang, C., Wei, D., Cui, B., Li, T., Luo, N., 2017. Effects of curvature radius on separation behaviors of the hydrocyclone with a tangent-circle inlet. Powder Technology 305, 156-165.

Zhang, Y., Qian, P., Liu, Y., Wang, H., 2011. Experimental Study of Hydrocyclone Flow Field with Different Feed Concentration. Industrial & Engineering Chemistry Research 50, 8176-8184.

Zhou, Z.Y., Kuang, S.B., Chu, K.W., Yu, A.B., 2010. Discrete particle simulation of particle–fluid flow: model formulations and their applicability. Journal of Fluid Mechanics 661, 482-510.

Zhu, G., Liow, J.-L., Neely, A., 2012. Computational study of the flow characteristics and separation efficiency in a mini-hydrocyclone. Chemical Engineering Research and Design 90, 2135-2147.

Linking Paragraph between Chapter 3 and Chapter 4

A key conclusion from the review of CFD modelling of the hydrocyclone was the lack of particle velocity data in opaque, high solid concentration flows. Positron Emission Particle Tracking (PEPT), explained in detail in the following chapter, provides a unique tool for the visualisation of particle flow in opaque slurries. PEPT has been used to validate the particle flow predicted from CFD models in a range of other unit operations, including a mixing vessel (Boucher *et al.*, 2015), stirred grinding mill (Jayasundara *et al.*, 2011), tumbling mill (Mayank *et al.*, 2015) and fluidised bed (Link *et al.*, 2008). All these units contain conditions suited to particle tracking *via* PEPT; having relatively low speeds, large particle sizes (allowing for large tracer activities), and a closed domain. This allows for very detailed, time averaged velocity flow fields to be produced. The hydrocyclone represents a significant challenge. The high particle velocities (up to 8 m·s⁻¹), small residence times (less than 1 s), tight curvature, and small particle sizes (low particle activities) all make particle tracking difficult within the hydrocyclone. Two previous studies have been conducted on PEPT in the hydrocyclone (Chang *et al.*, 2011; Radman *et al.*, 2014), however, both were limited in scope and did not produce any significant particle velocity data. Radman *et al.* (2014), showed that the ADAC Forte positron camera, the standard camera used for PEPT measurements, was not able to capture the particle flow in enough detail to obtain velocity profiles. Chapter 4 outlines the application and characterisation of a new PEPT camera made up of modular detector blocks. The detectors were assembled to create a highly sensitive field of view that matched the geometry of the hydrocyclone.

References

Boucher, D., Gharib, N., Deng, Z., Leadbeater, T., Langlois, R., Waters, K.E., 2015. PEPT Validation of a CFD-DEM Model of a Fine Quartz Particle (60μm) Behaviour in Stirred Water. Procedia Engineering 102, 1305-1315.

Chang, Y.F., Ilea, C.G., Aasen, Ø.L., Hoffmann, A.C., 2011. Particle flow in a hydrocyclone investigated by positron emission particle tracking. Chemical Engineering Science 66, 4203-4211.

Jayasundara, C.T., Yang, R.Y., Guo, B.Y., Yu, A.B., Govender, I., Mainza, A., Westhuizen, A., Rubenstein, J., 2011. CFD–DEM modelling of particle flow in IsaMills – Comparison between simulations and PEPT measurements. Minerals Engineering 24, 181-187.

Link, J.M., Deen, N.G., Kuipers, J.A.M., Fan, X., Ingram, A., Parker, D.J., Wood, J., Seville, J.P.K., 2008. PEPT and discrete particle simulation study of spout-fluid bed regimes. AIChE Journal 54, 1189-1202.

Mayank, K., Malahe, M., Govender, I., Mangadoddy, N., 2015. Coupled DEM-CFD Model to Predict the Tumbling Mill Dynamics. Procedia IUTAM 15, 139-149.

Radman, J.R., Langlois, R., Leadbeater, T., Finch, J., Rowson, N., Waters, K., 2014. Particle flow visualization in quartz slurry inside a hydrocyclone using the positron emission particle tracking technique. Minerals Engineering 62, 142-145.

Chapter 4: Performance Analysis of a New Positron Camera Geometry for High Speed, Fine Particle Tracking

4.1   Abstract

A new positron camera arrangement was assembled using 16 ECAT951 modular detector blocks. A closely packed, cross pattern arrangement was selected to produce a highly sensitive cylindrical region for tracking particles with low activities and high speeds. To determine the capabilities of this system a comprehensive analysis on the tracking performance was conducted to determine the 3D location error and location frequency as a function of tracer activity and speed. The 3D error was found to range from 0.54 mm for a stationary particle, consistent for all tracer activities, up to 4.33 mm for a tracer with an activity of 3 MBq and a speed of 4 m·s^{-1}. For lower activity tracers ($< 10^{-2}$ MBq), the error was more sensitive to increases in speed, increasing to 28 mm (at 4 m·s^{-1}), indicating that at these conditions a reliable trajectory is not possible. These results expanded on, but correlated well with, previous literature that only contained location errors for tracer speeds up to 1.5 m·s^{-1}. The camera was also used to track directly activated mineral particles inside a two-inch hydrocyclone and a 142 mm diameter flotation cell. A detailed trajectory, inside the hydrocyclone, of a $-212 + 106$ μm (10^{-1} MBq) quartz particle displayed the expected spiralling motion towards the apex. This was the first time a mineral particle of this size had been successfully traced within a hydrocyclone, however more work is required to develop detailed velocity fields.

4.2   Introduction

The positron emission particle tracking (PEPT) technique was designed to study particle dynamics, granular systems and multiphase flows (Parker *et al.*, 1993). Derived from the medical diagnostic tool Positron Emission Tomography (PET), PEPT allows for a radioactively labelled particle to be traced as it moves within a set field of view. Isotopes with proton rich nuclei are created *via* direct activation or ion exchange techniques. These isotopes decay *via* positive beta emission which is shortly followed by the annihilation of the emitted positron with a surrounding electron. This annihilation produces two gamma rays which are constrained to having equal and opposite momenta, and are therefore emitted back to back (180°±0.5°) (Charlton and Humberston, 2000). The detection of both gamma rays, termed a coincidence, and processing of multiple such

coincidences, allows for the triangulation of a particle's location in space and hence determination of its trajectory in three dimensions.

The gamma-radiation emitted from the radioactive source particle is of relatively high energy and can penetrate a considerable amount of material. This allows for the detailed study of particle behaviour in three dimensions while in dense, opaque systems and through solid vessel walls (Leadbeater *et al.*, 2012). This advantage over conventional optical or laser diffraction tracking methods has meant that PEPT has been utilised to study a variety of process equipment. Fluidised beds (Laverman *et al.*, 2012), stirred (Jayasundara *et al.*, 2011) and tumbling mills (Morrison *et al.*, 2016; Volkwyn *et al.*, 2011), and mixing vessels (Guida *et al.*, 2009) have all had particle flow fields well characterised using PEPT. These unit operations have been the primary focus of initial PEPT studies as the particle behaviour and characteristics (being low speeds, high residence times, and large particle sizes) are conducive to a high tracking rate and statistically meaningful, time averaged data. Recently, however, the PEPT technique has been employed in more difficult unit operations such as hydrocyclones (Chang *et al.*, 2011; Radman *et al.*, 2014), spiral concentrators (Boucher *et al.*, 2016) and flotation cells (Cole *et al.*, 2014); with the latter being the most advanced due to its higher residence times. The high particle speeds, low residence times (requiring a large amount of recirculation or multiple particle tracking), and small particle sizes has limited the gathering of statistically meaningful data, with velocity and location details typically being represented by a single pass rather than time average velocity fields.

For challenging process units, activation and triangulation techniques and detector set-up must be improved to increase the location rate and the positional accuracy and precision of the tracer particles. There are two fundamental ways to improve the accuracy and precision of particle tracking: the first is to improve the particle's activation level, and the second is to capture more of the radiation released by the radioisotope. If direct activation and breakage is used for the creation of fine (< 1 mm) mineral tracer particles, in the manner detailed by Boucher *et al.* (2014), particle activation is highly variable and therefore cannot be reliably depended upon. In this sense, constructing a positron camera that has a large detector face area (with its associated volumetric component) in a small volume should increase the rate of detection. Radman *et al.* (2014) showed that for the high particle speeds (> 2 m·s^{-1}) experienced in the hydrocyclone, the conventional positron camera used for PEPT (ADAC Forte) is not suitable for producing detailed trajectories.

There also exists some misconceptions on the relevance of certain errors on tracer locations. For example, Chang *et al.* (2011) reported that because they have a low location error for a stationary tracer, they could be confident in the trajectory of a very fast moving tracer moving within a hydrocyclone. To attempt to clarify any misconceptions, the purpose of this work was to first detail the error analysis technique used for a new modular PEPT detector configuration, focused on errors at high tracer speeds and a discussion on error. Some examples of improvements obtained from tailoring the detection camera design to the geometry of the process unit is also included.

4.3   Experimental

4.3.1   *Determining Tracer Location – The PEPT Algorithm*

For a particle to be tracked, the simultaneous (coincident) detection of both gamma photons, created by the aforementioned annihilation event, is required on a continuous basis. This back to back photon trajectory is defined as a Line of Response (LoR). The annihilation event, and therefore the position of the radioisotope source, is assumed to lie along or near this line (neglecting scatter). It should be noted that the annihilation photons are emitted from the point at which the positron annihilates with an electron, and this may in principle be some distance from the point at which the original radioactive decay occurred (at the particle's surface). The maximum range of the ^{18}F positrons is approximately 1 mm in quartz (distance from emission site to annihilation site), but the mean distance is much less (Parker *et al.*, 1993). The maximum range for ^{18}F positrons in water, the other dominant medium the positron could travel through, is 2.4 mm and the mean is 0.6 mm (Bailey *et al.*, 2006). While this seems like a large source of error, the random direction of the positron emission should average the particle location to the centroid of radiation source. This distance is relatively small when compared to other common nuclides, such as ^{68}Ga, which has maximum positron range of 8.2 mm in water and a mean of 2.9 mm. The shorter distance travelled by the positrons of ^{18}F, along with its half-life of 110 minutes (a practical length for experimental runs), makes it an ideal nuclide for PEPT.

Ideally with just a single radioactive particle within the field of view, all of the recorded LoRs should intersect at the position of the particle, within the minimum sphere of confidence. This sphere of confidence, or location error, is estimated based upon the particle size; the distance the positron travels before annihilation; the angle of the back to back gamma photons; and the resolution of the camera (crystal size and detector distance and alignment). In reality, some of the

detected events are corrupt, and are uniformly broadcast across space, creating a background noise in the signal and increasing the location error of the tracer. Corrupt events can be due to Compton scattering; but a majority come from simultaneous detection of two unrelated photons. This is termed a random coincidence and occurs when two (or more) uncorrelated gamma rays are detected within the coincidence window. This occurs when the activation level of the source is too high for the detector geometry and therefore photons from different interactions can be received within the same timing window. For reference, the coincidence window for the modular positron detector, described in Section 4.3.2, is 12 ns.

An iterative triangulation algorithm termed *track*, developed at the University of Birmingham, is used to identify and reject these corrupt events and to determine the location of the tracer particle (Parker *et al.*, 1993). After data acquisition of a full experiment, a number of consecutive LoRs, N, are selected and an initial tracer location estimate is calculated which minimises the sum of the perpendicular distance between all the LoRs in the set N. Those LoRs that are furthest from this point are assumed to be corrupt events and are subsequently removed. The minimum distance between all remaining LoRs is then recalculated. This process continues until only a predefined fraction, f, of lines remain from the initial set of events.

A supplementary technique, referred to as the sliding window technique, can be used to artificially increase the number of perceived locations. This works by reprocessing some of LoRs already used to calculate the previous location (Figure 4.1). For instance, if N is set to 500 and S, the number of slides per set of LoRs, is set to 2, the first location will use line 1-500, the second 250-750, the third 500-1000, *etc*. This technique is advantageous when processing data of tracers travelling at high velocities or with low activities. The LoRs of a moving particle will not converge upon a single point but rather spread across the path of the tracer (Leadbeater *et al.*, 2012). The resultant convergence points are then an average of the LoRs used, therefore reusing lines enables a higher location frequency, spread across the tracer path. A schematic of this process is shown in Figure 4.1.

Although simplistic in nature, this approach does need significant post processing to obtain the most optimal inputs to produce an accurate and detailed particle trajectory. Values for the initial set of events N, fraction of lines retained, f, and number of slides per number set, S, are all variable depending upon particle activation, speed, camera geometry, *etc*. In theory, stationary or slow

moving tracers should be more accurately located using large numbers for N, whereas at high speeds, large values of N should cause higher location errors and minimise trajectory features (*e.g.* reducing the perceived radius of a tracer moving in a circular motion). The *track* code is limited to inputs of $N \leq 5000$, $S \leq 5000$ and f values ranging between 0 and 100 (which represents the percentage of lines kept). While the *track* code is the original and most prominent PEPT algorithm, new approaches based off PET technology have been recently published (Bickell *et al.*, 2012; Wiggins *et al.*, 2016).
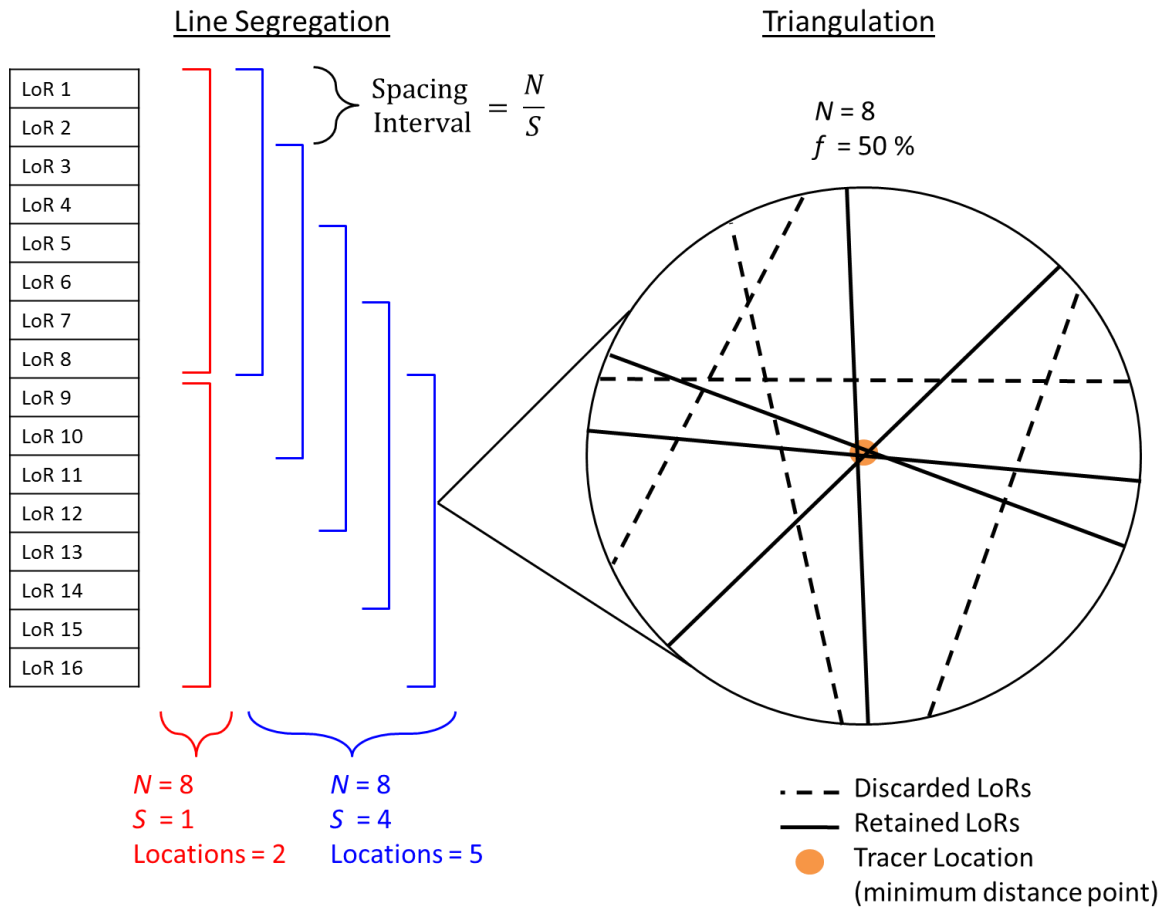
Figure 4.1: Diagram showing how LoRs are first segregating into groups, using various *N* and *S* parameters, followed by a representation of the 3D location triangulation process condensed to 2D (determined by *f*).

4.3.2   PEPT Detection Cameras – Positron Cameras

The test work for this project was undertaken at the Positron Imaging Centre at the University of Birmingham, UK. At this location there are currently two types of radiation detection cameras in operation. Most conventional PEPT imaging is conducted using the ADAC Forte (ADAC Laboratories, USA - later acquired by Philips) dual-headed gamma camera operating in coincidence mode, as described by Parker *et al.* (2002). For this camera the intrinsic efficiency for detecting annihilation photons is around 25% giving raw data acquisition rates up to 100 kHz (Leadbeater *et al.*, 2012). This camera, although well established and characterised, does not allow for high tracking rates in unit operations with geometries unsuited to the parallel nature of the two large detector heads.

To address this, a modular camera system, containing modules of four blocks of ECAT951 detectors (Siemens, USA), has been developed to allow for specific detector geometries that can be tailored to the specific unit operation to be studied. These modular positron cameras are described in detail by Leadbeater and Parker (2011), Leadbeater et al. (2011) and Parker et al. (2009). Each detector block is segmented into an 8×8 array of high efficiency Bismuth Germanium Oxide (BGO) crystals (crystal pitches are 6.25 mm transverse and 6.75 mm axial with 30 mm depth). The intrinsic efficiency of the modular cameras is around 45 %, an intrinsic step change in performance over the ADAC camera. Coupled with the parallel nature of the data handling systems, has meant the raw data acquisition rates are significantly higher than for the ADAC camera. The maximum data acquisition rate for the modular system is 4 MHz, however this is rarely achieved due to the dependence upon particle activity, detector geometry and intrinsic efficiency. Theoretically, with an increase in acquisition rates, the particle location rate and precision can both be increased. In practice, however, although higher location rates are typically observed, the precision is limited by the ability to position the individual modules accurately in comparison to their defined position and orientation in the data processing software (Leadbeater *et al.*, 2012).

It was decided that for detailed trajectories of low activity or high speed tracer particles the best detector arrangement was a coupled cross pattern (Figure 4.2a), as recommended by Leadbeater and Parker (2011). To determine the spatial dependence of the sensitivity of this camera geometry, a Monte-Carlo simulation (Figure 4.3) was conducted (Leadbeater *et al.*, 2011). It ensured that the

closely packed modular assembly created a highly sensitive cylindrical region approximately 100 mm in diameter and 400 mm in height. The assembly was made up of sixteen individual detector modules, with each of the four groups containing modules stacked in a 2x2 grid. A restriction was imposed that only allowed the detector groups opposite one another to record coincidence events. This enforced that the gamma radiation originated within the region between the detectors (not accounting for scatter or random coincidences), as shown in Figure 4.2b. While individual photons were still detected from outside the highly sensitive zone, which will contribute to random coincidences, this limitation helps reduce the coincidence processing dead-time and the number of random coincidences.
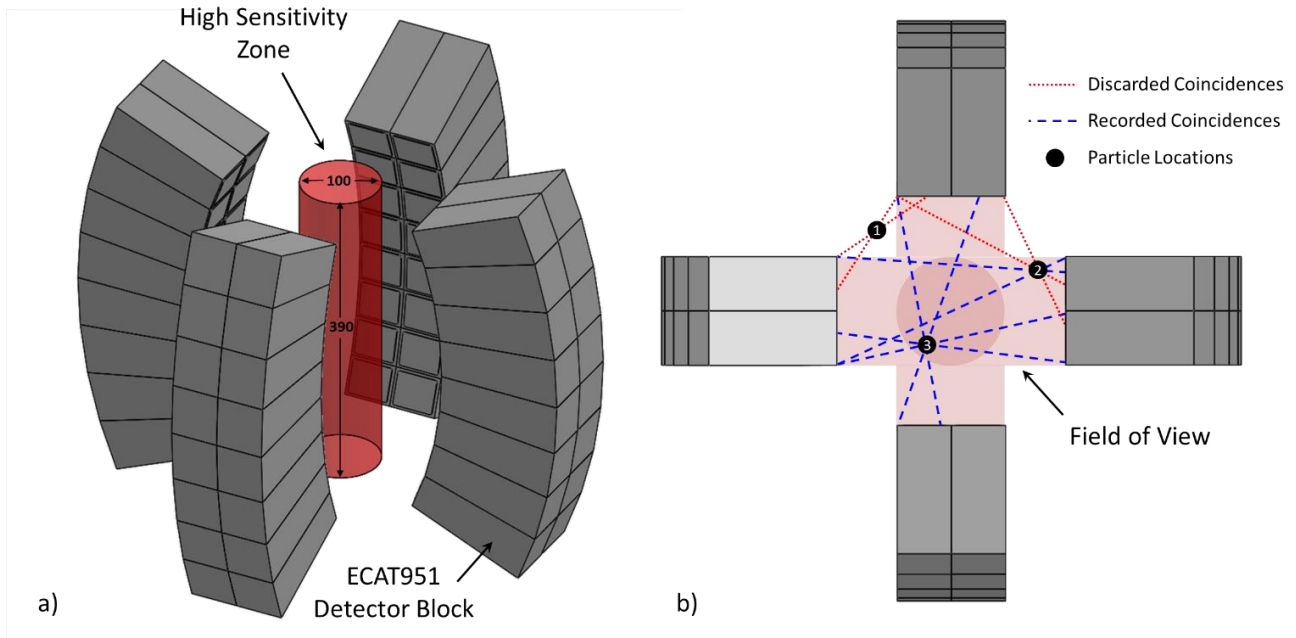
Figure 4.2: The cross pattern modular camera design showing (a) the physical setup (dimensions in mm) and (b) the field of view with various particle locations in the 1. Undetectable zone 2. Low detection zone and 3. Highly sensitive zone.
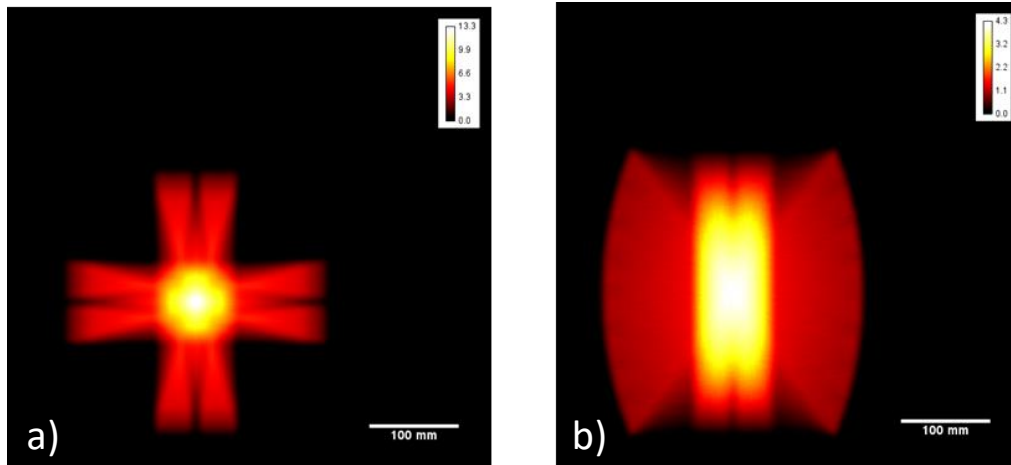
Figure 4.3: The modular assembly sensitivity profiles in the (a) xz and (b) xy plane: derived from a Monte-Carlo simulation (scale represents absolute efficiency for coincidence detection).

4.3.3 Constrained Trajectory Setup

Before any trajectories or velocity fields can be meaningfully presented, any detector arrangement must first be analysed in order to determine the location error at various speeds and particle activity. To do this a particle with a known trajectory must be used. In this instance, a planar circular path was created by fixing a tracer particle to the edge of one of the six paddles of a standard two-inch Rushton impeller, as detailed by Boucher et al (2016). It is known that the accuracy of locating a particle is not only dependent upon its speed, but also the curvature of its trajectory (Parker *et al.*, 1993). Therefore a small radius was chosen (25.4 mm radius compared to 95 mm chosen by Parker *et al.* (1993); or 120 mm and 38 mm by Cole *et al.* (2012)) as this coincides with the motion likely to be captured inside the camera. The impeller, attached to a digital mixer (Caframo, BDC 1850, Canada), allowed for various speeds to be tested at each tracer activity level. The tested parameters are shown in Table 4.1 and Table 4.2. The activity of the three highest activity tracers were measured with a CRC-25PET ionisation chamber (Capintec, USA). For the tracer with the smallest activity, an uncertainty in the exact activity arose due to it being under the detectable limits of the ionisation chamber (3.7×10^{-2} MBq). Therefore the activity was measured with a T401 contamination monitor (Tracerco, UK). However, the activity was large enough to overload this sensors upper limit (4.0×10^{-3} MBq), creating the range seen in Table 4.1. As the Tracerco T401 uses a flat pancake probe, which can at most cover one hemisphere of the released radiation (if directly on top of the tracer particle), it is likely that the particles activity was at least twice the reported lower boundary.

The impeller head was completely submerged in a 200 mm diameter water filled bucket at a depth of approximately 100 mm from the water's surface (Figure 4.4). This was to simulate the shielding of the source particle that would occur when tracking in aqueous systems. The expected locations over time were assumed to form a sinusoid of various amplitudes in the in the x, y and z axes when plotted against time. The amplitude in each axis will be dependent upon the rotational plane of the impeller. As the plane of rotation was perpendicular to the vertical axis of the modular detection system, the y axis will have an amplitude equal to zero, and the amplitude for the x and z axis should be equal to the impeller radius.

Table 4.1: Tested tracer activities
*Uncertainty caused by measurement technique of the lowest activity tracer.

Tracer Activity (MBq)
$4.0 \times 10^{-3} - 3.7 \times 10^{-2}$*
3.7×10^{-1}
3.3×10^{0}
1.1×10^{2}

Table 4.2: Tested tracer speed parameters, including the revolutions per minute set on the mixer and the equivalent impeller tip (particle) speed.

Revolutions per minute	Impeller Tip Speed (m·s^{-1})
0	0.00
25	0.07
125	0.33
250	0.67
500	1.34
1000	2.67
1500	4.01
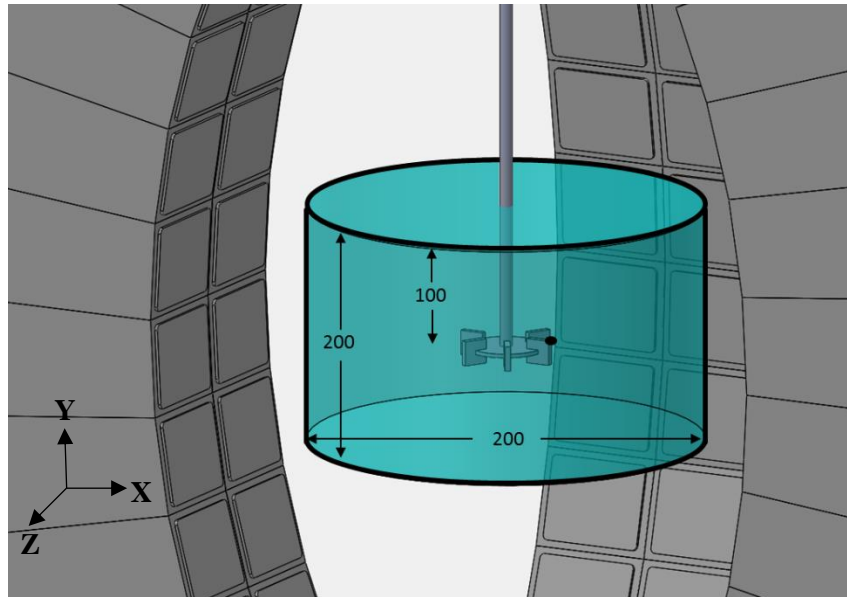
Figure 4.4: Representation of the particle location on the Rushton impeller inside the modular detector assembly (dimensions in mm).

4.3.4   Trajectory Error Analysis Code Development

An analysis of the raw data, obtained from the rotating impeller tests, is needed to determine the optimum input parameters for the *track* code for each corresponding speed and tracer activity level. The metric for this was minimising the three dimensional location error. This error represents the radius of the aforementioned sphere of confidence, which incorporates all inaccuracies involved in locating a tracer *via* PEPT. A script was developed (found in Appendix B.1) that allowed for the automated input of multiple combinations of *N*, *f*, and *S* values into the previously described traditional *track* algorithm. This process produced a set of locations for each set of *N*, *f*, and *S* values. The range of values for each parameter is shown in Table A.1.1 in Appendix A.1.

Following this, a subsequent script was compiled (found in Appendix B.2) that allowed for each tracer location data set to be automatically imported; compared to the known particle trajectory; have the distance from this trajectory, or residuals, calculated; and the location error recorded. To begin, a section of the trajectory was selected for each independent axis, equating to ten wavelengths or impeller rotations. A sinusoidal function with a fixed amplitude was then fit to the data, *via* the nonlinear least-squares solver method in Matlab©. The amplitude was initially allowed to vary for each data set, as implemented by Cole *et al.* (2012). In this case, the amplitude was determined by the average circular path created from the locations over the ten impeller rotations.

111

This process could not, however, allow for a large range of N values to be tested. It was found that as the value of N was increased, the perceived amplitude (or impeller radius) was reduced to unrealistic values, due to the averaging of points over a curved path (Parker *et al.*, 1993). Therefore, the amplitude in the x and z axis was set as the measured impeller diameter, further imposing a realistic trajectory, which was determined to be 25.9 mm (25.4 mm impeller radius plus 0.5 mm tracer radius). This was found to closely match the asymptotic value (as N approached the lower range of tested values) of the amplitude when plotted as a function of N. The frequency of the sinusoidal wave was estimated based on the impeller speed but allowed to vary due to inconsistencies created by the variability of the mixer motor rotation. This meant that the variable frequency could be used as a parameter check, to ensure the real trajectory was representative. The fitted frequency for data with low location rates will tend vary to better fit the locations, reducing the perceived location error. Values with a difference greater than 1 % from the recorded impeller speed were flagged and constrained to have a frequency equal to the impeller speed.

For the tests where the tracer particle was stationary, a straight-line fit (in the form $x, y, or\ z = m_{x,y,or\ z} \cdot time + constant$) was used as the theoretical trajectory of the x, y and z coordinates when plotted against time. An analysis of the calculated gradient ensured the tracer location was consistent throughout the whole time interval chosen to be analysed. Optimum parameters were not comprehensively investigated for the stationary tracers as large values of N will always give the smallest location errors for a stationary particle. Values of f between 0.35 and 0.60 gave very similar location errors, however 0.50 gave the lowest location error. Therefore, the parameters N = 5000, S = 5000, and f = 0.50 gave the lowest location error within the allowable *track* parameter range for stationary cases.

In both stationary and moving data sets the residuals were determined and plotted for each ten wavelength sample. The residuals were defined as the perpendicular distance (with regards to time) from the calculated tracer positions and the fitted sine curve. Under the assumption that the residuals are inherently random, a Gaussian distribution curve was fit to a histogram of the residuals. The mean, which should be close to zero, was used to confirm that there was no systematic offset caused by improper fitting of the known trajectory. The overall reported location error was equal to two standard deviations from the mean. This represents the region for which approximately 95 % of all residuals should lie within, and comparatively where 95 % of all

locations should occur. An example of this process, for the 3.7×10^{-1} MBq tracer, is shown at two different tracer speeds in Figure 4.5 and Figure 4.6. It is common to present location error as either the Root Mean Squared error (RMS) (Boucher *et al.*, 2016; Cole *et al.*, 2012) or, equivalently, one standard deviation (Parker *et al.*, 1993). Although it is relatively simple to convert between these values, to ensure the error was not under estimated two standard deviations was chosen.

The three-dimensional location error was calculated using the standard distance formula shown in Equation 4.1. If the actual particle location is taken as the origin, with the coordinates (0, 0, 0), the axial errors can be used to calculate the total error in three dimensions (Equation 4.2).

$$d = \sqrt{(x_2 - x_1)^2 + (y_2 - y_1)^2 + (z_2 - z_1)^2}$$ **Equation 4.1**

$$3D_{error} = \sqrt{(x_{error})^2 + (y_{error})^2 + (z_{error})^2}$$ **Equation 4.2**
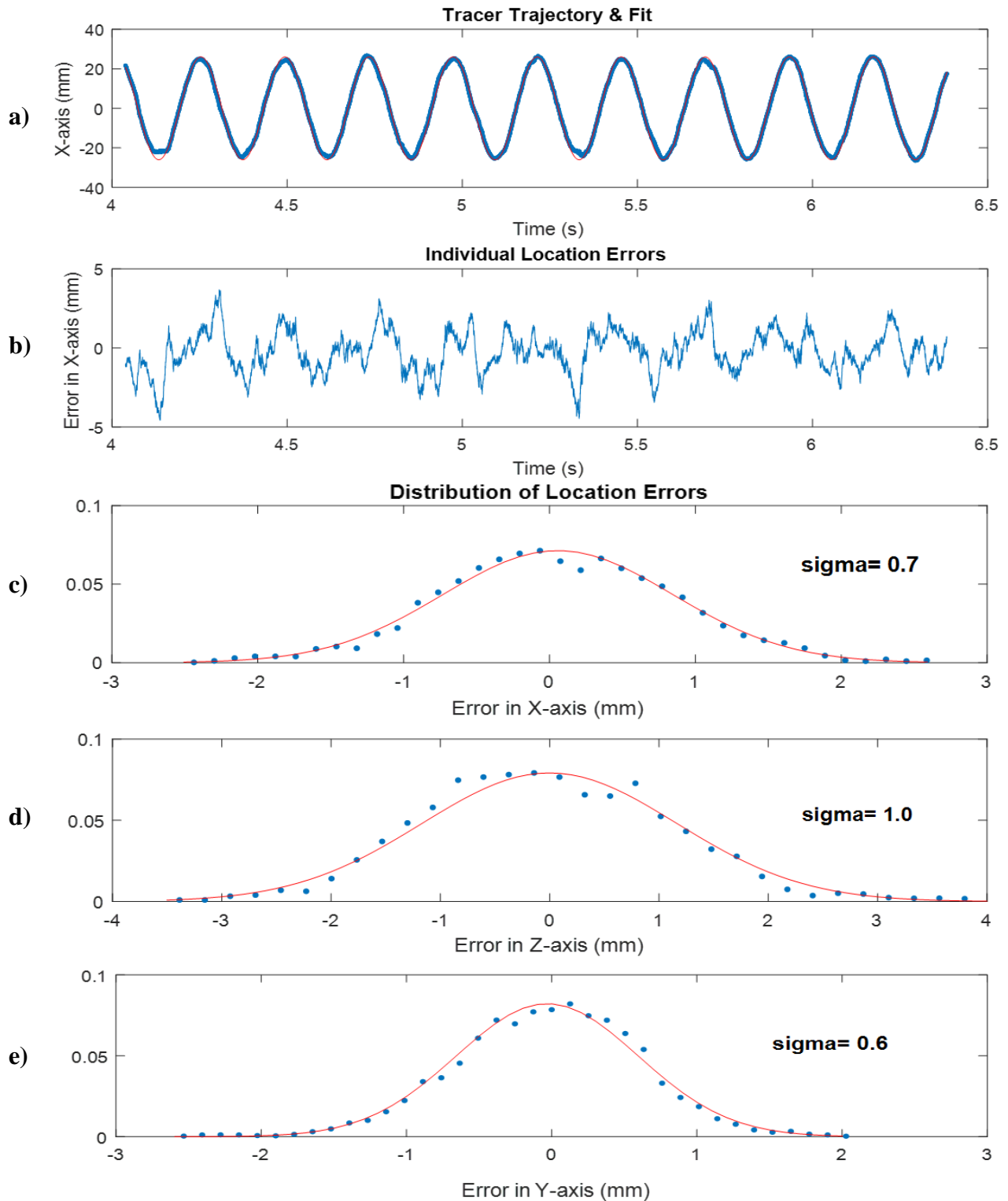
Figure 4.5: An example of the script output for the 3.7 × 10⁻¹ MBq tracer particle moving at 0.67 m·s⁻¹ which shows: (a) the tracer trajectory with fit (in x-axis); (b) the residuals or location errors for each single location (in x-axis); and (c) the distribution of these location errors, with fitted Gaussian distribution curve and standard deviation shown (in x-axis). The distribution of errors in the (d) Z-axis and (e) Y axis are also included for comparison.
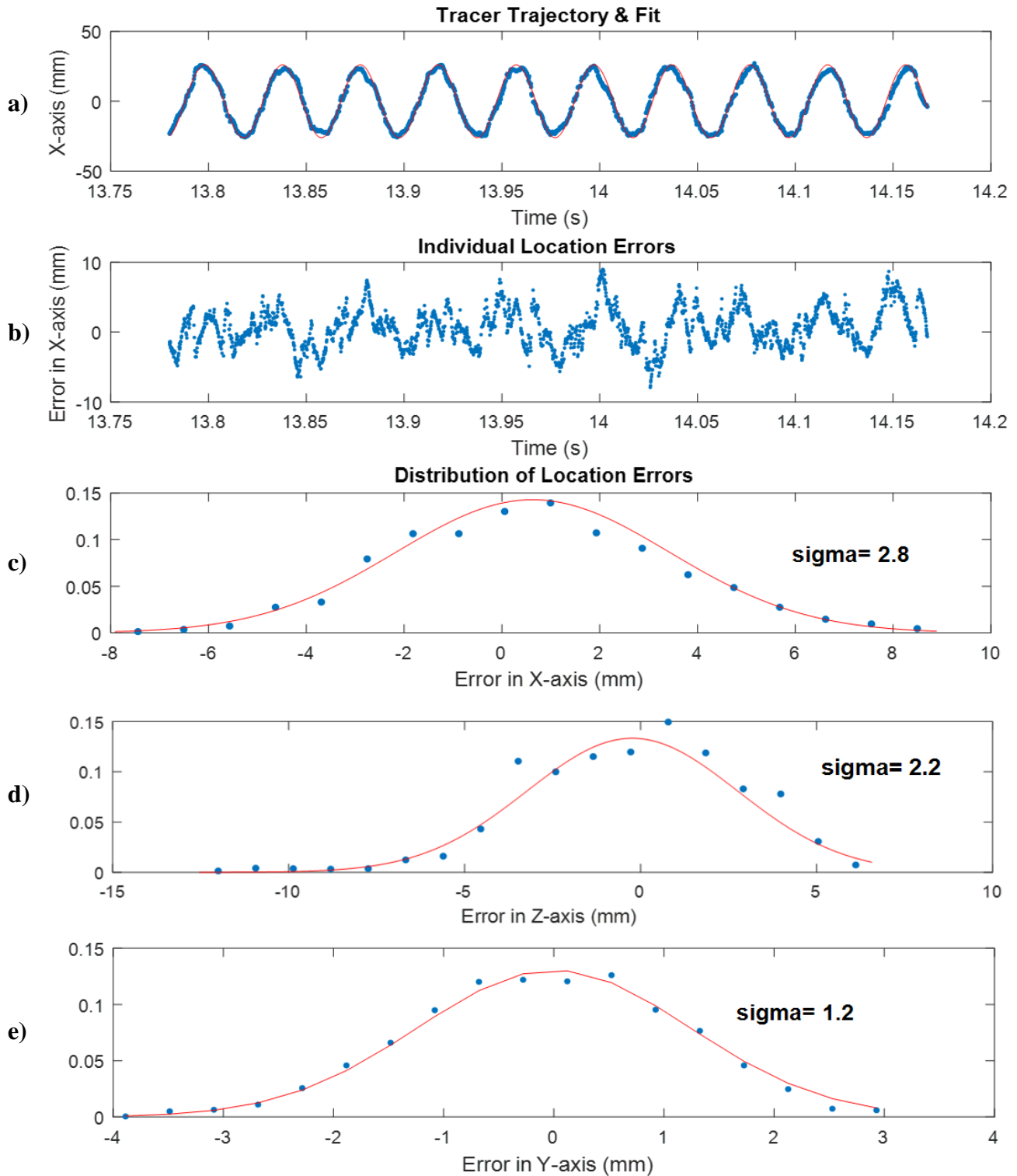
Figure 4.6: An example of the script output for the 3.7 × 10-1 MBq tracer particle moving at 4.01 m·s-1 which shows: (a) the tracer trajectory with fit (in x-axis); (b) the residuals or location errors for each single location (in x-axis); and (c) the distribution of these location errors, with fitted Gaussian distribution curve and standard deviation shown (in x-axis). The distribution of errors in the (d) Z-axis and (e) Y axis are also included for comparison.

4.4   Results and Discussion

Once the trajectory error analysis was complete, the location error for all combinations of N, S and f parameters could be compared. Plotting the three-dimensional location error against location frequency, allowed for the most simplistic selection of the optimum parameters. Figure 4.7a shows the location error for each N, S and f combination, for a particular tracer activity and speed. The curve which describes the minimum location error for a particular location frequency, follows a distinct trend. For low location frequencies, the error is restricted to a minimum value (due to system properties), while at high location frequencies location error is sacrificed for any further increase in location rate. Location error is typically reported as a single number, defined by the input parameters chosen, however, Figure 4.7 shows that both the location frequency and error can be manipulated based upon the desired outcomes of the tracking data. For this analysis, it was decided that the point at which the location frequency is maximised, without any loss in location precision, would be selected. This point is distinguished as the triangle in Figure 4.7 and is at the inflection point of the bottom curve. In this instance, the parameters that gave this location frequency and error were $N = 400$, $S = 400$ and $f = 0.55$.

a)   b)
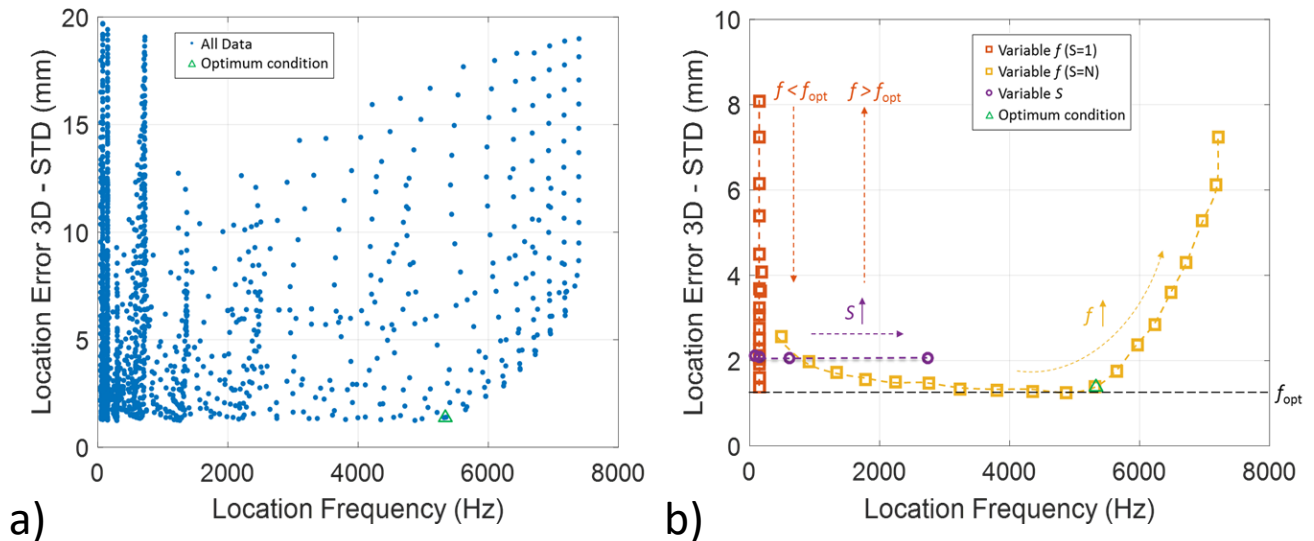
Figure 4.7: (a) Location frequency vs three dimensional location error for all combinations of N, S and f parameters for the 3.7×10^{-1} MBq tracer particle moving at 0.67 m·s^{-1} and (b) a simplified version showing trends for f and S parameters while other parameters are kept constant.

Figure 4.7b also shows some example trend lines for the f or S parameters, while the other parameters are kept constant. This illustrates that increasing S allows for a higher location rate without any increase in location error. To better understand what effect N and f had on the location error and frequency, contour plots were produced, as seen in Figure 4.8. The location frequency plot shows that as f increases and N decreases there is a higher tracking rate (moving from bottom right [dark region] to top left [light region] of figure). The effect of N is straightforward to understand, if there are fewer number of lines grouped together there will be more individual locations recorded. The reason for the location frequency increase, with increasing f is more complex. Firstly, this occurrence is only in cases where the value of S is not equal to one. For cases of S=1, f does not have any effect on location rate. This is shown in Figure 4.7b by the vertical line of square symbols where the location error varies for various f values, but no change in location rate is seen. For other cases ($S \neq 1$), the location rate increases with increasing f because there are fewer duplicated tracer locations, which are automatically removed by the *track* code. Duplicated locations occur when reusing a large portion of LORs (the purpose of S) and the addition of any new LORs are discarded without any effect on the triangulation process. For instance, if using N=500 and S=500, after each single line addition a new location is calculated. If this single added line is not part of the triangulation process (determined by f), along with the removed line not being a part of the previous triangulation, then the location would be duplicated. The number of duplicate locations decreases as we increase the chance of the new line being a part of the triangulation process (large values of f). Therefore, f is not increasing the actual location rate, but instead it is increasing the number of unique locations. This gives the appearance of a higher location rate, however, the location rate would be equal for all values of f if duplicate points were not removed by the *track* code. This again is shown in Figure 4.7b where an increase in f increases the location rate, while also having an effect on location error.
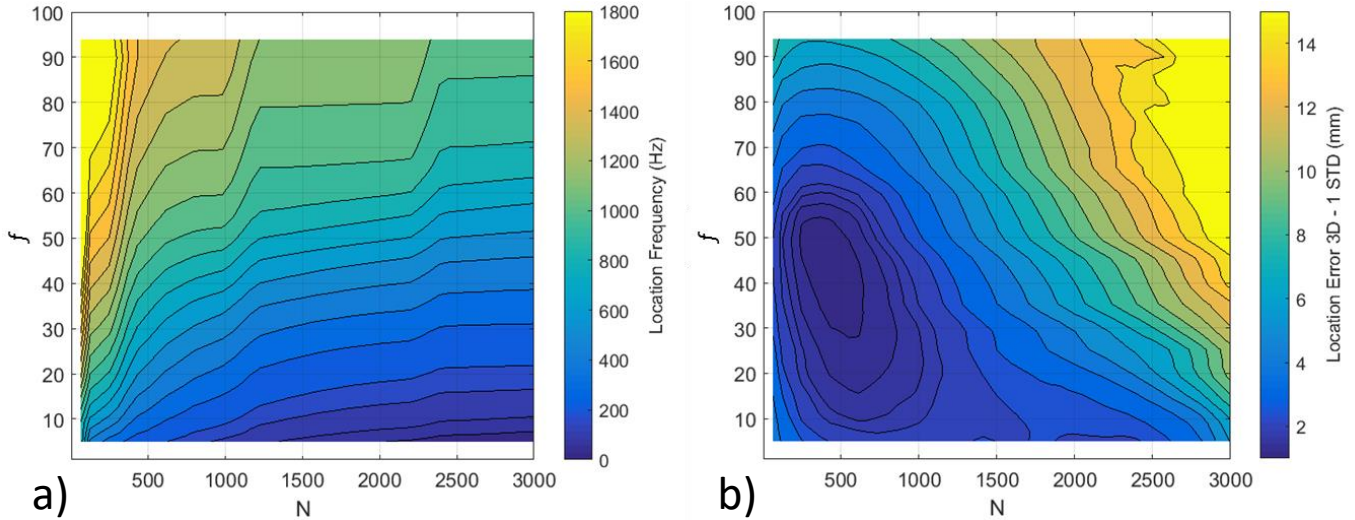
Figure 4.8: Effect of *N* and f parameters on (a) location frequency and (b) error for the 3.7×10^{-1} MBq tracer particle moving at 0.67 m·s^{-1}.

The location error, also shown in Figure 4.8, constricts the choice of *N* and *f* parameters. The dark region, centered at *N* = 500, shows the area at which there is the lowest error. The location of this region is dependent upon the tracer particle's speed and activity. In general, however, high values of *f* will cause more scattered or random coincidences to be included in the triangulation, therefore causing biases away from the true particle location. Conversely, if the value for *f* is too low, the statistics of the triangulation process becomes dominated by Poisson noise (Leadbeater *et al.*, 2012). Leadbeater *et al.* (2012) states that there is an optimum value of *f* for each system (camera geometry, detector material, electronics, signal processing, *etc.*) and tracer activity (scattering, attenuating, associated and random coincidences, *etc.*). In this case enough corrupt events are rejected whilst retaining enough events to reduce the statistical noise. Table 4.5 provides the optimum parameters for each particle speed and activity, and shows that the optimal value for *f* is dependent upon particle activity.

The effects of *N* are dependent upon the tracer speed. For stationary tracer particles, the precision in each location can be made arbitrarily small provided *N* is sufficiently large (Chang *et al.*, 2011; Leadbeater *et al.*, 2012). There is little need to optimise *N* for stationary particles, as larger values for *N* will always produce more time averaged accurate locations. For moving tracers, however, the LoRs in each set of *N* are spread along the particle trajectory and therefore will not converge to a single location. High values of *N* will tend to remove or reduce features of the trajectory, such as the curvature, as larger portions of the trajectory are averaged to a single location. Low values

of N will incur more statistical variance as scattered or random coincidences become more prevalent. These ranges will change depending upon the amount of LORs captured per distance travelled. This is seen in Table 4.5, where optimal N values decrease for increasing speed and with decreasing activity. The optimum conditions taken from Figure 4.7 ($N = 400$, $S = 400$ and $f = 0.55$) can be obtained by combining the results of the two contour plots shown in Figure 4.8. The selection would need to minimise error, and therefore be in the aforementioned dark region centered at $N = 500$ (Figure 4.8b), whilst maximising the location rate (top left region – Figure 4.8a). This would mean the selection would be in the top left corner of the dark region, which corresponds to $N = 400$ and $f = 0.55$.

This process was completed for all tracer activities and speeds, with the resultant three dimension location errors, location frequencies and optimal *track* code parameters shown in Table 4.3, Table 4.4, and Table 4.5 respectively. The individual axial errors, that the total error was calculated from, can be found in Tables A.1.2-A.1.4 (Appendix A.1) .The trend seen in the three dimensional error is primarily due to statistics, and is well described elsewhere (Parker *et al.*, 1993). When processing faster moving, or lower activity, tracers the amount of LoRs used per location must be less as the distance travelled per detected coincidence is lower. Therefore, the resultant locations are more effected by random coincidences.

Due to the high sensitivity of the modular positron camera design, experiments conducted with the 110 MBq tracer particle were seen to overload the detection and data acquisition systems (*i.e.* two unrelated LoRs were detected in a coincidence window and incorrectly grouped). To triangulate a position both ends of a single LoR must be correctly attributed to one another. If it is not possible to distinguish between consecutive individual LoRs, a common occurrence at high tracer activities, the detection system will incorrectly group unrelated LoRs, creating a signal dominated by randomly distributed noise (Leadbeater *et al.*, 2011). This was the case for the 110 MBq tracer, as locations close to the known trajectory could not be achieved. More tests will have to be conducted to determine the exact tracer activity at which these randomly distributed signals dominate true LoR coincidences.

Comprehensive studies of location errors, as a function of speed and tracer activity, for different PEPT cameras are not common. Numerous authors have presented errors based upon stationary tracer particles, (Chang *et al.*, 2011; García-Triñanes *et al.*, 2016; Leadbeater and Parker, 2011).

While some authors use this to characterise different features of PEPT tracking (error from linear module displacement; error from relative position in field of view; *etc.*), it is not particularly relevant for particle tracking as the error cannot be extrapolated to moving particles. As Leadbeater *et al.* (2012) states, and the data presented in Table 4.3 shows, the location error of a stationary particle is independent from the tracer activity, and is purely dependent upon the spatial resolution of the camera and the parameters used in the *track* algorithm. This is contrary to what García-Triñanes *et al.* (2016) states, that processed data of a stationary particle has been shown to correlate with processed data from a moving particle.

There also exists some confusion as to what location error truly represents. This confusion stems from the *track* code, which outputs an "error" of each individual tracer location. This "error" is defined as the average of the perpendicular distance from each LoR to the final location point. This should only be used as a guide to estimate optimal N and f parameters, as large distances between the set of LoRs could mean random coincidences are being used in the triangulation process. This "error", however, cannot be presented as a location error as seen in some cases (Chiti *et al.*, 2011; García-Triñanes *et al.*, 2016), since the location error can only be obtained by comparing the calculated locations to a known trajectory.

Cole *et al.* (2012) conducted a study on location errors for fine tracer particles, with low activity, in an ECAT 'EXACT3D' (Model: CTI/Siemens 966) camera in the laboratories of PEPT, Cape Town (South Africa). The data, presented in Table 4.6, shows that the values for the three-dimensional location error is relatively close to those presented in this work (when comparing data from similar speed and activity levels). The location errors presented by Boucher *et al.* (2016) who conducted a similar project in the ADAC Forte camera at Birmingham (UK) and a modular ECAT951 Ring Assembly are also shown in Table 4.6. Both Cole *et al.* (2012) and Boucher *et al.* (2016) did allow the known trajectory to vary slightly by not fixing the amplitude of the sine function, which could underestimate the error to varying degrees. This could explain the surprisingly low location error reported by Boucher *et al.* (2016) (particularly for the ADAC results, considering the tracers low activity), which does not seem to correlate with the results presented in this chapter. Figure 4.9 displays the three dimensional location error data at various speeds from this work, as well as the work of Cole *et al.* (2012) and Boucher *et al.* (2016). The data has been grouped into various tracer activity ranges to allow for comparison, while also

allowing for extrapolation of errors between the tested velocities. The location frequency in the present case, however, is an order of magnitude bigger than that reported by Cole *et al.* (2012) and Boucher *et al.* (2016). This improvement in location frequency, without any loss in location error, is evidence of the increased performance of the system. This increase was attributed to the closely packed camera geometry and the optimisation of the *track* code parameters.

Table 4.3: Three-dimensional location errors (mm) for each speed and tracer activity.

Location Errors (mm)			
Impeller Tip Speed (m·s^{-1})	Tracer Activity (MBq)		
	4.0×10^{-3} - 3.7×10^{-2}	3.7×10^{-1}	3.3×10^{0}
0.00	0.54	0.52	0.54
0.07	8.27	1.72	1.24
0.33	9.51	1.85	1.48
0.67	10.74	2.76	2.46
1.34	12.61	3.27	2.56
2.67	16.94	5.42	2.46
4.01	27.84	7.51	4.33

Table 4.4: Location rate (Hz) for each speed and tracer activity, with the associated coincidence rate for each tracer activity included as reference.

Location Rate (Hz)			
Impeller Tip Speed (m·s^{-1})	Tracer Activity (MBq)		
	4.0×10^{-3} - 3.7×10^{-2}	3.7×10^{-1}	3.3×10^{0}
0.00	1,989	5,158	14,528
0.07	1,916	5,442	21,903
0.33	1,927	4,884	20,428
0.67	1,730	5,320	20,476
1.34	1,754	5,138	20,685
2.67	1,682	5,382	20,178
4.01	1,976	5,723	20,624
Coincidence Rate (Hz)	21,000	41,000	114,000

Table 4.5: Optimum *track* code parameters for each speed and tracer activity. For each case *N* is the first number and *f* is the second number. *S* is not shown as it was equal to *N* in all cases.

Optimum *track* code parameters ($N \mid f$)				
Impeller Tip Speed ($m \cdot s^{-1}$)	Tracer Activity (MBq)			
	$4.0 \times 10^{-3} - 3.7 \times 10^{-2}$	3.7×10^{-1}	3.3×10^{0}	
0.00	5000 | 50	5000 | 50	5000 | 50	
0.07	400 | 45	2800 | 55	5000 | 70	
0.33	100 | 45	800 | 50	3500 | 65	
0.67	100 | 40	400 | 55	2000 | 65	
1.34	100 | 40	250 | 50	1000 | 65	
2.67	100 | 35	100 | 45	600 | 65	
4.01	50 | 45	100 | 45	250 | 65	

Table 4.6: Three dimensional location errors and location frequencies for various tracer speeds and activities taken from data presented by Cole *et al.* (2012) and Boucher *et al.* (2016). (*Activity measured as counts per second with a flat probe radiation detector)

Camera Type	Fluid Medium	Speed ($m \cdot s^{-1}$)	Activity (MBq)	3D Location Error (mm)	Location Frequency (Hz)
Cole *et al.* (2012)					
ECAT 'EXACT3D' (Model: CTI/Siemens 966)	water	0	5.0×10^{-2}	6.51	16
	water	0.10	5.0×10^{-2}	7.69	15
	air	0	6.0×10^{-2}	10.89	23
	air	0	4.9×10^{-1}	4.98	71
	air	0.98	4.5×10^{-1}	4.14	72
	air	1.43	6.0×10^{-2}	14.28	19
Boucher *et al.* (2016)					
ADAC	air	0.28	2,600*	7.6	12.4
	air	0.14	2,300*	5.8	5.6
	air	0.03	2,100*	3.6	1.5
Modular ECAT951 Ring Assembly	air	0.38	850*	6.4	10.0
	air	0.19	710*	3.8	8.6
	air	0.04	620*	3.2	7.3
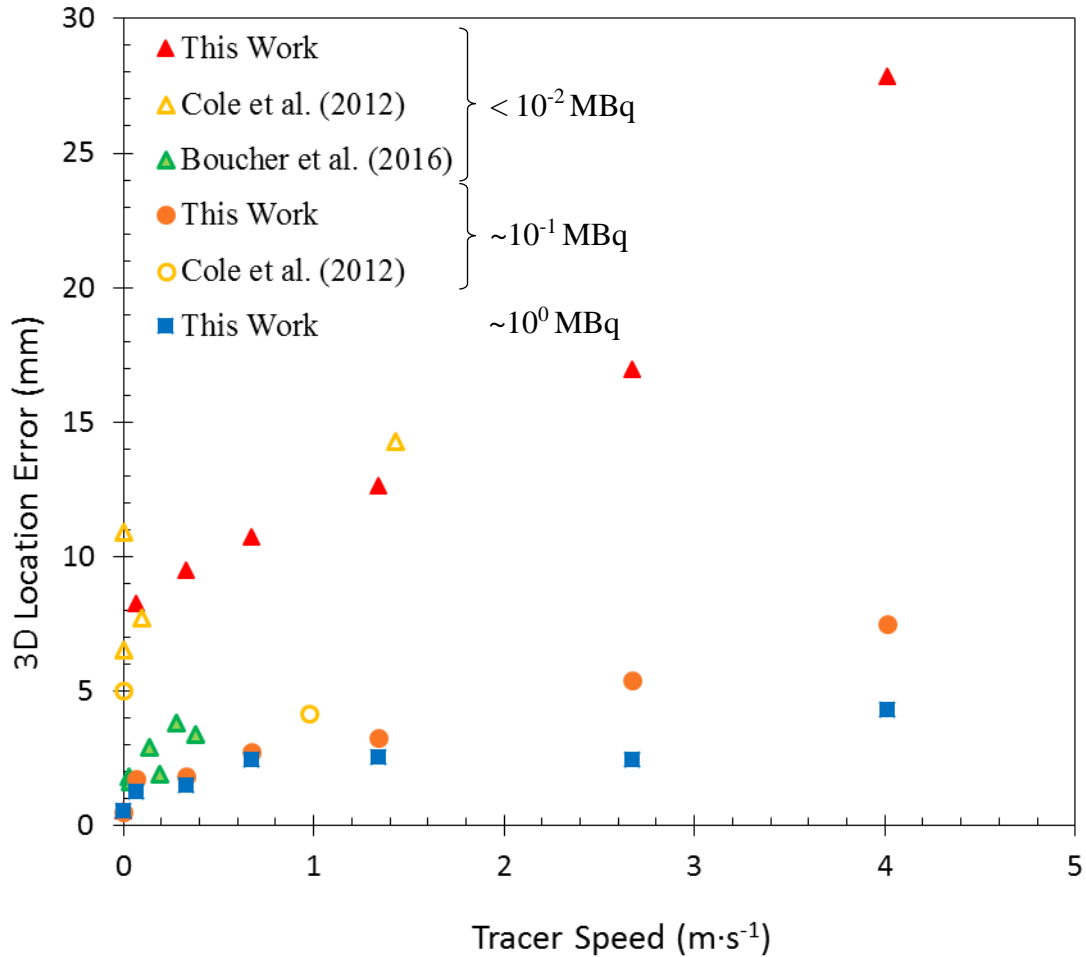
Figure 4.9: Tracer speed ($m \cdot s^{-1}$) vs three-dimensional location errors (mm) for various activities. Data represented by triangles depicts tracers with an activity under 6.0×10^{-2} MBq; circles represent activities between $3.7\text{-}4.5 \times 10^{-1}$ MBq; and squares an activity of 3.3×10^{0} MBq. Specific activities for the data of Cole *et al.* (2012) and Boucher *et al.* (2016) are presented in **Table 4.6**.

4.5   Applications

4.5.1   *Hydrocyclone trajectory*

Typically used as a classifying device, the hydrocyclone separates particle based on size, shape and density. The high particle velocities (up to 8 $m \cdot s^{-1}$) seen within a hydrocyclone have limited previous PEPT studies to relatively large particle sizes due to the high activation requirement. Tracers created *via* direct activation have only provided trajectories at a particle diameter of ‑2000+1700 µm, which had an activity of 1×10^{4} MBq (Radman *et al.*, 2014). Tracers created *via* ion exchange (indirect activation) have been tracked at approximately 390 to 700 µm in diameter, with the associated activity ranging from 1.67 to 5.33×10^{1} MBq (this uncertainty is due to the

actual size and activity of the tracer particle, whose trajectory was published, not being presented) (Chang *et al.*, 2011).

For the work presented in this chapter, the tracer particles were activated *via* the direct labelling technique using a cyclotron beam as described by Fan *et al.* (2006). The activated particles were initially between 1180 and 1700 μm in diameter due to practical handling considerations (Fan *et al.*, 2006). Smaller tracers were created *via* breakage of the initial large particle, followed by screening and selection as detailed by Boucher *et al.* (2014). The cyclone apparatus consisted of a two-inch diameter Salter hydrocyclone (SC224-P) (shown in Figure 4.10). The total height of the hydrocyclone was 375 mm; the apex and vortex diameters were 9.4 and 14 mm respectively; and the tangential feed inlet was rectangular, 12 x 5 mm in size. For simplicity, a single tracer particle in water was used rather than a dense slurry. Prior to adding the tracer, the system was operated until the pressure stabilised at 30 PSI by adjusting the bypass valve. A closed system allows for the tracer particle to be re-circulated multiple times over its lifetime, which then develops an average flow pattern. In this case, the particle only recirculated three times through the cyclone before breaking into smaller fragments. This is well below the typical 30 minutes plus data acquisition time in most PEPT applications.

Figure 4.10: The two-inch hydrocyclone inside the modular camera assembly (overflow piping removed for picture clarity).

The trajectory of a -212+106 µm diameter quartz particle, with an activity of 3.7×10^{-1} MBq, is shown in Figure 4.11b. A tracking rate of 2540 Hz was achieved using the parameters of $N = 250$, $f = 50$ and $S = 250$. These parameters were chosen based upon the average speed of the tracer particle, which was approximately 1.5 m·s^{-1}. In a hydrocyclone, the cut-size defines the particle diameter at which the particle has a 50 % chance of reporting to the underflow or overflow. In this case, the size of the quartz tracer was above the cut-size of the two-inch hydrocyclone (cut-size ~ 10 µm), *i.e.*, under the experimental conditions the tracer particle should report to the underflow. This trajectory clearly shows the spiralling motion of a particle caught in the outer vortex of the cyclone and, as expected, exiting out the underflow. For comparison, a previous trajectory of a similar sized quartz tracer, published by Radman *et al.* (2014), showed very little detail of the particles trajectory (Figure 4.11a). The activity of the tracer particle was not reported, however the *track* code parameters were $N = 10$, $f = 0.05$ and $S = 1$ (these parameters were not optimised and therefore could have affected the quality of the reported trajectory). This figure shows the clear improvement in the PEPT scientific method and technology over recent years, in particular the higher sensitivity of the more modern ECAT951 detectors; improved data acquisition electronics; and the flexibility of the modular camera design (Leadbeater and Parker, 2009; Leadbeater and Parker, 2011; Leadbeater *et al.*, 2011; Parker *et al.*, 2009). While the improvement is substantial, there is still some deficiencies in the track. The feed and apex zones are not clearly defined as they are at the extremities of the field of view of the camera, where less radiation is captured. A larger field of view would allow the complete trajectory through the cyclone to be captured. Alternatively, simply shifting the cyclone up or down, to center the feed or apex in the field of view, would allow the behaviour in either of these regions to be focused upon.
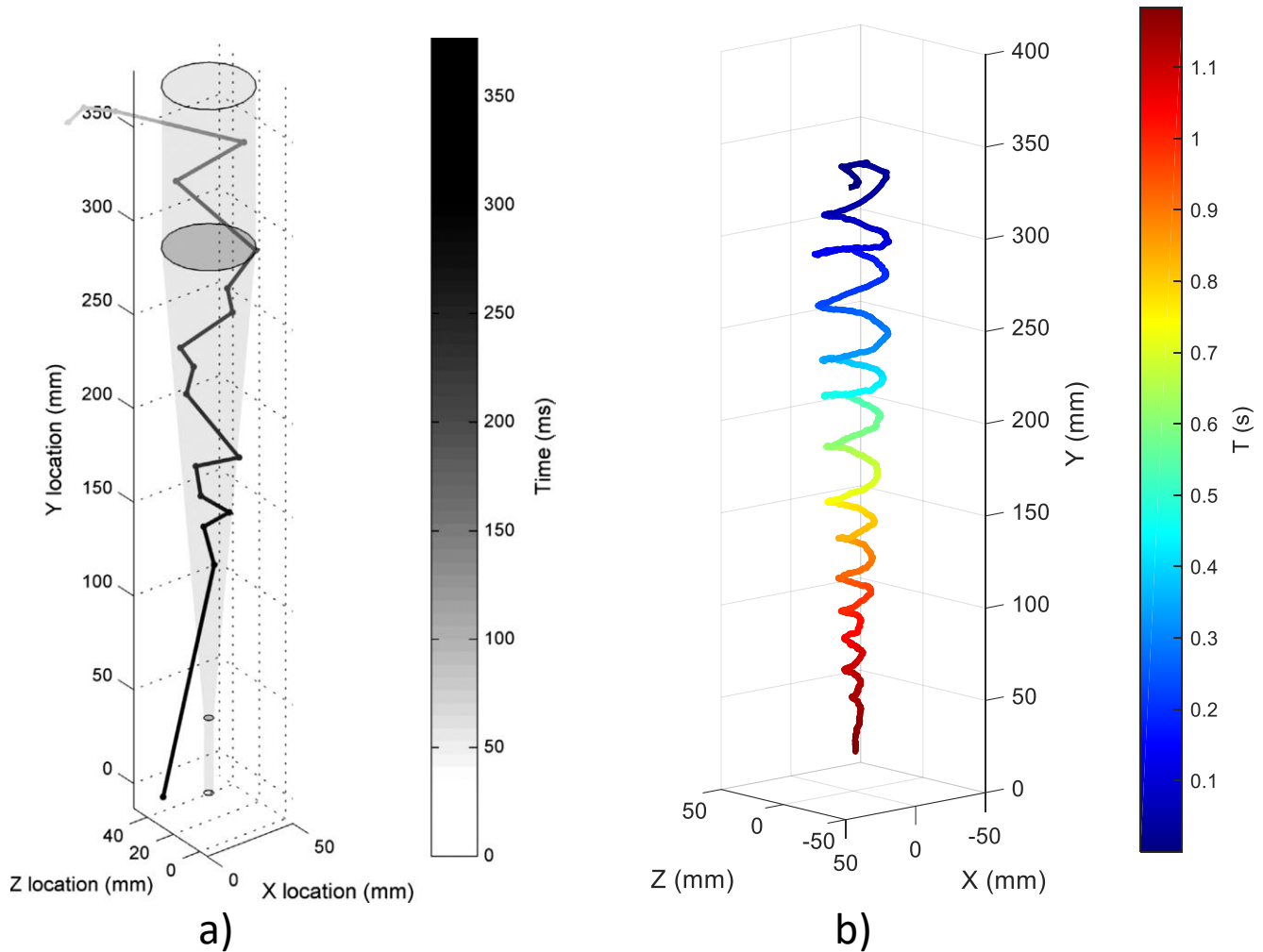
Figure 4.11: Comparison of (a) a previous track in a hydrocyclone (Radman *et al.*, 2014), to (b) the track of a -212+106 µm quartz mineral tracer completed in the modular assembly.

4.5.2 Flotation track

Another application of the cross pattern modular assembly was to capture the behaviour of mineral particles within an operating lab-scale flotation cell. Boucher *et al.* (2017) were able to use directly activated mineral tracers, both hydrophobic and hydrophilic, to study the particulate flow patterns within a 142 mm diameter mechanical flotation cell. This was the first time that particles with real bulk mineral properties and surface chemistry were tracked in a flotation cell at a size range typically seen in industrial flotation cells. Although the single trajectories of a tracer particle can be of interest, it is often more informative to convert the trajectory data into time averaged flow fields (Morrison *et al.*, 2016). This can only be achieved after a sufficient amount of experimental data has been acquired, and is possible using curve fitting and binning, as described in detail by

126

Morrison *et al.* (2016). This is a current limitation in process units such as the hydrocyclone, however, for flotation this practice is standard. Figure 4.12 displays the velocity magnitudes and flow field of a -106+90 µm diameter quartz particle in the flotation cell (Boucher *et al.*, 2017). These results, obtained from a fitted trajectory of the raw data points, show the typical double recirculation pattern (above and below the impeller) seen in cylindrical mixing containers, and can be used to validate theoretical modelling to within the experimental error. The activity of the particle was between $4.0 \times 10^{-3} - 3.7 \times 10^{-2}$ MBq (due to reasons discussed earlier), resulting in a three dimensional error, in the case of the tracer moving at the impeller speed, of approximately 12.6 mm. For the region of low speed outside of the impeller region, the error was approximately 9.5 mm. While this number seems relatively large, when compared to the 2 mm bin size, this error represents the error of the raw data. The fit, reported by Boucher *et al.* (2017), was applied to the constrained trajectory data and the three dimensional location error was lowered to 8.5 mm for a tracer speed of 0.33 m·s^{-1}. This is primarily due to the reduction of noise in the fitted data when measured against the raw data obtained from the track code. This process was also completed for the higher speed tracer (1.34 m·s^{-1}), at the same activity range, however the resultant error was not significantly different from the location error of the raw data. This is most likely due to the dominance of the error due to the under estimation of the curvature (more apparent at high tracer speeds) compared to the error from scatter or noise. More work is needed in optimising trajectory fits, as this could further reduce the measured location error and give more confidence in PEPT tracking. The effect of bin averaging could also be tested to determine if errors can be further reduced.
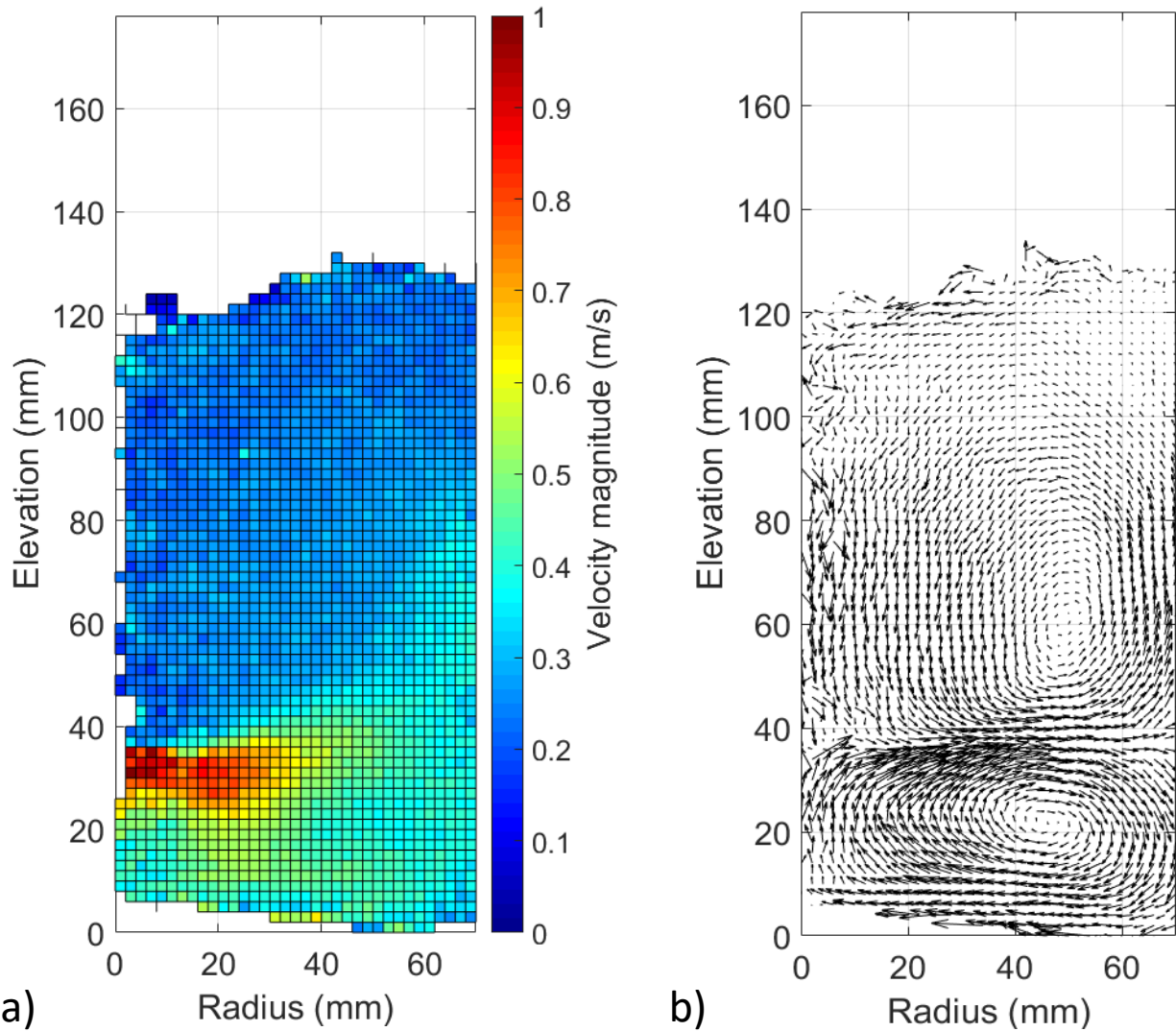
Figure 4.12: Velocity magnitude (a) and field (b) for a -106+90 µm directly activated quartz tracer inside of a mechanical flotation cell. Reproduced with permission from Boucher *et al.* (2017).

4.6   Conclusions

This chapter describes the successful assembly, and performance analysis, of a new PEPT modular detector system made up of 16 ECAT951 detectors. The high coverage of detectors in a small region meant a large percentage of emitted radiation can be captured, producing very high tracking rates when compared to similar experiments in other detector systems. A comprehensive error analysis method was developed to ensure the best combinations of *N*, *f* and *S* were used to determine a moving particles location with a minimum error. The three dimensional location error for stationary particles was constant for all tracer activities tested, with a value of approximately 0.54 mm. For moving particles, the location error, based off a comparison to a known trajectory,

was highest for low activity levels and high speeds and was shown to be unrelated to that of the stationary tracers of the same activity level. Error ranged from 4.3 mm to 27.8 mm at the highest tracer speed tested (~ 4 m·s^{-1}) depending on the activity (4.0×10^{-3} - 3.3×10^{0} MBq). The corresponding location rates ranged from ~2,000 Hz to ~ 20,000 Hz for the same tracer activity range.

With the use of this new modular assembly, a substantial improvement was seen in the recorded trajectory of a -212+106 µm quartz tracer travelling within a two-inch hydrocyclone. As only a few single passes could be recorded, more improvement is required to develop particle velocity fields. Another application of this camera arrangement was the production of populated velocity fields for -106+90 µm mineral tracers in a 142 mm mechanical flotation cell, possible due to the longer tracer residence time in the cell. This work extends the capabilities of PEPT in the study of real mineral particles to under 500 µm in size, travelling at speeds over 1 m·s^{-1}, which has previously been limited by the low activity of small tracers (< 500 µm) created *via* direct activation.

In the future, analysis of location error of new modular systems should be carried out using a tracer moving in a known trajectory in all three dimensions. This would allow for errors in all axes to be calculated without bias. As well as speed and activity, various amplitudes would also ensure absolute confidence in the reported error for a range of particle trajectories. An alternative to the *track* code used in this work would also be beneficial as it would reduce the time needed to optimise the input parameters for each tracer speed and activity and open new data treatment possibilities.

4.7   Acknowledgments

4.8   References

Bailey, D.L., Townsend, D.W., Valk, P.E., Maisey, M.N., 2006. Positron Emission Tomography: Basic Sciences. Springer.

Bickell, M., Buffler, A., Govender, I., Parker, D.J., 2012. A new line density tracking algorithm for PEPT and its application to multiple tracers. Nuclear Instruments and Methods in Physics Research Section A: Accelerators, Spectrometers, Detectors and Associated Equipment 682, 36-41.

Boucher, D., Deng, Z., Leadbeater, T., Langlois, R., Waters, K.E., 2016. Observation of iron ore beneficiation within a spiral concentrator by positron emission particle tracking of large (Ø=1440 μm) and small (Ø=58 μm) hematite and quartz tracers. Chemical Engineering Science 140, 217-232.

Boucher, D., Deng, Z., Leadbeater, T.W., Langlois, R., Renaud, M., Waters, K.E., 2014. PEPT studies of heavy particle flow within a spiral concentrator. Minerals Engineering 62, 120-128.

Boucher, D., Jordens, A., Sovechles, J., Langlois, R., Leadbeater, T.W., Rowson, N.A., Cilliers, J.J., Waters, K.E., 2017. Direct mineral tracer activation in positron emission particle tracking of a flotation cell. Minerals Engineering 100, 155-165.

Chang, Y.F., Ilea, C.G., Aasen, Ø.L., Hoffmann, A.C., 2011. Particle flow in a hydrocyclone investigated by positron emission particle tracking. Chemical Engineering Science 66, 4203–4211.

Charlton, M., Humberston, J.W., 2000. Positron Physics. Cambridge University Press, Cambridge, UK.

Chiti, F., Bakalis, S., Bujalski, W., Barigou, M., Eaglesham, A., Nienow, A.W., 2011. Using positron emission particle tracking (PEPT) to study the turbulent flow in a baffled vessel agitated by a Rushton turbine: Improving data treatment and validation. Chemical Engineering Research and Design 89, 1947-1960.

Cole, K., Buffler, A., Cilliers, J.J., Govender, I., Heng, J.Y.Y., Liu, C., Parker, D.J., Shah, U.V., van Heerdend, M., Fan, X., 2014. A surface coating method to modify tracers for positron emission particle tracking (PEPT) measurements of froth flotation. Powder Technology 263, 26-30.

Cole, K.E., Buffler, A., Meulen, N.P.v.d., Cilliers, J.J., Franzidis, J.-P., Govender, I., Liu, C., van Heerden, M.R., 2012. Positron emission particle tracking measurements with 50 micron tracers. Chemical Engineering Science 75, 235-242.

Fan, X., Parker, D.J., Smith, M.D., 2006. Labelling a single particle for positron emission particle tracking using direct activation and ion-exchange techniques Nuclear Instruments and Methods in Physics Research Section A: Accelerators, Spectrometers Detectors and Associated Equipment 562, 345-350.

García-Triñanes, P., Seville, J., Boissière, B., Ansart, R., Leadbeater, T., Parker, D., 2016. Hydrodynamics and particle motion in upward flowing dense particle suspensions: Application in solar receivers. Chemical Engineering Science 146, 346-356.

Guida, A., Fan, X., Parker, D.J., Nienow, A.W., Barigou, M., 2009. Positron emission particle tracking in a mechanically agitated solid–liquid suspension of coarse particles. Chemical Engineering Research and Design 87, 421-429.

Jayasundara, C.T., Yang, R.Y., Guo, B.Y., Yu, A.B., Govender, I., Mainza, A., van der Westhuizen, A., Rubenstein, J., 2011. CFD–DEM modelling of particle flow in IsaMills – Comparison between simulations and PEPT measurements. Minerals Engineering 24, 181-187.

Laverman, J.A., Fan, X., Ingram, A., van Sint Annaland, M., Parker, D.J., Seville, J.P.K., Kuipers, J.A.M., 2012. Experimental study on the influence of bed material on the scaling of solids circulation patterns in 3D bubbling gas–solid fluidized beds of glass and polyethylene using positron emission particle tracking. Powder Technology 224, 297-305.

Leadbeater, T.W., Parker, D.J., 2009. A high speed PC-based data acquisition and control system for positron imaging. Nuclear Instruments and Methods in Physics Research Section A: Accelerators, Spectrometers, Detectors and Associated Equipment 604, 355-358.

Leadbeater, T.W., Parker, D.J., 2011. A modular positron camera for the study of industrial processes. Nuclear Instruments and Methods in Physics Research Section A: Accelerators, Spectrometers, Detectors and Associated Equipment 652, 646-649.

Leadbeater, T.W., Parker, D.J., Gargiuli, J., 2011. Characterization of the latest Birmingham modular positron camera. Measurement Science and Technology 22, 104017 (104019pp).

Leadbeater, T.W., Parker, D.J., Gargiuli, J., 2012. Positron imaging systems for studying particulate, granular and multiphase flows. Particuology 10, 146-153.

Morrison, A.J., Govender, I., Mainza, A.N., Parker, D.J., 2016. The shape and behaviour of a granular bed in a rotating drum using Eulerian flow fields obtained from PEPT. Chemical Engineering Science 152, 186-198.

Parker, D.J., Broadbent, C.J., Fowles, P., Hawkesworth, M.R., McNeil, P., 1993. Positron emission particle tracking - a technique for studying flow within engineering equipment. Nuclear Instruments and Methods in Physics Research Section A: Accelerators, Spectrometers Detectors and Associated Equipment 326, 592-607.

Parker, D.J., Forster, R.N., Fowles, P., Takhar, P.S., 2002. Positron emission particle tracking using the new Birmingham positron camera. Nuclear Instruments and Methods in Physics Research Section A: Accelerators, Spectrometers Detectors and Associated Equipment 477, 540-545.

Parker, D.J., Leadbeater, T.W., Fan, X., Hausard, M.N., Ingram, A., Yang, Z., 2009. Positron emission particle tracking using a modular positron camera. Nuclear Instruments and Methods in Physics Research A 604, 339-342.

Radman, J.R., Langlois, R., Leadbeater, T.W., Finch, J., Rowson, N., Waters, K., 2014. Particle flow visualization in quartz slurry inside a hydrocyclone using the positron emission particle tracking technique. Minerals Engineering 62, 142-145.

Volkwyn, T.S., Buffler, A., Govender, I., Franzidis, J.-P., Morrison, A.J., Odo, A., van der Meulen, N.P., Vermeulen, C., 2011. Studies of the effect of tracer activity on time-averaged positron emission particle tracking measurements on tumbling mills at PEPT Cape Town. Minerals Engineering 24, 261-266.

Wiggins, C., Santos, R., Ruggles, A., 2016. A novel clustering approach to positron emission particle tracking. Nuclear Instruments and Methods in Physics Research Section A: Accelerators, Spectrometers, Detectors and Associated Equipment 811, 18-24.

Linking Paragraph between Chapter 4 and Chapter 5

Chapter 4 detailed the performance of the cross-pattern camera assembly. Results indicated that the trajectories of tracers with an activity greater than 0.37 MBq can be accurately determined at speeds up to 4 m·s^{-1}. This led to the primary goal of this work, which was the measurement of the trajectories of real mineral tracers inside of a hydrocyclone. The data processing technique and final velocity profiles are presented in the following chapter. As results from previous studies on PEPT in the hydrocyclone have been insufficiently detailed, it was imperative to study the location error of the new camera system to ensure confidence in the measured trajectories. Tracers with an activity below 0.37 MBq were not studied as the measured location error was too large to ensure an accurate trajectory was determined. Without this error analysis, and the associated optimum process parameters, it would be impossible to obtain meaningful data from any trajectories within the hydrocyclone. This is highlighted in Section 5.4.1, which outlines the differences in trajectories when using various *track* code input parameters. A comparison between the ADAC Forte camera and the modular camera assembly is also included in Chapter 5, which demonstrates the step change in performance achieved in this work. The Matlab script that was used to produce the results found in Chapter 5 can be found in Appendix B.3.

Chapter 5: Improvements in Positron Emission Particle within a Hydrocyclone

5.1   Abstract

Current understanding of the particulate flow within a hydrocyclone is limited. Computational modelling aims to alleviate this problem; however, validation of particle flow is also limited. Due to the opacity of slurries, visual or laser diffraction techniques are only able to measure particle velocities in flows with low solids concentrations (< 1 % w/w), which are not consistent with industrial conditions. Positron Emission Particle Tracking (PEPT) is a technique that allows for a radioactive particle to be tracked through the triangulation of the emitted gamma rays, therefore no optical observation is required. The high particle velocities within the hydrocyclone fall outside of the typical dynamic range studied by PEPT, which has hitherto limited PEPT experimentation. The implementation of a modular positron camera design allowed for the creation of a highly sensitive field of view, necessary for the tracking of high speed, low activity tracers. This cross-pattern assembly allowed for the capture of highly detailed particle trajectories within the hydrocyclone for particle sizes down to the 106-212 μm size range, a large improvement when compared with previous studies (Chang *et al.*, 2011; Radman *et al.*, 2014). Results show that repeatable velocity fields can be produced, which is the first time a velocity profile has been reported for the hydrocyclone using the PEPT technique.

5.2   Introduction

The hydrocyclone is a continuously operating classifying device that separates particles based on their size, shape and density. The first patent for a hydrocyclone can be traced back to the late nineteenth century, however it was not until the 1940s that it gained wide spread use in industry (Aldrich, 2015). The simple design, low cost, easy operation, and low maintenance of hydrocyclones, when compared to other classification equipment, has made them a popular selection for the separation of solids and liquids. Hydrocyclones are currently used in a number of mineral processing applications, with their main use being in closed circuit grinding. This role is critical for circuits that involve a concentration stage, as it controls both the feed size to the concentration stage (effecting the concentration efficiency) and the amount of material sent back for further grinding (effecting energy usage). Therefore, the separation efficiency of the

hydrocyclone can have a large impact on plant performance. Other uses of hydrocyclones include desliming, liquid clarification, degritting, and thickening operations.

In a hydrocyclone, slurry enters through a tangential feed inlet, creating a vortex in the stationary body with a low-pressure zone along the vertical axis. The particles are subjected to two opposing forces: an 'outward' acting inertial force, and an opposing inwardly-acting drag force provided by the carrying fluid. Separation occurs in the radial direction, with larger, denser material migrating to the outer wall of the hydrocyclone chamber, while the smaller, less dense material moves toward the low-pressure zone of the inner axis (Wills and Finch, 2016). Flow in the cyclone is characterised by two vortices that flow in opposite directions. The feed is initially forced downward due to the extension of the vortex finder into the feed zone, creating the primary downward vortex. As this flow leaves the cylindrical section of the feed zone, and enters the conical section, the increased radial restriction causes a majority of the water flow and the smaller, less dense material to invert their direction. This creates a secondary upward vortex that travels upwards towards the vortex finder. The heavier material tends to travel along the outer boundary of the primary vortex and therefore continues to travel downwards towards the underflow (Brennan *et al.*, 2007). These features are shown visually in Figure 5.1.
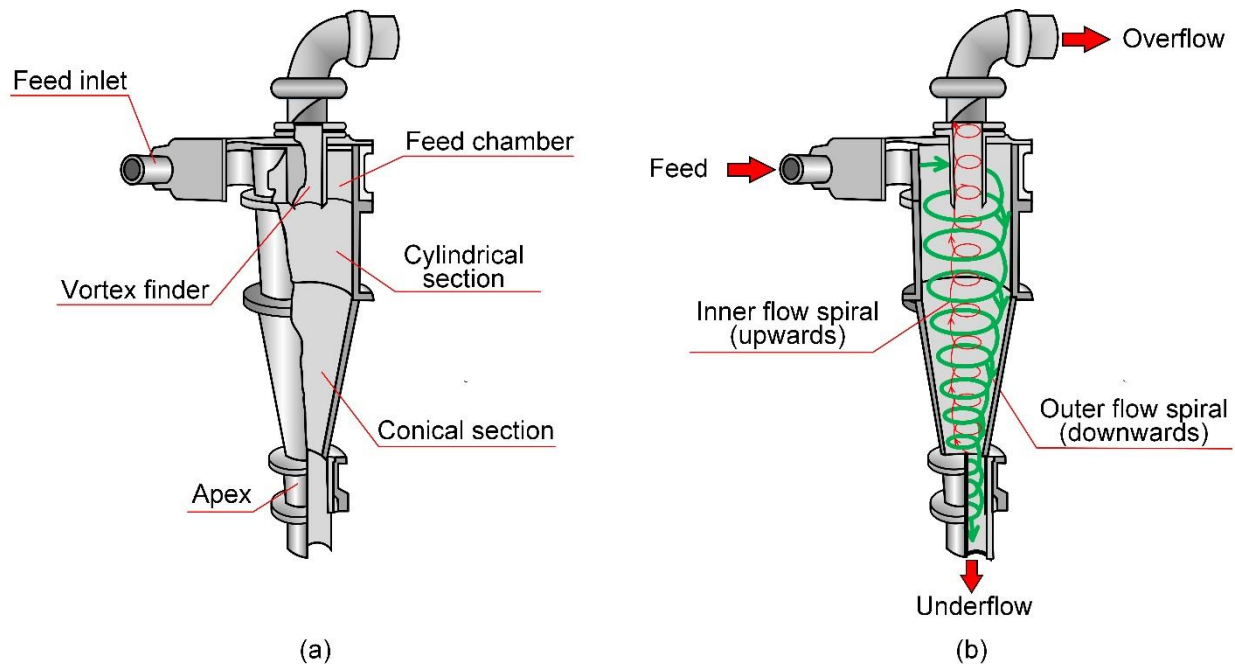
Figure 5.1: A diagram of the hydrocyclone showing: (a) the main geometric components, and (b) the formation of the double vortex flow pattern. Reproduced with permission from Wills and Finch (2016).

Mechanically hydrocyclones are simple, having no moving parts; however, their complex internal flow is highly turbulent and performance is therefore difficult to model and predict. They are typically characterised by their holistic performance, *e.g.* sharpness of separation, the overflow particle size distribution, and the overall pressure loss. Early semi-empirical models, based upon the equilibrium orbit theory (Bradley, 1965) and the residence time theory (Rietema, 1961), helped provide a fundamental understanding of key principles of how hydrocyclones work. These models were not used in industry however, as they did not incorporate the effects of all design features. More recent strictly empirical models, such as those presented by Flintoff *et al.* (1987) and Nageswararao *et al.* (2004), characterise a number of variables and are easily incorporated into spreadsheets, and so are particularly useful in process design and optimisation. This has meant that all the models commonly used in industry, for the selection of hydrocyclones, are still essentially empirical in nature. This leads to problems when extrapolating results, from the empirical test regime, to geometries or operating conditions outside the specific systems used for model development (Chen *et al.*, 2000; Kraipech *et al.*, 2006).

In recent years, the development of predictive models for the hydrocyclone, based on a more fundamental treatment of the laws governing flow, has been the goal of many researchers. With the ever increasing power of modern computers, computationally expensive techniques, such as Computational Fluid Dynamics (CFD) and discrete element method (DEM), can be used as a cost effective way to design and test a range of new hydrocyclone geometries. While these techniques provide great versatility, they are not without difficulties. The fundamental principles that these models are based on, which includes effects of turbulence; formation of the air-core; and viscosity considerations in high solids content slurry flow (which is non-Newtonian in nature), need to be subjected to thorough validation with rigorous experimental data (Marins *et al.*, 2010).

The separation mechanisms inside the hydrocyclone are governed by the three velocity components of the flow field, which in decreasing magnitude are the tangential, axial, and radial velocities (Fisher and Flack, 2002). Although complex in nature, the study of the microscopic processes inside a hydrocyclone are essential to its further development. Particle and fluid tracking techniques also provide a unique tool for the validation of computational models. The two main techniques used to study the velocity fields in the hydrocyclone are the Phase Doppler Particle Analyser (PDPA) or Laser Doppler Velocimetry (LDV) techniques; and the particle image

velocimetry (PIV) technique. PDPA and LDV use the frequency difference between the light from an illumination source (a laser) and the light scattered by moving particles to estimate velocity, whereas PIV cross-correlates consecutive photo frames.

While the PDPA and LDV methods provide average velocity fields, PIV allows for an individual particle of a dispersed phase to be tracked in space and time, *i.e.* Lagrangian tracking. By obtaining the trajectory, it can be seen how a particle reacts to, and interacts with, the flow around it under specific conditions and any local instabilities can be observed in detail (Chang *et al.*, 2011). Wang *et al.* (2016) reviewed the measurement of the three velocity components in hydrocyclones using these techniques. The authors stated that when using PDPA or LDV, the radial velocity component was difficult to measure accurately and therefore it was often omitted. It is also extremely time consuming to develop three dimensional flow fields, using PDPA or LDV, as they are single point measurement techniques. Wang *et al.* (2016) presented a new PIV technique, using a three camera system, which allowed for the three dimensional tracking of a 100 µm particle with a spatial resolution of 2 mm.

A significant drawback to PDPA, LDV, and PIV is that they all rely on optical tracking or laser diffracting techniques, which limits the particle tracking to translucent systems. Several authors have noted this limit to be approximately 1 % solids by weight (Chu *et al.*, 2002; Fisher and Flack, 2002; Zhang *et al.*, 2011). This has restricted velocity studies to predominately small, neutrally buoyant particles to estimate the velocity fields of water.

The three-dimensional tracking of single particle flow in opaque slurries, allows for more relevant information to be captured for the validation of multiphase computational models. The positron emission particle tracking (PEPT) technique was developed at the University of Birmingham (UK) in the 1980s (Hawkesworth *et al.*, 1986; Parker *et al.*, 1993) and has been previously described in detail by Leadbeater *et al.* (2012). The technique is based on the same principles as positron emission tomography (PET), which is an imaging tool used predominantly in the medical field. PEPT differs from PET by tracking an individual particle labelled with a positron emitting radionuclide. The gamma-radiation emitted from the positron source can penetrate a considerable amount of material, allowing for the detailed study of opaque systems.

In PEPT, the tracer particle is labelled with proton rich isotopes, which rapidly decay *via* positive beta emission (emitting positrons). Annihilation of each positron occurs shortly after, producing two γ rays (511 keV each) which are constrained to have equal and opposite momenta and are therefore emitted back to back (180° ± 0.5°) (Charlton and Humberston, 2000). Simultaneous (coincident) detection of both gamma photons defines a Line of Response (LoR) along the photon trajectory. After a number of LoRs have been recorded, an iterative triangulation algorithm is used to remove corrupt events and calculate the point which minimises the distance to all the remaining lines. This point is assumed to be the location of the tracer at that specific time. This process is described in detail by Parker *et al.* (1993).

The PEPT technique has been applied to a range of unit operations. In mineral processing, particle behaviour in tumbling (Govender *et al.*, 2013) and stirred mills (Jayasundara *et al.*, 2011), flotation cells (Boucher *et al.*, 2017; Waters *et al.*, 2008), spirals (Boucher *et al.*, 2014; Boucher *et al.*, 2016) and hydrocyclones (Chang *et al.*, 2011; Radman *et al.*, 2014) have all been investigated using PEPT. Typically, unit operations that involve residence times over 10 seconds; operate with particle sizes over 1 mm (allowing for more active tracers); or have particle speeds less than 1 m·s^{-1} are more suited to PEPT. These conditions allow for the production of time averaged, well populated flow fields. Under optimum conditions, PEPT can track a particle moving at 1 m·s^{-1} with up to 1000 locations per second and a three dimensional location precision of approximately 1 mm. The work presented here has conditions far from the quoted optimum operating regime (Leadbeater *et al.*, 2012).

Trajectories obtained from low activity tracers (0.37 MBq) moving at high speeds (> 4 m·s^{-1}) is currently at the boundaries of the PEPT technique's capabilities, with the accuracy and precision of these trajectories needing stringent validation *via* a location error analysis. This has limited hydrocyclone tracking to single passes of radiochemically produced synthetic tracer particles (0.7 mm) or large (2 mm) real mineral tracer particles produced *via* direction radiation. To date there have not been any published velocity profiles for the hydrocyclone using PEPT.

This chapter expands on current PEPT practices by studying the flow of high speed, low activity tracer particles. A comparison between an ADAC Forte PET scanner (Parker *et al.*, 2002) and a customised modular camera assembly was conducted to determine whether the increased density of detector heads and their proximity to the equipment would allow for accurate trajectories to be

recorded. The basis for the modular camera system used in this work was developed by Leadbeater (2009) Leadbeater and Parker (2011). Results include the presentation of trajectories and velocity profiles for real mineral tracer particles flowing within a two-inch hydrocyclone. All PEPT experimentation was carried out at the Positron Imaging Centre at the University of Birmingham (UK).

5.3   Experimental

5.3.1   Creation of tracer particles

The tracer particles were activated *via* the direct labelling technique using a 35 MeV ^{3}He beam, produced by the MC40 cyclotron located at the University of Birmingham, as described by Fan *et al.* (2006). Two types of materials were used for the creation of tracers: quartz mineral particles (ArcelorMittal Exploitation Minière, Canada) and synthetic glass beads. Quartz is a favourable material to study as it contains the oxygen atoms required for the production of the proton rich isotope, ^{18}F, and is the major gangue material for most mining operations. The activated quartz particles were required to initially be approximately 1 mm in diameter due to practical handling considerations, heat dissipation and beam focusing in the cyclotron (Boucher *et al.*, 2017; Fan *et al.*, 2006). As the trajectories of smaller particle sizes were desired (to achieve results closer to industrial conditions), the larger particles (once activated) were broken, followed by screening and selection as detailed by Boucher *et al.* (2014). As screens were used to separate particles, only the size classes of the tracers are known. However, as particles were chosen based upon their activity, and activity is linked to the surface area of the radiated particle, it is likely that most tracers are at the upper limit of the size range reported. Properties of the tracers used in this chapter can be found in Tables A.2.1-A.2.3 in Appendix A.2.

Direct activation was chosen over other methods, such as ion-exchange resin tracers, as this technique allows for tracer particles with the exact composition of real ore to be tracked. A down side of direct activation, however, is the weakening of the mineral tracers. This was attributed to the thermal stress the particles went through inside the cyclotron (Boucher *et al.*, 2017), where impurities in the crystalline structure could cause micro fractures. This meant the quartz particles consistently, and relatively quickly (1-10 individual recirculations), broke into multiple smaller fragments during experiments, therefore making the subsequent data collection useless. Due to the limited supply of activated particles (four per three hour cyclotron run) this greatly hampered the

amount of data collection, which is required for reliable, well populated velocity fields. As a way to improve the total acquisition time, a 1 mm glass bead was also studied. Although this could not be broken into smaller sizes, the durability of the synthetically made bead meant that more passes could be recorded per experiment.

5.3.2 Positron Cameras - ADAC Forte Camera

The ADAC Forte camera (ADAC Laboratories, USA - later acquired by Philips), described in detail by Parker *et al.* (2002), comprises of a pair of standard clinical gamma cameras operating in coincidence. Figure 5.2 displays the camera with the hydrocyclone apparatus in place. Each head consists of a sheet of thallium-doped sodium iodide scintillator (with an area of 500×400 mm^2 and thickness of 16 mm) backed by an array of 55 photomultiplier tubes. The intrinsic efficiency for detecting incident 511 keV gamma photons is approximately 23 % with raw data acquisition rates up to 100 kHz (Leadbeater and Parker, 2013). The ADAC Forte camera is well characterised and requires no auxiliary work before operating. It is therefore the standard positron camera used in most conventional PEPT imaging at the Positron Imaging Centre. However, the inflexibility of the detector restricts tracking rates in unit operations with geometries unsuited to the parallel nature of the two large detector heads. This coupled with its low intrinsic efficiency limit the ability of tracking fast, low activity tracers, with activities of approximately 3.7 MBq or below considered insufficient to produce useful trajectories (Leadbeater *et al.*, 2012). For the high speeds in the hydrocyclone, however, Radman *et al.* (2014) have shown that even tracer activities up to 1 GBq produce low quality trajectories.
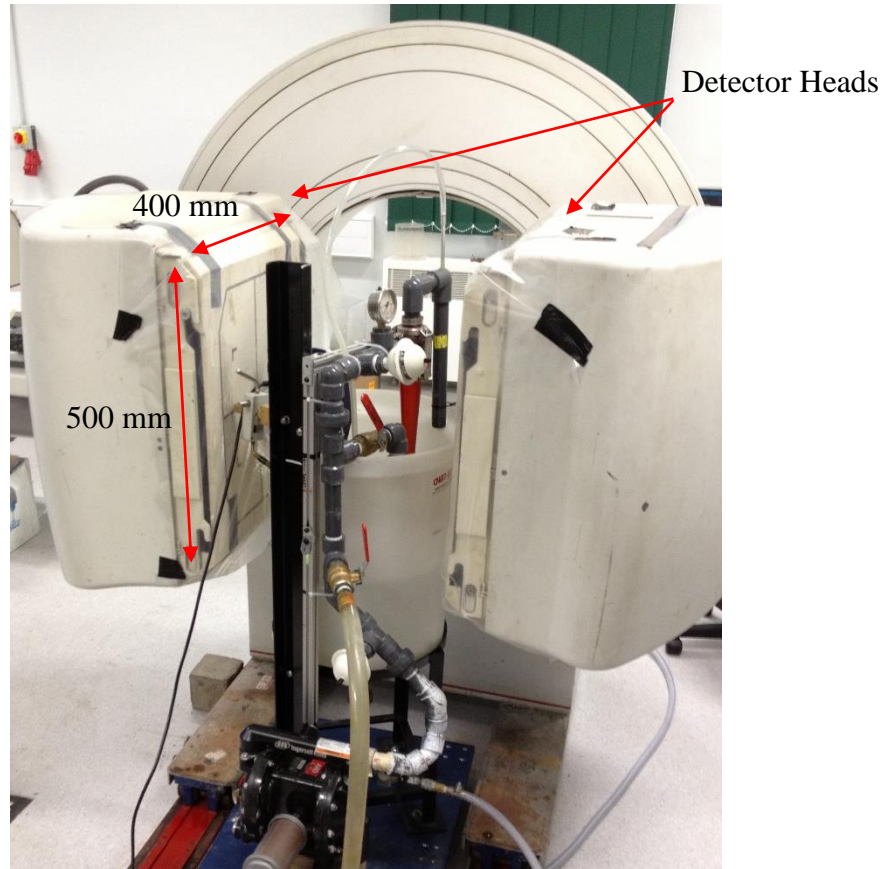
Figure 5.2: The hydrocyclone apparatus in the ADAC Forte camera.

5.3.3   *Positron Cameras - Modular detector assembly*

Recently, at the Positron Imaging Centre, a modular camera system has been developed from parts of an ECAT 951 PET scanner (Siemens, Germany), described in detail by Leadbeater and Parker (2011). The system consists of a number of detector modules which can be arranged in a custom geometry with a field of view (FOV) tailored to the specific application. Tracking small, low activity tracers, moving at high speeds requires the detection of a large percentage of the emitted radiation. Therefore, to increase sensitivity, detector blocks should be closely packed. After considering various designs, 64 detector blocks were used in a coupled cross pattern (Figure 5.3). This assembly produces a highly sensitive cylindrical FOV at the intersection of the four detector groups, which is approximately 100 mm in diameter and 390 mm in height (optimised for the hydrocyclone geometry). Before assembling the modular detector geometry, Monte Carlo simulations of the detection area were created, as per those described in Leadbeater and Parker (2013), to assess the sensitivity and uniformity of the field of view. The results of these simulations and more detail about the cross-pattern set-up is presented elsewhere (Section 4.3.2). The modular

141

detectors are also constructed with bismuth germanium oxide scintillator crystals, which has a significantly higher intrinsic efficiency (around 40%) when compared to the ADAC camera. This aids in the detection of a higher percentage of incident radiation.

| (a) | (b) |
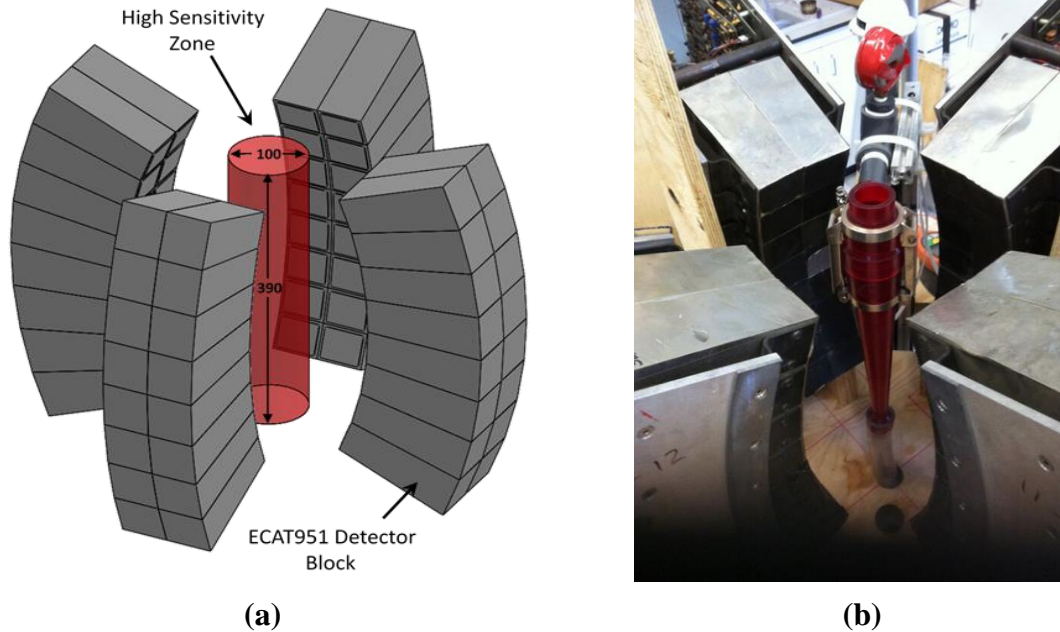
Figure 5.3: The cross pattern modular camera design showing (a) the CAD design with FOV (dimensions in mm) and (b) the two-inch hydrocyclone inside the assembly (overflow piping removed for picture clarity).

5.3.4   *Hydrocyclone apparatus and operating procedure*

The apparatus consisted of a two-inch (50.8 mm) diameter hydrocyclone (Salter Cyclones Ltd, England), a diaphragm pump, water tank and pressure gauge. A diagram of the apparatus is shown in Figure 5.4. The total height of the hydrocyclone was 350 mm; the apex and vortex diameters were 9.4 and 14 mm respectively; and the rectangular feed inlet was 12 x 5 mm in size. The size of quartz tracers were all well above the cut-size of the hydrocyclone (~10 μm), and therefore were expected to report to the underflow. Cut-size represents the size for which 50 % of the particles in the feed report to the underflow.

Prior to adding the tracer to the water tank, the system was operated until the pressure stabilised at 207 kPa. This was controlled by adjusting the bypass valve. The closed system allowed for the tracer particle to be re-circulated multiple times over its lifetime, which built up an average flow pattern. Modifications to the feed entry, pressure gauge, pump entry and exit piping, water tank and valves were required to minimise locations where the tracer could become stagnant. Even after

these modifications, however, on some occasions the particle did manage to become trapped and the system needed restarting. To simplify this process, it was decided to conduct tests of a single particle in water. While this does not utilise the main benefit of PEPT, being the observation of particle flow in opaque slurries, the main objective of this work was to explore the capabilities of PEPT tracking. Therefore, the tracking of particles in slurries was left for future studies.
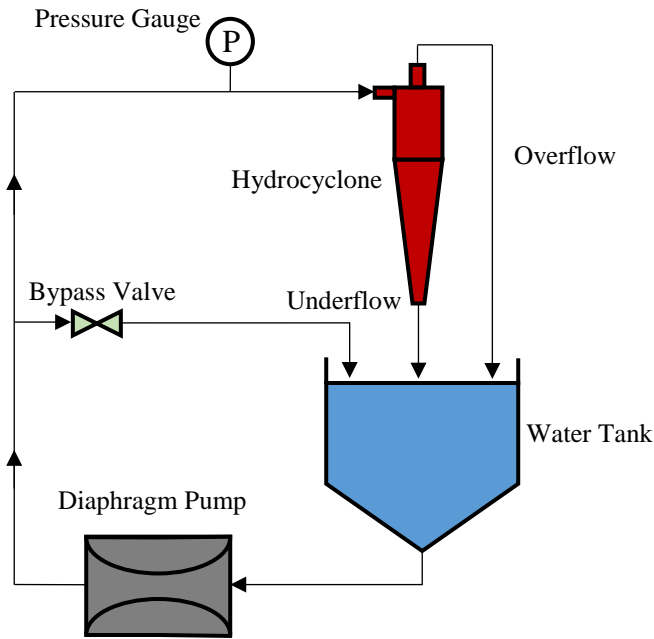
Figure 5.4: Flow diagram of the recirculating hydrocyclone set-up.

5.4   Data Processing

The PEPT technique involves a large amount of post processing to determine trajectories or velocities. The electronics of the PEPT detector system records, in real time, the x, y, z coordinates of the two detection points (detectors A and B) of the emitted gamma radiation, and the time at which this detection occurs, *i.e.* (t; x_A, y_A, z_A; x_B, y_B, z_B). These x, y, z coordinates are taken as the central position of the excited crystal elements and allow for the creation of a Line of Response (LoR) in three-dimensional space but does not determine the particle location. A schematic of the steps taken to process the raw data is shown in Figure 5.5, with detailed explanations provided below. As the process conditions within the hydrocyclone (high speeds, low activity tracers) are at the edge of current PEPT capabilities, obtaining useful data proved a significant challenge.
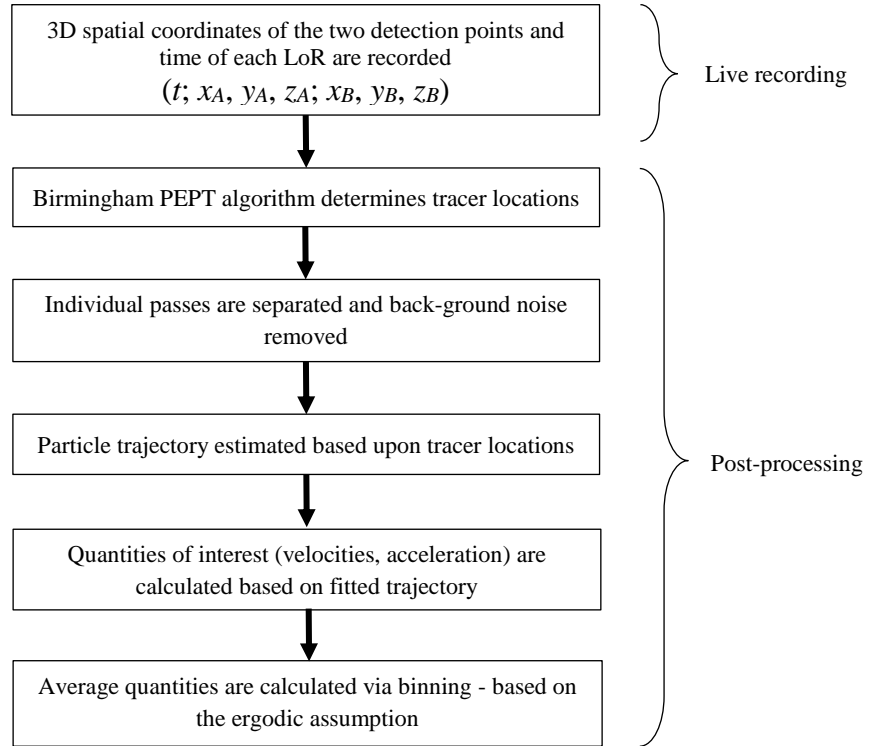
Figure 5.5: Schematic showing the steps involved in the data processing procedure under taken in this work.

5.4.1 *Determining tracer location and optimising track code parameters*

Particle locations were determined *via* the PEPT algorithm first described by Parker *et al.* (1993). This triangulation technique, hence referred to as the *track* code, is based on the premise that for a given number of chronologically recorded events, N, all LoRs should intersect at a single point in space, which is taken to be the location of the tracer. In practice, however, LoRs do not intersect perfectly since a proportion of the LoRs are corrupted by phenomena such as Compton scattering or the detection of uncorrelated gamma rays in coincidence. Therefore, a point is calculated that minimises the sum of perpendicular distances between all of the LoRs. Lines furthest from this point, considered to be corrupt, are then removed and the minimum distance point is recalculated. This iterative process continues until only a predetermined fraction of lines, f, remain. In addition to this, a third parameter, S, can be used to determine the fraction of lines that are reprocessed when calculating consecutive locations. This is beneficial when processing data of tracers travelling at high velocities or with low activities. A detailed explanation of these parameters is presented in Chapter 4.

The current implementation of the algorithm requires the user to specify *N*, *S* and *f*. These parameters have a significant effect on the locations output by the *track* code. For instance, a large value of *N* is required for statistical purposes, however, too high a number of *N* means large distances are travelled by the tracer within the group of processed LoRs, which minimises trajectory features. An example of this can be seen in Figure 5.6, which shows the difference in locations determined by various *track* code parameters for the same tracer moving within a hydrocyclone. While this is an extreme example, it does show the limitations of not knowing the optimum input parameters, as trajectories may appear to be smooth but still be incorrect. All the optimum *track* code parameters used for this work were based upon the parameters reported in Chapter 4, where the various parameters' effects on the location uncertainty for a given tracer activity and speed were studied. In the case of Figure 5.6, the values of $N = 250$, $S = 250$, and $f = 65$ gave the lowest location uncertainty as the tracer had an average speed of approximately 4 m·s^{-1} and an activity of approximately 3.7 MBq.
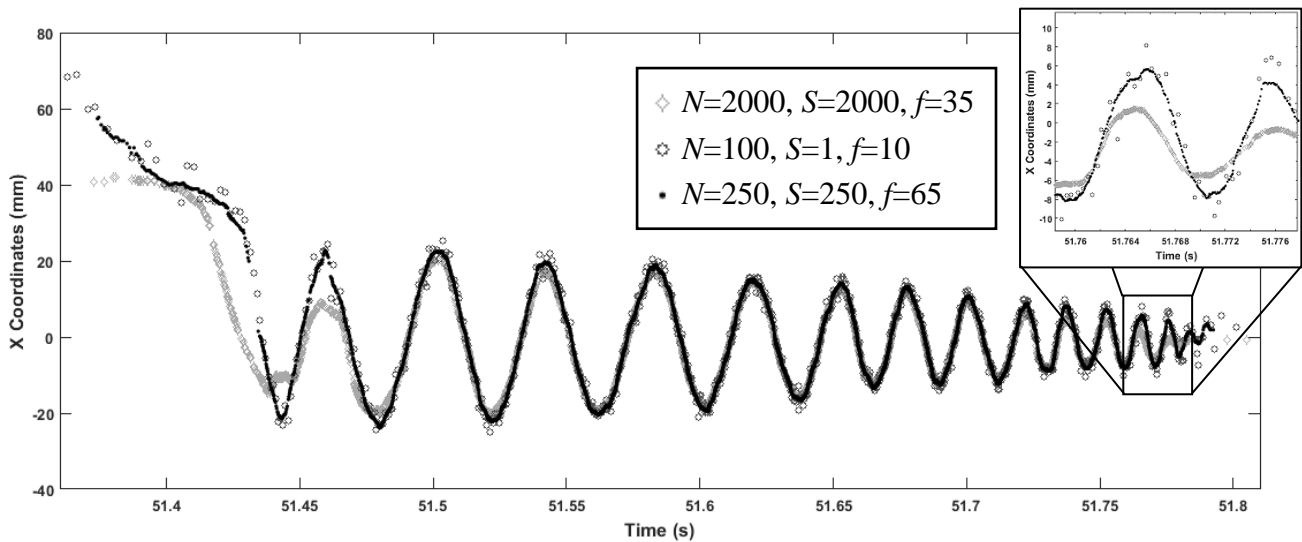
Figure 5.6: X-axis coordinates for a hydrocyclone trajectory, showing the effect of the *track* input parameters on the output locations. In this case the optimum input parameters were *N*=250, *S*=250, and *f*=65.

5.4.2 *Data Clean-up*

It was evident that in several tests there was an increased amount of background noise recorded, in comparison to other tests. An example of this is shown in Figure 5.7. This occurrence was more prevalent in longer running tests, or in tests conducted shortly after a previous test. As the water was replaced between tests, the increased noise was attributed to the contamination of the hydrocyclone itself. The high levels of abrasion known to take place within the hydrocyclone likely caused a transfer of the radiated tracer particle's surface to the walls of the cyclone. This smearing creates a dispersed field of gamma emitting sources, increasing the signal to noise ratio and therefore the difficulty in post processing. To remove the unwanted data the difference in activity between the tracer particle and the back-ground radiation was used. Location rates in the modular camera ranged from 43,000 to 4000 Hz for tracer activities of 18.9 to 0.37 MBq (represented by the 1 mm glass bead and 106-212 µm tracers respectively). Once the approximate location rate was determined for a single pass, the entirety of the test was scanned for time intervals with lower location rates and the data removed. Particle breakage also needed to be considered when processing the data. This was detected by the occurrence of low activity passes, termed *ghost passes*, or those recorded back to back (< 1 second of recirculation time).
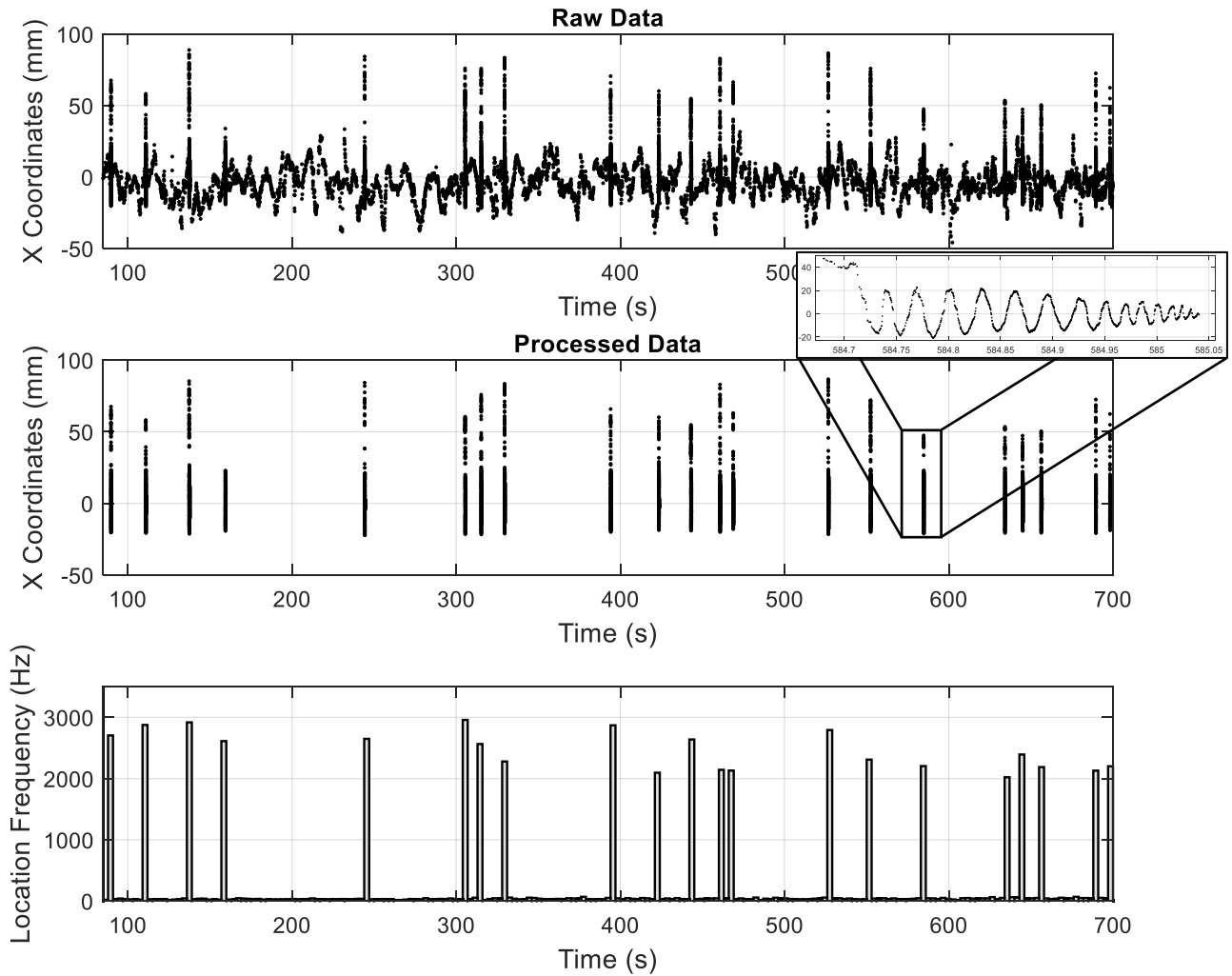
Figure 5.7: Comparison between the raw and processed data for a 106-212 µm quartz tracer. Location frequency was used to differentiate between the background noise and the signal.

5.4.3 Trajectory Smoothing Technique

When processing data obtained from a low activity tracer, the measured locations will contain a large amount of variability, as the number of LoRs used per location must be small. This situation is particularly relevant for tracers moving at high speeds, and in the case of the hydrocyclone speeds are often above 3 m·s^{-1}. For a particular tracer activity and speed, there will be an associated three-dimensional location uncertainty represented by an ellipsoid (which is spherical when all dimensional uncertainties are equal). For a trajectory, this uncertainty represents a cylinder wrapped around the measured tracer trajectory (Boucher *et al.*, 2017). The true trajectory of the particle can theoretically be anywhere inside of this cylinder. Therefore, the data smoothing or

147

fitting technique should aim to maintain the low frequency behaviour of the trajectory, while removing the high frequency features which fall within the undetectable limit of the positron cameras. This may remove small scale motion caused by turbulence or particle collisions, which is of interest. However, due the spatial resolution of the camera, these features are currently indistinguishable from the fluctuations caused by location uncertainty.

In this work, individual runs were first separated and then a smoothing function was applied to each axis independently. The fit used was the smoothing splines function inside of Matlab©. The smoothing spline s, which is a piecewise third order polynomial, is constructed by minimising the function shown in Equation 5.1. This is referred to as a Tikhonov regularisation and aims to minimise both the residual error and the complexity of the solution, which is represented by the roughness or the intensity of fluctuations (Forney and Rothman, 2012).

$$p \sum_i w_i \big(y_i - s(x_i)\big)^2 + (1-p) \int \left(\frac{d^2 s}{dx^2}\right)^2 dx \qquad \textbf{Equation 5.1}$$

In Equation 5.1, the positional data points in the X, Y or Z axes are represented by y_i and their corresponding time is represented by x_i. The relative weights of each location can be specified by w_i. As the sensitivity of the modular camera varies, the recorded location rate in different regions of the FOV also changes. In order to standardise the fit across the entire pass, a weighting function was used to equalise the relative significance of each time domain. This meant that locations obtained at lower location rates were given higher weights to ensure that the fit did not incorrectly smooth trajectory features. The comparative influence of the residuals and roughness is controlled by the smoothing parameter p, which is defined between 0 and 1. When $p=0$ a least-squares straight-line fit is produced, while $p=1$ produces a cubic spline interpolant. The value of p used for all data sets was 0.999999, which was concluded to effectively balance the residual error (keeping it within the measured location error) and smooth any unrealistic variations in trajectory. An example of this process can be seen in Figure 5.8. The smoothing equation was discretised using the same location rate as the initial data set and the corresponding velocities for each location were calculated using the respective equation's derivative.
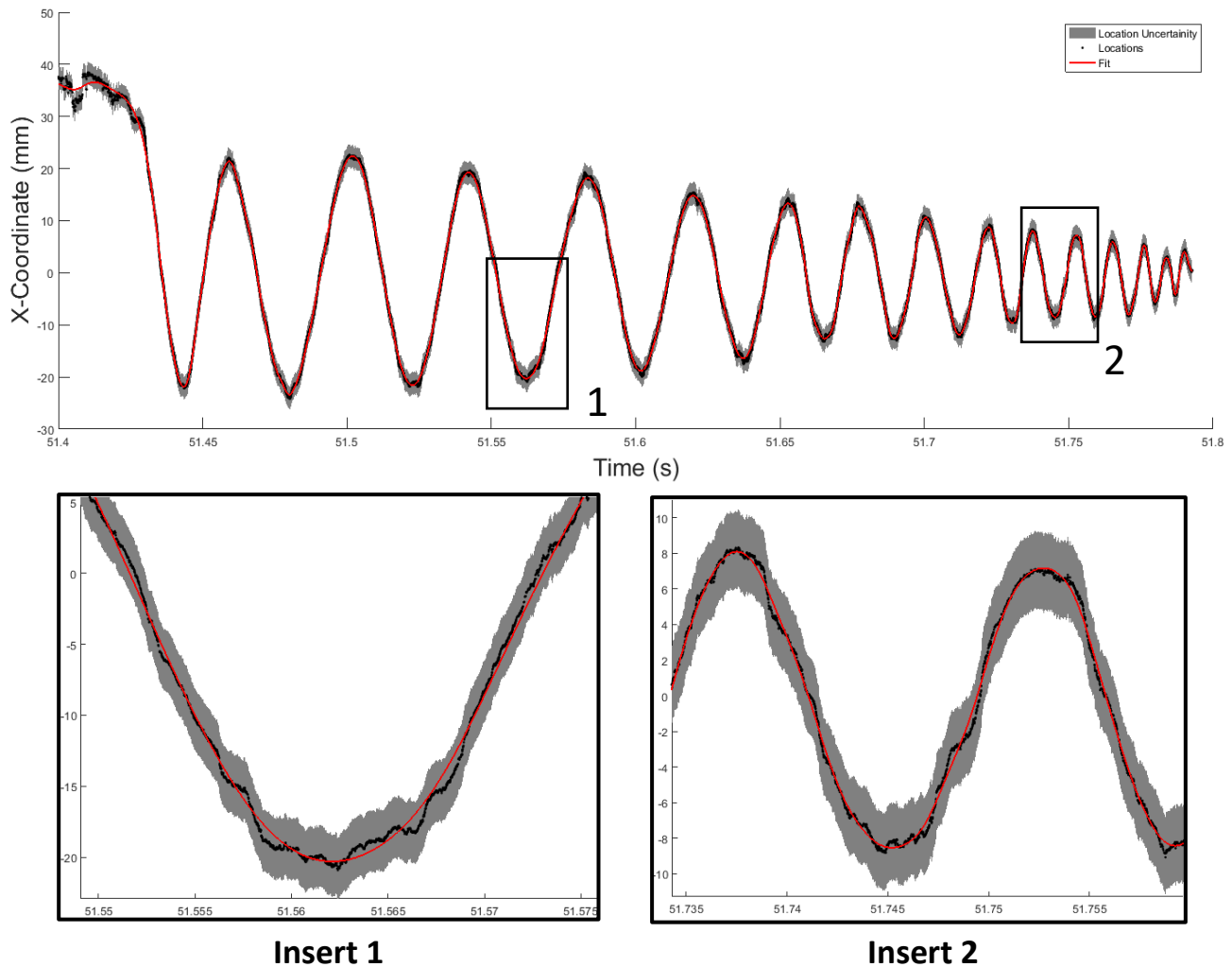
Figure 5.8: Smoothing of the raw data set for a single pass of a 355-500 μm quartz tracer in the hydrocyclone. The greyed region represents the average location uncertainty detailed in Chapter 4 (equal to one standard deviation).

5.4.4 *Averaged Quantities – Lagrangian to Eulerian particle tracking*

Single trajectories, while they can provide some useful information, are hard to compare quantitatively with other data types. To allow for comparison with data from computational models, the end objective of this work, velocity fields are a more useful metric. It is therefore necessary to convert the data from the Lagrangian reference frame of single passes, to the fixed Eulerian reference frame. This is achieved through the ergodic assumption: that a single particle's behaviour, over a length of time, is representative of the behaviour of all particles with the same properties (size, shape, density, *etc.*). In other words, a tracked particle will exhibit all possible

combinations of position, momentum, *etc.* if recorded for a sufficiently long period of time (Morrison *et al.*, 2016). Therefore, the measured properties of a given discrete volume, termed voxel, represents the proportional behaviour of any particle, of the same type, in that zone (assuming statistical relevance).

One issue with the hydrocyclone results is the likelihood of obtaining a sufficiently large quantity of data points in each voxel, which is needed to obtain acceptable accuracy (Leadbeater *et al.*, 2012). There is a limited number of passes for each experiment due to particle breakage and contamination of the hydrocyclone itself. To compensate for this, the volume of the hydrocyclone was divided by using a 2 mm by 2 mm grid rotated around the central axis, as seen in Figure 5.9. Therefore, each two-dimensional pixel in the velocity profiles, represents an annular prism centred at the vertical axis of the hydrocyclone. Locations, once converted into cylindrical coordinates, are grouped into their corresponding voxels and their velocities can then be calculated and averaged. The size of the particle, compared to the cut-size, ensures its location is predominately at the outer perimeter of the hydrocyclone. While this helps improve the location density in the measured regions, this limits the particle velocity fields to a small volume space.

This method assumes that a particle's behaviour is a function of the particle's distance from the centre axis of the hydrocyclone, and its vertical position within the hydrocyclone. To test this assumption the distribution of velocities in each voxel were studied. It was determined that a majority of the voxels exhibited a Gaussian distribution, with some examples shown in Figure 5.9. This indicated that each voxel is accurately represented by the mean and standard deviation profiles, as seen in Figure 5.9. The high standard deviation in some voxels in the feed zone, which coincided with non-Gaussian distributions, was due to the asymmetrical variances caused by the feed inlet. However, for simplicity these imperfections were ignored.
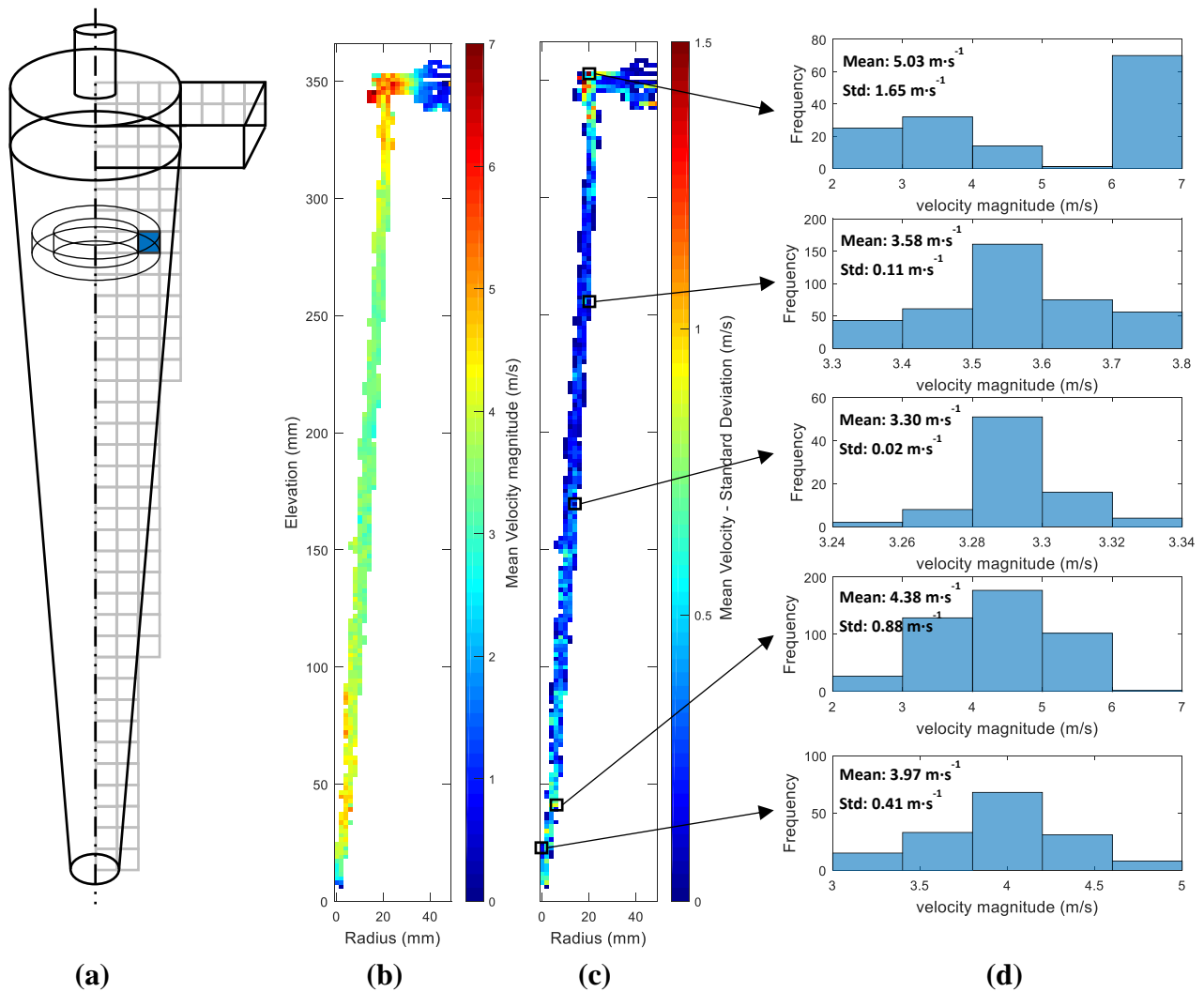
Figure 5.9: (a) Schematic of the 2 mm by 2 mm toroid bins used for creating the averaged velocity profiles; (b) the mean velocity magnitude and (c) standard deviation profiles for a 355-500 μm quartz tracer particle; and (d) examples of the velocity distributions within the voxels.

5.5   Results and Discussion

5.5.1   *Comparison of ADAC and Modular Cameras*

Figure 5.10, Figure 5.11 and Figure 5.12 display a direct comparison between trajectories obtained from the ADAC Forte camera (Figure 5.10 and Figure 5.11) and the cross-pattern modular assembly (Figure 5.12). Figure 5.10 and Figure 5.12 show a comparison of two tracers with a similar activity, while Figure 5.11 and Figure 5.12 compare the recorded locations of a 1 mm glass bead tracer in each camera. The most obvious difference is the large increase in location rate when using the modular camera (from 400 Hz in the ADAC to 120 000 Hz in the modular). A particles radial position within a hydrocyclone is an essential parameter when determining its behaviour, as it will determine both its classifying outlet and its general path within the cyclone. It is therefore critical to obtain a large number of locations so that the radial path of the tracer can be determined accurately. This is even more relevant for the underflow area, where small changes in radial position should lead to vastly different vertical velocities, as the conical constriction causes particles to recirculate upward. It is clear that the trajectories measured in the ADAC Forte camera lack the location rate required to produce accurate velocity profiles. This is more apparent at the two extremities of the hydrocyclone, where it is impossible to determine the likely trajectory.

Another important factor to consider is the reduced location precision in the secondary horizontal axis, represented by the Z-axis in this case. The ADAC Forte Camera is unable to obtain equal tracking accuracy in both planes due to the parallel nature of the two detector heads. The radius of the spiralling particle appears to grow to a maximum at the middle of the cyclone before reducing again, which does not conform to the expected trajectory. This anomaly is due to the increased sensitivity at the middle of the detector FOV, meaning more LoRs are obtained and a more accurate trajectory is recorded. This lack of accuracy in the Z-axis effects the calculation of three dimensional trajectories, as well as radial and angular velocities. The cross-pattern modular camera therefore has a distinct advantage, as it allows for equal tracking in both horizontal axes.
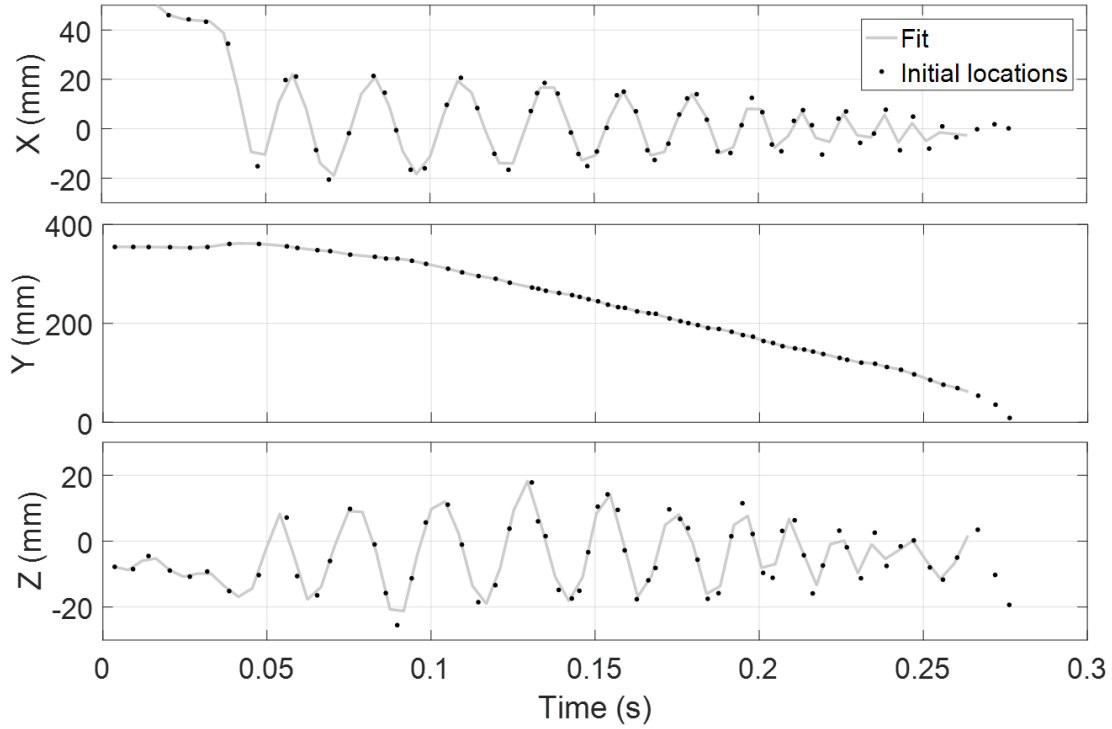
Figure 5.10: Location coordinates as a function of time for a 500-600 μm quartz particle in the ADAC Forte camera. Tracer activity was measured as 21.5 MBq, which led to a location rate of 240 Hz.
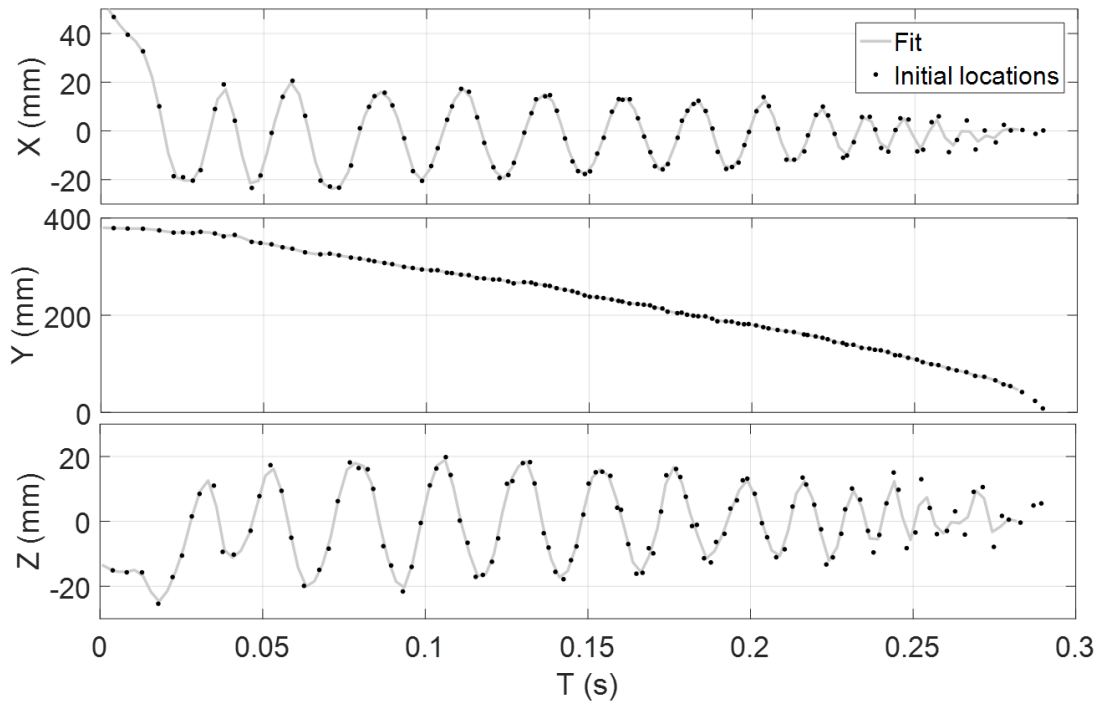
Figure 5.11: Location coordinates as a function of time for a 1 mm glass bead quartz particle in the ADAC Forte camera. Tracer activity was measured as 48.8 MBq, which led to a location rate of 410 Hz.
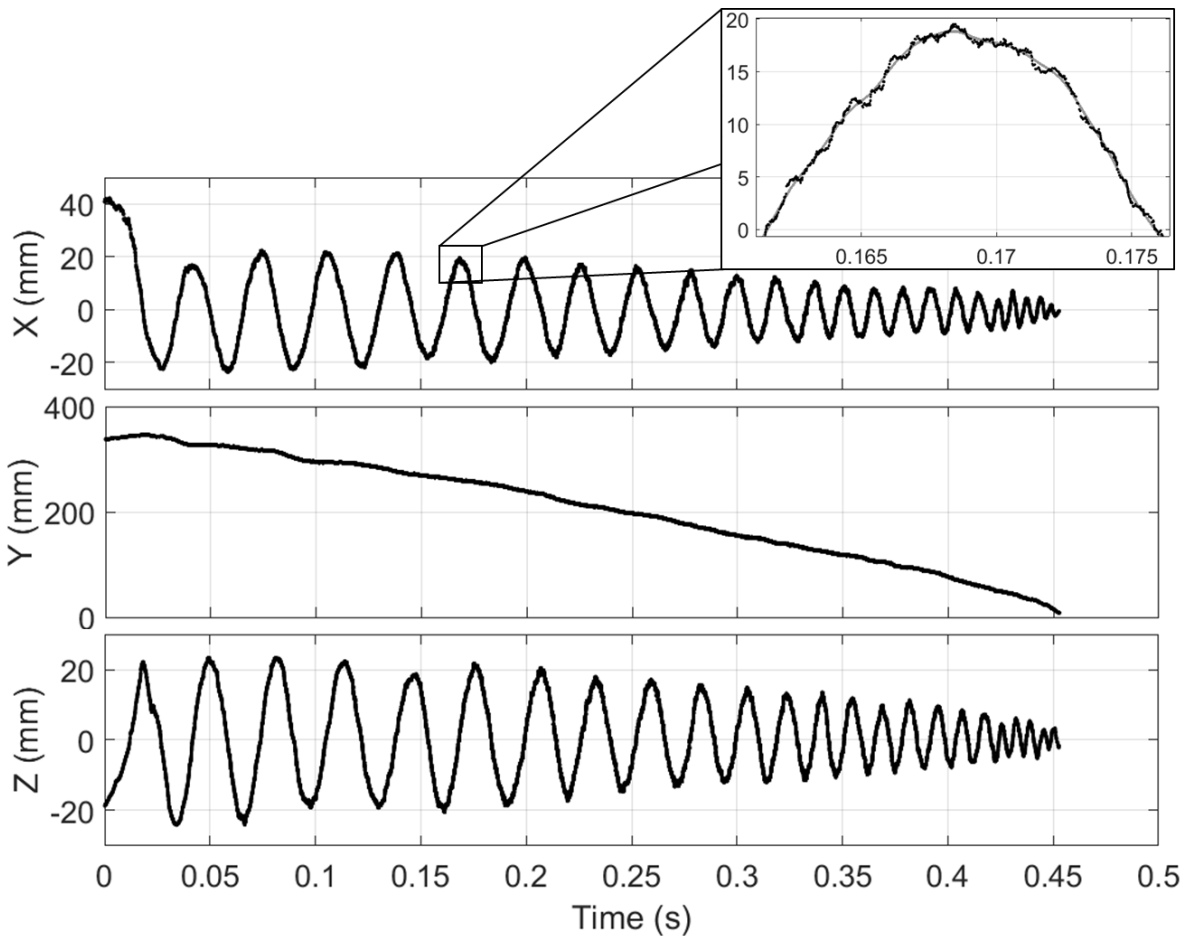
Figure 5.12: Location coordinates as a function of time for a 1 mm glass bead in the Cross-pattern modular camera. Tracer activity was measured as 18.9 MBq, which led to a location rate of 120 000 Hz.

5.5.2 *Three dimensional trajectories*

Figure 5.13 displays three dimensional trajectories, coloured by velocity, for a 106-212 µm quartz particle, 355-500 µm quartz particle, and 1 mm glass bead. These trajectories are based upon the filtered and fitted locations, not the raw data. The trajectories show the typical swirling motion associated with the hydrocyclone (Figure 5.1). The glass bead has a much larger number of revolutions inside the hydrocyclone, which corresponds to a longer residence time when compared to the real mineral tracers (0.44 s compared to 0.36 s). This counters the theoretical assumption that a larger particle will have a smaller residence time. The high activity of the glass bead tracer meant that only a single run could be recorded before the noise caused by erosion occurred, and so no meaningful conclusions can be made.
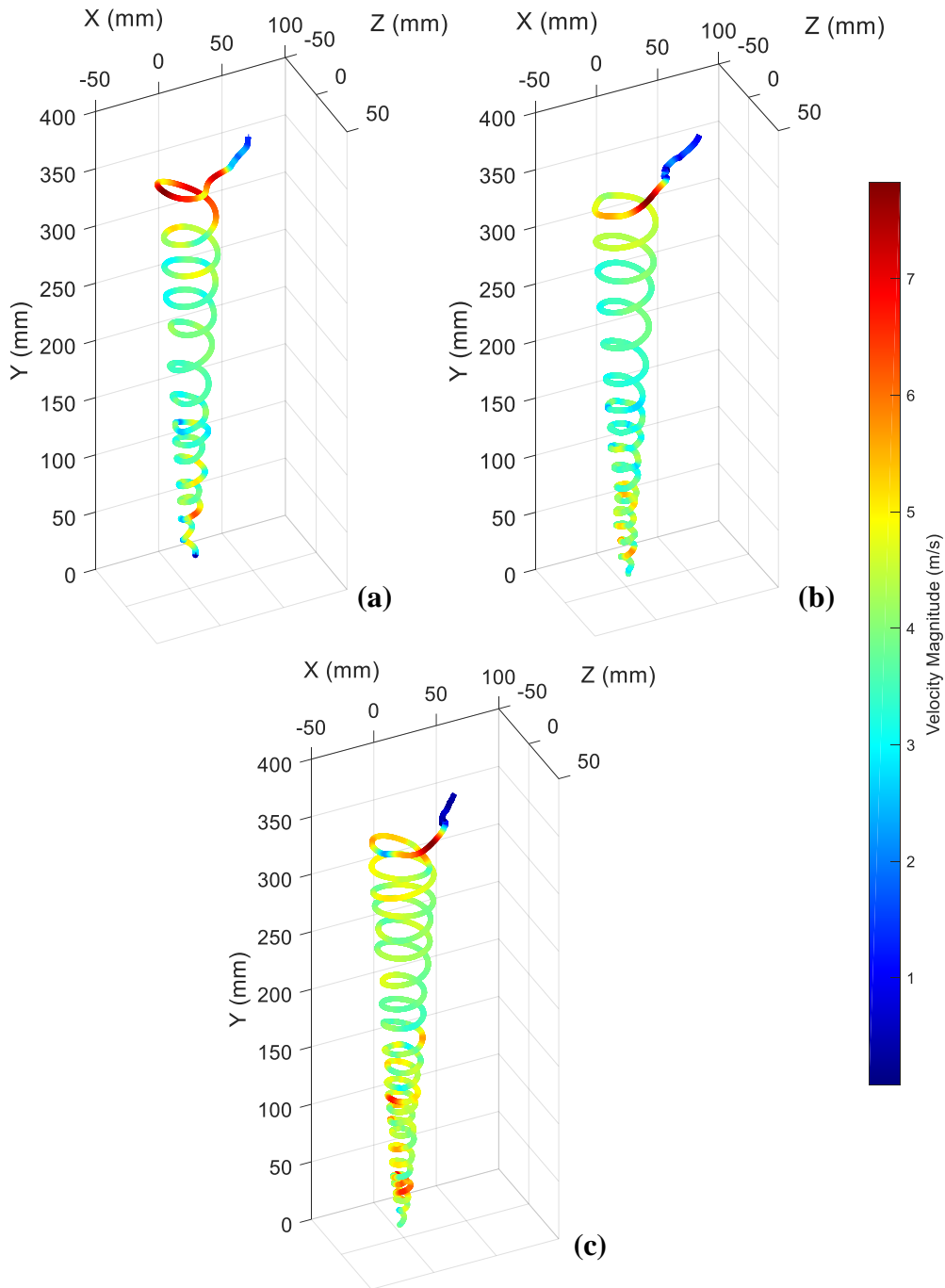
Figure 5.13: Single 3D trajectories for a (a) 106-212 µm quartz particle; (b) a 355-500 µm quartz particle; and (c) a 1 mm glass bead tracer all coloured by velocity magnitude.

5.5.3 *Velocity Profiles*

Figure 5.14 displays the mean velocity magnitude for five separate 355-500 µm quartz tracers. The results from the five experiments are shown to illustrate the repeatability of the velocity measurements. Run 3 varies significantly from the remaining four runs, likely due to the lower

location rate (10 500 Hz) compared to the other runs (> 21 300 Hz). Therefore, the average velocity field was calculated based upon the data collected in Runs 1, 2, 4 and 5. The velocity field displays the typical behaviour of a particle within a hydrocyclone. Initially, in the feed pipe, the particle moves slowly (1 m·s^{-1}) but accelerates significantly in the constriction of the feed zone, up to speeds of 7 m·s^{-1}. The particle slowly decelerates and then reaches a constant speed through a majority of the cyclone body.
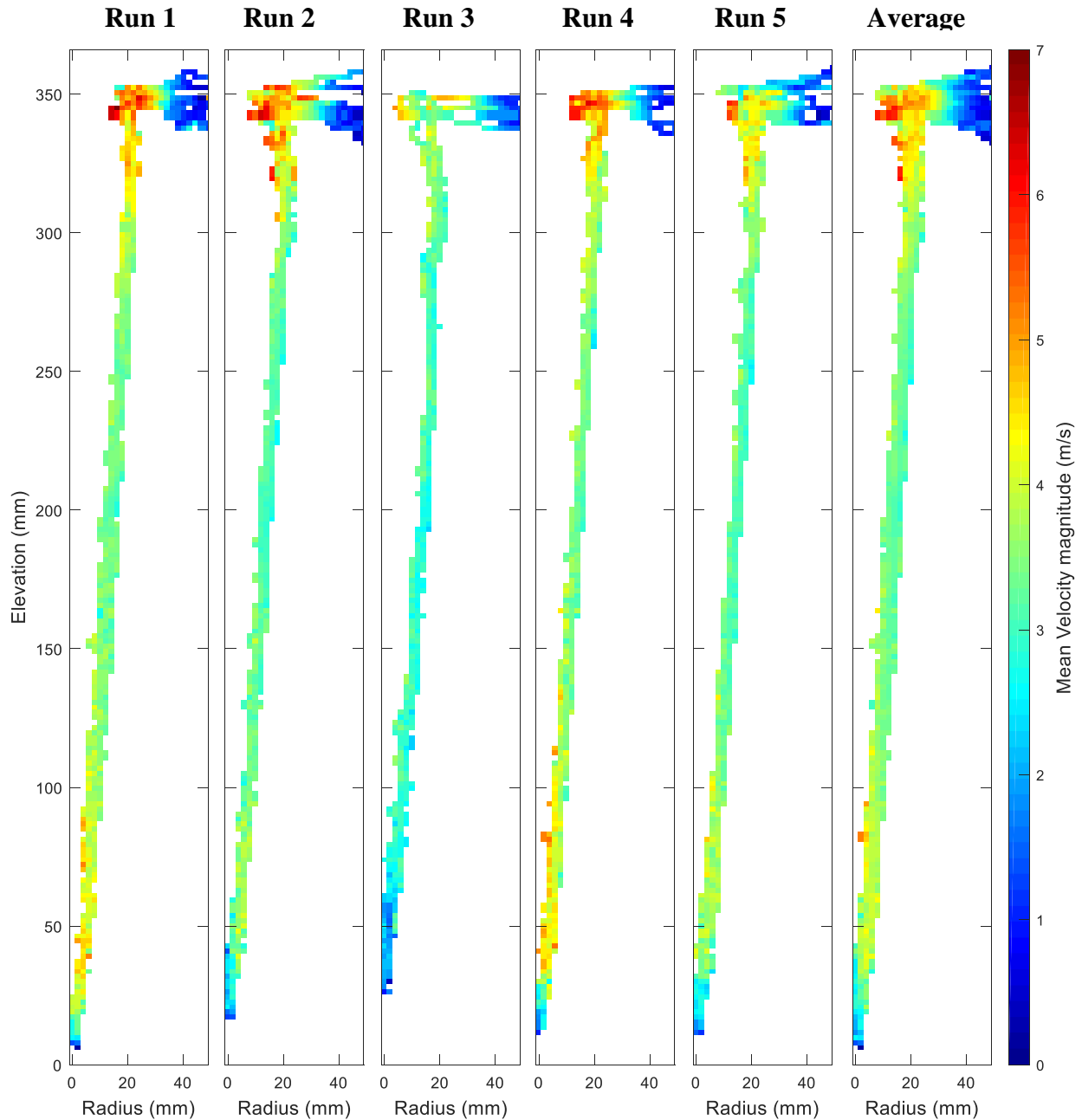
Figure 5.14: Velocity profiles for a 355-500 µm quartz particle inside the hydrocyclone.

Figure 5.15 displays the various other properties of the particle trajectories for all combined runs of the 355-500 µm tracers (excluding Run 3). This includes the calculated standard deviation of the mean velocity magnitude; the average number of locations per voxel in each separate run; and the mean radial, vertical and angular velocities. The same repeatability was observed for all velocity components and therefore only the averaged fields are shown. The calculated standard deviation was lower in the middle of the hydrocyclone where the sensitivity of the modular camera is at its highest and there were a large number of recorded locations. The feed and underflow zone had the highest standard deviation as these zones were at the extremities of the camera's FOV, which is shown in the lower number of locations per voxel. These zones are also more turbulent and therefore may not be properly represented in an averaged velocity field. Both the radial and vertical velocity remains consistent throughout the hydrocyclone suggesting that the flow in the outer wall region is relatively smooth in nature. As expected the angular velocity increases as the particle travels towards the centre of the hydrocyclone, as seen in the conical restriction.

Figure 5.16 and Figure 5.17 shows the same properties for four 106-212 µm tracer particles. In this case, the results from Run 4 were removed from the averaging process. The difference in the measured velocity profile was again attributed to the tracer's low activity (see Table A.2.2 in Appendix A.2). The overall lower activity when compared to the 355-500 µm tracers meant that the location uncertainty is higher (7.51 mm compared to 4.33 mm). This in turn led to an increased standard deviation and a greater variance in the measured locations. In terms of the measured velocity, the 106-212 µm tracers displayed a similar behaviour and magnitude to the 355-500 particles, showing a constant radial and vertical velocity with and increasing angular velocity when moving inward. The results from the three velocity components, namely the tangential, axial and radial velocities are all similar in magnitude to those reported by Wang *et al.* (2016). As previously mentioned, the authors reported the velocities of a 100 µm particle (specific density of 1.6) captured inside of a 35 mm hydrocyclone, which is similar to the conditions of this work. The measured radial velocity varied between –0.63 m·s^{-1} (inward) and 0.51 m·s^{-1} (outward); the axial velocity in the outer wall region varied between –0.47 and -1.0 m·s^{-1} (downward); and the tangential velocity ranged from 2 to 4 m·s^{-1}. These ranges correspond closely with the velocities displayed in Figure 5.15 and Figure 5.17, which further validates PEPT as a technique for the measurement of particle velocities within the hydrocyclone as well as the data processing procedure outlined in this work.
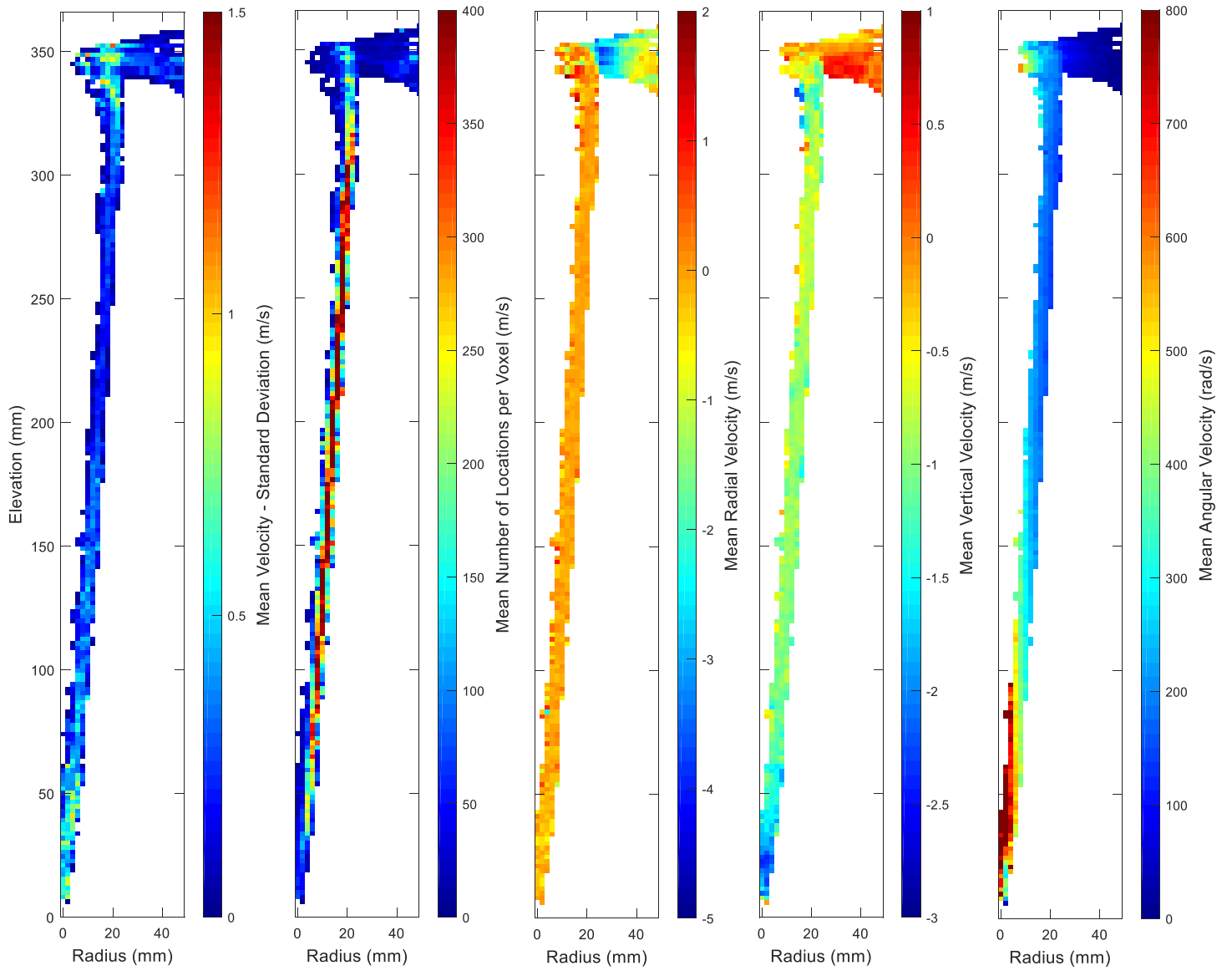
Figure 5.15: The standard deviation, mean number of locations per voxel, and the radial, vertical and angular velocities for a 355-500 µm tracer particle inside the hydrocyclone.
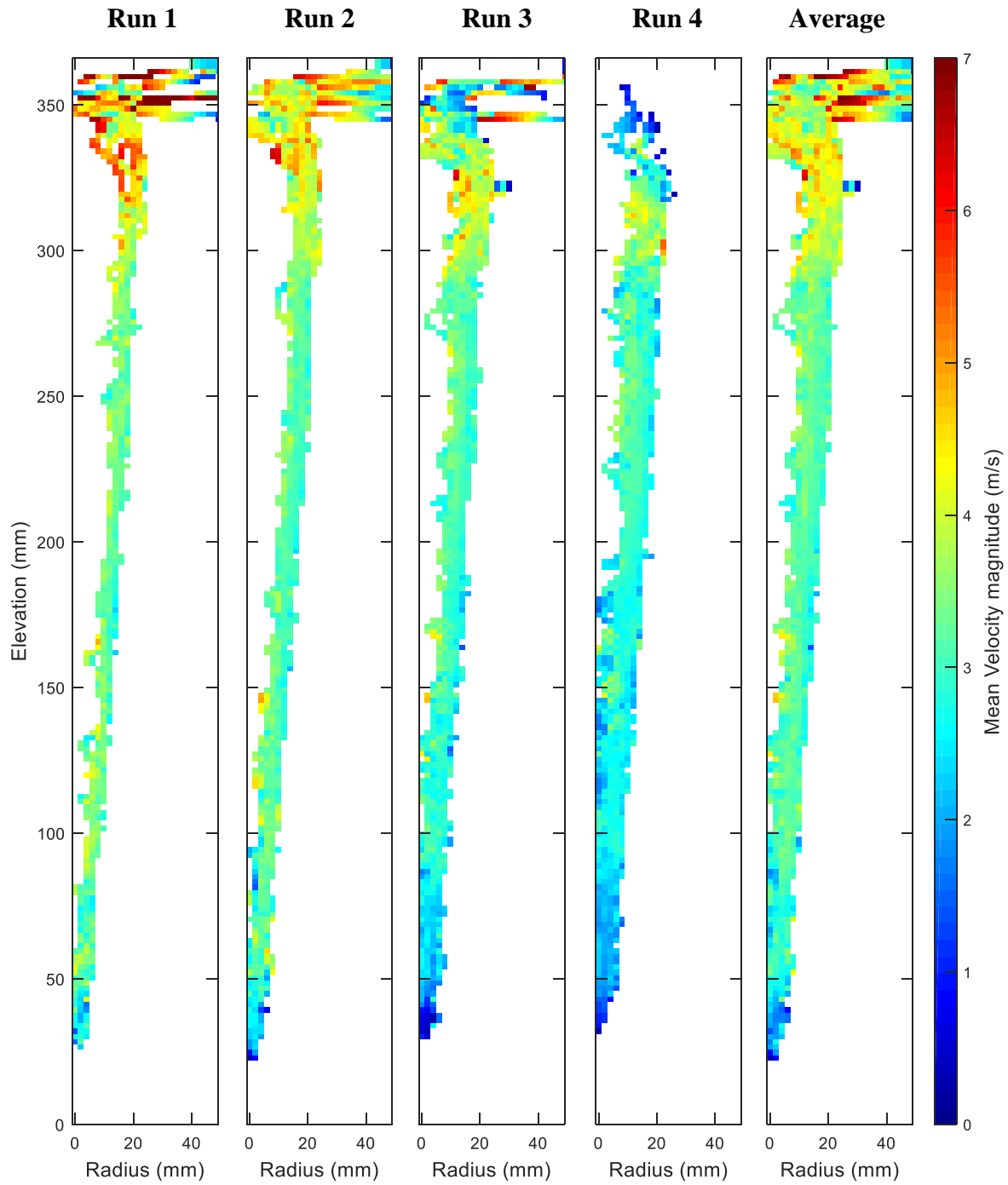
Figure 5.16: Velocity profiles for a 106-212 µm quartz particle inside the hydrocyclone.
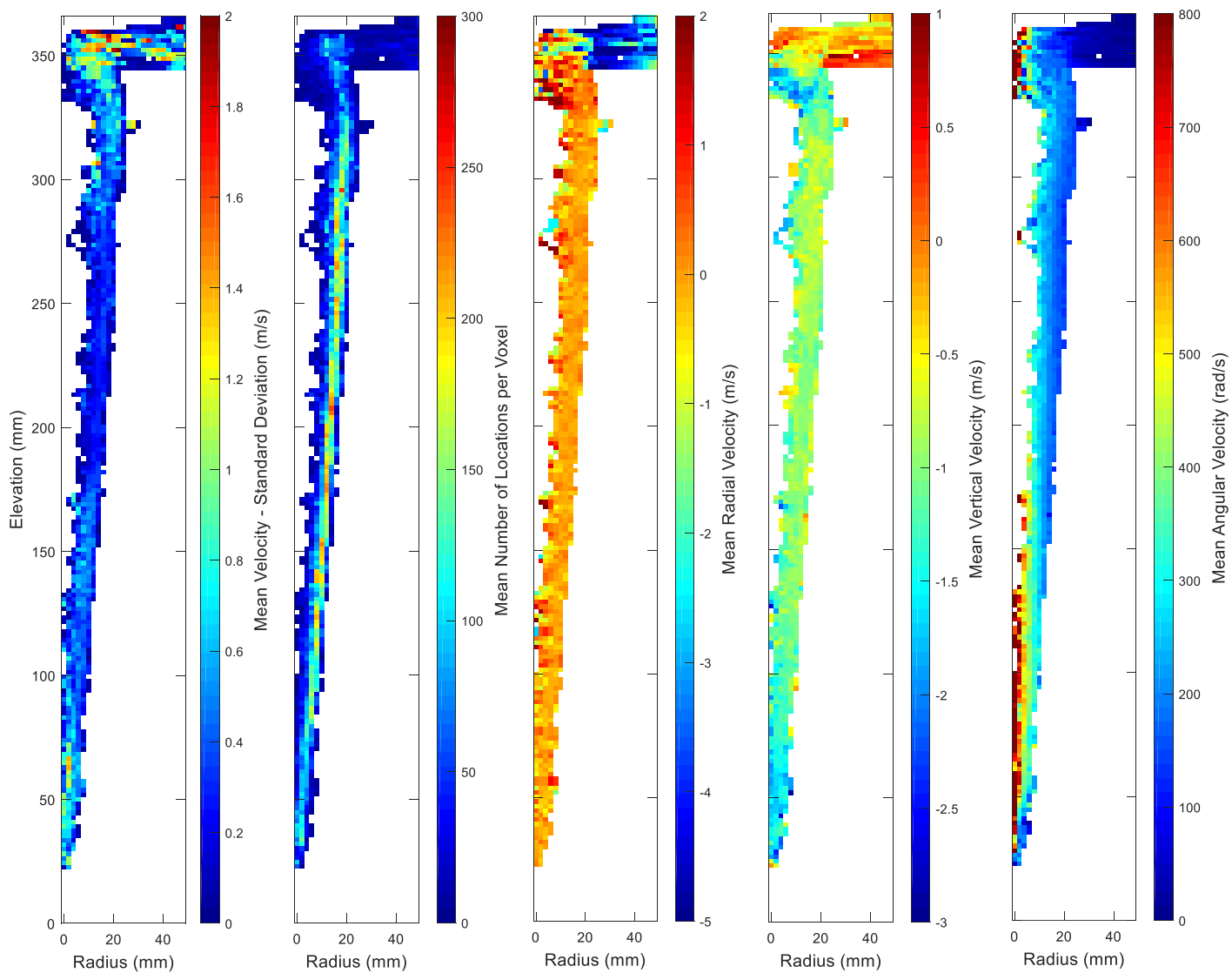
Figure 5.17: The standard deviation, mean number of locations per voxel, and the radial, vertical and angular velocities for a 106-212 µm tracer particle inside the hydrocyclone.

5.6   Conclusions

The tracking of mineral particles in opaque flows through PEPT represents a significant but worthwhile challenge. Obtaining particle velocity profiles, at conditions close to industrial operation, is critical for the future development and validation of computational models. The sensitivity of the ADAC Forte camera has been shown to be too low for the tracking of low activity (<50 MBq) particles travelling at speeds over 3 ms^{-1}. The cross-pattern modular camera represents a step change in tracking performance for low activity, high speed tracers inside the hydrocyclone. This improvement in trajectory quality allowed for the calculation of velocity profiles, a first for

160

the hydrocyclone using the PEPT technique. Tracking of particles down to 106-212 µm was also possible, a significant improvement on trajectories previously published. Future testing will aim to study particle flow in hydrocyclones operating with high solid content slurries, while also trying to study particle sizes close to the cut-size of the chosen hydrocyclone. It is likely that a larger hydrocyclone, with a larger cut-size, will be required for this to be achievable. The improvements presented in this work are not limited to the study of opaque flows in the hydrocyclone. It demonstrates that the measurement of particle flows in any unit operation can be improved by using a detector apparatus tailored to its specific geometry.

5.7 Acknowledgements

5.8 References

Aldrich, C., 2015. Chapter One - Hydrocyclones, Progress in Filtration and Separation. Academic Press, Oxford, pp. 1-24.

Boucher, D., Deng, Z., Leadbeater, T., Langlois, R., Waters, K.E., 2016. Observation of iron ore beneficiation within a spiral concentrator by positron emission particle tracking of large (Ø=1440 µm) and small (Ø=58 µm) hematite and quartz tracers. Chemical Engineering Science 140, 217-232.

Boucher, D., Deng, Z., Leadbeater, T.W., Langlois, R., Renaud, M., Waters, K.E., 2014. PEPT studies of heavy particle flow within a spiral concentrator. Minerals Engineering 62, 120-128.

Boucher, D., Jordens, A., Sovechles, J., Langlois, R., Leadbeater, T.W., Rowson, N.A., Cilliers, J.J., Waters, K.E., 2017. Direct mineral tracer activation in positron emission particle tracking of a flotation cell. Minerals Engineering 100, 155-165.

Bradley, D., 1965. The Hydrocyclone, 4th ed. Pergamon Press, London.

Brennan, M.S., Fry, M., Narasimha, M., Holtham, P.N., 2007. Water velocity measurements inside a hydrocyclone using an Aeroprobe & Comparison with CFD predictions, 16th Australasian Fluid Mechanics Conference, Gold Coast, Australia, pp. 1131-1136.

Chang, Y.F., Ilea, C.G., Aasen, Ø.L., Hoffmann, A.C., 2011. Particle flow in a hydrocyclone investigated by positron emission particle tracking. Chemical Engineering Science 66, 4203–4211.

Charlton, M., Humberston, J.W., 2000. Positron Physics. Cambridge University Press, Cambridge, UK.

Chen, W., Zydek, N., Parma, F., 2000. Evaluation of hydrocyclone models for practical applications. Chemical Engineering Journal 80, 295-303.

Chu, L.-Y., Chen, W.-M., Lee, X.-Z., 2002. Effects of geometric and operating parameters and feed characters on the motion of solid particles in hydrocyclones. Separation and Purification Technology 26, 237-246.

Fan, X., Parker, D.J., Smith, M.D., 2006. Labelling a single particle for positron emission particle tracking using direct activation and ion-exchange techniques Nuclear Instruments and Methods in Physics Research Section A: Accelerators, Spectrometers Detectors and Associated Equipment 562, 345-350.

Fisher, M.J., Flack, R.D., 2002. Velocity distributions in a hydrocyclone separator. Experiments in Fluids 32, 302-312.

Flintoff, B.C., Plitt, L.R., Turak, A.A., 1987. Cyclone modelling: a review of present Technology. CIM Bulletin 80, 39-50.

Forney, D.C., Rothman, D.H., 2012. Inverse method for estimating respiration rates from decay time series. Biogeosciences 9, 3601-3612.

Govender, I., Cleary, P.W., Mainza, A.N., 2013. Comparisons of PEPT derived charge features in wet milling environments with a friction-adjusted DEM model. Chemical Engineering Science 97, 162-175.

Hawkesworth, M.R., O'Dwyer, M.A., Walker, J., Fowles, P., Heritage, J., Stewart, P.A.E., Witcomb, R.C., Bateman, J.E., Connolly, J.F., Stephenson, R., 1986. A Positron Camera for Industrial Applications. Nuclear Instruments and Methods A253, 145-157.

Jayasundara, C.T., Yang, R.Y., Guo, B.Y., Yu, A.B., Govender, I., Mainza, A., van der Westhuizen, A., Rubenstein, J., 2011. CFD–DEM modelling of particle flow in IsaMills – Comparison between simulations and PEPT measurements. Minerals Engineering 24, 181-187.

Kraipech, W., Chen, W., Dyakowski, T., Nowakowski, A., 2006. The performance of the empirical models on industrial hydrocyclone design. International Journal of Mineral Processing 80, 100-115.

Leadbeater, T., Parker, D.J., 2013. Current trends in positron emission particle tracking, 7th World Congress on Industrial Process Tomography. Elsevier, Krakow, Poland, pp. 85-94.

Leadbeater, T.W., 2009. The Development of Positron Imaging Systems for Applications in Industrial Process Tomography, School of Physics & Astronomy. University of Birmingham, Birmingham.

Leadbeater, T.W., Parker, D.J., 2011. A modular positron camera for the study of industrial processes. Nuclear Instruments and Methods in Physics Research Section A: Accelerators, Spectrometers, Detectors and Associated Equipment 652, 646-649.

Leadbeater, T.W., Parker, D.J., Gargiuli, J., 2012. Positron imaging systems for studying particulate, granular and multiphase flows. Particuology 10, 146-153.

Marins, L.P.M., Duarte, D.G., Loureiro, J.B.R., Moraes, C.A.C., Freire, A.P.S., 2010. LDA and PIV characterization of the flow in a hydrocyclone without an air-core. Journal of Petroleum Science and Engineering 70, 168-176.

Morrison, A.J., Govender, I., Mainza, A.N., Parker, D.J., 2016. The shape and behaviour of a granular bed in a rotating drum using Eulerian flow fields obtained from PEPT. Chemical Engineering Science 152, 186-198.

Nageswararao, K., Wiseman, D.M., Napier-Munn, T.J., 2004. Two empirical hydrocyclone models revisited. Minerals Engineering 17, 671-687.

Parker, D.J., Broadbent, C.J., Fowles, P., Hawkesworth, M.R., McNeil, P., 1993. Positron emission particle tracking - a technique for studying flow within engineering equipment. Nuclear Instruments and Methods in Physics Research Section A: Accelerators, Spectrometers Detectors and Associated Equipment 326, 592-607.

Parker, D.J., Forster, R.N., Fowles, P., Takhar, P.S., 2002. Positron emission particle tracking using the new Birmingham positron camera. Nuclear Instruments and Methods in Physics Research Section A: Accelerators, Spectrometers, Detectors and Associated Equipment 477, 540-545.

Radman, J.R., Langlois, R., Leadbeater, T.W., Finch, J., Rowson, N., Waters, K., 2014. Particle flow visualization in quartz slurry inside a hydrocyclone using the positron emission particle tracking technique. Minerals Engineering 62, 142-145.

Rietema, K., 1961. Performance and design of hydrocyclones - parts I-IV. Chemical Engineering Science 15, 298-325.

Wang, J., Bai, Z., Yang, Q., Fan, Y., Wang, H., 2016. Investigation of the simultaneous volumetric 3-component flow field inside a hydrocyclone. Separation and Purification Technology 163, 120-127.

Waters, K., Rowson, N.A., Fan, X., Parker, D.J., Cilliers, J.J., 2008. Positron emission particle tracking as a method to map the movement of particles in the pulp and froth phases. Minerals Engineering 21, 877-882.

Wills, B.A., Finch, J.A., 2016. Chapter 9 - Classification, Wills' Mineral Processing Technology (Eighth Edition). Butterworth-Heinemann, Boston, pp. 199-221.

Zhang, Y., Qian, P., Liu, Y., Wang, H., 2011. Experimental Study of Hydrocyclone Flow Field with Different Feed Concentration. Industrial & Engineering Chemistry Research 50, 8176-8184.

Linking Paragraph between Chapter 5 and Chapter 6

Chapter 6 presents the formulation of a CFD model of the two inch hydrocyclone with validation through PEPT, which represents the culmination of the work presented in Chapters 3, 4 and 5. The CFD simulation's structure follows the guidelines outlined in Chapter 3, and so much of the detailed reasoning behind model choices are omitted. The computational fluid dynamics (CFD) package Fluent$^{©}$ (ANSYS Inc., USA) was selected as the modelling software, and all simulations were conducted through McGill University's centre for High Performance Computing (HPC), which is a part of the Compute Canada national HPC platform.

The primary purpose of the particle trajectories and velocity profiles obtained in Chapter 5 is for the validation of future CFD models. The error analysis performed in Chapter 4, also provided confidence in the data measured with the PEPT technique, which is crucial in the development of any new characterisation tool. Therefore the PEPT data will form the primary method for model validation, a first for hydrocyclone modelling.

Chapter 6: A CFD Simulation of a Single Particle's Trajectory inside a Hydrocyclone with Validation through PEPT

6.1 Abstract

A Computational Fluid Dynamics (CFD) model of the hydrocyclone, simulating the trajectory of a single 1 mm quartz particle in a two phase (air-water) flow, was created. The turbulence within the hydrocyclone was modelled using the Large Eddy Simulation (LES) model, which has been shown to be the most accurate turbulence model for hydrocyclone simulations. The air core was modelled using the Volume Of Fluid (VOF) model and the particle addition was carried out using the Discrete Phase Model (DPM). Comparison of the simulated water split ratios and mass flow rates to experimental data demonstrated that the model was capable of accurately predicting the global water flow. The tangential and axial velocity components of the air-water mixture were compared to literature and was shown to be similar in magnitude. The particle's trajectory was compared to a trajectory of the same particle type measured via the Positron Emission Particle Tracking (PEPT) technique. Results showed that while the trajectories were comparable, the velocities of the simulated particle were much higher than those measured by PEPT. This lead to the simulated particle having a residence time less than half that of the experimental particle track. The difference was attributed to the near wall velocity resolution and the particle's interaction with the wall. This work highlights the need for further study of the simulation particle velocities in the hydrocyclone.

6.2 Introduction

Hydrocyclones are used extensively in the chemical, petroleum and mineral processing industries to remove or classify particles in particle laden fluid flows (Brennan, 2006). The popularity of hydrocyclones is primarily attributed to its apparently simple design and operational features. In reality, however, the particle separation mechanisms in the hydrocyclone are very complex (Vakamalla and Narasimha, 2017). Particles are separated by the balance of inertial forces (provided by the swirling water flow) and the counter acting drag forces. A typical hydrocyclone consists of a cylindrical chamber, where the feed enters tangential to the stationary body, attached to a conical section. The growing restriction in the conical section causes a majority of the water flow to reverse its direction, meaning only the coarsest material will continue its path out of the underflow. Finer particles will move with the water into the inner vortex, which continues upward

166

towards the overflow (Wills and Finch, 2016). The vortexing flow also creates a low-pressure zone along the central vertical axis that entrains air from the underflow (which is opened to the atmosphere) and forms an air core. This air core formation is crucial to the efficient operation of the hydrocyclone (Davailles *et al.*, 2012; Delgadillo and Rajamani, 2009; Dlamini *et al.*, 2005; Doby *et al.*, 2008; Gupta *et al.*, 2008; Sripriya *et al.*, 2007).

Hydrocyclone operation typically suffers from two inherent deficiencies. The first is the short circuiting of coarse particles along the boundary layer of the vortex finder, ending in the misclassification of coarse particles in the overflow stream. The second is the by-passing of fine particles to the underflow stream. Particles under a certain size do not possess sufficient drag force to resist moving with the fluid medium, and therefore, the amount of fines reporting to the underflow is proportional to the fraction of feed water reporting to the underflow (Delgadillo and Rajamani, 2007).

This misclassification of both fine and coarse particles understandably has a negative impact on performance, and so much effort has gone into optimising the hydrocyclone geometry and operating conditions to minimise these features. Empirically based models, such as those presented by Flintoff *et al.* (1987) and Nageswararao *et al.* (2004), were the first models to appear in literature and have since gained widespread use in the design and selection of industrial hydrocyclones, in part due to the ease in which they can be implemented into flow sheet simulation packages (Delgadillo and Rajamani, 2005). While these models are capable of predicting cut-size, pressure drops, and water flow splits within a reasonable degree of accuracy, they are only accurate within the limited range of experimental data from which the model parameters were developed. Extrapolating trends outside of the tested regimes requires the model to be calibrated with experimental data obtained close to the conditions in which the hydrocyclone will be used. However, the number of experiments needed for proper calibration is impractical in many situations, and therefore the performance of industrial scale hydrocyclones is often not optimised (Banerjee *et al.*, 2016).

To gain a better understanding of the geometrical and operating parameters and to provide true predictive capabilities, a more fundamental model of the hydrocyclone, based on physical principles, is essential. Computational fluid dynamics (CFD) provides the tools required to obtain a solution for the internal flow field. In the past decade considerable progress has been made in

the mathematical modelling of hydrocyclones with CFD (see Chapter 3). Previous CFD models have been used to study the effect of a range of different geometrical properties on the classification efficiencies of particles, including the vortex finder length and shape, feed inlet design, conical section length and shape, and apex diameter. While this has provided insight into the interactions of these components, most of these simulations have been carried out in low solid concentration flows due to the difficulties in modelling high solids content slurries. This has limited their applicability to industry.

While recent models have begun to simulate the flow of high solid concentration slurries (Ghodrat *et al.*, 2016; Kuang *et al.*, 2012; Vakamalla and Narasimha, 2017), which is more in line with industrial conditions, validation techniques for the complex particle flow are limited. The opaque nature of the particle laden flow makes visual and laser diffraction techniques invalid. Therefore, to date only global validation via particle separation curves has been used. This does not help validate the internal flow profiles which help determine the cause of the particle's behaviour within the hydrocyclone. The aim of this chapter is to use experimental particle velocity data to validate the flow of a single particle in a hydrocyclone, simulated using the CFD package Fluent© 16 (ANSYS, United States). The particle's properties will be validated with experimental data obtained from the positron emission particle tracking (PEPT) technique, presented in Chapters 4 and 5.

6.3   Simulation Method

6.3.1   Turbulence Model

When modelling hydrocyclones, turbulence plays a crucial role in predicting an accurate velocity flow field, air-core diameter and thereby particle separation efficiency. Therefore, the selection of an appropriate turbulence model is very important. The turbulence model chosen for this work was the Large Eddy Simulation (LES) model. Fundamentally, LES is based on the theory by Kolmogorov (1941), who noted that large turbulent eddies are typically geometry dependent, while the smaller scale eddies are more universal in nature. This feature allows one to explicitly solve the large eddies, while simulating the small eddies using a subgrid-scale (SGS) model. Although this makes the model computationally expensive, when compared to the Reynolds Averaged Navier-Stokes (RANS) equation based turbulence models, it has been shown by numerous authors (Banerjee *et al.*, 2016; Brennan, 2006; Brennan *et al.*, 2007; de Souza *et al.*, 2012; Delgadillo and

Rajamani, 2005; Karimi *et al.*, 2012; Lim *et al.*, 2010; Narasimha *et al.*, 2006; Narasimha *et al.*, 2012; Vakamalla and Narasimha, 2017) to be the most accurate model to capture the turbulent fluctuations in the hydrocyclone.

In the LES model, a filtering operation (determined by the cell volume) is applied to the governing Navier–Stokes equations to remove the small scale eddies. The resulting equations are of the standard form, but contain the stress tensor term, $\tau_{ij}{}^{sgs}$, which arises from the residual motions caused by the smaller eddies. The final LES model equations are given in Equation 6.1 and 6.2, where the quantities with an overbar denote the filtered quantities which are resolved.

$$\frac{\partial \rho}{\delta t} + \frac{\partial (\rho \bar{u}_\iota)}{\delta x_i} = 0 \qquad \qquad \textbf{Equation 6.1}$$

$$\frac{\delta (\rho \bar{u}_i)}{\delta t} + \frac{\delta \left(\rho \bar{u}_i \bar{u}_j\right)}{\delta x_j} = -\frac{\delta \bar{p}}{\delta x_i} + \rho g_i + \frac{\delta}{\delta x_j}\left(\mu \frac{\delta \bar{u}_i}{\delta x_j}\right) - \frac{\delta \tau_{ij}{}^{sgs}}{\delta x_j} \qquad \textbf{Equation 6.2}$$

The residual stress tensor is modelled following the Boussinesq eddy viscosity assumption, producing Equation 6.3. The turbulent viscosity was modelled with the Smagorinsky–Lilly model, as this is the simplest method and has also been shown to be the most accurate SGS model for hydrocyclone simulations (Karimi *et al.*, 2012). It calculates the SGS eddy viscosity algebraically from a length scale L_S and the mean local strain rate (Equation 6.4). The length scale is normally equal to a third power of the finite volume of each cell (in regions of high turbulence) but also contains a correction for cells close to the wall regions (Equation 6.5). The model constant C_s was set to 0.1 as implemented by previous hydrocyclone models (Brennan *et al.*, 2007; Narasimha *et al.*, 2006). More details about the LES model can be found elsewhere (ANSYS, 2016; Versteeg and Malalasekera, 2007)

$$\tau_{ij}{}^{sgs} - \frac{1}{3}\tau_{kk}\delta_{ij} = -2\mu_{t,s}S_{ij} \qquad \qquad \textbf{Equation 6.3}$$

$$\mu_{t,s} = \rho L_S \left| \sqrt{2\bar{S}_{ij}\bar{S}_{ij}} \right| \qquad \qquad \textbf{Equation 6.4}$$

$$L_S = \min\left(\kappa D_w, C_s V_g^{\frac{1}{3}}\right) \qquad \qquad \textbf{Equation 6.5}$$

6.3.2 Multiphase Model

The air-core was modelled using the Volume Of Fluid (VOF) model. This method has been widely used when modelling the air core in two-phase or low solid concentration flows (Cui *et al.*, 2014; Delgadillo and Rajamani, 2007; Leeuwner and Eksteen, 2008; Narasimha *et al.*, 2006; Wang and Yu, 2008; Xu *et al.*, 2013) due to its cheap computational expense and proven accuracy. The volume fraction of each phase is calculated using the continuity equation (Equation 6.6), where α_k is the volume fraction of phase k (which varies between 1 and 0) and u_i is the velocity component in the direction i. This is used to track the interface between the air core and the water.

$$\frac{\delta \alpha_k}{\delta t} + u_j \frac{\delta \alpha_k}{\delta x_i} = 0 \qquad \textbf{Equation 6.6}$$

A single momentum equation is solved throughout the domain (Equation 6.7), with the resulting velocity field being shared by the two phases. This momentum equation is dependent on the volume fraction of fluid phase with the properties ρ and μ. The average density and viscosity are calculated using Equation 6.8 and Equation 6.9 respectively. The surface tension between air and water was also incorporated as a source term in the momentum equation (Vakamalla and Narasimha, 2017). A constant value of 0.078 N·m^{-1} was used.

$$\frac{\delta(\rho u_j)}{\delta t} + \frac{\delta(\rho u_i u_j)}{\delta x_j} = -\frac{\delta p}{\delta x_j} + \rho g_j + \frac{\delta}{\delta x_j} \mu \left(\frac{\delta u_i}{\delta x_j} + \frac{\delta u_j}{\delta x_i} \right) \qquad \textbf{Equation 6.7}$$

$$\rho_{mixture} = \alpha \rho_{water} + (1-\alpha)\rho_{air} \qquad \textbf{Equation 6.8}$$

$$\mu_{mixture} = \alpha \mu_{water} + (1-\alpha)\mu_{air} \qquad \textbf{Equation 6.9}$$

The particle trajectory was modelled using the Discrete Phase Model (DPM). The DPM allows for the simulation of a discrete particle phase in a Lagrangian frame of reference. The individual particle's trajectory was calculated via a force balance, which included the discrete phase inertia, hydrodynamic drag, buoyancy and gravity (Equation 6.10 and 6.11). The drag coefficient from Equation 6.11 was selected based on the spherical drag law, where a_1, a_2, and a_3 are constants based on the work of Morsi and Alexander (1972) (Equation 6.12). The additional force term F_B represents the contribution from both the virtual mass force and pressure gradient force, which is recommended to be implemented when the fluid to particle density ratio is larger than 0.1

(ANSYS, 2016). As the injected inert particle was silica, with a density of 2650 kg·m⁻³, the ratio is approximately 0.38 and therefore both forces were incorporated into the DPM. The virtual mass factor constant was kept at the default value of 0.5. The turbulent dispersion was predicted using the stochastic tracking model with the discrete random walk model enabled. This includes the effect of instantaneous turbulent velocity fluctuations on the particle trajectories, important when modelling the hydrocyclone.

$$\frac{\delta u_p}{\delta t} = F_D\big(u_{mixture} - u_p\big) + \frac{g(\rho_p - \rho)}{\rho_p} + F_B \qquad \textbf{Equation 6.10}$$

$$F_D = \frac{18 u_{mixture}}{d_p{}^2 \rho_p} C_D \frac{Re_p}{24} \qquad \textbf{Equation 6.11}$$

$$C_D = a_1 + \frac{a_2}{Re_p} + \frac{a_3}{Re_p{}^2} \qquad \textbf{Equation 6.12}$$

The main assumptions behind the DPM is that the particle-particle interactions and the effects of the particle volume fraction on the liquid phase are negligible, meaning it should only be used to model low solids concentration flows. The DPM has been shown to accurately predicted particle separation in systems with solid concentrations under 5 % by volume (Delgadillo and Rajamani, 2005, 2007; Hwang *et al.*, 2013; Wang and Yu, 2006; Wang *et al.*, 2007; Wang and Yu, 2008; Xu *et al.*, 2012). As only a single particle is modelled, the dispersed phase volume fraction is virtually zero. Coupled with the low computational demand of the DPM, this model is the most suitable selection.

6.3.3 Mesh Structure and Qualities

The hydrocyclone geometry modelled in this work is based upon the two-inch hydrocyclone manufactured by Salter Cyclones© (England). The total height of the hydrocyclone was 375 mm; the apex and vortex diameters were 9.4 and 14 mm respectively; and the tangential feed inlet was rectangular, 12 × 5 mm in size. The geometry and mesh are shown in Figure 6.1. The mesh contested of 281,532 cells, broken down into 224,275 hexahedral cells, 57,017 tetrahedral cells and 240 pyramidal cells. Hexahedral cells were chosen to mesh the main body of the hydrocyclone as this element type allows for the alignment of the cell with the primary flow direction, reducing numerical diffusion. Although tetrahedral cells are not recommended for discretising the

hydrocyclone (Bhaskar *et al.*, 2007b; Mousavian *et al.*, 2009; Murthy and Bhaskar, 2012; Slack *et al.*, 2004), the complex top entry inlet geometry required tetrahedral cells to improve the quality of the mesh in this region. This procedure has been successfully used elsewhere (Gupta *et al.*, 2008; Leeuwner and Eksteen, 2008).

The mesh characteristics for all three mesh types can be found in Figure 6.2 and Figure 6.3. Skewness values ranged from 0.001 to 0.85 for all mesh types, while aspect ratio ranged from 1 to 13.7. Ideally values for aspect ratio should be below 10 (Bhaskar *et al.*, 2007b; Mousavian *et al.*, 2009; Murthy and Bhaskar, 2012) and skewness below 0.85, as higher values can cause numerical inaccuracies. As a large majority of the cells had a skewness value below 0.7 and a skewness value below 6, the mesh quality was deemed satisfactory. A mesh independence study was conducted in which the mesh was refined to over two million cells. The predicted values for the overall water split ratio and tangential velocity components were used as metrics to determine whether any significant difference occurred at the smaller mesh size. As the predicted values differed by less than 5 %, the larger mesh size was used to help alleviate the computational expense of the LES model.
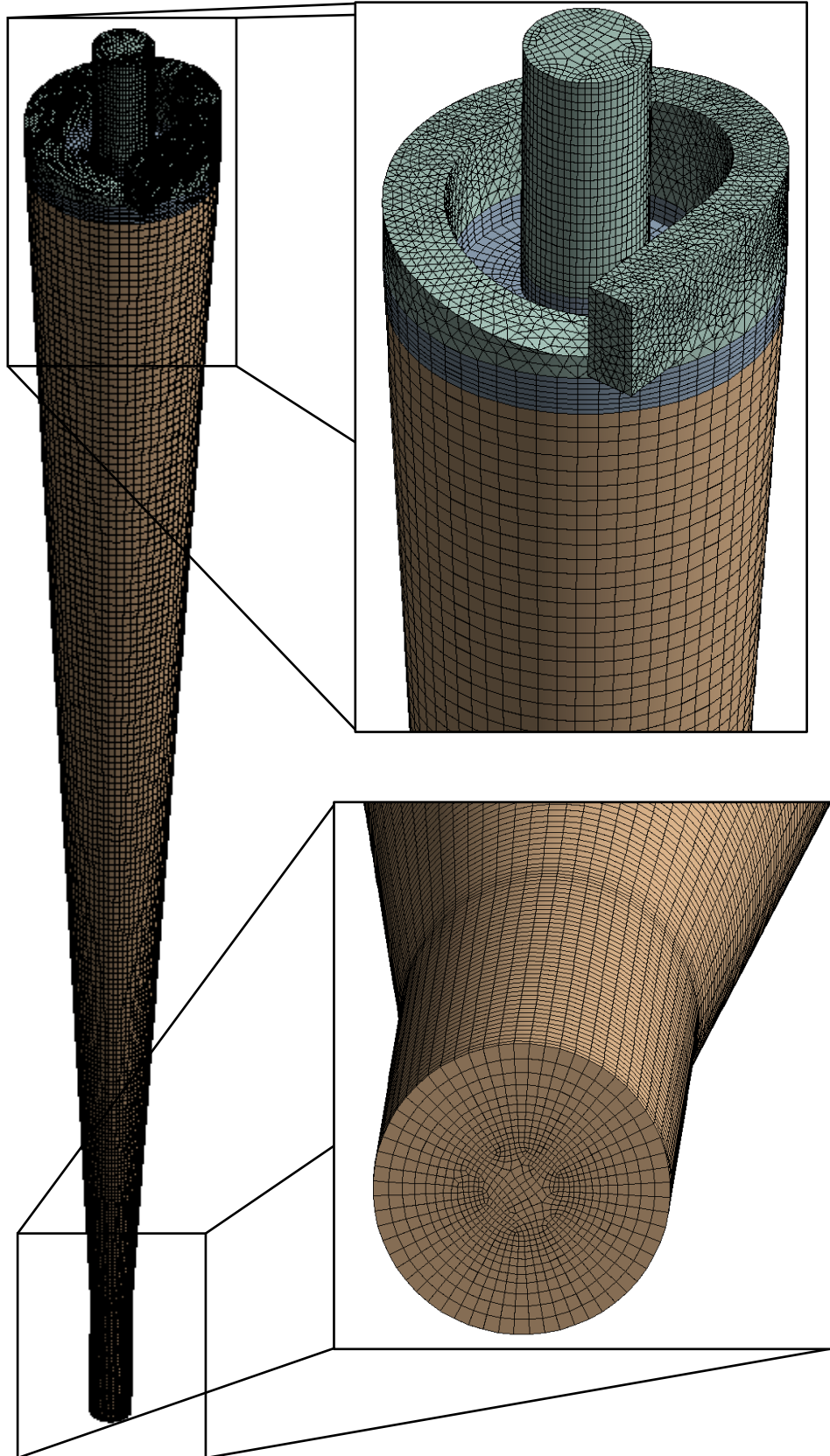
Figure 6.1: Hydrocyclone mesh, with close ups of the feed area and underflow zone.
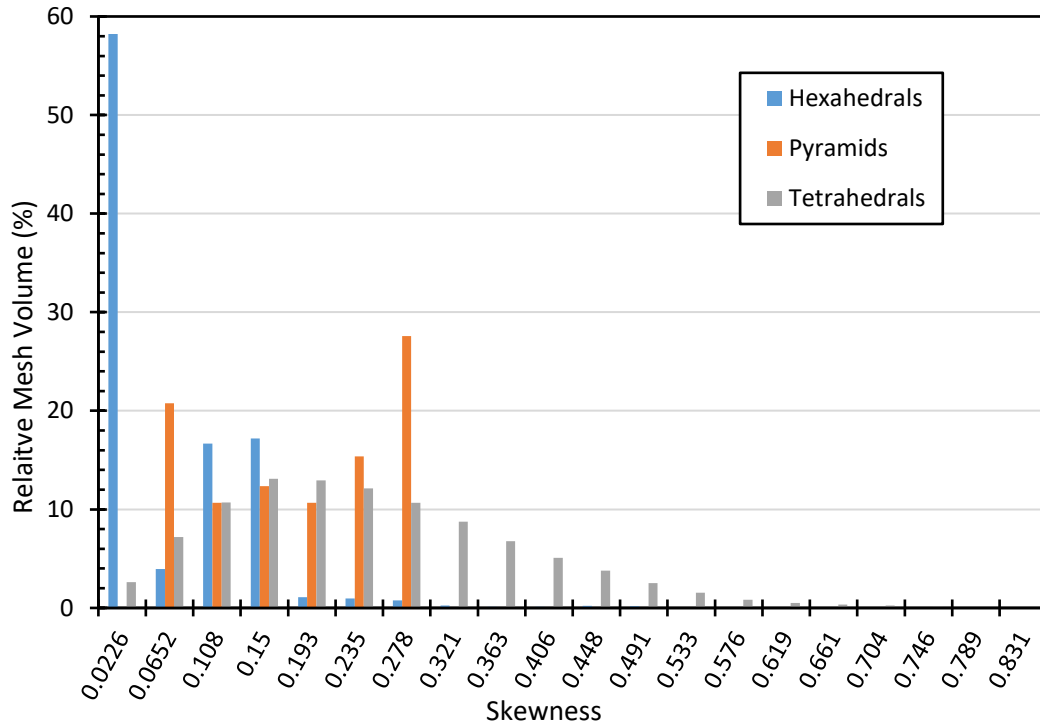
Figure 6.2: Cell aspect ratio distribution for the hydrocyclone mesh. Relative mesh volume represents the volume of each mesh type in relation to its overall mesh volume, which was 96 %, 0.1%, and 3.9 % for hexahedral, pyramidal, and tetrahedral cells respectively.
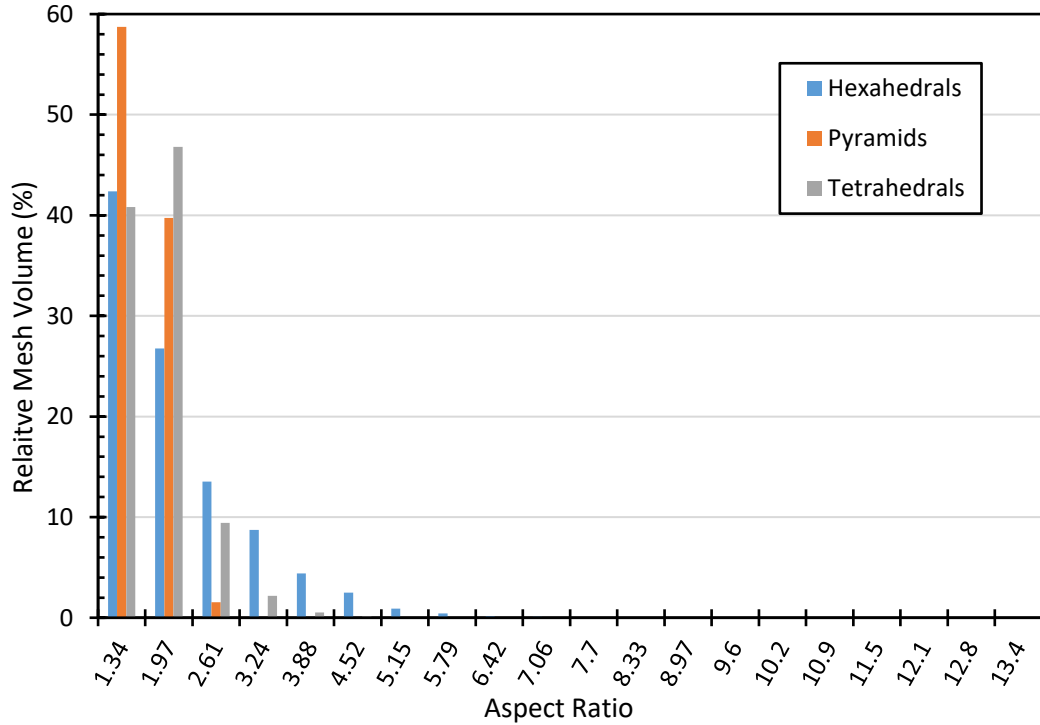
Figure 6.3: Cell skewness distribution for the hydrocyclone mesh. Relative mesh volume represents the volume of each mesh type in relation to its overall mesh volume, which was 96 %, 0.1%, and 3.9 % for hexahedral, pyramidal, and tetrahedral cells respectively.

174

6.3.4 Solution Initialisation and Methods

All simulation methods were based upon the review presented in Chapter 3. Both the overflow and underflow boundary conditions were set as pressure outlets with the back-flow air volume fraction set to one and the radial equilibrium pressure distribution applied. The feed boundary condition was set as a mass flow inlet, which was set at the experimentally measured flow rate of 969 g·s^{-1}. Under relaxation values were left unchanged and, in general, high order discretisation schemes were selected to reduce the effects of numerical diffusion (Bhaskar *et al.*, 2007a; Mousavian *et al.*, 2009; Murthy and Bhaskar, 2012; Noroozi and Hashemabadi, 2011; Slack *et al.*, 2004). A summary of the simulation methods can be found in Tables 6.1 to 6.5.

The initialisation procedure undertaken in this paper was based upon the work of Brennan (2006). First a single phase (water) simulation was run using a steady state solver, with the RNG *k-ε* turbulence model and the air backflow volume fraction set to zero for the overflow and underflow boundary conditions. This allowed for a better initial approximation of the pressure and velocity flow fields within the hydrocyclone without the increased computational expense of added phases or complex turbulence models. The turbulence model was then changed to the LES model, which requires the unsteady solver, and the air backflow volume fraction at both outlets was set to one, allowing the air core to form. The simulation was run until the mass flow rates at the underflow and overflow stabilised (typically taking 1 s of simulation time, which is equivalent to approximately two residence times). Once stabilised the particle was added (at the centre of the feed area), and the simulation continued until the particle had exited the domain.

Table 6.1: Simulation conditions – Solution Methods

Solution Methods	
Pressure-Velocity Coupling	SIMPLE
Spatial Discretisation	
Gradient	Least Squares Cell Based
Pressure	PRESTO!
Momentum	Bounded Central Differencing
Volume Fraction	Modified HRIC
Transient Formulation	Bounded Second Order Implicit

Table 6.2: Simulation conditions – Multiphase Model

Multiphase Model	
Volume Fraction Formulation	Implicit
Volume Fraction Cut-off	1×10^{-6}
Interface Modelling	Sharp

Table 6.3: Simulation conditions – Simulation Parameters

Simulation Parameters	
Time Step	1×10^{-5}
Residual Convergence criteria	1×10^{-5}
Under Relaxation Values	Default

Table 6.4: Simulation conditions – Particle Injection

Particle Injection	
Physical Models	Virtual Mass Force Pressure Gradient Force
Particle Type	Inert Silica
Particle Diameter	1 mm
Particle Density	$2650 \ \text{kg} \cdot \text{m}^{-3}$
Particle Shape	Spherical
Drag Law Parameters	Spherical
Turbulent Dispersion	Discrete Random Walk Model

Table 6.5: Simulation conditions – Boundary Conditions

Boundary Conditions			
	Feed Inlet	**Overflow**	**Underflow**
Boundary Type	Mass Flow Inlet	Pressure Outlet	Pressure Outlet
Mass Flow Rate (kg·s⁻¹)	Water - 0.969	-	-
Gauge Pressure (Pa)	0	0	0
Air Volume Fraction	0	1	1
Feed Direction /Backflow Direction	Normal to Boundary	Normal to Boundary	Normal to Boundary
Special Features	-	Radial Pressure Distribution	Radial Pressure Distribution

6.4 Results and Discussion

6.4.1 Water flow split measurements

Both the underflow and overflow water mass flow rates were measured using the hydrocyclone apparatus detailed in Chapters 4 and 5. A comparison between the experimentally measured mass flow rates and those predicted by the CFD model can be found in Table 6.6. The feed was reconstituted based on the measured values of the overflow and underflow. The predicted flow rates were similar to those measured experimentally, with the underflow difference falling within the measurement error. The percentage of water that reported to the underflow (termed water split ratio) also closely matched the measured value.

Table 6.6: Comparison of predicted and measured mass flow rates for water, where CI stands for confidence interval.

	Measured ($g·s^{-1}$)	Measurement Error (95 % CI)	Predicted ($g·s^{-1}$)	Difference between predicted and measured
Feed	969	-	-	-
Underflow	206	7.8 %	191	7.3 %
Overflow	763	3.1 %	801	5.0 %
Water Split Ratio	21.3 %	-	19.7 %	-

6.4.2 Comparison of tangential velocities to literature

While the global validation of the water flow is necessary, the local validation of the velocity components is more important. The internal water flow fields have not been measured for the hydrocyclone studied in this chapter, therefore a comparison to models conducted with similar hydrocyclone geometries was performed. Figure 6.4 and Figure 6.5 show the tangential and axial velocity components over a single horizontal plane, 0.015 m below the bottom of the vortex finder. The results are compared to the simulation of Banerjee *et al.* (2016). While their results cannot provide the validation that experimental values could, it still provides a metric to determine the accuracy of the internal flow phenomena. The magnitude of both velocity components appear to match those reported by Banerjee *et al.* (2016), with the tangential velocity components showing a similar trend. When comparing the axial velocities, both simulations determined the locus of zero vertical velocity to be at comparable radial positions, however, the overall trends do not match closely.
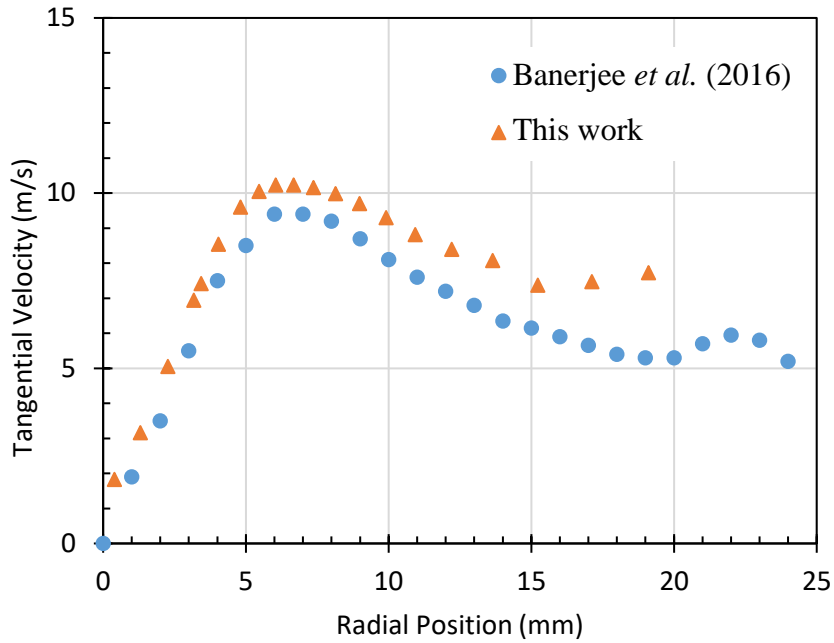
Figure 6.4: Comparison of the tangential velocity components as a function of radial position to those of Banerjee *et al.* (2016)
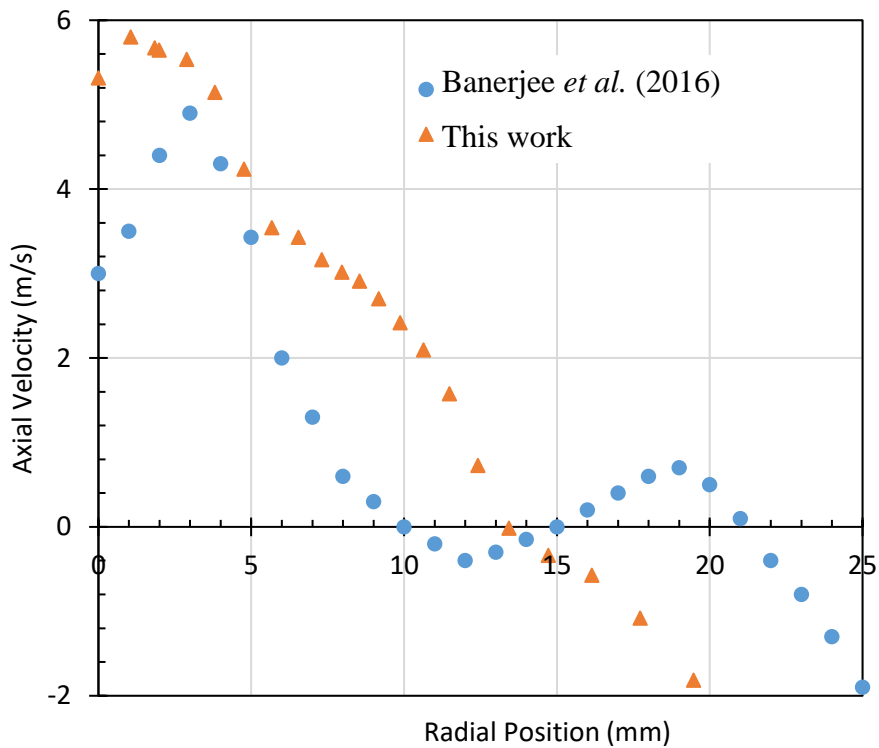
Figure 6.5: Comparison of the axial velocity components as a function of radial position to those of Banerjee *et al.* (2016)

6.4.3 *Particle trajectory comparison to PEPT.*

The trajectory of the single quartz bead measured by the PEPT technique and predicted by the CFD technique are shown in Figures 6.6 and 6.7 respectively. It is evident that the two particle trajectories are similar in nature. A key deficiency in the particle trajectory predicted by the CFD simulation is the overall particle residence time. The measured residence time was more than double the predicted particle residence time. This is due to the high velocity magnitude of the simulated particle. Figure 6.8 shows the particle's velocity magnitude as a function of height in the hydrocyclone. Both the simulation and PEPT results shown a decrease in velocity once leaving the feed zone and then a steady increase in velocity towards the underflow zone. While the results from the CFD simulation have a similar trend to the PEPT data, the magnitude of the velocities is significantly different. As the particle is much larger in diameter than the hydrocyclone cut-size, which is 10 μm, the particle spends most of its time at the outer wall boundary. Therefore, the inaccuracies in the simulated velocities could be attributed to the near wall velocity resolution or an increased friction between the particle and the wall.
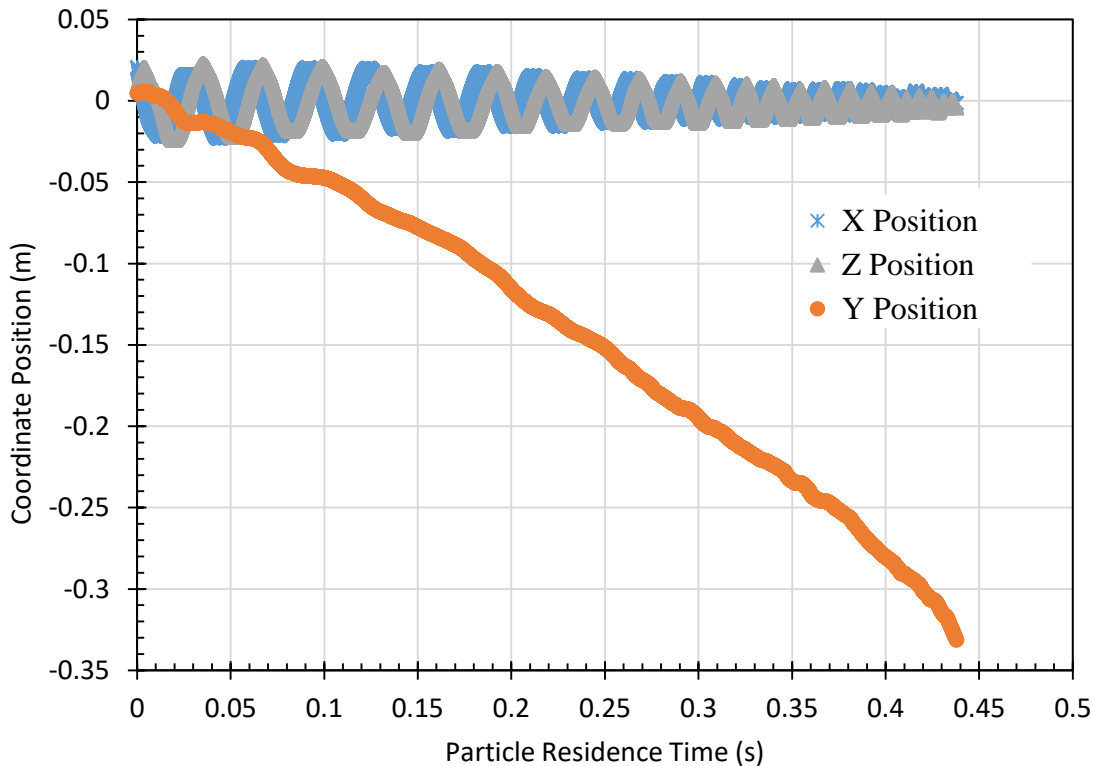
Figure 6.6: Particle location data as a function of residence time for the 1 mm quartz bead as measured *via* PEPT.
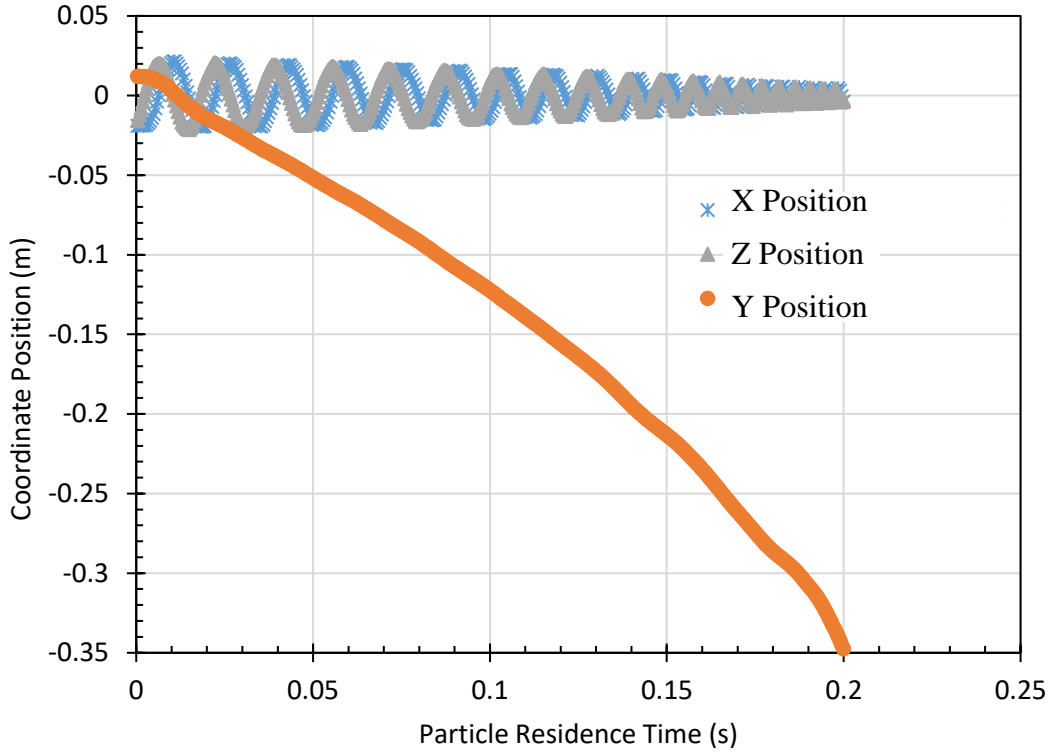
Figure 6.7: Particle location data as a function of residence time for the 1 mm quartz bead as predicted *via* CFD.
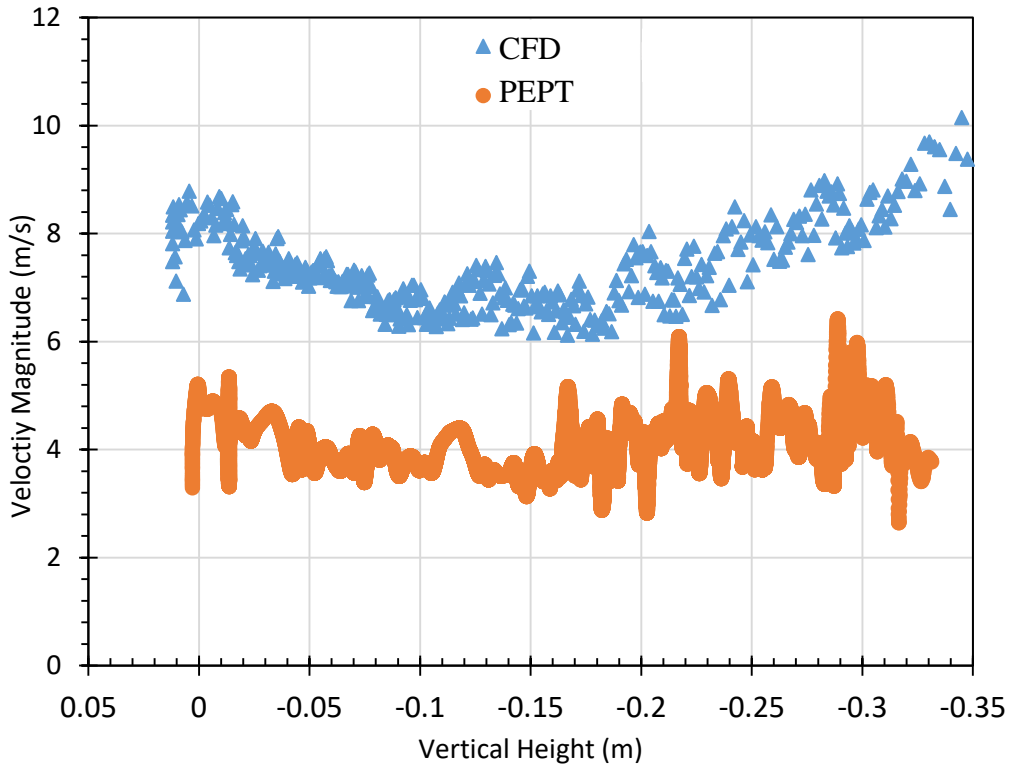
Figure 6.8: A comparison of the velocity magnitude predicted by CFD and measured by PEPT as a function of vertical position (the most negative values represent the bottom of the hydrocyclone).

6.5   Conclusions

A CFD simulation and validation study of a two-inch Salter hydrocyclone has indicated that the water distribution values, in terms of throughput and split, closely match the experimental results. The tangential and axial velocity components of the mixture at a single horizontal plane were shown to be similar to those reported in literature. These results validate the use of the LES and VOF models to simulate the turbulence and multiphase interactions, respectively, within in the hydrocyclone. The simulated particle trajectory of a 1 mm quartz sphere was found to match the trajectory measured using the PEPT technique, however, the velocity magnitude was significantly different. With the flow of the air-water mixture appearing reasonable, the differences were hypothesised to be due to the near wall velocity resolution or an increased friction between the particle and the wall. Future work will focus on further validating the air-water flow by measuring the air core diameter and local velocity components to ensure that the particle flow is not biased by an incorrect fluid flow. It is clear that more research is needed to model the complex particle interactions within the hydrocyclone if detailed particle trajectories are to be simulated.

6.6   Nomenclature

C_D	Drag Coefficient
C_s	Smagorinsky Lilly constant
d_p	Particle diameter
D_w	Distance to the closest wall
F_B	Buoyancy Force
F_D	Drag Force
g	Gravity
L_S	Length scale of the SGS stresses
Re_p	Relative Reynolds Number
S_{ij}	Mean strain rate
t	Time
u_i	i component of velocity
V_g	Volume of finite grid cell
x_i	i coordinate

Greek Symbols

α_k	Volume fraction of phase k
δ_{ij}	Kronecker delta
κ	von Kármán constant
$\mu_{t,s}$	SGS eddy viscosity
ρ	Density
$\tau_{ij}{}^{sgs}$	Turbulent or SGS stress tensor
τ_{kk}	Isotropic part of the SGS stresses

6.7   Acknowledgements

6.8   References

ANSYS, 2016. Fluent 16 Theory Guide, USA.

Banerjee, C., Climent, E., Majumder, A.K., 2016. Mechanistic modelling of water partitioning behaviour in hydrocyclone. Chemical Engineering Science 152, 724-735.

Bhaskar, K.U., Murthy, Y.R., Raju, M.R., Tiwari, S., Srivastava, J.K., Ramakrishnan, N., 2007a. CFD simulation and experimental validation studies on hydrocyclone. Minerals Engineering 20, 60-71.

Bhaskar, K.U., Murthy, Y.R., Ramakrishnan, N., Srivastava, J.K., Sarkar, S., Kumar, V., 2007b. CFD validation for flyash particle classification in hydrocyclones. Minerals Engineering 20, 290-302.

Brennan, M.S., 2006. CFD Simulations of Hydrocyclones with an Air Core: Comparison Between Large Eddy Simulations and a Second Moment Closure. Chemical Engineering Research and Design 84, 495-505.

Brennan, M.S., Narasimha, M., Holtham, P.N., 2007. Multiphase modelling of hydrocyclones – prediction of cut-size. Minerals Engineering 20, 395-406.

Cui, B.-y., Wei, D.-z., Gao, S.-l., Liu, W.-g., Feng, Y.-q., 2014. Numerical and experimental studies of flow field in hydrocyclone with air core. Transactions of Nonferrous Metals Society of China 24, 2642-2649.

Davailles, A., Climent, E., Bourgeois, F., 2012. Fundamental understanding of swirling flow pattern in hydrocyclones. Separation and Purification Technology 92, 152-160.

de Souza, F.J., de Vasconcelos Salvo, R., de Moro Martins, D.A., 2012. Large Eddy Simulation of the gas–particle flow in cyclone separators. Separation and Purification Technology 94, 61-70.

Delgadillo, J.A., Rajamani, R.K., 2005. A comparative study of three turbulence-closure models for the hydrocyclone problem. International Journal of Mineral Processing 77, 217-230.

Delgadillo, J.A., Rajamani, R.K., 2007. Exploration of hydrocyclone designs using computational fluid dynamics. International Journal of Mineral Processing 84, 252-261.

Delgadillo, J.A., Rajamani, R.K., 2009. Computational fluid dynamics prediction of the air-core in hydrocyclones. International Journal of Computational Fluid Dynamics 23, 189-197.

Dlamini, M.F., Powell, M.S., Meyer, C.J., 2005. A CFD simulation of a single phase hydrocyclone flow field. The Journal of The South African Institute of Mining and Metallurgy 105, 711-718.

Doby, M.J., Nowakowski, A.F., Yiu, I., Dyakowski, T., 2008. Understanding air core formation in hydrocyclones by studying pressure distribution as a function of viscosity. International Journal of Mineral Processing 86, 18-25.

Flintoff, B.C., Plitt, L.R., Turak, A.A., 1987. Cyclone modelling: a review of present Technology. CIM Bulletin 80, 39-50.

Ghodrat, M., Qi, Z., Kuang, S.B., Ji, L., Yu, A.B., 2016. Computational investigation of the effect of particle density on the multiphase flows and performance of hydrocyclone. Minerals Engineering 90, 55-69.

Gupta, R., Kaulaskar, M.D., Kumar, V., Sripriya, R., Meikap, B.C., Chakraborty, S., 2008. Studies on the understanding mechanism of air core and vortex formation in a hydrocyclone. Chemical Engineering Journal 144, 153-166.

Hwang, K.-J., Hwang, Y.-W., Yoshida, H., 2013. Design of novel hydrocyclone for improving fine particle separation using computational fluid dynamics. Chemical Engineering Science 85, 62-68.

Karimi, M., Akdogan, G., Dellimore, K.H., Bradshaw, S.M., 2012. Quantification of numerical uncertainty in computational fluid dynamics modelling of hydrocyclones. Computers & Chemical Engineering 43, 45-54.

Kolmogorov, A., 1941. The local structure of turbulence in incompressible viscous fluids at very large Reynolds numbers. Proceedings of the Royal Society 434, 9-13.

Kuang, S.B., Chu, K.W., Yu, A.B., Vince, A., 2012. Numerical study of liquid–gas–solid flow in classifying hydrocyclones: Effect of feed solids concentration. Minerals Engineering 31, 17-31.

Leeuwner, M.J., Eksteen, J.J., 2008. Computational fluid dynamic modelling of two phase flow in a hydrocyclone. The Journal of The Southern African Institute of Mining and Metallurgy 108, 231-236.

Lim, E.W.C., Chen, Y.-R., Wang, C.-H., Wu, R.-M., 2010. Experimental and computational studies of multiphase hydrodynamics in a hydrocyclone separator system. Chemical Engineering Science 65, 6415-6424.

Morsi, S.A., Alexander, A.J., 1972. An investigation of particle trajectories in two-phase flow systems. Journal of Fluid Mechanics 55, 193-208.

Mousavian, S.M., Ahmadvand, M., Najafi, A.F., 2009. One-Way and Two-Way Coupling Analyses on Three Phase Flows in Hydrocyclone Separator. Journal of Applied Mechanics 76, 061005-061005-061010.

Murthy, Y.R., Bhaskar, K.U., 2012. Parametric CFD studies on hydrocyclone. Powder Technology 230, 36-47.

Nageswararao, K., Wiseman, D.M., Napier-Munn, T.J., 2004. Two empirical hydrocyclone models revisited. Minerals Engineering 17, 671-687.

Narasimha, M., Brennan, M.S., Holtham, P.N., 2006. Large eddy simulation of hydrocyclone—prediction of air-core diameter and shape. International Journal of Mineral Processing 80, 1-14.

Narasimha, M., Brennan, M.S., Holtham, P.N., 2012. CFD modeling of hydrocyclones: Prediction of particle size segregation. Minerals Engineering 39, 173-183.

Noroozi, S., Hashemabadi, S.H., 2011. CFD analysis of inlet chamber body profile effects on de-oiling hydrocyclone efficiency. Chemical Engineering Research and Design 89, 968-977.

Slack, M.D., Del Porte, S., Engelman, M.S., 2004. Designing automated computational fluid dynamics modelling tools for hydrocyclone design. Minerals Engineering 17, 705-711.

Sripriya, R., Kaulaskar, M.D., Chakraborty, S., Meikap, B.C., 2007. Studies on the performance of a hydrocyclone and modeling for flow characterization in presence and absence of air core. Chemical Engineering Science 62, 6391-6402.

Vakamalla, T.R., Narasimha, M., 2017. Numerical simulation of industrial hydrocyclones performance: Role of turbulence modelling. Separation and Purification Technology 176, 23-39.

Versteeg, H., Malalasekera, W., 2007. An Introduction to Computational Fluid Dynamics: The Finite Volume Method, 2nd ed. Pearson, London.

Wang, B., Chu, K.W., Yu, A.B., 2007. Numerical Study of Particle−Fluid Flow in a Hydrocyclone. Industrial & Engineering Chemistry Research 46, 4695-4705.

Wang, B., Yu, A.B., 2006. Numerical study of particle–fluid flow in hydrocyclones with different body dimensions. Minerals Engineering 19, 1022-1033.

Wang, B., Yu, A.B., 2008. Numerical study of the gas–liquid–solid flow in hydrocyclones with different configuration of vortex finder. Chemical Engineering Journal 135, 33-42.

Wills, B.A., Finch, J.A., 2016. Chapter 9 - Classification, Wills' Mineral Processing Technology (Eighth Edition). Butterworth-Heinemann, Boston, pp. 199-221.

Xu, Y., Song, X., Sun, Z., Lu, G., Li, P., Yu, J., 2012. Simulation Analysis of Multiphase Flow and Performance of Hydrocyclones at Different Atmospheric Pressures. Industrial & Engineering Chemistry Research 51, 443-453.

Xu, Y., Song, X., Sun, Z., Tang, B., Li, P., Yu, J., 2013. Numerical Investigation of the Effect of the Ratio of the Vortex-Finder Diameter to the Spigot Diameter on the Steady State of the Air Core in a Hydrocyclone. Industrial & Engineering Chemistry Research 52, 5470-5478.

Chapter 7:   Conclusions, Contributions, and Future Work

7.1   Conclusions

The results from the PEPT experimentation, presented in Chapters 4 and 5, demonstrated that it is a suitable technique for the tracking of particles in the hydrocyclone. The new cross-pattern modular assembly, made up of 16 ECAT951 detectors, produced very high tracking rates when compared to similar experiments in other detector systems. This was attributed to the high surface area density of the detectors, which in turn meant a large percentage of emitted radiation was captured. An error analysis of the detector arrangement showed that the three-dimensional error was found to range from 0.54 mm for a stationary particle, consistent for all tracer activities, up to 4.33 mm for a tracer with an activity of 3 MBq and a speed of 4 m·s^{-1}. For lower activity tracers ($< 10^{-2}$ MBq), the error was more sensitive to increases in speed, increasing to 28 mm (at 4 m·s^{-1}), indicating that at these conditions a reliable trajectory is not possible. These results expanded on, but correlated well with, previous literature that only contained location errors for tracer speeds up to 1.5 m·s^{-1}. A qualitative comparison to the work of Radman *et al.* (2014), indicated that there was a significant increase in quality of the measured trajectory of a 106−212 μm quartz particle in the hydrocyclone. This improvement in trajectory quality allowed for the calculation of velocity profiles, a first for the hydrocyclone using the PEPT technique. The measured velocities were shown to closely match previous literature that used high speed video analysis. This further validated PEPT as a technique for the measurement of particle velocities within the hydrocyclone as well as the outlined data processing procedure. The improvements presented in this work are not limited to the study of opaque flows in the hydrocyclone, as shown by the flotation experiments detailed in Chapter 4. The thesis demonstrates that the measurement of particle flows in any unit operation can be improved by using a detector apparatus tailored to its specific geometry.

A review on the use of CFD for modelling the hydrocyclone indicated that it was a useful tool for simulating the flow within the hydrocyclone. Two phase water and air in the hydrocyclone has been shown to be accurately modelled *via* CFD. The modelling of particle flow, particularly in high solid concentration flows, is less established. Validation of particle velocities has not yet been achieved through CFD. The simulation of the particle showed that while an accurate trajectory can be achieved, the velocity magnitude was significantly different to the experimentally measured

value. This shows that further work is required in the simulation of particle velocities within the hydrocyclone.

7.2   Contributions to Original Knowledge

The main contribution to original knowledge from this work was to prove the capabilities of the PEPT technique in applications with high speed, small diameter tracers. This involved being the first to publish tracer location errors at speeds over 1 m·s⁻¹ and provide *track* code parameters for a range of different tracer activities and speeds. By validating the location accuracy of the detector system at high tracer speeds and low activities, this work has extended the ability of PEPT to produce reliable particle trajectories of real mineral particles under 500 μm in size, travelling at speeds over 1.5 m·s⁻¹. This has previously been limited by the low activity of small tracers (< 500 μm) created via direct activation. Using the PEPT technique three-dimensional particle trajectories and velocity profiles were, for the first time, presented in the hydrocyclone for two particle size fractions: 106-212 µm and 355-500 µm. These results will be beneficial for the validation of particle flow simulations in the hydrocyclone in the future.

7.3   Considerations for Future PEPT Experimentation in the Hydrocyclone

There were several experiences which if learnt from, can improve PEPT experimentation in hydrocyclones in the future. Below is a list of the key findings:

- The breakage of real mineral tracers, due to weaknesses created during the direct activation process, limits the acquisition time. This reduces the accuracy of time average velocity profiles. The use of sturdier, synthetic tracers (such as glass beads) would be a significant improvement, as it would allow for longer tests and a higher tracer activity (for the same particle size). These tracers would need to be created via indirect activation techniques as the current limit in particle size for direction activation is approximately 1 mm, which is larger than the desired tracer size. It should be noted that the smaller particles (~100 µm) were less prone to breakage.

- It was concluded that the abrasion of the tracer particles on the internal walls of the hydrocyclone led to increased noise in the data. While this effect would be reduced if the particle spent less time at the cyclone wall (such as using a tracer under the cut size of the

hydrocyclone), a simple solution could be to implement a rotating test schedule with multiple hydrocyclones.

- Results showed that the flow in the main body of the cyclone is relatively consistent, whereas in the feed and underflow zone the results were not as uniform. The high speed in the feed zone and the tight curvature and reversal of flow in the underflow zone creates a large amount of turbulence in these regions. This unpredictable flow makes them the most significant areas to study via the PEPT technique. The detector arrangement used in this work was not optimised for the capture of the flow in the feed and underflow regions as both zones were at the edge of cameras sensitivity limits. To rectify this the geometry should be changed in future testing. The addition of an additional two detector modules to each of the four blocks would increase the height of the FOV making the two extremities of the hydrocyclone still within the high sensitivity zone of the detectors. If the number of modules is restricted, the module blocks (from the current arrangement) could be separated into two groups of four, each group centred around the feed and underflow regions. Both methods would allow for greater resolution in the feed and underflow regions. It is not recommended to run separated tests focused on various regions of the hydrocyclone.

- Throughout this work, only particles much larger than the hydrocyclone's cut size were tracked using the PEPT technique. This meant that particle velocities could only be determined in a small area of the hydrocyclone (the outer wall region). The volume occupied by a particle could be increased by either decreasing the size of the tracked particle or increasing the cut size of the hydrocyclone. As the particle size is limited due to the required activity strength, a larger diameter hydrocyclone is recommended. This should be the focus of future work, as tracking particles above, below and near the cut size of a hydrocyclone would provide great insight into its classification mechanics.

7.4 Suggestions for Future Work

Now that the PEPT method has been established for the tracking of particles in the hydrocyclone, future testing should include the acquisition of trajectories from different sized particles over a range of different solid concentrations. As mentioned, the particle size range should cover particle sizes above and below the cut size of the hydrocyclone to ensure that particle velocities inside the inner vortex can be studied. Several improvements can be made to the fundamental aspects of the PEPT technique. While not focused on in this thesis, improvements to the *track* algorithm, the direct activation of sub 1 mm particles, and the development of more sensitive camera arrangements or materials, would all lead to more accurate trajectories. These features will never be truly optimised and so will always be the focus of future study. For CFD models, more focus should be put into the validation of the internal particle flow. This will require the testing of parameters such as wall friction models, particle shape factors, and near wall velocity resolution.

Appendix A: Supplementary Data

Appendix A.1: Supplementary Results from Chapter 4

Table A.1.1: Range of tested values used for N, S and f parameters

Parameter	Tested Values
f	5 - 95 (at an increment of 5)
N	20, 50, 100, 250, 400 - 3000 (at an increment of 200)
S (N=20)	1, 2, 4, 10, 20
S (N=50)	1, 2, 5, 10, 50
S (N=100)	1, 2, 4, 10, 20, 100
S (N=250)	1, 2, 5, 25, 50, 250
S (N=400)	1, 2, 4, 8, 40, 400
S (N=600)	1, 2, 4, 12, 30, 600
S (N=800)	1, 2, 4, 8, 40, 800
S (N=1000)	1, 2, 5, 10, 50, 1000
S (N=1200)	1, 2, 3, 6, 12, 60, 1200
S (N=1400)	1, 2, 4, 7, 14, 70, 1400
S (N=1600)	1, 2, 4, 8, 16, 80, 1600
S (N=1800)	1, 2, 4, 9, 18, 90, 1800
S (N=2000)	1, 2, 4, 10, 20, 100, 2000
S (N=2200)	1, 2, 4, 11, 22, 110, 2200
S (N=2400)	1, 2, 4, 6, 12, 24, 120, 2400
S (N=2600)	1, 2, 4, 8, 13, 26, 130, 2600
S (N=2800)	1, 2, 4, 7, 14, 28, 140, 2800
S (N=3000)	1, 2, 3, 6, 15, 30, 150, 3000

Table A.1.2: X-axis location errors (mm) for each speed and tracer activity.

Impeller Tip Speed (m·s⁻¹)	Tracer Activity (MBq)		
	4.0×10^{-3} - 3.7×10^{-2}	3.7×10^{-1}	3.3×10^{0}
0.00	0.25	0.27	0.33
0.07	5.85	1.24	0.90
0.33	6.80	1.00	1.03
0.67	7.67	1.46	1.73
1.34	8.87	2.50	1.31
2.67	11.29	3.88	1.01
4.01	19.14	5.59	2.74

Table A.1.3: Y-axis location errors (mm) for each speed and tracer activity.

Impeller Tip Speed (m·s⁻¹)	Tracer Activity (MBq)		
	4.0×10^{-3} - 3.7×10^{-2}	3.7×10^{-1}	3.3×10^{0}
0.00	0.23	0.33	0.29
0.07	0.96	0.84	0.38
0.33	1.82	0.96	0.45
0.67	1.88	1.22	0.42
1.34	2.01	1.13	0.79
2.67	2.40	1.87	0.91
4.01	4.48	2.37	1.40

Table A.1.4: Z-axis location errors (mm) for each speed and tracer activity.

Impeller Tip Speed (m·s⁻¹)	Tracer Activity (MBq)		
	4.0×10^{-3} - 3.7×10^{-2}	3.7×10^{-1}	3.3×10^{0}
0.00	0.42	0.29	0.31
0.07	5.77	0.86	0.78
0.33	6.39	1.22	0.98
0.67	7.28	1.99	1.70
1.34	8.74	1.80	2.05
2.67	12.40	3.30	2.05
4.01	19.71	4.42	2.74

Appendix A.2: Supplementary Results from Chapter 5

Table A.2.1: Information for the 355-500 μm diameter quartz particles.

Run Number	Tracer Activity (MBq)	Number of Individual Passes	Average Location Rate (Hz)	*track* code parameters
1	3.85	8	52 500	$N = 250$, $S = 250\, f = 65$
2	1.92	10	21 300	$N = 250$, $S = 250\, f = 65$
3	0.74	6	10 500	$N = 250$, $S = 250\, f = 65$
4	4.63	8	54 600	$N = 250$, $S = 250\, f = 65$
5	2.78	9	24 800	$N = 250$, $S = 250\, f = 65$

Table A.2.2: Information for the 106-212 μm diameter quartz particles.

Run Number	Tracer Activity (MBq)	Number of Individual Passes	Average Location Rate (Hz)	*track* code parameters
1	0.55	7	6 200	$N = 100$, $S = 100\, f = 45$
2	0.44	21	5 800	$N = 100$, $S = 100\, f = 45$
3	0.37	27	3 800	$N = 100$, $S = 100\, f = 45$
4	0.30	40	3 600	$N = 100$, $S = 100\, f = 45$

Table A.2.3: Information for the 1 mm glass bead.

Run Number	Tracer Activity (MBq)	Number of Individual Passes	Average Location Rate (Hz)	*track* code parameters
1	18.9	1	120 000	$N = 400$, $S = 400\, f = 65$

Appendix B: Matlab Code

Appendix B.1: Matlab Code for Automated Parameter Input into the *track* Code

```matlab
%run mc
clear all; clc; close all;
%base data file

bd{1} = '1'; %First event
bd{2} = '999999999'; %last event
bd{3} = 'F'; %Fixed/variable
bd{4} = '250'; %Events/slice (N)
bd{5} = '1'; %Locations/slice (S)
bd{6} = '5'; %Fopt percentage of lines kept per slice (F)
bd{7} = '300'; %X,Y,Z cutoff (max detectable volume)
bd{8} = '400'; %Y cutoff
bd{9} = '1500'; %Z cutoff
bd{10} = '50'; %Max allowable error (E)
bd{11} = 'defname.txt'; %file to ouput to
bd{12} = 'A'; %Ascii or Binary


S01 = [1 2 4 10 20];
S02 = [1 2 5 10 25 50];
S03 = [1 2 4 10 20 100];
S04 = [1 2 5 25 50 250];
S05 = [1 2 4 8 40 400];
S06 = [1 2 4 12 30 600];
S07 = [1 2 4 8 40 800];
S08 = [1 2 5 10 50 1000];
S09 = [1 2 3 6 12 60 1200];
S10 = [1 2 4 7 14 70 1400];
S11 = [1 2 4 8 16 80 1600];
S12 = [1 2 4 9 18 90 1800];
S13 = [1 2 4 10 20 100 2000];
S14 = [1 2 4 11 22 110 2200];
S15 = [1 2 4 6 12 24 120 2400];
S16 = [1 2 4 8 13 26 130 2600];
S17 = [1 2 4 7 14 28 140 2800];
S18 = [1 2 3 6 15 30 150 3000];


%filename structure = trends18Feb14_121704.txt


aa = dir('*.da*');
len_aa = length(aa);


filenames_selected = [];
fn = [];
fnn = [];
mcRT = [];
counter = 0;
for i=6:7 %length(aa)
    filename = aa(i).name;
    counter = counter+1;
```

```matlab
    filenames_selected = [filenames_selected; filename];
    mcR = [];
    for N=[20, 50, 100, 250, 400:200:3000] %1000 50
        if N==20;
            S=S01;
        elseif N==50;
            S=S02;
        elseif N=100;
            S=S03;
        elseif N==250;
            S=S04;
        elseif N==400;
            S=S05;
        elseif N==600;
            S=S06;
        elseif N==800;
            S=S07;
        elseif N==1000;
            S=S08;
        elseif N==1200;
            S=S09;
        elseif N==1400;
            S=S10;
        elseif N==1600;
            S=S11;
        elseif N==1800;
            S=S12;
        elseif N==2000
            S=S13;
        elseif N==2200;
            S=S14;
        elseif N==2400;
            S=S15;
        elseif N==2600;
            S=S16;
        elseif N==2800;
            S=S17;
        else
            S=S18;
        end


        for S %10 2
            for F=5:5:95 %40 5:10:45
                inserts = ['_N' num2str(N) '_S' num2str(S) '_F' num2str(F)
'_E' char(bd(10))];
                s1 = regexprep(filename, '.d', [inserts '.'])

                %insert new values into data array to be written
                bd{4} = num2str(N); %Events/slice (N)
                bd{5} = num2str(S); %Locations/slice (S)
                bd{6} = num2str(F); %Fopt percentage of lines kept per
slice (F)
                bd{11} = s1; %file to ouput to

                %write file to be used by mc
                fileID = fopen('data.txt','w');
```

```matlab
                    formatSpec = '%s\n';
                    for row = 1:12
                        fprintf(fileID,formatSpec,bd{row});
                    end
                    fclose(fileID);
                    %close written file

                    %run mc
                    %[status, result] =  system('mc CAL_MM_01.da01 <
data.txt')
                    s = ['[status, result] =  system(''' 'mc ' filename ' <
data.txt''' ');'];
                    eval(s);

                %get data from results string (includes some error checking)
                    qAver = regexpi(result, 'Averages');
                    averages = result(qAver+9:qAver+9+53);
                    A = sscanf(averages, '%f %f %f +/- %f %f %f');
                    if length(A)  ~= 6
                        for zzz = length(A)+1:6
                            A = [A; -1];
                        end
                    end

                    qsd = regexpi(result, 'standard deviations:');
                    sds = result(qsd+20:qsd+20+53);
                    B = sscanf(sds, '%f %f %f +/- %f %f %f');
                    if length(B)  ~= 6
                        for zzz = length(B)+1:6
                            B = [B; -1];
                        end
                    end

                    qD = regexpi(result, 'D=');
                    dvalue = result(qD+2:qD+2+8);
                    CC = sscanf(dvalue, '%f');
                    if length(CC)  ~= 1
                        CC = -1;
                    end

                    qdelta = regexpi(result, 'delta:');
                    delta = result(qdelta+6:qdelta+6+18);
                    C = sscanf(delta, '%f +/- %f');
                    if length(C)  ~= 2
                        C = [C; -1];
                    end

                    qNE = regexpi(result, 'No of events used');
                    NE = result(qNE+17:qNE+17+9);
                    D = sscanf(NE, '%f');
                    if length(D)  ~= 1
                        D = -1;
                    end

                    qNLE = regexpi(result, 'No of locations expected');
```

```matlab
                    NLE = result(qNLE+24:qNLE+24+7);
                    EE = sscanf(NLE, '%f');
                    if length(EE) ~= 1
                        EE = -1;
                    end

                    qNLA = regexpi(result, 'No of locations actual');
                    NLA = result(qNLA+22:end);
                    FF = sscanf(NLA, '%f');;
                    if length(FF) ~= 1
                        FF = -1;
                    end

                    mc_results = [N; S; F; str2num(char(bd(10)));  A; B; C;
CC; D; EE; FF];
                    mcR = [mcR mc_results];

                end
            end
    end %of N loop

    mcRT = [mcRT mcR];

    s2 = regexp(filename, '.d', 'split');
    fn = [fn s2(1)];
    fnn = [fnn s2(2)];


end %of outside loop (filenames)

sizeR = size(mcR)
sizeRT = size(mcRT)
aaa = reshape(mcRT,sizeRT(1),sizeR(2),sizeRT(2)/sizeR(2))
size3d = size(aaa)
if length(size3d) == 2
    size3d(3) =1;
end

labels = [{'N'} {'S'} {'F'} {'E'} {'aveX'} {'aveY'} {'aveZ'} {'EaveX'}
{'EaveY'} {'EaveZ'} ... %10
        {'sdX'} {'sdY'} {'sdZ'} {'EsdX'} {'EsdY'} {'EsdZ'} ... %6
        {'delta'} {'Edelta'} {'D'} {'NoEvents'} ... %4
        {'Loc Exp'} {'Loc Act'} {'Loc E-A'}]; %3

for i=1:size3d(3)
    h = figure(1000+i)
    for j=1:size3d(1)
        subplot(5,5,j)
        plot(aaa(j,:,i))
        ylabel(labels(j))
    end
    subplot(5,5,j+1)
    plot(aaa(j-1,:,i)-aaa(j,:,i))
    ylabel(labels(j+1))
```

```matlab
    saveas(h,char( strcat(fn(i),'_',fnn(i), '_fig', num2str(1000+i), '.fig')
))
end

%save the stats file and figure
s2 = regexp(filename, '.d', 'split');
ffn = s2(1);
save(char(strcat(ffn,'_',s2(2), '_data_stats.mat')),'sizeR', 'sizeRT',
'size3d', 'aaa')
```

Appendix B.2: Matlab Code for Analysing Fixed Trajectory Data

```matlab
%By Josh Sovechles, Darryel Boucher and Randolph Pax 2016
clear all; clc; close all;


rpm = 1500;
Hz = rpm/60;
amplitude = 1;
slidewindsize = 10;
incre_wave = 2;

windowFlag = 1;
pauseFlag = 0;
pausetime = 0.2;
aa = dir('*.a07');


outvv = [];
for bigiter = 1:length(aa)
    filename = aa(bigiter).name;
%Initialization
%---------------------------------------------------------------------------%

%Load data set (file provided by TRACK.EXE without any header information)
%--------------------------------------%
%[Tini, Xini, Yini, Zini, Nbevent, Error] =
textread('CAL_MM_01_N50_S17_F25_E5.a02', '%f %f %f %f %f %f',
500000,'headerlines', 16); %500 000 is max number of row to be read.
[Tini, Xini, Yini, Zini, Nbevent, Error] = textread(char(aa(bigiter).name),
'%f %f %f %f %f %f', 5000000,'headerlines', 16); %500 000 is max number of
row to be read.

%T: Time (ms)
%X: X axis coordinate (mm)
%Y: Y axis coordinate (mm)
%Z: Z axis coordinate (mm)

% Data preparation
%---------------------------------------------------------------------------%
Tini=Tini/1000; %From (ms) to (s).
id=find(Tini);

%Center view on geometry
%--------------------------------%
Xtranslation=-0.5; %Translation on X axis (mm)
Ytranslation=64.3;
Ztranslation=-8.45;
Xini=Xini+Xtranslation;
Yini=Yini+Ytranslation;
Zini=Zini+Ztranslation;

%Rotate locations to align x, y, z axis to geometry
%--------------------------------%
thetaX=0/180*pi(); %Rotation angle on X axis (deg/180*pi()=rad)
thetaY=0/180*pi();
thetaZ=0/180*pi();
```

```matlab
RX = [1,0,0;0,cos(thetaX),sin(thetaX);0,-sin(thetaX),cos(thetaX)]; % Rotation
matrix on X
RY = [cos(thetaY),0,-sin(thetaY);0,1,0;sin(thetaY),0,cos(thetaY)];
RZ = [cos(thetaZ),sin(thetaZ),0;-sin(thetaZ),cos(thetaZ),0;0,0,1];

Locations=[Xini Yini Zini]; %Creation of a matrix to be rotated
Locations=Locations*RX; %Applying the rotation around X axis
Locations=Locations*RY;
Locations=Locations*RZ;

Xini=Locations (:,1); %Replacing with the new rotated coordinates
Yini=Locations (:,2);
Zini=Locations (:,3);

%Motion calculations and cyclindrical coordinates
%-------------------------------------------------------------------------%
Rini=(Xini.^2+Zini.^2).^(1/2); %Radius determined around Y (the vertical
symetry axis)
Thetaini=atan2(Zini,Xini); %atan2 gives the four quadrant tangent inverse
angle in the interval [-pi, pi].

Tdiffini=diff(Tini); %Getting the Time difference between subsequent
datapoint
Xdiffini=diff(Xini);
Ydiffini=diff(Yini);
Zdiffini=diff(Zini);
Rdiffini=diff(Rini);
Thetadiffini=diff(Thetaini);
for i=1:length(Thetadiffini) %Loop to fix the angle difference
    if Thetadiffini(i)<=(-pi())
        Thetadiffini(i)=Thetadiffini(i)+2*pi();
    elseif Thetadiffini(i)>=pi()
        Thetadiffini(i)=Thetadiffini(i)-2*pi();
    else
    end
end

Tini(length(Tini))=[]; % making every array the same length
Xini(length(Xini))=[];
Yini(length(Yini))=[];
Zini(length(Zini))=[];
Rini(length(Rini))=[];
Thetaini(length(Thetaini))=[];
id(length(id))=[];

%Speed calculations
%---------------------------------%
vXini=Xdiffini./Tdiffini/1000; %Calculate velocity in X axis in m/s
vYini=Ydiffini./Tdiffini/1000;
vZini=Zdiffini./Tdiffini/1000;
vXYZini=(Xdiffini.^2+Ydiffini.^2+Zdiffini.^2).^(1/2)./Tdiffini/1000;
vRini=Rdiffini./Tdiffini/1000;
vAngularini=Thetadiffini./Tdiffini;
vThetaini=Rini.*vAngularini;
```

```matlab
%Keep only part of the data set
%--------------------------------%
Tmin=20; %Remove value with T value lower than (s)
Tmax=50; %Remove value with T value higher than (s)
tT=(Tini>=Tmin) & (Tini<Tmax);


Xmin=-500; %Remove points with X value lower than (mm)
Xmax=500; %Remove points with X value higher than (mm)
tX=Xini>=Xmin & Xini<Xmax;


Ymin=-500;
Ymax=500;
tY=Yini>=Ymin & Yini<Ymax;


Zmin=-500;
Zmax=500;
tZ=Zini>=Zmin & Zini<Zmax;


Select=ones(size(Tini)); %Creating a array with true (1) for each existing
locations
Select=Select.*tT.*tX.*tY.*tZ; %Applying the condition to convert from true
(1) to false (0) if locations to be rejected
Select=Select>0;


T=Tini(Select); %Switching to T instead of Tini (Tini is kept as unfiltered
data)
X=Xini(Select);
Y=Yini(Select);
Z=Zini(Select);
id=id(Select);
R=Rini(Select);
Theta=Thetaini(Select);


Tdiff=Tdiffini(Select);
Xdiff=Xdiffini(Select);
Ydiff=Ydiffini(Select);
Zdiff=Zdiffini(Select);
Rdiff=Rdiffini(Select);
Thetadiff=Thetadiffini(Select);


vX=vXini(Select);
vY=vYini(Select);
vZ=vZini(Select);
vXYZ=vXYZini(Select);
vR=vRini(Select);
vAngular=vAngularini(Select);
vTheta=vThetaini(Select);


%Data set basic info
%------------------------------------------------------------------------%
nbLocini=length(Tini);
nbLoc=length(T);
sampleT=max(T)-min(T);
locrate=nbLoc/sampleT; %Location frequency calculation
```

```matlab
T1=[T;mean(T)];
T2=[mean(T);T];
Tdelta=T2-T1;
MeanTdelta=mean(Tdelta);
StdTdelta=std(Tdelta);


X1=[X;mean(X)];
X2=[mean(X);X];
Xdelta=X2-X1;
MeanXdelta=mean(Xdelta);
StdXdelta=std(Xdelta);


Y1=[Y;mean(Y)];
Y2=[mean(Y);Y];
Ydelta=Y2-Y1;
MeanYdelta=mean(Ydelta);
StdYdelta=std(Ydelta);


Z1=[Z;mean(Z)];
Z2=[mean(Z);Z];
Zdelta=Z2-Z1;
MeanZdelta=mean(Zdelta);
StdZdelta=std(Zdelta);


XYZdelta=(Xdelta.^2.+Ydelta.^2.+Zdelta.^2).^(1/2);
MeanXYZdelta=mean(XYZdelta); %Average distance between subsequent locations
StdXYZdelta=std(XYZdelta);


%Display info
disp(['Initial number of locations: ',num2str(nbLocini)])
disp(['Final number of locations: ',num2str(nbLoc)])
disp(['Sample time (s): ',num2str(sampleT)])
disp(['Location rate (Hz): ',num2str(locrate)])
disp(['Mean delta subsequent locations (mm): ',num2str(MeanXYZdelta)])
disp(['Std dev delta subsequent locations (mm): ',num2str(StdXYZdelta)])
% disp(['Number of passes: ',num2str(pcount)])

% % %Display locations
% % %-------------------------------------------------------------------
-%
% % figure(01) %X, Y, Z, T values
% %
% % subplot(3,1,1)
% % plot(T,X,'-bo','LineWidth',1,'MarkerSize',5);
% % xlabel('T (s)','FontSize',20);
% % ylabel('X (mm)','FontSize',20);
% % grid on
% % set(gca,'FontSize',20)
% %
% % subplot(3,1,2)
% % plot(T,Y,'-bo','LineWidth',1,'MarkerSize',5);
% % xlabel('T (s)','FontSize',20);
% % ylabel('Y (mm)','FontSize',20);
% % grid on
```

```matlab
% % set(gca,'FontSize',20)
% %
% % subplot(3,1,3)
% % plot(T,Z,'-bo','LineWidth',1,'MarkerSize',5);
% % xlabel('T (s)','FontSize',20);
% % ylabel('Z (mm)','FontSize',20);
% % grid on
% % set(gca,'FontSize',20)
QQ=Y;
%-------------------------CURVE FITTING------------------------
T=T-Tmin;

%%%%%%%%%%%%%%%%%%%%%%%%%%%%%%%%%%%%%%%%%
if rpm~=0
    FFT = abs(fft(QQ));
    FFTlength = length(FFT);
    FFTSkip = 3;
    FFT2 = FFT(FFTSkip:(FFTlength/2));
    MaxFFT = (max(FFT2(:,1)));
    PosMax = find(FFT2(:,1) == MaxFFT)+FFTSkip-1;
    PosMax2 = PosMax*2;                              %Possible position of
second peak

    if PosMax2<(FFTlength-5)
        FFT3 = FFT(PosMax2-2:PosMax2+2);
        MaxFFT2 = (max(FFT3(:,1)));
        PosMax3 = find(FFT2(:,1) == MaxFFT2)+FFTSkip-1;       %Actual
position of second peak
        PeakRatio = MaxFFT2/MaxFFT;
    else
        FFT3 = FFT(PosMax2-2:FFTlength);
        MaxFFT2 = (max(FFT3(:,1)));
        PosMax3 = find(FFT2(:,1) == MaxFFT2)+FFTSkip-1;       %Actual
position of second peak
        PeakRatio = MaxFFT2/MaxFFT;
    end

    figure (1111)
    plot(FFT);
end
%%%%%%%%%%%%%%%%%%%%%%%%%%%%%%%%%%%%%%%%%%%

        %[b,a] = butter(4,12/1201,'high');
         %X = filter(b,a,X);
%XM=X-mean(X)-0.5;
figure (02)
subplot(2,1,1)
% if to define default Hz for stationary case%%%%%%%%%%%%%%%%%%%%%%%%%%
if rpm == 0
    Hz = 1; %making the first time selection work for stationary calib.
end
Tlength = length(T);
qqq = find(T > 1/Hz,1);
kkk = qqq;
if kkk<150
```

```matlab
    if kkk<100
        if kkk<50
        kkk=50;
        end
    else
        kkk=100;
    end
else
    kkk=150;
end
endindex = qqq;
startindex = 1;
deltaindex = qqq*slidewindsize;   %sliding window analysis
deltaindex2 = qqq*incre_wave; %incremental analysis
Tsmall=T(startindex:endindex);
QQsmall=QQ(startindex:endindex);
x0 = [0.1 1 Hz];
x1 = [0.1]; %inital guess for second sine
x2 =[0]; %1]; % for the stationary case
xs = [2000 0.1 3];
endFlag = 0;
sigmav = [];
Stdev = [];
while (endFlag == 0)
    if endindex == length(T)
        endFlag = 1;
    end



    if rpm == 0

        % Initial Guess for single sine function
        fun = @(xx,Tsmall)xx(1)*Tsmall+xx(2);
        %fun = @(xx,Tsmall)Tsmall-Tsmall;
        coeff = lsqcurvefit(fun,x2,Tsmall,QQsmall);
        %xx = coeff;
        %newx =
xx(1)*sin(xx(2)*2*pi*T+xx(3))+xx(4)*sin(2*xx(2)*2*pi*T+xx(5))+xx(6);
        newx = fun(coeff,Tsmall);
        subplot(3,1,1)
        plot(Tsmall,QQsmall,'.',Tsmall,newx,'r')

        subplot(3,1,2)
        WWW=newx-QQsmall;
        WWWmax=max(WWW);
        WWWmin=min(WWW);
        WWWrange=WWWmin:0.1:WWWmax;
        WWWStd=std(WWW);
        WWWmean=mean(WWW);
        WWWguas=normpdf(WWWrange,WWWmean,WWWStd);
        plot(Tsmall,WWW)

        subplot(3,1,3)
```

```matlab
        [yh,xh] = hist((newx-QQsmall),kkk/2);
        yh=yh/(sum(yh));
        funN = @(xs,xhh)abs(xs(1))/sqrt(2*pi)/abs(xs(3))*exp(-0.5*((xhh-
abs(xs(2)))/abs(xs(3))).^2);
        coeffN = lsqcurvefit(funN,xs,xh,yh);
        coeffN(3)= abs(coeffN(3));
        plot(xh,yh,'.',xh,funN(coeffN,xh),'r');
        hold on
        plot(WWWrange,WWWguas,'b');
        text(1,max(yh)*0.9,['sigma= ' num2str(coeffN(3))])
        hold off
        x2 = coeff;
        sigmav = [sigmav coeffN(3)];
        Stdev = [Stdev WWWStd];

        if coeffN(3) > 2
            coeffN(3)=0.8;
        end

    else

        % Initial Guess for single sine function
        if endindex == qqq;
            fun = @(xx,Tsmall)amplitude*sin(xx(3)*2*pi*Tsmall+xx(2));
        else
            % fun = @(xx,Tsmall)xx(1)+amplitude*sin(xx(2)*2*pi*Tsmall+xx(3))+
(amplitude*PeakRatio)*sin(2*xx(2)*2*pi*Tsmall+xx(4));
            fun = @(xx,Tsmall)amplitude*sin(xx(3)*2*pi*Tsmall+xx(2))+
(amplitude*PeakRatio*0)*sin(2*xx(3)*2*pi*Tsmall+xx(4));
            x0 = coeff;
            x1 = [];
        end



        coeff = lsqcurvefit(fun,x0,Tsmall,QQsmall);


        newx = fun(coeff,Tsmall);
        subplot(3,1,1)
        plot(Tsmall,QQsmall,'.',Tsmall,newx,'r')

        subplot(3,1,2)
        WWW=newx-QQsmall;
        WWWmax=max(WWW);
        WWWmin=min(WWW);
        WWWrange=WWWmin:0.1:WWWmax;
        WWWStd=std(WWW);
        WWWmean=mean(WWW);
        WWWguas=normpdf(WWWrange,WWWmean,WWWStd);
        plot(Tsmall,WWW)

        subplot(3,1,3)

        [yh,xh] = hist((newx-QQsmall),kkk/2);
```

```matlab
        yh=yh/(sum(yh));
        funN = @(xs,xhh)abs(xs(1))/sqrt(2*pi)/abs(xs(3))*exp(-0.5*((xhh-
abs(xs(2)))/abs(xs(3))).^2);
        coeffN = lsqcurvefit(funN,xs,xh,yh);
        coeffN(3)= abs(coeffN(3));
        plot(xh,yh,'.',xh,funN(coeffN,xh),'r');
        text(1,max(yh)*0.9,['sigma= ' num2str(coeffN(3))])
        hold on
        plot(WWWrange,WWWguas,'b');
        hold off
        xs=coeffN;
        coeff = [coeff x1];
        sigmav = [sigmav coeffN(3)];
        Stdev = [Stdev WWWStd];

        if abs(coeff(3) - Hz) > 0.05
            coeff(3)=Hz;
        end
        if coeffN(3) >2
            coeffN(3)=0.8;
        end
    end

    %xx = coeff;
    if endindex == qqq;
        endindex = endindex + 1;
    else
        endindex = endindex + deltaindex2;
    end

    endindex = min(endindex,length(T));

    if windowFlag == 1 %moving window analysis
        if endindex - startindex > deltaindex
            startindex = endindex-deltaindex;
        end
    end

    Tsmall=T(startindex:endindex);
    QQsmall=QQ(startindex:endindex);

    if pauseFlag == 1
        pause(pausetime)
    end
end %while

    if rpm~=0
        if windowFlag==1
            sigmav(1:3) = [];
        else
            sigmav(1:8)=[];
        end
    end

    figure(333);
    plot(sigmav);
```

```matlab
        end


    if rpm~=0
        if windowFlag==1
            Stdev(1:4) = [];
        else
            Stdev(1:8)=[];
        end
    end



    ss1 = regexp(aa(bigiter).name,'_N','split');
    ss2 = regexp(ss1(2),'.a','split');
    ss3 = ss2{1,1}(1);
    ss4 = regexp(ss3,'_S','split');
    NNs = ss4{1,1}(1);
     NN = sscanf(char(NNs),'%f');
    ss5 = ss4{1,1}(2);
    ss6 = regexp(ss5,'_F','split');
    SSs = ss6{1,1}(1);
     SS = sscanf(char(SSs),'%f');
    ss7 = ss6{1,1}(2);
    ss8 = regexp(ss7,'_E','split');
    FFs = ss8{1,1}(1);
     FF = sscanf(char(FFs),'%f');
    EEs = ss8{1,1}(2);
     EE = sscanf(char(EEs),'%f');

    if rpm==0
        outv = [NN SS FF EE min(sigmav) qqq min(Stdev) WWWStd WWWmean coeff
coeffN]; %(((coeff(3)-Hz)^2)/Hz)];
        outvv = [outvv; outv];
    else
        outv = [NN SS FF EE min(sigmav) qqq min(Stdev) WWWStd WWWmean coeff
coeffN (((coeff(3)-Hz)^2)/Hz) locrate];
        outvv = [outvv; outv];
    end

    if windowFlag==1
      save('windowYY5.txt', 'outvv', '-ascii')
    else
      save('incremental.txt', 'outvv', '-ascii')
    end

end %bigiter
```

Appendix B.3: Matlab Code for Analysing Hydrocyclone Trajectory Data

```matlab
%By Joshua Sovechles & Darryel Boucher, 2016

%INITIALIZATION
%-------------------------------------------------------------------------%
clear all; clc; close all; format shortEng;

%Load location data set (file provided by TRACK.EXE) - 1 000 000 is max
number of row to be read and headliners removes written information in each
file
%--------------------------------%
[T, X, Y, Z, Nbevent, Error] = textread('HY_21_K02_N100_S100_F45_E50.a01','%f
%f %f %f %f %f',1000000,'headerlines',16);
Traw=T; % T: Time (ms)
Xraw=X; % X: X axis coordinate (mm)
Yraw=Y; % Y: Y axis coordinate (mm)
Zraw=Z; % Z: Z axis coordinate (mm)


T=T/1000; %From (ms) to (s).
id=find(T);


%%%%%%%%%%SWITCHES%%%%%%%%%%%%%
% 1 = On / 0 = Off --- Determine what features of the code you wish to use
SwitchInitialDataFix=0;
SwitchDataRefinement=0;    % Turn off when using SwitchReuseDataFiltered
SwitchSplitPass=0;         % Turn off when using SwitchReuseDataFiltered
SwitchManuallyremovedata=0; % Turn off when using SwitchReuseDataFiltered
SwitchReuseDataFiltered=1;  % Turn on once you have already filtered your
data once

SwitchDataFit=0;              % Turn off when using SwitchReuseDataFit
SwitchReuseDataFit=0;         % Turn on once you have already fit your data
once

SwitchVelocityCalculations=0;
SwitchToroidBinning=0;     % SwitchVelocityCalculations should also be
turned on when this is used
SwitchVolumetricBinning=0;  % SwitchVelocityCalculations should also be
turned on when this is used
SwitchFigures=0;
SwitchMovie=0;
%%%%%%%%%%%% INPUT PARAMETERS %%%%%%%%%%%%%

% Data Refinement Inputs
Xtranslation= -10; %Field of view translation X - making the origin the
centre of your equipment
Ytranslation= 200;
Ztranslation= 1;
Xrotation= 0; %Field of view rotation around X
Yrotation= 0;
Zrotation= 0.95;
StartTime= 0; % Start time for data analysis
EndTime= 500;
MaxXvalue= 100; % Max range of field of view X
```

```matlab
MinXvalue= -100; % Min range of field of view X
MaxYvalue= 400;
MinYvalue= 0;
MaxZvalue= 100;
MinZvalue= -100;

% Pass Split Inputs
PassMinNumLoc=100; %Minimum Number of Locations per pass
MaxNumLocations=10000; %Maximum Number of Locations per pass
MinNumberofPass=8; %Minimum Number of Passes (can set at zero if unsure -
just used for process speed)
MaxTimeInterval=0.01; %Max Time between consecutive points to be kept
RemData=[1.984 2.37; 113.456 113.785; 122.97 123.312; 132.895 133.32;
         141.9 142.255; 160.325 160.72; 168.183 168.52; 182.18 182.6];

%Fitting Inputs
IntervalLength=0.01; % Seconds
IntervalOverlap=0.25; %Fraction
NumberofPolynomialPieces=8;
OutputLocationRate=10000; % Hz
MinNumberofPointsPerSegment=50; %If number of data points is below this
number there will be no fit for this interval
OrderofSpline=4; %Order of the spline 4=cubic spline, 2=linear

% Binning Inputs
BinSize=2; %(mm) - Bin size for output graphs
BinAngle=2; % (°) - Bin angle in degrees for volumetric binning output graphs
MinNumPtsBin=0; % Minimum Number of points needed in each bin

%%%%%%%%%%%%%%%%% END INPUTS %%%%%%%%%%%%%%%%%%%%%%%%%%

%%%%%%%%%%%%%%%%% LOAD PREFILTERED DATA %%%%%%%%%%%%%%%%
if SwitchReuseDataFiltered==1;
    if SwitchDataRefinement==1;
        disp(['SwitchDataRefinement must be turned off if reusing already
filtered data.'])
        return
    else
        if SwitchSplitPass==1;
            disp(['SwitchSplitPass must be turned off if reusing already
filtered data.'])
            return
        else
            if exist('Datafiltered.mat', 'file') == 2

                %[T, X, Y, Z] = textread('Datafiltered.mat','%f %f %f
%f',1000000);

load('Datafiltered','T','X','Y','Z','nbpass','pT','pX','pY','pZ','n');
                figure (01)
                plot(T,X,'bo','LineWidth',1,'MarkerSize',3);
                title('Processed Data')
                xlabel('time (s)','FontSize',20)
                ylabel('x coordinates (mm)','FontSize',20)
                axis([StartTime EndTime MinXvalue MaxXvalue])
```

```matlab
                disp(['Number of passes: ',num2str(nbpass)])

            else
                % File does not exist.
                disp(['File does not exist, rerun with SwitchDataFit turned
on.'])
                return
            end
        end
    end
end


%%%%%%%%%%%%%%%% END LOAD PREFILTERED DATA %%%%%%%%%%%%%%%%%

%%%%%%%%%%%%%%%%%%%%%% DATA PREPARATION%%%%%%%%%%%%%%%%%%%%%%

if SwitchDataRefinement==1

%Center view on geometry - Translation of X, Y, & Z axis (mm)
X=X+Xtranslation;
Y=Y+Ytranslation;
Z=Z+Ztranslation;

%Rotate locations to align x, y, z axis to geometry (degrees)
(deg/180*pi()=rad)
thetaX=Xrotation/180*pi();
thetaY=Yrotation/180*pi();
thetaZ=Zrotation/180*pi();

RX = [1,0,0;0,cos(thetaX),sin(thetaX);0,-sin(thetaX),cos(thetaX)]; % Rotation
matrix on X
RY = [cos(thetaY),0,-sin(thetaY);0,1,0;sin(thetaY),0,cos(thetaY)];
RZ = [cos(thetaZ),sin(thetaZ),0;-sin(thetaZ),cos(thetaZ),0;0,0,1];

Locations=[X Y Z]; %Creation of a matrix to be rotated
Locations=Locations*RX; %Applying the rotation around X axis
Locations=Locations*RY;
Locations=Locations*RZ;

X=Locations (:,1); %Replacing with the new rotated coordinates
Y=Locations (:,2);
Z=Locations (:,3);

if SwitchInitialDataFix==1;
    figure (666)
    plot3(X,Y,Z,'.')
    grid on
    xlabel('x coordinates (mm)','FontSize',12)
    ylabel('y coordinates (mm)','FontSize',12)
    zlabel('Z coordinates (mm)','FontSize',12)
end

figure(01)
```

```matlab
subplot(2,1,1)
plot(T,X,'b.','LineWidth',1,'MarkerSize',5);
title('Raw Data')
xlabel('time (s)','FontSize',12)
ylabel('x coordinates (mm)','FontSize',12)
axis([StartTime EndTime MinXvalue MaxXvalue])
grid on
end
%%%%%%%%%%%%%%% END DATA PREPARATION %%%%%%%%%%%%%%%%%%%%%

%%%%%%%%%%%%%%%%%% DATA REFINEMENT %%%%%%%%%%%%%%%%%%%%%

[T, index32, ~] = unique(T(:, 1), 'rows');
X=X(index32);
Y=Y(index32);
Z=Z(index32);

Tmin=StartTime; %Remove value with T value lower than (s)
Tmax=EndTime; %Remove value with T value higher than (s)
tT=(T>=Tmin & T<Tmax);

Xmin=MinXvalue; %Remove points with X value lower than (mm)
Xmax=MaxXvalue;  %Remove points with X value higher than (mm)
tX=(X>=Xmin & X<Xmax);

Ymin=MinYvalue;
Ymax=MaxYvalue;
tY=(Y>=Ymin & Y<Ymax);

Zmin=MinZvalue;
Zmax=MaxZvalue;
tZ=(Z>=Zmin & Z<Zmax);

SelectIni=ones(size(T)); %Creating a array with true (1) for each existing
locations
SelectIni=SelectIni.*tT.*tX.*tY.*tZ; %Applying the condition to convert from
true (1) to false (0) if locations to be rejected
SelectIni=SelectIni>0;

T=T(SelectIni); %Keep only the initial data corresponding to boundaries (for
comparison)
X=X(SelectIni);
Y=Y(SelectIni);
Z=Z(SelectIni);

%%%%%%%%%%%%%%%%%% END DATA REFINEMENT %%%%%%%%%%%%%%%%%%%%%%%%%%

%%%%%%%%%%%%%%%%%%%%%%%%SPLITING DATA INTO INDIVIDUAL PASSES%%%%%%%%%%%%%%%%%%%%%
if SwitchSplitPass==1

    if isempty(T)
        nbpass=0;
        disp(['Number of passes: ',num2str(nbpass)])
        return
    else
```

```matlab
        maxlength=MaxNumLocations; %Max number of location in a pass
        pcount=0; %initialise pass count


        pTadd=zeros(maxlength,1); pTadd(:)=NaN; %Creating an array for the
first passes with every array value to Not a Number marker
        pTaddreset=pTadd; %Creating an array for the pass time reseted to 0
at the begining of the pass
        pXadd=pTadd; %Array for the X value of each location of the pass
        pYadd=pTadd;
        pZadd=pTadd;


        aTi=0;
        Treset=T(1); %used to make pass time starting at 0.
        minlocpass=PassMinNumLoc; %min number of location per pass
        tic
        for i=1:length(T)-1
            if T(i+1)-T(i)<MaxTimeInterval %checking time interval between
point i and i+1 and detecting end of pass if time too long
                aTi=aTi+1; %Counting the location rank in the pass
                pTadd(aTi)=T(i); %attributin the T value to the pass
                pTaddreset(aTi)=T(i)-Treset; %attributing the reseted time
value to the pass
                pXadd(aTi)=X(i); %attributin the X value to the pass
                pYadd(aTi)=Y(i);
                pZadd(aTi)=Z(i);

                pTaddlast=pTadd;
                pTaddlast(isnan(pTaddlast))=[];
                lastvaluepTadd=(pTaddlast(length(pTaddlast)));

                if pcount > MinNumberofPass
                    if lastvaluepTadd==T(length(T)-1)
                        if aTi>minlocpass

                            pcount=pcount+1; %a new pass has been completed

                            pT=[pT pTadd]; %addng the pass to the T matrix of
passes
                            pTreset=[pTreset pTaddreset];
                            pX=[pX pXadd];
                            pY=[pY pYadd];
                            pZ=[pZ pZadd];
                        end
                    end
                end
            else
                if pcount==0 %(if time between location is too long, means
end of pass), check if first pass
                    if aTi>minlocpass %Check how many location per pass
                        % only keep the one with enough location
                        pcount=pcount+1; %a new pass has been completed

                        pT=pTadd; %attributing the pass to the T matrix of
pass
```

212

```matlab
                        pTreset=pTaddreset;
                        pX=pXadd;
                        pY=pYadd;
                        pZ=pZadd;
                    end

                    pTadd(:)=NaN; %Reseting the pass array
                    pTaddreset=pTadd;
                    pXadd=pTadd;
                    pYadd=pTadd;
                    pZadd=pTadd;

                    aTi=0; %reseting the location rank in the pass
                    Treset=T(i+1); %getting the time of the first location of
the next pass as the reset time

                else %if not first pass
                    if aTi>minlocpass

                        pcount=pcount+1; %a new pass has been completed

                        pT=[pT pTadd]; %addng the pass to the T matrix of
passes
                        pTreset=[pTreset pTaddreset];
                        pX=[pX pXadd];
                        pY=[pY pYadd];
                        pZ=[pZ pZadd];
                    end

                    pTadd(:)=NaN; %Reseting the pass array
                    pTaddreset=pTadd;
                    pXadd=pTadd;
                    pYadd=pTadd;
                    pZadd=pTadd;

                    aTi=0; %reseting the location rank in the pass
                    Treset=T(i+1); %getting the time of the first location of
the next pass as the reset time
                end
            end
        end
        toc

        %Reconstruct the dataset with only the good passes
        %----------------------------------------------------------------
-----%
        [m,n]=size(pT);
        nbpass=n;
        T=[]; %Reinitialise the T array
        X=[];
        Y=[];
        Z=[];

        if SwitchManuallyremovedata==1  %Maunally remove additional bad data
```

```matlab
        for i=1:n
            RunT=pT(:,i);
            RunX=pX(:,i);
            RunY=pY(:,i);
            RunZ=pZ(:,i);
            RunselectT(1:MaxNumLocations)=NaN;
            RunselectX(1:MaxNumLocations)=NaN;
            RunselectY(1:MaxNumLocations)=NaN;
            RunselectZ(1:MaxNumLocations)=NaN;
            RungooddataT=RunT(RunT > (RemData(i,1)) & RunT <
(RemData(i,2)));
            RungooddataX=RunX(RunT > (RemData(i,1)) & RunT <
(RemData(i,2)));
            RungooddataY=RunY(RunT > (RemData(i,1)) & RunT <
(RemData(i,2)));
            RungooddataZ=RunZ(RunT > (RemData(i,1)) & RunT <
(RemData(i,2)));
            RunselectT(1:length(RungooddataT))=RungooddataT;
            RunselectX(1:length(RungooddataT))=RungooddataX;
            RunselectY(1:length(RungooddataT))=RungooddataY;
            RunselectZ(1:length(RungooddataT))=RungooddataZ;
            pT(:,i)=RunselectT';
            pX(:,i)=RunselectX';
            pY(:,i)=RunselectY';
            pZ(:,i)=RunselectZ';
        end
    end

    for i=1:n; %put all T,X,Y,Z values back into 1 array
        T=cat(1,T,pT(:,i));
        X=cat(1,X,pX(:,i));
        Y=cat(1,Y,pY(:,i));
        Z=cat(1,Z,pZ(:,i));
    end

    T(isnan(T))=[]; %remove the NaN from the array
    X(isnan(X))=[];
    Y(isnan(Y))=[];
    Z(isnan(Z))=[];

    pT0=pT;
    for i=1:n
        pT0(:,i)=pT0(:,i)-(pT0(1,i));
    end
end

pT0(isnan(pT0(:,1)),:)=[];
subplot(2,1,2)
plot(T,X,'bo','LineWidth',1,'MarkerSize',3);
title('Processed Data')
xlabel('time (s)','FontSize',20)
ylabel('x coordinates (mm)','FontSize',20)
axis([StartTime EndTime MinXvalue MaxXvalue])
grid on

figure (666)
```

214

```matlab
    plot3(X,Y,Z,'.')
    grid on
    xlabel('x coordinates (mm)','FontSize',12)
    ylabel('y coordinates (mm)','FontSize',12)
    zlabel('Z coordinates (mm)','FontSize',12)

    disp(['Number of passes: ',num2str(nbpass)])
    save('Datafiltered','T','X','Y','Z','nbpass','pT','pX','pY','pZ','n')
end

%%%%%%%%%%%%%%%%%%%%%% FINISH SPLIT DATA %%%%%%%%%%%%%%%%%%%%%%%%%%%

%%%%%%%%%%%%%%%%%%%% NEW FIT AND INTERPOLATION %%%%%%%%%%%%%%%%%%%%%%%%%

if SwitchDataFit==1

    pW=pT.^0;
    Tfit=[];
    Xfit=[];
    Xfitvel=[];
    Xfitacc=[];
    Yfit=[];
    Yfitvel=[];
    Yfitacc=[];
    Zfit=[];
    Zfitvel=[];
    Zfitacc=[];
    tic
    for i=1:n
        TData=pT(:,i);
        XData=pX(:,i);
        YData=pY(:,i);
        ZData=pZ(:,i);
        WData=pW(:,i);
        WDataedit=WData;
        WDataedit(isnan(WDataedit))=[];
        WDend=length(WDataedit);
        WDid03=ceil(0.001*WDend);
        WDid08=ceil(0.10*WDend);
        WDid57=ceil(0.57*WDend);
        WDid86=ceil(0.86*WDend);
        WDid96=ceil(0.96*WDend);
        WDataedit(WDid03:WDid08)=50;
        WDataedit(WDid08:WDid57)=5;
        WDataedit(WDid57:(WDid86-1))=50;
        WDataedit(WDid86:(WDid96-1))=100;
        WDataedit(WDid96:(WDend))=1000;
        WData(1:WDend)=WDataedit;
        WDataReset=WData;

        % Set up fittype and options.
        ft = fittype( 'smoothingspline' );
        opts = fitoptions( 'Method', 'SmoothingSpline' );
        opts.SmoothingParam = 0.999999;
        opts.Weights = WData;
```

```matlab
        % Fit model to data.
        [TData, XData, WData] = prepareCurveData( TData, XData, WData );
        opts.Weights = WData;
        [fitresult, gof] = fit( TData, XData, ft, opts );
        TTT = linspace(TData(1),TData(end),(2*numel(TData)))';
        YYY = zeros(numel(TTT), 1);

        for qq = 1:size(fitresult.p.coefs, 1)
            a = find(TTT >= fitresult.p.breaks(qq) & TTT <
fitresult.p.breaks(qq + 1));
            p = fitresult.p.coefs(qq, :);
            YYY(a) = p(1)*(TTT(a) - fitresult.p.breaks(qq)).^3 + p(2)*(TTT(a)
- fitresult.p.breaks(qq)).^2  + p(3)*(TTT(a) - fitresult.p.breaks(qq)) +
p(4);
        end

        YYYvel=0.001*diff(YYY)./diff(TTT);
        YYYacc=diff(YYYvel)./diff(TTT(1:length(YYYvel)));
        YYYacc(length(YYYacc))=[];
        eval(['Xfitvel' num2str(i) '= YYYvel;']);
        eval(['Xfitacc' num2str(i) '= YYYacc;']);
        eval(['Xfit' num2str(i) '= YYY;']);
        Xfit=[Xfit; YYY(1:length(YYYacc))];
        Xfitvel=[Xfitvel; YYYvel(1:length(YYYacc))];
        Xfitacc=[Xfitacc; YYYacc];

        % Fit model to data.
        TData=pT(:,i);
        WData=WDataReset;
        [TData, YData, WData] = prepareCurveData( TData, YData, WData );
        opts.Weights = WData;
        [fitresult, gof] = fit( TData, YData, ft, opts );
        YYY = zeros(numel(TTT), 1);

        for qq = 1:size(fitresult.p.coefs, 1)
            a = find(TTT >= fitresult.p.breaks(qq) & TTT <
fitresult.p.breaks(qq + 1));
            p = fitresult.p.coefs(qq, :);
            YYY(a) = p(1)*(TTT(a) - fitresult.p.breaks(qq)).^3 + p(2)*(TTT(a)
- fitresult.p.breaks(qq)).^2  + p(3)*(TTT(a) - fitresult.p.breaks(qq)) +
p(4);
        end

        YYYvel=0.001*diff(YYY)./diff(TTT);
        YYYacc=diff(YYYvel)./diff(TTT(1:length(YYYvel)));
        YYYacc(length(YYYacc))=[];
        eval(['Yfitvel' num2str(i) '= YYYvel;']);
        eval(['Yfitacc' num2str(i) '= YYYacc;']);
        eval(['Yfit' num2str(i) '= YYY;']);
        Yfit=[Yfit; YYY(1:length(YYYacc))];
        Yfitvel=[Yfitvel; YYYvel(1:length(YYYacc))];
        Yfitacc=[Yfitacc; YYYacc];

        % Fit model to data.
```

```matlab
        TData=pT(:,i);
        WData=WDataReset;
        [TData, ZData, WData] = prepareCurveData( TData, ZData, WData );
        opts.Weights = WData;
        [fitresult, gof] = fit( TData, ZData, ft, opts );
        YYY = zeros(numel(TTT), 1);

        for qq = 1:size(fitresult.p.coefs, 1)
            a = find(TTT >= fitresult.p.breaks(qq) & TTT <
fitresult.p.breaks(qq + 1));
            p = fitresult.p.coefs(qq, :);
            YYY(a) = p(1)*(TTT(a) - fitresult.p.breaks(qq)).^3 + p(2)*(TTT(a)
- fitresult.p.breaks(qq)).^2  + p(3)*(TTT(a) - fitresult.p.breaks(qq)) +
p(4);
        end

        YYYvel=0.001*diff(YYY)./diff(TTT);
        YYYacc=diff(YYYvel)./diff(TTT(1:length(YYYvel)));
        YYYacc(length(YYYacc))=[];
        eval(['Zfitvel' num2str(i) '= YYYvel;']);
        eval(['Zfitacc' num2str(i) '= YYYacc;']);
        eval(['Zfit' num2str(i) '= YYY;']);
        Zfit=[Zfit; YYY(1:length(YYYacc))];
        Zfitvel=[Zfitvel; YYYvel(1:length(YYYacc))];
        Zfitacc=[Zfitacc; YYYacc];
        eval(['Tfit' num2str(i) '= TTT;']);
        Tfit=[Tfit; TTT(1:length(YYYacc))];
    end

    toc

    figure (331)
    subplot(3,1,1)
    plot(T,X,'o',Tfit,Xfit,'-.')
    axis([Tmin Tmax Xmin Xmax])
    xlabel('T (s)','FontSize',20);
    ylabel('X (mm)','FontSize',20);
    grid on
    legend('Fit', 'Initial locations')
    set(gca,'FontSize',20)

    subplot(3,1,2)
    plot(T,Y,'o',Tfit,Yfit,'-.')
    axis([Tmin Tmax Ymin Ymax])
    xlabel('T (s)','FontSize',20);
    ylabel('Y (mm)','FontSize',20);
    grid on
    set(gca,'FontSize',20)

    subplot(3,1,3)
    plot(T,Z,'o',Tfit,Zfit,'-.')
    axis([Tmin Tmax Zmin Zmax])
    xlabel('T (s)','FontSize',20);
    ylabel('Z (mm)','FontSize',20);
    grid on
    set(gca,'FontSize',20)
```

```matlab
    figure (332)
    subplot(3,1,1)
    plot(Tfit,Xfitvel,'o')
    subplot(3,1,2)
    plot(Tfit,Yfitvel,'o')
    subplot(3,1,3)
    plot(Tfit,Zfitvel,'o')
    figure (333)
    subplot(3,1,1)
    plot(Tfit,Xfitacc,'o')
    subplot(3,1,2)
    plot(Tfit,Yfitacc,'o')
    subplot(3,1,3)
    plot(Tfit,Zfitacc,'o')


save('Datafitvel3','Tfit','Xfit','Yfit','Zfit','Xfitvel','Yfitvel','Zfitvel')


end


%%%%%%%%%%%%%%%%%%% END NEW FIT AND INTERPOLATION %%%%%%%%%%%%%%%%%%


%%%%%%%%%%%%%%%%%%% REUSE DATA FIT %%%%%%%%%%%%%%%%%%%%%%%%%%%%%%%%%


if SwitchReuseDataFit==1
    if SwitchDataFit==1
        disp(['SwitchDataFit must be turned off if reusing already fit
data.'])
        return
    else
        if exist('Datafitvel3.mat', 'file') == 2 % File exists.


load('Datafitvel3','Tfit','Xfit','Yfit','Zfit','Xfitvel','Yfitvel','Zfitvel')

            idfit=find(Tfit);
            locrunall=[];
            loctimeall=[];
            hzall=[];

            for i=1:n
                pts=pT(:,i);
                pts(isnan(pts))=[];
                locrun=length(pts);
                locrunall=[locrunall locrun];
                loctime=pts(end)-pts(1);
                loctimeall=[loctimeall loctime];
                hz=locrun/loctime;
                hzall=[hzall hz];
            end

            disp(['No. Locations: ',num2str(locrunall)])
            disp(['Time of pass: ',num2str(loctimeall)])
```

```matlab
disp(['Location Rate: ',num2str(hzall)])
AAHz=[hzall; loctimeall; locrunall];

figure(341)
subplot(3,1,1)
plot(Tfit,Xfit,'r.-','LineWidth',2,'MarkerSize',5);
hold on
plot(T,X,'bo','LineWidth',1,'MarkerSize',3);
axis([Tmin Tmax Xmin Xmax])
xlabel('T (s)','FontSize',20);
ylabel('X (mm)','FontSize',20);
grid on
legend('Fit', 'Initial locations')
set(gca,'FontSize',20)

subplot(3,1,2)
plot(Tfit,Yfit,'r.-','LineWidth',2,'MarkerSize',5);
hold on
plot(T,Y,'bo','LineWidth',1,'MarkerSize',3);
axis([Tmin Tmax Ymin Ymax])
xlabel('T (s)','FontSize',20);
ylabel('Y (mm)','FontSize',20);
grid on
set(gca,'FontSize',20)

subplot(3,1,3)
plot(Tfit,Zfit,'r.-','LineWidth',2,'MarkerSize',5);
hold on
plot(T,Z,'bo','LineWidth',1,'MarkerSize',3);
axis([Tmin Tmax Zmin Zmax])
xlabel('T (s)','FontSize',20);
ylabel('Z (mm)','FontSize',20);
grid on
set(gca,'FontSize',20)

figure(342)
plot3(Xfit,Yfit,Zfit,'o','MarkerSize',3)
axis([Xmin Xmax Ymin Ymax Zmin Zmax])
xlabel('X (mm)','FontSize',20);
ylabel('Y (mm)','FontSize',20);
zlabel('Z (mm)','FontSize',20);
grid on
set(gca,'FontSize',20)

figure (332)
subplot(3,1,1)
plot(Tfit,Xfitvel,'o')
subplot(3,1,2)
plot(Tfit,Yfitvel,'o')
subplot(3,1,3)
plot(Tfit,Zfitvel,'o')
%     figure (333)
%     subplot(3,1,1)
%     plot(Tfit,Xfitacc,'o')
%     subplot(3,1,2)
%     plot(Tfit,Yfitacc,'o')
```

```matlab
%             subplot(3,1,3)
%             plot(Tfit,Zfitacc,'o')

            if SwitchSplitPass==1
                disp(['Number of passes: ',num2str(nbpass)])
            end

        else
            % File does not exist.
            disp(['File does not exist, rerun with SwitchDataFit turned
on.'])
            return
        end
    end
end


%%%%%%%%%%% VELOCITY CALCULATIONS FOR FITTED OR PROCESSED DATA
%%%%%%%%%%%%%

if SwitchVelocityCalculations==1
    if SwitchDataFit==1 || SwitchReuseDataFit==1
        %Converting to polar
        Rfit=(Xfit.^2+Zfit.^2).^(1/2);  % Radius around y axis
        %Afit=atan2(Zfit,Xfit);

        % For continuously growing theta
        Afit=Tfit; %Angle from first position on xz plan
        Afit(1)=0;
        Afitprev=0;
        for i=2:length(Tfit)
            vect1=[Xfit(i-1) 0 Zfit(i-1)];
            vect2=[Xfit(i) 0 Zfit(i)];

Afit(i)=Afitprev+atan2(norm(cross(vect1,vect2)),dot(vect1,vect2));
            Afitprev=Afit(i);
        end

        vRfit=Tfit; %Radial velocity
        endi=0;
        starti=0;
        for i=1:length(Tfit)
            j=i;
            if i<6 %if you are at the begining of the pass, use the later
points
                starti=1; i=i+6;
            end
            if i>=(length(Tfit)-6) %if you are at the end of the pass, use
the previous pooints
                endi=1; i=i-6;
            end
            vRfit(j)=...
                0.10*((Rfit(i+5)-Rfit(i-0))/(Tfit(i+5)-Tfit(i-0)))+...
                0.15*((Rfit(i+4)-Rfit(i-1))/(Tfit(i+4)-Tfit(i-1)))+...
                0.25*((Rfit(i+3)-Rfit(i-2))/(Tfit(i+3)-Tfit(i-2)))+...
                0.25*((Rfit(i+2)-Rfit(i-3))/(Tfit(i+2)-Tfit(i-3)))+...
                0.15*((Rfit(i+1)-Rfit(i-4))/(Tfit(i+1)-Tfit(i-4)))+...
```

```matlab
                    0.10*((Rfit(i+0)-Rfit(i-5))/(Tfit(i+0)-Tfit(i-5)));
            if starti==1 %reset i to its original value
                i=i-6;
            end
            if endi==1 %reset i to its original value
                i=i+6;
            end
            starti=0; endi=0;
        end
        vRfit=vRfit/1000; %from mm/s to m/s

        vAfit=Tfit; %Angular velocity
        endi=0;
        starti=0;
        for i=1:length(Tfit)
            j=i;
            if i<6 %if you are at the begining of the pass, use the later
points
                starti=1; i=i+6;
            end
            if i>=(length(Tfit)-6) %if you are at the end of the pass, use
the previous pooints
                endi=1; i=i-6;
            end
            vAfit(j)=...
                    0.10*((Afit(i+5)-Afit(i-0))/(Tfit(i+5)-Tfit(i-0)))+...
                    0.15*((Afit(i+4)-Afit(i-1))/(Tfit(i+4)-Tfit(i-1)))+...
                    0.25*((Afit(i+3)-Afit(i-2))/(Tfit(i+3)-Tfit(i-2)))+...
                    0.25*((Afit(i+2)-Afit(i-3))/(Tfit(i+2)-Tfit(i-3)))+...
                    0.15*((Afit(i+1)-Afit(i-4))/(Tfit(i+1)-Tfit(i-4)))+...
                    0.10*((Afit(i+0)-Afit(i-5))/(Tfit(i+0)-Tfit(i-5)));

%                   0.5*((Afit(i+1)-Afit(i-0))/(Tfit(i+1)-Tfit(i-0)))+...
%                   0.5*((Afit(i+0)-Afit(i-1))/(Tfit(i+0)-Tfit(i-1)));
            if starti==1 %reset i to its original value
                i=i-6;
            end
            if endi==1 %reset i to its original value
                i=i+6;
            end
            starti=0; endi=0;
        end

        vXfit=Tfit; %X velocity
        endi=0;
        starti=0;
        for i=1:length(Tfit)
            j=i;
            if i<6 %if you are at the begining of the pass, use the later
points
                starti=1; i=i+6;
            end
            if i>=(length(Tfit)-6) %if you are at the end of the pass, use
the previous pooints
                endi=1; i=i-6;
            end
```

```
        vXfit(j)=...
            0.10*((Xfit(i+5)-Xfit(i-0))/(Tfit(i+5)-Tfit(i-0)))+...
            0.15*((Xfit(i+4)-Xfit(i-1))/(Tfit(i+4)-Tfit(i-1)))+...
            0.25*((Xfit(i+3)-Xfit(i-2))/(Tfit(i+3)-Tfit(i-2)))+...
            0.25*((Xfit(i+2)-Xfit(i-3))/(Tfit(i+2)-Tfit(i-3)))+...
            0.15*((Xfit(i+1)-Xfit(i-4))/(Tfit(i+1)-Tfit(i-4)))+...
            0.10*((Xfit(i+0)-Xfit(i-5))/(Tfit(i+0)-Tfit(i-5)));
        if starti==1 %reset i to its original value
            i=i-6;
        end
        if endi==1 %reset i to its original value
            i=i+6;
        end
        starti=0; endi=0;
    end
    vXfit=vXfit/1000; %from mm/s to m/s

    vYfit=Tfit; %Y velocity
    endi=0;
    starti=0;
    for i=1:length(Tfit)
        j=i;
        if i<6 %if you are at the begining of the pass, use the later
points
            starti=1; i=i+6;
        end
        if i>=(length(Tfit)-6) %if you are at the end of the pass, use
the previous pooints
            endi=1; i=i-6;
        end
        vYfit(j)=...
            0.10*((Yfit(i+5)-Yfit(i-0))/(Tfit(i+5)-Tfit(i-0)))+...
            0.15*((Yfit(i+4)-Yfit(i-1))/(Tfit(i+4)-Tfit(i-1)))+...
            0.25*((Yfit(i+3)-Yfit(i-2))/(Tfit(i+3)-Tfit(i-2)))+...
            0.25*((Yfit(i+2)-Yfit(i-3))/(Tfit(i+2)-Tfit(i-3)))+...
            0.15*((Yfit(i+1)-Yfit(i-4))/(Tfit(i+1)-Tfit(i-4)))+...
            0.10*((Yfit(i+0)-Yfit(i-5))/(Tfit(i+0)-Tfit(i-5)));
        if starti==1 %reset i to its original value
            i=i-6;
        end
        if endi==1 %reset i to its original value
            i=i+6;
        end
        starti=0; endi=0;
    end
    vYfit=vYfit/1000; %from mm/s to m/s

    vZfit=Tfit; %Z velocity
    endi=0;
    starti=0;
    for i=1:length(Tfit)
        j=i;
        if i<6 %if you are at the begining of the pass, use the later
points
            starti=1; i=i+6;
        end
```

```matlab
        if i>=(length(Tfit)-6) %if you are at the end of the pass, use
the previous pooints
                endi=1; i=i-6;
        end
        vZfit(j)=...
            0.10*((Zfit(i+5)-Zfit(i-0))/(Tfit(i+5)-Tfit(i-0)))+...
            0.15*((Zfit(i+4)-Zfit(i-1))/(Tfit(i+4)-Tfit(i-1)))+...
            0.25*((Zfit(i+3)-Zfit(i-2))/(Tfit(i+3)-Tfit(i-2)))+...
            0.25*((Zfit(i+2)-Zfit(i-3))/(Tfit(i+2)-Tfit(i-3)))+...
            0.15*((Zfit(i+1)-Zfit(i-4))/(Tfit(i+1)-Tfit(i-4)))+...
            0.10*((Zfit(i+0)-Zfit(i-5))/(Tfit(i+0)-Tfit(i-5)));
        if starti==1 %reset i to its original value
            i=i-6;
        end
        if endi==1 %reset i to its original value
            i=i+6;
        end
        starti=0; endi=0;
    end

    vZfit=vZfit/1000; %from mm/s to m/s

    vMfit=(vXfit.^2+vYfit.^2+vZfit.^2).^(1/2); %3D velocity magnitude as
the sqrt of the sum of square of each axis speed

    figure(21)

    subplot(4,1,1)
    plot(Tfit,vRfit,'bo','LineWidth',2,'MarkerSize',2);
    axis([Tmin Tmax min(vRfit) max(vRfit)])
    xlabel('T (s)','FontSize',20);
    ylabel('vR (m/s)','FontSize',20);
    grid on
    set(gca,'FontSize',20)

    subplot(4,1,2)
    plot(Tfit,vAfit,'bo','LineWidth',2,'MarkerSize',2);
    axis([Tmin Tmax min(vAfit) max(vAfit)])
    xlabel('T (s)','FontSize',20);
    ylabel('vA (m/s)','FontSize',20);
    grid on
    set(gca,'FontSize',20)

    subplot(4,1,3)
    plot(Tfit,vYfit,'bo','LineWidth',2,'MarkerSize',2);
    axis([Tmin Tmax min(vYfit) max(vYfit)])
    xlabel('T (s)','FontSize',20);
    ylabel('vY (m/s)','FontSize',20);
    grid on
    set(gca,'FontSize',20)

    subplot(4,1,4)
    plot(Tfit,vMfit,'bo','LineWidth',2,'MarkerSize',2);
    axis([Tmin Tmax min(vMfit) max(vMfit)])
    xlabel('T (s)','FontSize',20);
```

```matlab
        ylabel('vM (m/s)','FontSize',20);
        grid on
        set(gca,'FontSize',20)

        figure(22)

        subplot(4,1,1)
        plot(Tfit,vXfit,'bo','LineWidth',2,'MarkerSize',2);
        axis([Tmin Tmax min(vXfit) max(vXfit)])
        xlabel('T (s)','FontSize',20);
        ylabel('vX (m/s)','FontSize',20);
        grid on
        set(gca,'FontSize',20)

        subplot(4,1,2)
        plot(Tfit,vYfit,'bo','LineWidth',2,'MarkerSize',2);
        axis([Tmin Tmax min(vYfit) max(vYfit)])
        xlabel('T (s)','FontSize',20);
        ylabel('vY (m/s)','FontSize',20);
        grid on
        set(gca,'FontSize',20)

        subplot(4,1,3)
        plot(Tfit,vZfit,'bo','LineWidth',2,'MarkerSize',2);
        axis([Tmin Tmax min(vZfit) max(vZfit)])
        xlabel('T (s)','FontSize',20);
        ylabel('vZ (m/s)','FontSize',20);
        grid on
        set(gca,'FontSize',20)

        subplot(4,1,4)
        plot(Tfit,vMfit,'bo','LineWidth',2,'MarkerSize',2);
        axis([Tmin Tmax min(vMfit) max(vMfit)])
        xlabel('T (s)','FontSize',20);
        ylabel('vM (m/s)','FontSize',20);
        grid on
        set(gca,'FontSize',20)

    else

        Rvel=(X.^2+Z.^2).^(1/2); %Radius around y axis

        Avel=T; %Angle from first position on xz plan
        Avel(1)=0;
        Avelprev=0;
        for i=2:length(T)
            vect1=[X(i-1) 0 Z(i-1)];
            vect2=[X(i) 0 Z(i)];

Avel(i)=Avelprev+atan2(norm(cross(vect1,vect2)),dot(vect1,vect2));
            Avelprev=Avel(i);
        end


        vR=T; %Radial velocity
```

```matlab
        endi=0;
        starti=0;
        for i=1:length(T)
            j=i;
            if i<6 %if you are at the begining of the pass, use the later
points
                starti=1; i=i+6;
            end
            if i>=(length(T)-6) %if you are at the end of the pass, use the
previous pooints
                endi=1; i=i-6;
            end
            vR(j)=...
                0.10*((Rvel(i+5)-Rvel(i-0))/(T(i+5)-T(i-0)))+...
                0.15*((Rvel(i+4)-Rvel(i-1))/(T(i+4)-T(i-1)))+...
                0.25*((Rvel(i+3)-Rvel(i-2))/(T(i+3)-T(i-2)))+...
                0.25*((Rvel(i+2)-Rvel(i-3))/(T(i+2)-T(i-3)))+...
                0.15*((Rvel(i+1)-Rvel(i-4))/(T(i+1)-T(i-4)))+...
                0.10*((Rvel(i+0)-Rvel(i-5))/(T(i+0)-T(i-5)));
            if starti==1 %reset i to its original value
                i=i-6;
            end
            if endi==1 %reset i to its original value
                i=i+6;
            end
            starti=0; endi=0;
        end
        vR=vR/1000; %from mm/s to m/s

        vA=T; %Angular velocity
        endi=0;
        starti=0;
        for i=1:length(T)
            j=i;
            if i<6 %if you are at the begining of the pass, use the later
points
                starti=1; i=i+6;
            end
            if i>=(length(T)-6) %if you are at the end of the pass, use the
previous pooints
                endi=1; i=i-6;
            end
            vA(j)=...
                0.5*((Avel(i+1)-Avel(i-0))/(T(i+1)-T(i-0)))+...
                0.5*((Avel(i+0)-Avel(i-1))/(T(i+0)-T(i-1)));
            %        0.10*((Afit(i+5)-Afit(i-0))/(Tfit(i+5)-Tfit(i-0)))+...
            %        0.15*((Afit(i+4)-Afit(i-1))/(Tfit(i+4)-Tfit(i-1)))+...
            %        0.25*((Afit(i+3)-Afit(i-2))/(Tfit(i+3)-Tfit(i-2)))+...
            %        0.25*((Afit(i+2)-Afit(i-3))/(Tfit(i+2)-Tfit(i-3)))+...
            %        0.15*((Afit(i+1)-Afit(i-4))/(Tfit(i+1)-Tfit(i-4)))+...
            %        0.10*((Afit(i+0)-Afit(i-5))/(Tfit(i+0)-Tfit(i-5)));
            if starti==1 %reset i to its original value
                i=i-6;
            end
            if endi==1 %reset i to its original value
                i=i+6;
            end
```

```matlab
                starti=0; endi=0;
        end

        vX=T; %X velocity
        endi=0;
        starti=0;
        for i=1:length(T)
            j=i;
            if i<6 %if you are at the begining of the pass, use the later
points
                starti=1; i=i+6;
            end
            if i>=(length(T)-6) %if you are at the end of the pass, use the
previous pooints
                endi=1; i=i-6;
            end
            vX(j)=...
                0.10*((X(i+5)-X(i-0))/(T(i+5)-T(i-0)))+...
                0.15*((X(i+4)-X(i-1))/(T(i+4)-T(i-1)))+...
                0.25*((X(i+3)-X(i-2))/(T(i+3)-T(i-2)))+...
                0.25*((X(i+2)-X(i-3))/(T(i+2)-T(i-3)))+...
                0.15*((X(i+1)-X(i-4))/(T(i+1)-T(i-4)))+...
                0.10*((X(i+0)-X(i-5))/(T(i+0)-T(i-5)));
            if starti==1 %reset i to its original value
                i=i-6;
            end
            if endi==1 %reset i to its original value
                i=i+6;
            end
            starti=0; endi=0;
        end
        vX=vX/1000; %from mm/s to m/s

        vY=T; %Y velocity
        endi=0;
        starti=0;
        for i=1:length(T)
            j=i;
            if i<6 %if you are at the begining of the pass, use the later
points
                starti=1; i=i+6;
            end
            if i>=(length(T)-6) %if you are at the end of the pass, use the
previous pooints
                endi=1; i=i-6;
            end
            vY(j)=...
                0.10*((Y(i+5)-Y(i-0))/(T(i+5)-T(i-0)))+...
                0.15*((Y(i+4)-Y(i-1))/(T(i+4)-T(i-1)))+...
                0.25*((Y(i+3)-Y(i-2))/(T(i+3)-T(i-2)))+...
                0.25*((Y(i+2)-Y(i-3))/(T(i+2)-T(i-3)))+...
                0.15*((Y(i+1)-Y(i-4))/(T(i+1)-T(i-4)))+...
                0.10*((Y(i+0)-Y(i-5))/(T(i+0)-T(i-5)));
            if starti==1 %reset i to its original value
                i=i-6;
            end
```

```matlab
            if endi==1 %reset i to its original value
                i=i+6;
            end
            starti=0; endi=0;
        end
        vY=vY/1000; %from mm/s to m/s

        vZ=T; %Z velocity
        endi=0;
        starti=0;
        for i=1:length(T)
            j=i;
            if i<6 %if you are at the begining of the pass, use the later
points
                starti=1; i=i+6;
            end
            if i>=(length(T)-6) %if you are at the end of the pass, use the
previous pooints
                endi=1; i=i-6;
            end
            vZ(j)=...
                0.10*((Z(i+5)-Z(i-0))/(T(i+5)-T(i-0)))+...
                0.15*((Z(i+4)-Z(i-1))/(T(i+4)-T(i-1)))+...
                0.25*((Z(i+3)-Z(i-2))/(T(i+3)-T(i-2)))+...
                0.25*((Z(i+2)-Z(i-3))/(T(i+2)-T(i-3)))+...
                0.15*((Z(i+1)-Z(i-4))/(T(i+1)-T(i-4)))+...
                0.10*((Z(i+0)-Z(i-5))/(T(i+0)-T(i-5)));
            if starti==1 %reset i to its original value
                i=i-6;
            end
            if endi==1 %reset i to its original value
                i=i+6;
            end
            starti=0; endi=0;
        end

        vZ=vZ/1000; %from mm/s to m/s

        vM=(vX.^2+vY.^2+vZ.^2).^(1/2); %3D velocity magnitude as the sqrt of
the sum of square of each axis speed

        figure(21)

        subplot(4,1,1)
        plot(T,vR,'bo','LineWidth',2,'MarkerSize',2);
        axis([Tmin Tmax min(vR) max(vR)])
        xlabel('T (s)','FontSize',20);
        ylabel('vR (m/s)','FontSize',20);
        grid on
        set(gca,'FontSize',20)

        subplot(4,1,2)
        plot(T,vA,'bo','LineWidth',2,'MarkerSize',2);
        axis([Tmin Tmax min(vA) max(vA)])
        xlabel('T (s)','FontSize',20);
        ylabel('vA (m/s)','FontSize',20);
```

227

```matlab
grid on
set(gca,'FontSize',20)

subplot(4,1,3)
plot(T,vY,'bo','LineWidth',2,'MarkerSize',2);
axis([Tmin Tmax min(vZ) max(vZ)])
xlabel('T (s)','FontSize',20);
ylabel('vY (m/s)','FontSize',20);
grid on
set(gca,'FontSize',20)

subplot(4,1,4)
plot(T,vM,'bo','LineWidth',2,'MarkerSize',2);
axis([Tmin Tmax min(vM) max(vM)])
xlabel('T (s)','FontSize',20);
ylabel('vM (m/s)','FontSize',20);
grid on
set(gca,'FontSize',20)

figure(22)

subplot(4,1,1)
plot(T,vX,'bo','LineWidth',2,'MarkerSize',2);
axis([Tmin Tmax min(vX) max(vX)])
xlabel('T (s)','FontSize',20);
ylabel('vX (m/s)','FontSize',20);
grid on
set(gca,'FontSize',20)

subplot(4,1,2)
plot(T,vY,'bo','LineWidth',2,'MarkerSize',2);
axis([Tmin Tmax min(vY) max(vY)])
xlabel('T (s)','FontSize',20);
ylabel('vY (m/s)','FontSize',20);
grid on
set(gca,'FontSize',20)

subplot(4,1,3)
plot(T,vZ,'bo','LineWidth',2,'MarkerSize',2);
axis([Tmin Tmax min(vZ) max(vZ)])
xlabel('T (s)','FontSize',20);
ylabel('vZ (m/s)','FontSize',20);
grid on
set(gca,'FontSize',20)

subplot(4,1,4)
plot(T,vM,'bo','LineWidth',2,'MarkerSize',2);
axis([Tmin Tmax min(vM) max(vM)])
xlabel('T (s)','FontSize',20);
ylabel('vM (m/s)','FontSize',20);
grid on
set(gca,'FontSize',20)

end
```

```matlab
    end

%%%%%%%%%%%%%%% END VELOCITY CALCULATIONS FOR FITTED DATA %%%%%%%%%%%%%%%%%%

%%%%%%%%%%%%%%% TOROID BINNING (WRAPPING INTO SINGLE PLANE) %%%%%%%%%%%%%%%%%

if SwitchToroidBinning==1
    if SwitchDataFit==1 || SwitchReuseDataFit==1
        if SwitchVelocityCalculations==0
            disp(['SwitchVelocityCalculations must be turned on for Toroid
Binning'])
        else
            binsize=BinSize; %Spacing of the square grid defining bins (mm)
(same as cubic bin)
            %binangle=(BinAngle/180)*pi;
            Rmin=0;
            Rmax=Xmax;
            Amin=-pi;
            Amax=pi;

            EdgesA=linspace(Amin,Amax,(180/BinAngle));
            EdgesR=[Rmin:binsize:Rmax]; % Creating the bins boundaries
            EdgesY=[Ymin:binsize:Ymax];

            nbbinA=(length(EdgesA)-1);
            nbbinR=(length(EdgesR)-1); % Counting the bins
            nbbinY=(length(EdgesY)-1);

            MatRCount=zeros(nbbinR,nbbinY); %Initialisation of a 2D (R, Y)
matrix to count location in the bins.
            MatRCenterR=MatRCount; %Initialisation of a 2D matrix to store R
location of the center of the bins.
            MatRCenterY=MatRCount;
            MatRT=MatRCount; %Initialisation of a 2D matrix to store Time in
the bins.
            MatRVol=MatRCount; %Volume of the bin
            MatRvMmean=MatRCount;
            MatRvMmode=MatRCount;
            MatRvMstd=MatRCount;
            MatRvMdis=cell([nbbinR nbbinY]);
            MatRvRmean=MatRCount;
            MatRvRmode=MatRCount;
            MatRvRstd=MatRCount;
            MatRvYmean=MatRCount;
            MatRvYmode=MatRCount;
            MatRvYstd=MatRCount;
            MatRvAmean=MatRCount;
            MatRvAmode=MatRCount;
            MatRvAstd=MatRCount;

            for jj=1:nbbinY
                ET=Tfit; %Set the matrix of locations
                ER=Rfit;
                EY=Yfit;
                Eid=idfit;
```

229

```
                EYmin=EdgesY(jj); %Selecting the bin Y lower boundary
                EYmax=EdgesY(jj+1); %Selecting the bin Y upper boundary
                EtY=EY>=EYmin & EY<EYmax; %Filtering the data to keep only
data point found into the Y Edges of the bin

                ET=ET(EtY);
                ER=ER(EtY);
                EY=EY(EtY);
                Eid=Eid(EtY);

                for rr=1:nbbinR
                    EET=ET; %Set the matrix of locations
                    EER=ER;
                    EEY=EY;
                    EEid=Eid;

                    EERmin=EdgesR(rr); %Selecting the bin R lower boundary
                    EERmax=EdgesR(rr+1); %Selecting the bin R upper boundary
                    EEtR=EER>=EERmin & EER<EERmax; %Filtering the data to
keep only data point found into the R Edges of the bin

                    EET=EET(EEtR);
                    EER=EER(EEtR);
                    EEY=EEY(EEtR);
                    EEid=EEid(EEtR);

                    nbpoints=length(EET); % Counting how many locations
remains in the Y and R boundaries
                    MatRCount(rr,jj)=nbpoints;% Writting the number of
location in the bin
                    MatRVol(rr,jj)=pi()*((EdgesR(rr)+binsize)^2-
EdgesR(rr)^2)*binsize; %Writting the volume of the bin (mm3)
                    MatRCenterR(rr,jj)=EdgesR(rr)+binsize/2; %Writting the
bin center R coordinate
                    MatRCenterY(rr,jj)=EdgesY(jj)+binsize/2;

                    id1=EEid; % Getting the id of each location in the bin

                    Tbin=0; % Initialisation of time count
                    Ybin=0;
                    Rbin=0;
                    Abin=0;
                    vYbin=0;
                    vMbin=0;
                    vRbin=0;
                    vAbin=0;
                    % section to add -
                    if nbpoints>=MinNumPtsBin;
                        for iT=1:nbpoints
                            if id1(iT)-1<1 %if first point of whole data set
                                Tbin=Tbin+(Tfit(id1(iT)+1)-Tfit(id1(iT)));
                            else
                                if Tfit(id1(iT))-Tfit(id1(iT)-
1)>MaxTimeInterval
```

```matlab
                                                Tbin=Tbin+(Tfit(id1(iT)+1)-
Tfit(id1(iT))); % If first point of pass use following point
                                    else
                                                Tbin=Tbin+(Tfit(id1(iT))-Tfit(id1(iT)-
1)); % If not first point use previous point
                                    end
                            end
                    end

                    Ybin=Yfit(id1);
                    Rbin=Rfit(id1);
                    Abin=Afit(id1);
                    vYbin=vYfit(id1);
                    vMbin=vMfit(id1);
                    vRbin=vRfit(id1);
                    vAbin=vAfit(id1);

                    MatRT(rr,jj)=Tbin;
                    MatRvMdis{rr,jj}=vMbin;
                    MatRvMmean(rr,jj)=mean(vMbin);
                    MatRvMmode(rr,jj)=mode(vMbin);
                    MatRvMstd(rr,jj)=std(vMbin);
                    MatRvRmean(rr,jj)=mean(vRbin);
                    MatRvRmode(rr,jj)=mode(vRbin);
                    MatRvRstd(rr,jj)=std(vRbin);
                    MatRvYmean(rr,jj)=mean(vYbin);
                    MatRvYmode(rr,jj)=mode(vYbin);
                    MatRvYstd(rr,jj)=std(vYbin);
                    MatRvAmean(rr,jj)=mean(vAbin);
                    MatRvAmode(rr,jj)=mode(vAbin);
                    MatRvAstd(rr,jj)=std(vAbin);
                end
            end

            MatRCount(MatRCount==0)=NaN;
            MatRT(MatRT==0)=NaN;
            MatRVol(MatRVol==0)=NaN;
            %MatRvM(MatRvM==0)=NaN;
            MatRvMmean(MatRvMmean==0)=NaN;
            MatRvRmean(MatRvRmean==0)=NaN;
            MatRvYmean(MatRvYmean==0)=NaN;
            MatRvAmean(MatRvAmean==0)=NaN;
        end

            %%%%%%%%%%%%%%%%%%%%%%%% FIGURES OUTPUT
%%%%%%%%%%%%%%%%%%%%%%%%%%%%


save('velocitydata','MatRvMdis','MatRvMmean','MatRvMstd','MatRvRmean','MatRvA
mean','MatRvYmean','MatRCount','MatRVol')
            save('plotxandy','MatRCenterR','MatRCenterY')

            %DISPLAY VELOCITY PROFIL (TOROID BINS)
            %-------------------------------------------------------------
---------%
            figure (11)
```

```matlab
            quiver(MatRCenterR-binsize/2, MatRCenterY-binsize/2, MatRvRmean,
MatRvYmean,1,'color','k') %Be carefull with scale
            axis equal
            grid on
            axis([Rmin Rmax-binsize Ymin Ymax-binsize])
            box on
            xlabel('Radius (mm)','FontSize',20)
            ylabel('Elevation (mm)','FontSize',20)
            set(gca,'FontSize',20)


            %DISPLAY VELOCITY MAGNITUDE (TOROID BINS)
            %-------------------------------------------------------------
---------%
            figure(14)
            subplot(1,3,1)
            C=MatRvMmean;
            surf(MatRCenterR-binsize/2,MatRCenterY-binsize/2,MatRvMmean,C);
            col = colorbar;
            ylabel(col,'Mean Velocity magnitude (m/s)','FontSize',20);
            caxis([0,8])
            colormap(hot)
            axis equal
            axis([Rmin Rmax-binsize Ymin Ymax-binsize])
            box on
            xlabel('Radius (mm)','FontSize',20);
            ylabel('Elevation (mm)','FontSize',20);
            %zlabel('Z (mm)','FontSize',20);
            set(gca,'FontSize',20)
            view(2);

            subplot(1,3,2)
            C=MatRCount;
            surf(MatRCenterR-binsize/2,MatRCenterY-binsize/2,MatRCount,C);
            col = colorbar;
            ylabel(col,'Mode Velocity magnitude (m/s)','FontSize',20);
            caxis([0,500])
            colormap(hot)
            axis equal
            axis([Rmin Rmax-binsize Ymin Ymax-binsize])
            box on
            xlabel('Radius (mm)','FontSize',20);
            ylabel('Elevation (mm)','FontSize',20);
            %zlabel('Z (mm)','FontSize',20);
            set(gca,'FontSize',20)
            view(2);

            subplot(1,3,3)
            C=MatRvMstd;
            surf(MatRCenterR-binsize/2,MatRCenterY-binsize/2,MatRvMstd,C);
            col = colorbar;
            ylabel(col,'Std Velocity magnitude (m/s)','FontSize',20);
            caxis([0,3])
            colormap(hot)
            axis equal
```

```matlab
axis([Rmin Rmax-binsize Ymin Ymax-binsize])
box on
xlabel('Radius (mm)','FontSize',20);
ylabel('Elevation (mm)','FontSize',20);
%zlabel('Z (mm)','FontSize',20);
set(gca,'FontSize',20)
view(2);

figure (141)
plot(MatRCount(:),MatRvMstd(:),'.');

%DISPLAY VERTICAL VELOCITY (TOROID BINS)
%-----------------------------------------------------------------
---------%
figure(15)
subplot(1,3,1)
C=MatRvRmean;
surf(MatRCenterR-binsize/2,MatRCenterY-binsize/2,MatRvRmean,C);
col = colorbar;
ylabel(col,'Radial velocity (m/s)','FontSize',20);
caxis([-3,3])
colormap(hot)
axis equal
axis([Rmin Rmax-binsize Ymin Ymax-binsize])
box on
xlabel('Radius (mm)','FontSize',20);
ylabel('Elevation (mm)','FontSize',20);
%zlabel('Z (mm)','FontSize',20);
set(gca,'FontSize',20)
view(2);

%DISPLAY ANGULAR VELOCITY (TOROID BINS)
%-----------------------------------------------------------------
---------%
subplot(1,3,2)
C=MatRvAmean;
surf(MatRCenterR-binsize/2,MatRCenterY-binsize/2,MatRvAmean,C);
col = colorbar;
ylabel(col,'Angular velocity (rad/s)','FontSize',20);
caxis([0,1000])
colormap(hot)
axis equal
axis([Rmin Rmax-binsize Ymin Ymax-binsize])
box on
xlabel('Radius (mm)','FontSize',20);
ylabel('Elevation (mm)','FontSize',20);
%zlabel('Z (mm)','FontSize',20);
set(gca,'FontSize',20)
view(2);

subplot(1,3,3)
C=MatRvYmean;
surf(MatRCenterR-binsize/2,MatRCenterY-binsize/2,MatRvYmean,C);
col = colorbar;
ylabel(col,'Vertical velocity (m/s)','FontSize',20);
caxis([-3,1])
```

```matlab
            colormap(hot)
            axis equal
            axis([Rmin Rmax-binsize Ymin Ymax-binsize])
            box on
            xlabel('Radius (mm)','FontSize',20);
            ylabel('Elevation (mm)','FontSize',20);
            %zlabel('Z (mm)','FontSize',20);
            set(gca,'FontSize',20)
            view(2);


        end
    end
end


%%%%%%%%%%%% END TOROID BINNING (WRAPPING INTO SINGLE PLANE) %%%%%%%%%%%%

%%%%%%%%%% CUBIC BINNING (For volume averaging of quantities)%%%%%%%%%%%%


if SwitchVolumetricBinning==1
    if SwitchDataFit==1 || SwitchReuseDataFit==1
        if SwitchVelocityCalculations==0
            disp(['SwitchVelocityCalculations must be turned on for Cubic
Binning'])
        else
            %Cartesian Coordinates
            binsize=BinSize; % Edge length of the cubic occupancy bin (mm)

            EdgesX=[Xmin:binsize:Xmax]; % Creating the bin boundaries
            EdgesY=[Ymin:binsize:Ymax];
            EdgesZ=[Zmin:binsize:Zmax];

            nbbinX=(length(EdgesX)-1); % Counting the bins
            nbbinY=(length(EdgesY)-1);
            nbbinZ=(length(EdgesZ)-1);
            nbbin=nbbinX*nbbinY*nbbinZ;
            bincount=0;

            MatCount=zeros(nbbinX,nbbinY,nbbinZ); %Initialisation of a 3D
matrix to count location in the bins.

            MatCenterX=MatCount; %Initialisation of a 3D matrix to store X
location of the center of the bins.
            MatCenterY=MatCount;
            MatCenterZ=MatCount;

            MatTime=MatCount; %Initialisation of a 3D matrix to store the
Time in the bin.
            % MatX=MatCount; %Initialisation of a 3D matrix to store the X
axis travel distance in the bin.
            % MatY=MatCount;
            % MatZ=MatCount;
            MatvX=MatCount; %Initialisation of a 3D matrix to store X speed
in the bin.
            MatvY=MatCount;
            MatvZ=MatCount;
```

234

```matlab
            %MatR=MatCount;
            MatvR=MatCount;
            MatvA=MatCount;

            for kk=1:nbbinZ
                ET=Tfit; %Reset the matrix of locations
                EX=Xfit;
                EY=Yfit;
                EZ=Zfit;
                Eid=idfit;

                EZmin=EdgesZ(kk); %Selecting the bin Z lower boundary
                EZmax=EdgesZ(kk+1); %Selecting the bin Z upper boundary
                EtZ=EZ>=EZmin & EZ<EZmax; %Filtering the data to keep only
data point found into the Z Edges of the bin

                ET=ET(EtZ);
                EX=EX(EtZ);
                EY=EY(EtZ);
                EZ=EZ(EtZ);
                Eid=Eid(EtZ);

                for jj=1:nbbinY
                    EET=ET; %Reset the matrix of locations
                    EEX=EX;
                    EEY=EY;
                    EEZ=EZ;
                    EEid=Eid;

                    EEYmin=EdgesY(jj); %Selecting the bin Y lower boundary
                    EEYmax=EdgesY(jj+1); %Selecting the bin Y upper boundary
                    EEtY=EEY>=EEYmin & EEY<EEYmax; %Filtering the data to
keep only data point found into the Y Edges of the bin

                    EET=EET(EEtY);
                    EEX=EEX(EEtY);
                    EEY=EEY(EEtY);
                    EEZ=EEZ(EEtY);
                    EEid=EEid(EEtY);

                    for ii=1:nbbinX
                        EEET=EET; %Reset the matrix of locations
                        EEEX=EEX;
                        EEEY=EEY;
                        EEEZ=EEZ;
                        EEEid=EEid;

                        EEEXmin=EdgesX(ii); %Selecting the bin X lower
boundary
                        EEEXmax=EdgesX(ii+1); %Selecting the bin X upper
boundary
                        EEEtX=EEEX>=EEEXmin & EEEX<EEEXmax; %Filtering the
data to keep only data point found into the X Edges of the bin

                        EEET=EEET(EEEtX);
```

```matlab
                            EEEX=EEEX(EEEtX);
                            EEEY=EEEY(EEEtX);
                            EEEZ=EEEZ(EEEtX);
                            EEEid=EEEid(EEEtX);

                            nbpoints=length(EEET); % Counting how many locations
                            MatCount(ii,jj,kk)=nbpoints; % Writting the number of
location in the bin
                            MatCenterX(ii,jj,kk)=EdgesX(ii)+binsize/2; %Writting
the bin center X coordinate
                            MatCenterY(ii,jj,kk)=EdgesY(jj)+binsize/2;
                            MatCenterZ(ii,jj,kk)=EdgesZ(kk)+binsize/2;

                            id1=EEEid; % Getting the id of each location in the
bin
                            Tbin=0; % Initialisation of time count
                            Xbin=0; % Initialisation of distance count
                            Ybin=0;
                            Zbin=0;
                            Rbin=0;
                            Abin=0;
                            vXbin=0;
                            vYbin=0;
                            vZbin=0;
                            vRbin=0;
                            vAbin=0;


                            bincount=bincount+1;

                            if length(id1)>1
                                for iT=1:nbpoints
                                    Tbin=Tbin+Tfit(id1(iT));

                                    Xbin=Xbin+Xfit(id1(iT));
                                    Ybin=Ybin+Yfit(id1(iT));
                                    Zbin=Zbin+Zfit(id1(iT));
                                    Rbin=Rbin+Rfit(id1(iT));
                                    Abin=Abin+Afit(id1(iT));
                                    vXbin=vXbin+vXfit(id1(iT));
                                    vYbin=vYbin+vYfit(id1(iT));
                                    vZbin=vZbin+vZfit(id1(iT));
                                    vRbin=vRbin+vRfit(id1(iT));
                                    vAbin=vAbin+vAfit(id1(iT));

                                end
                                MatTime(ii,jj,kk)=Tbin;
                                MatvX(ii,jj,kk)=vXbin/nbpoints;
                                MatvY(ii,jj,kk)=vYbin/nbpoints;
                                MatvZ(ii,jj,kk)=vZbin/nbpoints;
                                MatvR(ii,jj,kk)=vRbin/nbpoints;
                                MatvA(ii,jj,kk)=vAbin/nbpoints;
                            else
                            end
                    end
```

```matlab
            end
%         clc;
%             percent_bin=bincount/nbbin*100
        end


        end
    end
end


%%%%%%%%%%%%%%%%%%%%%%%%%%%%%%%%%%%%%%%%%%%%%%%%%%%%%%%%%%%%%%%%%%%%%%%%%%%%%
%%%%%%%%%%%%%%%%%%%%%%%%%%%%%%%%%%%%%%%

% %DISPLAY 3D LOCATIONS COLORED BY VELOCITY MAGNITUDE
% %-------------------------------------------------------------------------%
% figure(67)
% NbPart=500; %Number of particle wanted in the animation
% NbLoc=20; %Number of location shown on the trace
%
% Tmarker=linspace(min(T),max(T),NbPart+1); %Time stamp to start trace
% NbFrame=length(T)/length(Tmarker-1)-NbLoc; %Number of point per time
interval
% Frate=(length(T)/length(Tmarker-1))/((max(T)-min(T))/length(Tmarker-1));
%Real frame rate
%
% NbFrame=floor(NbFrame)
% Frate=floor(Frate)
%
% for i=1:(NbFrame)
%     g=figure('position', [0, 0, 700, 850]); %700 900
%
% %     for n=1:length(R)-1
% %         [x1 z1
y1]=pol2cart((0+pi/2:maxA/nbp:maxA+pi/2),R(n),Zfull(:,n)');
% %         [x2 z2
y2]=pol2cart((0+pi/2:maxA/nbp:maxA+pi/2),R(n+1),Zfull(:,n+1)');
% %         surface([x1;x2],[y1;y2],[z1;z2],'FaceColor','[0.6 0.6
0.6]','FaceAlpha',0.3,'EdgeColor','[0.4 0.4 0.4]','EdgeAlpha',0.7);
% %     end
%
%     for j=1:NbPart
%         startI=j*NbFrame+i; %Starting index of the trace for each trace
%         stopI=startI+NbLoc; %Final index of the trace for each trace
%         %         hold on
%         %         scatter(X(startI),Y(startI),Z(startI))
%         hold on
%         if T(stopI)-T(startI)<5 %Time in seconds between passes
%             h = surface([X(startI:stopI), X(startI:stopI)],
[Y(startI:stopI), Y(startI:stopI)], [Z(startI:stopI),
Z(startI:stopI)],[vM(startI:stopI),
vM(startI:stopI)],'LineWidth',3,'EdgeColor','flat', 'FaceColor','none');
%         else
%         end
%     end
%
%     hold off
%     colormap cool
```

```matlab
%       col = colorbar;
%       ylabel(col,'Velocity Magnitude (m/s)','FontSize',14);
%       axis equal
%       caxis([0,8])
%       axis([-50 100 320 400 -100 50]);
%       xlabel('X (mm)','FontSize',14);
%       ylabel('Y (mm)','FontSize',14);
%       zlabel('Z (mm)','FontSize',14);
%       grid off
%       set(gca,'FontSize',14)
%       AZ=0;
%       EL=0;
%       view(AZ,EL);
%       %view(2)
%       %camorbit(-40,25,'camera') %50 15
%       %campos([-400 -30 740])
%       %camorbit(i*2,5,'camera')
%
%       fig=gcf;
%       fig.PaperUnits='inches';
%       fig.PaperPosition = [0 0 7 8.5];
%
%       I=getframe(gcf);
%       imwrite(I.cdata,sprintf('FIG%d.png',i));
%       %print(sprintf('FIG%d.png',i),'-dpng','-r150')
%       %saveas(g,sprintf('FIG%d.png',i)); %Save the image
%       clc;
%       close all;
%       NbFrame
%       Frate
%       percent_printing_images=i/NbFrame*100
%   end
% figure(6666)
%   subplot(3,1,1)
%       plot(Tfit,Xfit,'ro','LineWidth',2,'MarkerSize',5);
%       hold on
%       plot(T,X,'bo','LineWidth',1,'MarkerSize',3);
%       axis([Tmin Tmax Xmin Xmax])
%       xlabel('T (s)','FontSize',20);
%       ylabel('X (mm)','FontSize',20);
%       grid on
%       legend('Fit', 'Initial locations')
%       set(gca,'FontSize',20)

%%%%%%%% MOVIE -- DISPLAY 3D LOCATIONS COLORED BY VELOCITY MAGNITUDE %%%%%%
if SwitchMovie==1;

    close all
    NbPart=15000; %Number of particle wanted in the animation
    NbLoc=20; %Number of location shown on the trace

    Tmarker=linspace(min(Tfit),max(Tfit),NbPart+1); %Time stamp to start
trace
    NbFrame=length(Tfit)/length(Tmarker-1)-NbLoc; %Number of point per time
interval
```

```matlab
    Frate=(length(Tfit)/length(Tmarker-1))/((max(Tfit)-
min(Tfit))/length(Tmarker-1)); %Real frame rate


    NbFrame=floor(NbFrame)
    Frate=floor(Frate)



    for i=1:(NbFrame)
        g=figure('position', [0, 0, 700, 850]); %700 900

        %       for n=1:length(R)-1
        %               [x1 z1
y1]=pol2cart((0+pi/2:maxA/nbp:maxA+pi/2),R(n),Zfull(:,n)');
        %               [x2 z2
y2]=pol2cart((0+pi/2:maxA/nbp:maxA+pi/2),R(n+1),Zfull(:,n+1)');
        %               surface([x1;x2],[y1;y2],[z1;z2],'FaceColor','[0.6 0.6
0.6]','FaceAlpha',0.3,'EdgeColor','[0.4 0.4 0.4]','EdgeAlpha',0.7);
        %       end

        for j=1:NbPart
            startI=j*NbFrame+i; %Starting index of the trace for each trace
            stopI=startI+NbLoc; %Final index of the trace for each trace
            %           hold on
            %           scatter(X(startI),Y(startI),Z(startI))
            hold on
            if Tfit(stopI)-Tfit(startI)<5 %Time in seconds between passes
                h = surface([Xfit(startI:stopI), Xfit(startI:stopI)],
[Yfit(startI:stopI), Yfit(startI:stopI)], [Zfit(startI:stopI),
Zfit(startI:stopI)],[vMfit(startI:stopI),
vMfit(startI:stopI)],'LineWidth',3,'EdgeColor','flat', 'FaceColor','none');
            else
            end
        end

        hold off
        colormap cool
        col = colorbar;
        ylabel(col,'Velocity Magnitude (m/s)','FontSize',14);
        axis equal
        caxis([0,8])
        axis([-50 100 320 400 -100 50]);
        xlabel('X (mm)','FontSize',14);
        ylabel('Y (mm)','FontSize',14);
        zlabel('Z (mm)','FontSize',14);
        grid off
        set(gca,'FontSize',14)
        AZ=0;
        EL=0;
        view(AZ,EL);
        %view(2)
        %camorbit(-40,25,'camera') %50 15
        %campos([-400 -30 740])
        %camorbit(i*2,5,'camera')

        fig=gcf;
```

```matlab
        fig.PaperUnits='inches';
        fig.PaperPosition = [0 0 7 8.5];

        I=getframe(gcf);
        imwrite(I.cdata,sprintf('FIG%d.png',i));
        %print(sprintf('FIG%d.png',i),'-dpng','-r150')
        %saveas(g,sprintf('FIG%d.png',i)); %Save the image
        clc;
        close all;
        NbFrame
        Frate
        percent_printing_images=i/NbFrame*100
    end




    %COMBINE FRAME INTO VIDEO

    writerObj = VideoWriter('hydrovid.avi');
    writerObj.FrameRate=Frate/500;
    %writerObj.Quality=100;
    open(writerObj);
    %Number of repeats
    for ww=1:10
        for K = 1 : NbFrame
            clc;
            NbFrame
            Frate
            percent_video_writing=K/NbFrame*100+ww*100


            filename = sprintf('FIG%d.png', K);
            thisimage = imread(filename);
            writeVideo(writerObj, thisimage);
        end
    end
    close(writerObj);
end
```

Appendix C: Figure and Coauthor Permissions

Appendix C.1 Figure Permissions

ELSEVIER LICENSE
TERMS AND CONDITIONS

Nov 10, 2017

This Agreement between McGill University -- Joshua Sovechles ("You") and Elsevier ("Elsevier") consists of your license details and the terms and conditions provided by Elsevier and Copyright Clearance Center.

License Number	4225440252535
License date	Nov 10, 2017
Licensed Content Publisher	Elsevier
Licensed Content Publication	Global Environmental Change
Licensed Content Title	Resource depletion, peak minerals and the implications for sustainable resource management
Licensed Content Author	T. Prior,D. Giurco,G. Mudd,L. Mason,J. Behrisch
Licensed Content Date	Aug 1, 2012
Licensed Content Volume	22
Licensed Content Issue	3
Licensed Content Pages	11
Start Page	577
End Page	587
Type of Use	reuse in a thesis/dissertation
Intended publisher of new work	other
Portion	figures/tables/illustrations
Number of figures/tables/illustrations	2
Format	both print and electronic
Are you the author of this Elsevier article?	No
Will you be translating?	No
Original figure numbers	Figure 1 and Figure 3
Title of your thesis/dissertation	EXPLORING PARTICLE FLOW IN A HYDROCYCLONE CLASSIFIER THROUGH POSITRON EMISSION PARTICLE TRACKING (PEPT)
Expected completion date	Dec 2017
Estimated size (number of pages)	150
Requestor Location	McGill University 3610 Rue University Montreal, QC H3A 0C5 Canada Attn: McGill University
Total	0.00 CAD
Terms and Conditions	

ELSEVIER LICENSE
TERMS AND CONDITIONS

Feb 28, 2018

This Agreement between McGill University -- Joshua Sovechles ("You") and Elsevier ("Elsevier") consists of your license details and the terms and conditions provided by Elsevier and Copyright Clearance Center.

License Number	4225440640745
License date	Nov 10, 2017
Licensed Content Publisher	Elsevier
Licensed Content Publication	Chemical Engineering Science
Licensed Content Title	Mechanistic modelling of water partitioning behaviour in hydrocyclone
Licensed Content Author	Chandranath Banerjee,Eric Climent,Arun Kumar Majumder
Licensed Content Date	Oct 2, 2016
Licensed Content Volume	152
Licensed Content Issue	n/a
Licensed Content Pages	12
Start Page	724
End Page	735
Type of Use	reuse in a thesis/dissertation
Intended publisher of new work	other
Portion	figures/tables/illustrations
Number of figures/tables/illustrations	1
Format	both print and electronic
Are you the author of this Elsevier article?	No
Will you be translating?	No
Original figure numbers	Figure 2
Title of your thesis/dissertation	EXPLORING PARTICLE FLOW IN A HYDROCYCLONE CLASSIFIER THROUGH POSITRON EMISSION PARTICLE TRACKING (PEPT)
Expected completion date	Dec 2017
Estimated size (number of pages)	150
Requestor Location	McGill University 3610 Rue University
	Montreal, QC H3A 0C5 Canada Attn: McGill University
Total	0.00 USD

Terms and Conditions

242

ELSEVIER LICENSE
TERMS AND CONDITIONS

Feb 28, 2018

This Agreement between McGill University -- Joshua Sovechles ("You") and Elsevier
("Elsevier") consists of your license details and the terms and conditions provided by
Elsevier and Copyright Clearance Center.

License Number	4225440494042
License date	Nov 10, 2017
Licensed Content Publisher	Elsevier
Licensed Content Publication	Minerals Engineering
Licensed Content Title	Two empirical hydrocyclone models revisited
Licensed Content Author	K Nageswararao,D.M Wiseman,T.J Napier-Munn
Licensed Content Date	May 1, 2004
Licensed Content Volume	17
Licensed Content Issue	5
Licensed Content Pages	17
Start Page	671
End Page	687
Type of Use	reuse in a thesis/dissertation
Intended publisher of new work	other
Portion	figures/tables/illustrations
Number of figures/tables/illustrations	2
Format	both print and electronic
Are you the author of this Elsevier article?	No
Will you be translating?	No
Original figure numbers	Figure 1 and Figure 2
Title of your thesis/dissertation	EXPLORING PARTICLE FLOW IN A HYDROCYCLONE CLASSIFIER THROUGH POSITRON EMISSION PARTICLE TRACKING (PEPT)
Expected completion date	Dec 2017
Estimated size (number of pages)	150
Requestor Location	McGill University 3610 Rue University
	Montreal, QC H3A 0C5 Canada Attn: McGill University
Total	0.00 USD
Terms and Conditions	

243

**ELSEVIER LICENSE
TERMS AND CONDITIONS**

Feb 28, 2018

This Agreement between McGill University -- Joshua Sovechles ("You") and Elsevier ("Elsevier") consists of your license details and the terms and conditions provided by Elsevier and Copyright Clearance Center.

License Number	4225441302731
License date	Nov 10, 2017
Licensed Content Publisher	Elsevier
Licensed Content Publication	Separation and Purification Technology
Licensed Content Title	Numerical simulation of industrial hydrocyclones performance: Role of turbulence modelling
Licensed Content Author	Teja Reddy Vakamalla,Narasimha Mangadoddy
Licensed Content Date	Apr 4, 2017
Licensed Content Volume	176
Licensed Content Issue	n/a
Licensed Content Pages	17
Start Page	23
End Page	39
Type of Use	reuse in a thesis/dissertation
Intended publisher of new work	other
Portion	figures/tables/illustrations
Number of figures/tables/illustrations	1
Format	both print and electronic
Are you the author of this Elsevier article?	No
Will you be translating?	No
Original figure numbers	Figure 3
Title of your thesis/dissertation	EXPLORING PARTICLE FLOW IN A HYDROCYCLONE CLASSIFIER THROUGH POSITRON EMISSION PARTICLE TRACKING (PEPT)
Expected completion date	Dec 2017
Estimated size (number of pages)	150
Requestor Location	McGill University 3610 Rue University
	Montreal, QC H3A 0C5 Canada Attn: McGill University
Total	0.00 USD

Terms and Conditions

244

ELSEVIER LICENSE
TERMS AND CONDITIONS

Feb 28, 2018

This Agreement between McGill University -- Joshua Sovechles ("You") and Elsevier ("Elsevier") consists of your license details and the terms and conditions provided by Elsevier and Copyright Clearance Center.

License Number	4225441163652
License date	Nov 10, 2017
Licensed Content Publisher	Elsevier
Licensed Content Publication	Computers & Chemical Engineering
Licensed Content Title	Quantification of numerical uncertainty in computational fluid dynamics modelling of hydrocyclones
Licensed Content Author	M. Karimi,G. Akdogan,K.H. Dellimore,S.M. Bradshaw
Licensed Content Date	Aug 10, 2012
Licensed Content Volume	43
Licensed Content Issue	n/a
Licensed Content Pages	10
Start Page	45
End Page	54
Type of Use	reuse in a thesis/dissertation
Intended publisher of new work	other
Portion	figures/tables/illustrations
Number of figures/tables/illustrations	2
Format	both print and electronic
Are you the author of this Elsevier article?	No
Will you be translating?	No
Original figure numbers	Figure 5 and Figure 7
Title of your thesis/dissertation	EXPLORING PARTICLE FLOW IN A HYDROCYCLONE CLASSIFIER THROUGH POSITRON EMISSION PARTICLE TRACKING (PEPT)
Expected completion date	Dec 2017
Estimated size (number of pages)	150
Requestor Location	McGill University 3610 Rue University Montreal, QC H3A 0C5 Canada Attn: McGill University
Total	0.00 USD

Terms and Conditions

245

Copyright Clearance Center

RightsLink®

Chapter:	Chapter 9 Classification
Book:	Wills' Mineral Processing Technology
Author:	Barry A. Wills, James A. Finch
Publisher:	Elsevier
Date:	Jan 1, 2016

Copyright © 2016 Elsevier Ltd. All rights reserved.

Logged in as:
Joshua Sovechles
McGill University
Account #:
3001189452

LOGOUT

ELSEVIER

Order Completed

Thank you for your order.

This Agreement between Joshua M Sovechles ("You") and Elsevier ("Elsevier") consists of your order details and the terms and conditions provided by Elsevier and Copyright Clearance Center.

License number	Reference confirmation email for license number
License date	Sep, 11 2017
Licensed Content Publisher	Elsevier
Licensed Content Publication	Elsevier Books
Licensed Content Title	Wills' Mineral Processing Technology
Licensed Content Author	Barry A. Wills, James A. Finch
Licensed Content Date	2016
Licensed Content Volume	n/a
Licensed Content Issue	n/a
Licensed Content Pages	23
Type of Use	reuse in a thesis/dissertation
Portion	figures/tables/illustrations
Number of figures/tables/illustrations	10
Format	both print and electronic
Are you the author of this Elsevier chapter?	No
Will you be translating?	No
Original figure numbers	Figure 9.3, Figure 9.4, Figure 9.5, Figure 9.9, Figure 9.10, Figure 9.12, Figure 9.13, Figure 9.17, Figure 9.18, Figure 9.21
Title of your thesis/dissertation	EXPLORING PARTICLE FLOW IN A HYDROCYCLONE CLASSIFIER THROUGH POSITRON EMISSION PARTICLE TRACKING (PEPT)
Expected completion date	Dec 2017
Estimated size (number of pages)	150
Requestor Location	McGill University 3610 Rue University
	Montreal, QC H3A 0C5 Canada Attn: McGill University
Billing Type	Invoice
Billing address	McGill University 3610 Rue University
	Montreal, QC H3A 0C5 Canada Attn: McGill University
Total	0.00 USD

CLOSE WINDOW

Appendix C.2 Author Permissions

Appendix C.2.1 Darryel Boucher

Josh Sovechles

From:	darryel.boucher@gmail.com on behalf of Darryel Boucher <darryel.boucher@mail.mcgill.ca>
Sent:	Tuesday, 12 December 2017 1:14 PM
To:	Josh Sovechles; Kristian Edmund Waters, Prof
Subject:	Permission to use papers in Thesis

I, Darryel Boucher, as a co-author of 'Performance analysis of a new positron camera geometry for high speed, fine particle tracking.' and 'Improvements in positron emission particle tracking within a hydrocyclone.' allow Joshua Sovechles to submit these papers as part of his manuscript based PhD thesis submitted to McGill titled EXPLORING PARTICLE FLOW IN A HYDROCYCLONE CLASSIFIER THROUGH POSITRON EMISSION PARTICLE TRACKING (PEPT).

Darryel Boucher Ph.D., Jr. Eng.
Mineral Processing Group
McGill University, Wong Building
3610 University Street,
Montreal, Quebec, Canada, H3A 0C5

P. 1 514 632 1224
E. darryel.boucher@mail.mcgill.ca

Appendix C.2.2 Luis Vinnett

Josh Sovechles

From:	Luis Vinnett
Sent:	Tuesday, 12 December 2017 4:28 AM
To:	Josh Sovechles
Cc:	Kristian Edmund Waters, Prof
Subject:	Permission to use paper in Thesis

I, Luis Vinnett, as a co-author of 'Improvements in positron emission particle tracking within a hydrocyclone.' allow Joshua Sovechles to submit this paper as part of his manuscript based PhD thesis submitted to McGill titled EXPLORING PARTICLE FLOW IN A HYDROCYCLONE CLASSIFIER THROUGH POSITRON EMISSION PARTICLE TRACKING (PEPT).

Signed,

Luis Vinnett

Appendix C.2.3 Ray Langlois

I, Ray Langlois, as a co-author of *'Improvements in positron emission particle tracking within a hydrocyclone.'* allow Joshua Sovechles to submit this paper as part of his manuscript based PhD thesis submitted to McGill titled EXPLORING PARTICLE FLOW IN A HYDROCYCLONE CLASSIFIER THROUGH POSITRON EMISSION PARTICLE TRACKING (PEPT).

Signed,

Ray Langlois

Ray Langlois DEC 8, 2017

Appendix C.2.4 Randolph Pax

Josh Sovechles

From:	Randolph Pax <rpax@rapind.com.au>
Sent:	Friday, 8 December 2017 8:48 AM
To:	Josh Sovechles
Cc:	Kristian Edmund Waters, Prof
Subject:	Permission to use papers in Thesis

I, Randolph Pax, as a co-author of *'Performance analysis of a new positron camera geometry for high speed, fine particle tracking.'* and *'Improvements in positron emission particle tracking within a hydrocyclone.'* allow Joshua Sovechles to submit these papers as part of his manuscript based PhD thesis submitted to McGill titled EXPLORING PARTICLE FLOW IN A HYDROCYCLONE CLASSIFIER THROUGH POSITRON EMISSION PARTICLE TRACKING (PEPT).

Signed,

Randolph Pax

RAP Innovation and Development Pty Ltd
Randolph A Pax, *Principal*

PO Box 559, Indooroopilly, Qld, Australia, 4068
Ph: +61 (0)438 007 232
Email: rpax@rapind.com.au
Skype: rapaxaust
Web: www.rapind.com.au

Appendix C.2.5 Thomas Leadbeater

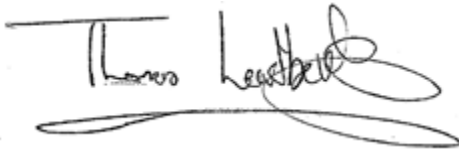|	
From:	Tom Leadbeater <tom.leadbeater@uct.ac.za>
Sent:	Wednesday, 20 December 2017 8:17 PM
To:	Kristian Edmund Waters, Prof; Josh Sovechles
Subject:	Permission to use papers in Thesis

I, Thomas Leadbeater, as a co-author of *'Performance analysis of a new positron camera geometry for high speed, fine particle tracking.'* and *'Improvements in positron emission particle tracking within a hydrocyclone.'* allow Joshua Sovechles to submit these papers as part of his manuscript based PhD thesis submitted to McGill titled EXPLORING PARTICLE FLOW IN A HYDROCYCLONE CLASSIFIER THROUGH POSITRON EMISSION PARTICLE TRACKING (PEPT).

Signed,

Thomas Leadbeater

Dept. Physics,
University of Cape Town,
Rondebosch,
Cape Town,
South Africa

Disclaimer - University of Cape Town This email is subject to UCT policies and email disclaimer published on our website at http://www.uct.ac.za/main/email-disclaimer or obtainable from +27 21 650 9111. If this email is not related to the business of UCT, it is sent by the sender in an individual capacity. Please report security incidents or abuse via https://csirt.uct.ac.za/page/report-an-incident.php.